

<b>REPORT DOCUMENTATION PAGE</b>			<i>Form Approved OMB No. 0704-0188</i>
<p>Public reporting burden for this collection of information is estimated to average 1 hour per response, including the time for reviewing instructions, searching existing data sources, gathering and maintaining the data needed, and completing and reviewing the collection of information. Send comments regarding this burden estimate of any aspect of this collection of information, including suggestions for reducing this burden, to Washington Headquarters Services, Directorate for Information Operations and Reports, 1215 Jefferson Davis Highway, Suite 1204, Arlington, VA 22202-4302, and to the office of Management and Budget, Paperwork Reduction Project (0704-0188), Washington, DC 20503.</p>			
<b>1. AGENCY USE ONLY</b> (Leave Blank)	<b>2. REPORT DATE</b> (MM/DD/YYYY)	<b>3. REPORT TYPE AND DATES COVERED</b>	
	07/07/1999	Final Technical Report, 07/10/1995 – 06/30/1999	
<b>4. TITLE AND SUBTITLE</b> Optimization of Textile Composite Toughness		<b>5. FUNDING NUMBERS</b> DAAH04-95-C-0050	
<b>6. AUTHOR(S)</b> Brian Cox			
<b>7. PERFORMING ORGANIZATION NAME(S) AND ADDRESSES</b> Rockwell Science Center, LLC 1049 Camino Dos Rios Thousand Oaks, CA 91360		<b>8. PERFORMING ORGANIZATION REPORT NUMBER</b> SC71113.FTR	
<b>9. SPONSORING/MONITORING AGENCY NAME(S) AND ADDRESS(ES)</b> U.S. Army Research Office P.O. Box 12211 Research Triangle Park, NC 27709-2211 Materials Science Division Attn: Dr. Wilbur C. Simmons		<b>10. SPONSORING/MONITORING AGENCY REPORT NUMBER</b>  <i>ARO 33972.1-MS</i>	
<b>11. SUPPLEMENTARY NOTES</b>			
<b>12a. DISTRIBUTION/AVAILABILITY STATEMENT</b> Distribution Unlimited		<b>12b. DISTRIBUTION CODE</b>	
<b>13. ABSTRACT</b> (Maximum 200 Words) <p>We have designed, made, and tested novel composites, including composites of chains, braided composites, and knitted composites, which show exceptionally high energy absorption under tensile loading. Values per unit volume range up to 60 MJ/m<sup>3</sup> and per unit mass up to 25 J/g.</p> <p>Analytical micromechanical models have led to design rules, which indicate that energy absorption per unit volume of up to 250 – 300 MJ/m<sup>3</sup> is attainable with chain composites and energy absorption per unit mass of 50 – 100 J/g with knitted or braided composites.</p> <p>The delocalisation mechanisms that underlie high energy absorption have been demonstrated by ballistic impact tests to continue at strain rates up to 104. In fact, the energy absorption increases at high strain rate, which is attributed to hardening of the polymeric matrix material.</p> <p>A computational model of failure and damage distribution in textile composites called the Binary Model has also been developed. The entire failure sequence, involving multiple, random local failure events, nonlinear load transfer mechanisms, plasticity, multiple matrix cracking, and pullout phenomena has been simulated successfully.</p>			
<b>14. SUBJECT TERMS</b> - Energy absorption, ballistic protection, chain composites, knitted composites, braided composites, lockup mechanisms, delocalised damage, Binary Model, computational model of textile composites		<b>15. NUMBER OF PAGES</b> 265	
<b>16. PRICE CODE</b>			
<b>17. SECURITY CLASSIFICATION OF REPORT</b> UNCLASSIFIED	<b>18. SECURITY CLASSIFICATION OF THIS PAGE</b> UNCLASSIFIED	<b>19. SECURITY CLASSIFICATION OF ABSTRACT</b> UNCLASSIFIED	<b>20. LIMITATION OF ABSTRACT</b> UNCLASSIFIED

NSN 7540-01-280-5500  
F-0045-SC

Standard Form 298 (Rev. 2-89)  
Prescribed by ANSI Std. Z39-18 298-102

## **Table of Contents**

<b>Section</b>		<b>Page</b>
<b>1. INTRODUCTION .....</b>		1
<b>2. STATEMENT OF THE PROBLEM STUDIED .....</b>		1
<b>Energy Absorption under Tensile Loading .....</b>		1
<b>Computational Model of Damage Distribution and Failure in         3D Textile Composites .....</b>		2
<b>3. SUMMARY OF THE MOST IMPORTANT RESULTS .....</b>		2
<b>Energy Absorption .....</b>		2
<b>Chain Composites .....</b>		3
<b>Dynamic Behaviour .....</b>		4
<b>Braided Composites .....</b>		5
<b>Knitted Composites .....</b>		5
<b>Computational Modeling .....</b>		7
<b>4. LIST OF PUBLICATIONS UNDER THIS CONTRACT.....</b>		9
<b>5. LIST OF PARTICIPATING SCIENTIFIC PERSONNEL.....</b>		10
<b>6. HONORS SINCE CONTRACT'S INCEPTION.....</b>		11
<b>7. INVENTIONS AND TECHNOLOGY TRANSFER.....</b>		12
<b>APPENDIX (As listed in Section 4) .....</b>		13

## **1. INTRODUCTION**

This is the final report for our contract No. DAAH04-95-C-0050 "Optimization of Textile Composite Toughness," covering the period July 10, 1995 through June 30, 1999. We will summarize major basic research results in designing, fabricating, and testing several classes of novel composites, including composites of chains, braided composites, and knitted composites. These composites achieve exceptionally high levels of energy absorption under tensile loading. Significant accomplishments include defining optimal reinforcement geometry, developing fabrication methods, determining damage mechanisms in static and dynamic loading, and modeling micromechanical phenomena to develop optimal design rules. We will also report the development of a computational model of failure and damage distribution in textile composites, which is illustrated by an application to understanding the origins of the unusually high work of fracture of 3D interlock weave composites. Leveraging collaborations at UC Santa Barbara and Wright Patterson AFB and activity in transferring the technology we have developed to various applications will be described.

## **2. STATEMENT OF THE PROBLEM STUDIED**

### **Energy Absorption under Tensile Loading**

Our primary goal in this program was to develop novel composites possessing exceptionally high work of fracture and capacity for energy absorption. We are especially interested in energy absorption under tensile loading, which arises in applications including backing plates in vehicular armour systems; body armour; containers subject to internal explosions; and casings designed to contain bursting rotors, turbines, or flywheels. Our solution is to develop a class of composites in which failure is delocalised, so that large volumes of the composite absorb energy before ultimate failure. We set as goals for this initial development work energy absorption levels of 100 MJ/m<sup>3</sup> in a notch insensitive material. This level would exceed anything currently available, being rivaled only by some ductile alloys, which are notch sensitive (vulnerable to localized failure and therefore limited in their energy absorption in practical applications). It

would also rival energy absorption levels achieved in systems of tubes designed to collapse continuously under uniaxial compression, which are popular as crash absorbers in vehicles.

### **Computational Model of Damage Distribution and Failure in 3D Textile Composites**

We sought to develop a computational model of the complex stochastic failure events that occur in a 3D textile composite, taking as a test case the closely studied system of 3D interlock weave composites. The computational model is a generalization of the so-called Binary Model, previously developed for calculating stress and strain distributions in the elastic regime. Our goal was to develop a tool for optimizing the work of fracture of 3D textile composites by understanding the roles of textile architecture and material choice in the failure sequence.

### **3. SUMMARY OF THE MOST IMPORTANT RESULTS**

#### **Energy Absorption**

Most of our research focused on the development and analysis of composites exhibiting delocalized damage. These fall into two main categories: composites of steel chains or other alloy reinforcement that is topologically equivalent to chains in various matrices; and composites of fiber tows braided or knitted into configurations possessing large strain capacity and lock-up mechanisms in epoxy or other polymer matrices. The chain composites are easy to make and possess very attractive energy absorption levels per unit volume.<sup>1</sup> The braided and knitted composites are lighter and therefore possess superior energy absorption per unit mass, making them attractive for weight sensitive applications.

---

<sup>1</sup> B.N. Cox, "Lockup, Chains, and the Delocalization of Damage," *J. Mater. Sci.*, **30**, 4871-4881 (1996).

*Chain Composites*

Our experimental accomplishments in fabricating chain composites and testing them under static loading are reported in [1,2] in our list of publications. Chain composites were made with links of conventional racetrack geometry. The energy absorbed per unit volume ranges up to nearly 60 MJ/m<sup>3</sup> and the specific energy absorption up to 14 J/g, figures comparable to or exceeding the best current candidate materials for energy absorption under tensile loading. The best results were achieved with polycarbonate matrices, but other matrices, including short fiber reinforced polycarbonate or epoxy or elastomers may be better still.

Damage mechanisms were determined and on their basis an analytical model of the failure and energy processes was then developed [3]. The model predicts the stress required to displace the chain links through the matrix. The condition that the maximum stress within the links be less than the link strength then leads to a criterion for transition from localized failure (involving failure of the links at small strains) to delocalized failure (with distributed damage and large plastic strains occurring via link displacement). The model was validated by correct prediction of the measured stress for link displacement [2]. It can therefore serve as a design guide for optimizing the energy absorption of this class of composites. Projections of optimal properties based on the simple model suggest that energy absorption levels of 160 MJ/m<sup>3</sup> or specific energy absorption levels of 40 J/g should be attainable with chain links of conventional racetrack geometry. These would be very useful values.

However, even higher values of energy absorption, probably ~ 400 MJ/m<sup>3</sup>, are projected for chain composites designed according to methods that remain proprietary [4].

*Dynamic Behaviour*

In a collaboration with Dr. Arnold Mayer of Wright Patterson Air Force Base, panels of chain composites were tested under ballistic impact conditions by shooting them with anti-personnel rounds in an instrumented test range [5]. The tests demonstrate that the lockup mechanism

operates at strain rates approaching  $10^4$  sec $^{-1}$ , with delocalised damage extending in several cases from the impact site to the edge of the test panel. Estimates of the energy absorbed per unit volume under impact conditions range from 30 to 75 MJ/m $^2$ , approximately 50 – 60 % higher than values measured in static tension for the same composites. The enhancement of energy absorption is tentatively attributed to strengthening of the resin at high strain rates. Implications of the tests for designing ballistic protection have been discussed [5].

The tests should be regarded as a demonstration of the lockup mechanism at high strain rate and not as a quantitative measurement of the performance of chain composites as ballistic protection. In their current configuration, the chain panels have several obvious limitations. Contact between the round and the chains tends to be interrupted by the round breaking the contacted links or slipping through or past them. Energy absorption is also restricted mainly to the rear layer of chains in any panel, which have the freedom to extend into the free space behind the panel, allowing a large zone of displaced links to develop. Chains in the front layers are constrained by the layers behind them and exhibit far smaller displacement zones.

These problems can be remedied by simple redesign. For example, persistent contact between links and the round can be achieved by using smaller links, with smaller holes and a higher density of chains per unit width of the panel. To first order under static loading, the lockup strain and the stress required for link displacement are invariant under changes of scale that preserve similarity [3]. Therefore, the energy absorption per unit volume or mass must be invariant too. Round penetration can also be combated by placing a hard plate or a set of hard tiles in front of the chains to flatten the projectile and spread it over a larger area of the chain panel, ensuring greater activation of links.

Better use of multiple layers of chains will be achieved if the layers are separated in space, so that each layer can be activated without constraint from succeeding layers. Multiple layers separated by layers of light polymer foam would seem an attractive option.

### *Braided Composites*

Analogues of the chain composites have been demonstrated by braiding continuous fibers [1,6]. Continuous fibers are advantageous because of their high specific strength. The braiding process also lends itself to low-cost mass production.

Braiding creates a reinforcement geometry that is closely analogous to the geometry of interpenetrating links in chains. The braided composites exhibit lockup mechanisms following loop displacement, thus delocalizing damage and achieving high levels of energy absorption. The energy absorbed per unit mass is especially attractive, ranging in the composites made to date up to 18 J/g. While this value already exceeds the best value achieved for chain composites, simple models indicate much higher values for composites that have been optimized: 50 J/g ought to be fairly easily realized.

Prospects for optimization lie in improving the volume fraction of reinforcing fibers, towards which automating the braiding process should be a major step, and selecting a tougher matrix to avoid premature loss of matrix during damage to large strains.

#### *Knitted Composites*

Braiding suffers from two potentially limiting characteristics. The topology of the braiding process makes inevitable the presence of loose ends of braided tows or cords when the desired amount of fabric has been braided. The loose ends must be secured by splicing them together prior to composite consolidation, but the splices can be a source of weak flaws. Second, the braided loops, being weaker in the transverse direction than steel links, tend to spread out sideways during loading to large strains. This tends to release matrix entrapped between braided loops, allowing the loops to approach one another too easily. Energy absorption is compromised.

An alternative approach to high energy absorption based on weft knitting avoids these difficulties [1,7]. The knitting process can be executed with a single continuous tow or cord, so that loose ends are never present. The geometry of the interlacing of the knitted loops leads to potentially

advantageous force distributions during loop displacement, with loops drawn tightly against one another to resist lateral separation. The knitted and braided composites yield similar energy absorption levels in their current states of development, but offer alternative manufacturing routes.

Delocalised damage has been demonstrated for the knits, with levels of energy absorption per unit volume reaching  $40 \text{ MJ/m}^3$  and, per unit mass,  $25 \text{ J/g}$  [7]. The essential mechanisms are loop displacement accompanied by extensive matrix cracking and plastic deformation, friction between interlaced loops at higher strains where the matrix has been ejected, and lockup at a critical value of the local strain, which triggers displacement elsewhere in the specimen.

With optimization, levels of  $120 - 200 \text{ MJ/m}^3$  or  $75 - 130 \text{ J/g}$  seem feasible for knitted composites.

The knitting process is straightforward and ought to be amenable to automation and low-cost production.

## **Computational Modeling**

Prior experiments have revealed exceptionally high values of the work of fracture ( $0.4 - 1.1 \text{ MJm}^{-2}$ ) in carbon/epoxy 3D interlock woven composites.<sup>2</sup> Detailed destructive examination of specimens suggested that much of the work of fracture occurred when the specimens were strained well beyond the failure of individual tows yet still carried loads  $\sim 1 \text{ GPa}$ . A mechanism of lockup amongst broken tows sliding across the final tensile fracture surface was suggested as the means by which high loads could still be transferred after tow failure. (In the history of the evolution of the ideas of this overall work, the lockup mechanism inferred from the tests on interlock weaves was the inspiration for the mechanism developed in chain composites.)

In this contract, the roles of weave architecture and the distribution of flaws in the mechanics of tow lockup have been investigated by Monte Carlo simulations using the so-called Binary Model [8,9]. The Binary Model was introduced previously as a finite element formulation specialized to the problem of simulating relatively large, three dimensional segments of textile composites, without any assumption of periodicity or other symmetry, and faithfully preserving the architecture and topology of the tow arrangement.<sup>3</sup> The simulations have been very successful in reproducing all aspects of measured stress-strain curves. They reveal that lockup can indeed account for high loads being sustained beyond tow failure, provided flaws in tows have certain spatial distributions. The importance of the interlock architecture in the phenomenon is highlighted.

The Binary Model has also been demonstrated to be a viable computational tool for simulating the details of ultimate tensile failure in textile composites. Various nonlinear mechanisms, which are all important at some stage of the evolution to failure, have been successfully incorporated, including irregularity in the tow deployment, continuous plastic shear, matrix cracking (here in

---

<sup>2</sup> B. N. Cox, M. S. Dadkhah, and W. L. Morris, "On the Tensile Failure of 3D Woven Composites," *Composites* **27A**, 447-58 (1996).

<sup>3</sup> B. N. Cox, W. C. Carter, and N. A. Fleck, "A Binary Model of Textile Composites: I Formulation," *Acta Metall. Mater.* **42**, 3463-79 (1994).

the form of cracking between tows), tow rupture, debonding and slip, enhanced friction (lockup) due to the constraint of 3D reinforcement, and pullout. The model does not assume periodicity in the structure or invoke the popular concept of a purportedly representative unit cell, which is an essential level of generality for simulating complex textile structures.

The entire stress-strain history through to ultimate failure, including an enduring hardening phase, the primary load drop, and the pullout phase, have been simulated realistically by Monte Carlo methods with reasonable values assumed for material parameters and probability distributions.

While not constituting a deductive proof, the Binary Model simulations quantify the roles of various material and geometrical factors in determining the work of fracture of 3D interlock weaves. The highest values of work of fracture arise when the hardening phase of the failure sequence endures significantly beyond the failure strain of individual tows. This phenomenon (an experimental observation<sup>2</sup>) has been shown to require an unusual spatial distribution of flaws in stuffers, as well as a strong lockup effect during the sliding of ruptured stuffers through the surrounding composite. The required spatial distribution of flaws is that planes of flaws should exist separated by 10 – 20 mm. The mechanism for the creation of such planes during the manufacture of a textile composite is unknown, but their existence is certainly feasible. For example, variations in tensioning or in the beating up of weft yarns during the weaving process can lead to bands of shear or buckling defects in the dry fiber preform. Post-mortem studies of the specimens from tests certainly suggest that flaws populated planes or near-planes. For designing materials with the highest possible work of fracture, a systematic method of introducing flaws of known strength at preferred locations would be very useful.

Regardless of the spatial distribution of flaws, the three-dimensional nature of the reinforcement in angle interlock weaves has a profound influence on the work of fracture through the lockup mechanism or enhanced friction. Even when the hardening phase terminates near the failure strain of individual tows, useful large values of the work of fracture are obtained, which are attributable to high friction prior to the primary load drop and the following substantial pullout loads.

#### **4. LIST OF PUBLICATIONS UNDER THIS CONTRACT**

1. B. N. Cox, J. B. Davis, N. Sridhar, F. W. Zok, and X.-Y. Gong, "Designing Composites for Energy Absorption under Tensile Loading," *Proc. ICCM12*, Paris, July, 1999, ed., T. Massard (1999).
2. B. N. Cox, J. Davis, N. Sridhar, F. Zok, and X. Gong, "The Energy Absorption Potential of Chain Composites," *Acta Materialia*, in press.
3. X. Gong, F. Zok, B. N. Cox, and J. Davis, "The Mechanics of Delocalization and Energy Absorption in Chain Composites," *Acta Materialia*, in press.
4. (Paper containing proprietary information – to be released early in 2000).
5. B. N. Cox, N. Sridhar, J. B. Davis, A. Mayer, T. J. McGregor, and A. G. Kurtz, "Chain Composites under Ballistic Impact Conditions," to be submitted to *J. Mater. Sci.*
6. B. N. Cox and J. B. Davis, "Braided Composites for Energy Absorption under Tensile Loading, " to be submitted to *J. Mater. Sci.*
7. B. N. Cox and J. B. Davis, "Knitted Composites for Energy Absorption under Tensile Loading," to be submitted to *J. Mater. Sci.*
8. B. N. Cox, R. M. McMeeking, and M. A. McGlockton, "The Binary Model – A Computational Approach to Textile Composites," *Proc. ICCM12*, Paris, July, 1999, ed., T. Massard (1999).
9. M. A. McGlockton, B. N. Cox, and R. M. McMeeking, "A Binary Model of Textile Composites: III High Failure Strain and Work of Fracture in 3D Weaves," to be submitted to *J. Mech. Phys. Solids.*

## **5. LIST OF PARTICIPATING SCIENTIFIC PERSONNEL**

Personnel listed below under Rockwell were either supported directly by this contract or by funds set aside for youth motivation or the encouragement of minorities and women in science. Personnel listed under other institutions very kindly collaborated without exchange of funding.

### **Rockwell Science Center**

Dr. Brian Cox, principal scientist, Materials Science

Dr. Janet Davis, Structural Ceramics Department

Dr. Sridhar Narayanaswamy, Design and Reliability Department

Mr. Christian Berg, undergraduate at California Lutheran University

Ms. Rachel Goldberg, undergraduate at Philadelphia College of Textiles and Science

Ms. Gloria Rios, undergraduate at California Lutheran University

Ms. Jenny Garredo, undergraduate at California Lutheran University

Ms. Amber Sands, undergraduate at UCLA

Ms. N. Altamirano, Mr. Jeff Butler, Mr. Chris Fyduk, Ms. Annalise Keen, and Ms. Amber Sands, all high school students in Rockwell's Youth Motivation Program

### **University of California, Santa Barbara**

The following colleagues collaborated on modeling chain composites:

Professor Frank Zok, Materials Department

Dr. Xiao-Yan Gong, postdoctoral fellow, Materials Department

The following colleagues collaborated on computational modeling:

Professor R. M. McMeeking, Department of Mechanical Engineering

Dr. Michael A. McGlockton, jointly supervised Ph. D. candidate (degree conferred in 1998)

**Wright Patterson Air Force Base**

The following collaborated on ballistic impact experiments on chain composite panels:

Dr. Arnold Mayer, Mr. T. J. McGregor, and Mr. A. G. Kurtz, all of the Materials Directorate

**Philadelphia College of Textiles and Science**

Professor Chris Pastore consulted on serving Kevlar tows in tightly wrapped light yarns of braided rayon.

**6. HONORS SINCE CONTRACT'S INCEPTION:**

Plenary paper on chain composites at the Third International Conference on Composites in Engineering, New Orleans, July, 1996

Invited lecture on damage tolerant brittle composites at the Second International Conference on Ceramic Matrix Composites, Santa Barbara, 1996

Invited departmental seminars on chain composites at UC San Diego, Stanford University, UCLA, Cambridge University, England, and the Aeronautical Research Laboratory, Melbourne, Australia.

Keynote paper on energy absorbing composites at ICCM-12, Paris, 1999.

Keynote paper on computational modeling of textile composites, Int. Conf. on Computational Mechanics, Boulder, 1999.

## **7. INVENTIONS AND TECHNOLOGY TRANSFER**

The basic ideas of the chain, braided, and knitted composites predate the beginning of this contract. The rights to these inventions have been assigned by Rockwell to the University of California. The university's Office of Technology Transfer has solicited expressions of interest from a number of firms. Discussions are under way with several of them to define potential commercial developments. The basic research executed under this contract will be very helpful in guiding optimization in any such development.

The Binary Model code is now being developed as a commercial code by Ceramic & Metal Composites Inc. (C&MC) of Santa Barbara, CA. The code is being used in textile structural development programs for airframes at Boeing, Seattle, WA, and for rocket motor components at Boeing, Rocketdyne, California. This code is a direct derivative of the basic ideas developed for textile composites under this contract.

We continue to look at teaming arrangements with armor developers to pursue the incorporation of our materials in a new generation of body armor, armor for tanks, aircraft, and other military vehicles, explosion and earthquake resistant infrastructure, and flywheel containers.

**8. APPENDIX.**

Drafts of all papers written under this contract are appended (see Section 4 for list of titles).

# **Rockwell Science Center**

## **DESIGNING COMPOSITES FOR ENERGY ABSORPTION UNDER TENSILE LOADING**

**B. N. Cox, J. B. Davis, and N. Sridhar**

Rockwell Science Center  
1049 Camino Dos Rios  
Thousand Oaks, CA 91360  
U.S.A.

**F. W. Zok and X.-Y. Gong**

Materials Department  
University of California, Santa Barbara  
Santa Barbara, CA 93106  
U.S.A.

# DESIGNING COMPOSITES FOR ENERGY ABSORPTION UNDER TENSILE LOADING

B. N. Cox <sup>1\*</sup>, J. B. Davis <sup>1</sup>, N. Sridhar <sup>1</sup>, F. W. Zok <sup>2</sup>, and X.-Y. Gong <sup>2</sup>

<sup>1</sup>Rockwell Science Center, 1049 Camino Dos Rios, Thousand Oaks, CA 91360, U.S.A.

<sup>2</sup>Materials Department, University of California, Santa Barbara, Santa Barbara, CA 93106, U.S.A.

**KEYWORDS:** energy absorption, delocalization, chains, textiles

**SUMMARY:** Novel composites have been developed possessing exceptionally high capacity for energy absorption. This was accomplished by arranging the geometry of the reinforcement in such a way that the composite hardens over large strains (~100%) following the onset of damage, leading to damage delocalization. Composites have been made using steel chains and fiber tows braided or knitted into configurations possessing large strain capacity, consolidated with polymeric or metallic matrices. The energy absorbed per unit volume by the first generation of these composites varies between 15 and 60 MJ/m<sup>3</sup>, which is already very favourable compared to other candidate materials for energy absorption. The energy absorbed per unit mass ranges from about 8-13 J/g for chain composites to more than 20 J/g for fibre-reinforced composites. These are also very attractive values. By optimizing the reinforcement geometry and the matrix properties, both the chain and textile composites can be tailored to have energy absorption still several times higher.

## INTRODUCTION

Many energy absorption problems involve loads that are tensile, for example, casings designed to contain bursting rotors, turbines, or flywheels; backing plates in armour systems; and containers subject to internal explosions. Here some results are shown for a new class of composites with unusually high energy absorption capacity under tensile loading.

The new composites incorporate mechanisms for ensuring that damage is broadly distributed throughout the body of a specimen or structure before the instability associated with ultimate

---

\* Currently EPSRC Visitor, Engineering Department, Cambridge University, Trumpington Street, Cambridge CB2 1PZ, England.

failure sets in. Damage delocalization is promoted by incorporating so-called lock-up mechanisms, in which components of the reinforcement are arrested by physical contact with one another after displacing through the matrix. The extent of the displacement allowed before the lock-up of two elements of the reinforcement determines the global strain up to which damage will be delocalized, denoted  $\varepsilon_c$ . The total energy absorbed per unit volume is bounded from below by the product of  $\varepsilon_c$  and the magnitude of the global stress required for reinforcement displacement,  $\sigma_d$ . Both  $\sigma_d$  and  $\varepsilon_c$  can be varied over quite wide ranges by selecting materials and the geometry of the reinforcement, so that composites can be designed, for example, to avoid large stresses during energy absorption; or for maximum total energy absorption without constraint on the stress level. The levels of total energy absorbed per unit volume or per unit mass by members of the new class of composites are potentially very high.

## COMPOSITES OF CHAINS

Composites of chains in epoxy matrices in which the links are initially in a contracted configuration (Fig. 1) fail with damage spread over the whole stressed volume and absorb unusually large energy per unit volume during failure. The underlying phenomena were first discussed in [1] and have now been analyzed quantitatively by analytical and computational methods [2,3]. Damage begins with extensive matrix cracking. Successive chain links slide towards contact with one another, crushing resin trapped between them in a state of near hydrostatic compression. The displacement of links through the resin absorbs most of the energy expended en route to ultimate failure. When two links come into direct contact, they are said to lock up: the material hardens locally, resisting further local displacement and triggering the displacement of links elsewhere in the same chain. Only when all links in a chain are in direct contact with their neighbors does the chain begin to fail by plastic deformation of the links followed by rupture of the weakest among them.

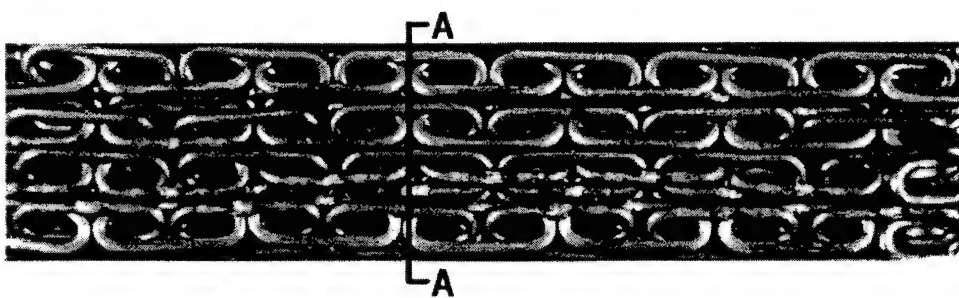


Fig. 1: Contracted chain configuration viewed through a transparent epoxy matrix.

### Estimates Based on Simple Models

A typical stress-strain curve is shown in Fig. 2. During link displacement, the applied engineering stress is approximately constant in most chain/polymer composites (strain less than 0.5 in Fig. 2). Its magnitude can be estimated by modeling the matrix as a rigid/perfectly plastic medium

through which the links must move. Stress transfer into the links from the matrix during the displacement can be partitioned conveniently into several contributions. 1) Hydrostatic compression in the resin trapped between two links as they approach one another exerts pressure over the inner surface of the crown of each link (the curved end). 2) Shear tractions develop over the crown of a link as it slides through the matrix. 3) Tensile tractions act on the outer surface of the crown where the matrix is being pulled apart between the crowns of abutting links, at least until the matrix fails (e.g., along line A-A in Fig. 1). 4) Shear stresses act over the legs (the straight portions) as the links slide through the matrix. The sum of the four contributions, when resolved in the direction of the motion of the links, must be balanced by tension in the legs, which takes its maximum value,  $\sigma_{\max}^{(leg)}$ , at the centre of the legs; and all four are proportional to the matrix shear flow stress,  $\sigma_{my}$ , the constants of proportionality depending on the link geometry. Summarizing the results of finite element calculations [2]

$$\sigma_{\max}^{(leg)} = \beta \sigma_{my}$$

$$\beta = \frac{2}{\pi} (C_1 + C_2 + 3.664 C_3) \left( 1 + \frac{R}{r} \right) - \left( \frac{C_1 - C_2}{2} \right) + C_4 \frac{H}{r} \quad (1)$$

where  $r$  is the radius of the wire in the link,  $R$  is the inner radius of the crown segment, and  $H$  is the length of the leg segment; and  $C_1$ ,  $C_2$ ,  $C_3$ , and  $C_4$  are dimensionless constants of proportionality corresponding in order to the four contributions listed above. The constants  $C_1$ ,  $C_2$ ,  $C_3$ , and  $C_4$  were evaluated in [2]. Equation (1) is restricted to links consisting of semi-toroidal crowns connected by cylindrical legs, which is the standard geometry of commercially available chains. For perfectly bonded link/matrix interfaces, the proportionality factor  $\beta$  reduces to the even simpler result

$$\beta = 2.37 + 3.32 \frac{R}{r} + 0.5 \frac{H}{r} \quad (2)$$

and for unbonded, frictionless interfaces to

$$\beta = 0.36 + 1.69 \frac{R}{r} \quad (3)$$

If the matrix is relatively compliant, then Eq. (1) multiplied by the area fraction occupied by the legs of the links on a plane through their centres (e.g., the plane A-A in Fig. 1) should be approximately equal to the composite stress during link displacement,  $\sigma_d$ . This is shown in Fig. 2 by the line marked " $\sigma_r = \beta \sigma_{my}$ ". It coincides with the measured plateau stress.

A transition from delocalized to localized failure should occur if  $\sigma_{\max}^{(leg)}$  exceeds the strength of the chain material,  $\sigma_{ch}$ , during link displacement through the matrix. This was not the case in the test of Fig. 2. However, when the composite stress divided by the area fraction of the links, which is denoted  $\sigma_r$ , exceeds  $\sigma_{ch}$  following link lockup, the chains must fail. This condition is indicated by the line marked " $\sigma_r = \sigma_{ch}$ " in Fig. 2, which is somewhat above the measured peak stress. The discrepancy is due to slightly unequal loading among the chains.

The estimates of the plateau stress and the failure stress based on Eq. (1) are very useful as design guides.

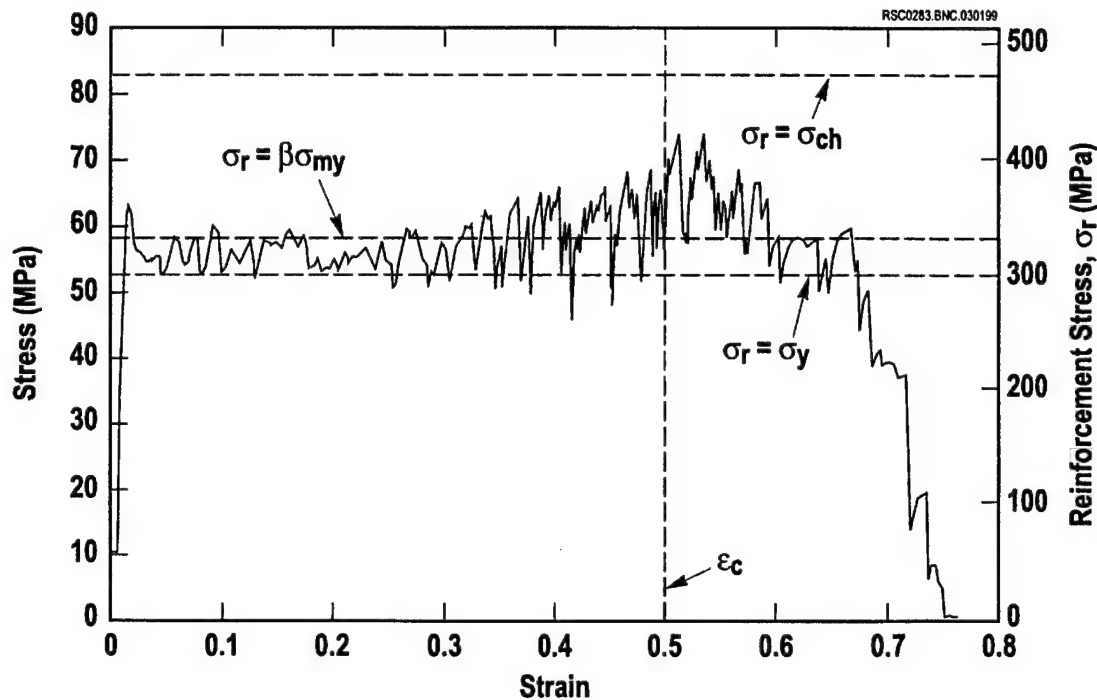


Fig. 2: Measured stress-strain curve for a chain/polycarbonate composite.

### Energy Absorption Values – Current and Ideal

The energy absorption per unit volume,  $W$ , is compared in Figure 3 for the chain composites and other energy-absorbing materials, including cold drawing polymers, monolithic alloys, and some recently developed braided composite tubes [4]. The cold drawing polymers are typified by polycarbonate, which sustains relatively low loads but can achieve strains of several hundred percent. The energy absorption of alloys is estimated as the area under typical tensile stress-strain curves prior to the formation of any necking instability. The energy absorption data are plotted in Fig. 3 against strength. The highest value of energy absorption for the chains composites was approximately 60 MJ/m<sup>3</sup> in a chain/polycarbonate composite (datum “8” in Fig. 3).

Barring idealized chain composites to be discussed below, monolithic alloys and cold-drawing polymers possess the highest values of  $W$ , but other aspects of behaviour must also be considered. The degree of global plasticity attained in both alloys and polymers is quite sensitive to the presence of notches or other stress concentrators, which might be created by the geometry of the part design or damage. Localized failure will occur in alloys if the notch size exceeds a few mm at most [5]. Polycarbonate, a typical cold-drawing polymer, is even more sensitive to notches. The presence of a sub-millimeter nick in the side of a polycarbonate sheet will lead to localized failure and pre-empt cold drawing [1]. Furthermore, cold drawing of polymers is also very rate sensitive, with failure at even moderately elevated strain rates reverting to brittle behaviour. The

localization/delocalization transition in chain composites will be much less sensitive to notches, because the chains do not communicate stress concentrations effectively. They are mechanically decoupled early in the failure process. Delocalization in the chain composites is also relatively insensitive to strain rate, a point that will be demonstrated elsewhere.

The values of  $W$  found for the chain composites are similar to those obtained for the braided composite tubes developed by Harte and Fleck [4]. Tubes braided at angles between  $23^\circ$  and  $55^\circ$  to the tube axis exhibit delocalized failure under axial tension, with a necking and drawing mechanism analogous to a cold drawing polymer. The failure involves shearing and scissoring of cross-braided tows, with lockup caused by rotation of the fibers and tows into hard contact with one another. The peak axial stress is typically  $\sim 30$  MPa and the total energy absorbed per unit volume can reach  $\sim 30$  MJ/m<sup>3</sup>, figures somewhat below the chain composites. However, the chain composites have further significant advantages. They do not need to be tubular; and their stiffness, strength, and energy absorbing capacity can be made even higher by a combination of material selection and redesign of the link geometry.

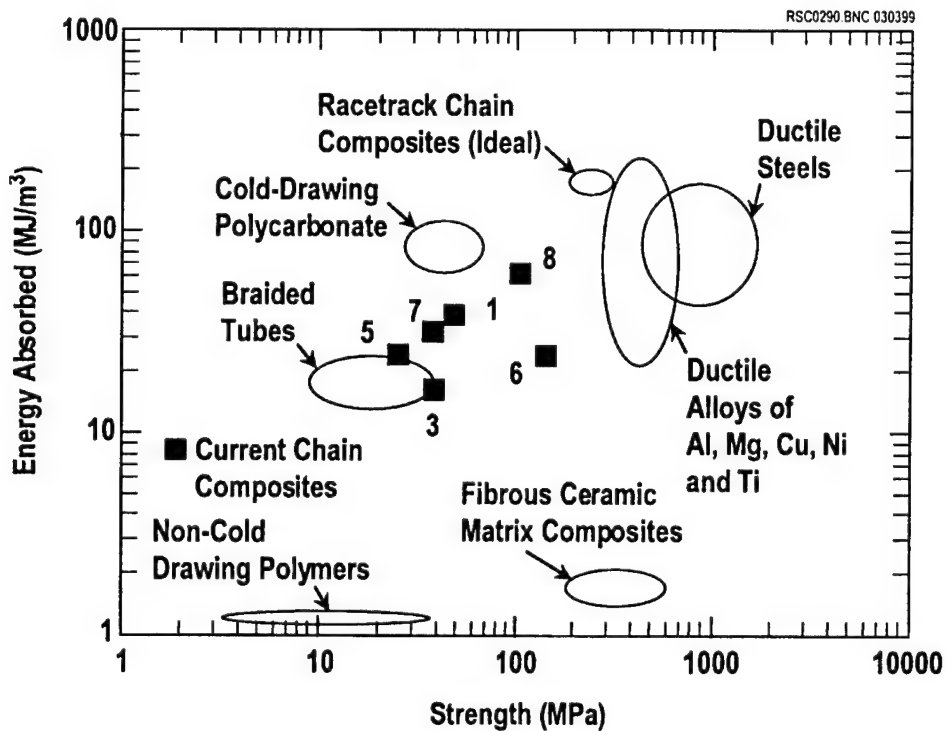


Fig. 3: The energy absorption,  $W$ , for chain composites that have already been tested (numbered data points), hypothetical, optimal chain composites, and other groups of materials. Typical scatter is represented by elliptical domains, following the style of the materials selection charts of Ashby [6]. The energy data are plotted against composite or material strength.

The appropriate figure of merit for applications demanding high energy absorption but low weight is the energy absorbed per unit volume or specific energy absorption,  $W_s = W/\rho_c$ , with  $\rho_c$  the composite density. This is plotted in Fig. 4 against the specific strength,  $\sigma_s = \sigma_c/\rho_c$ . Here the chain composites stand up very well against monolithic alloys and are not far from the braided tubes.

Again the highest value for the chain composites, 14 J/g, is for a chain/polycarbonate composite. Cold drawing polymers have the highest specific energy absorption, but even these levels can be equaled for optimized chain composites.

The energy absorption of the chain composites will be maximized by 1) packing the chains as closely as possible; 2) using the strongest possible chain material, thus maximizing the allowable stress,  $\sigma_d$ , during link displacement; 3) choosing a matrix with a flow stress,  $\sigma_{my}$ , for which the product  $\beta\sigma_{my}$  is as great as possible without exceeding the chain strength,  $\sigma_{ch}$ ; and 4) choosing a link geometry that maximizes the strain before lockup,  $\varepsilon_c$ . Commercial chains, such as those used in tests to date, do not have very high ultimate strength (< 500 MPa), because relatively ductile alloys must be used for safety. A chain must not break before showing visible signs of plastic strain. However, this is unnecessary in the chain composites, in which high strength steel ( $\sigma_{ch} \sim 1$  GPa) could be used without significant loss of composite ductility. By using longer links, the lockup strain,  $\varepsilon_c$ , can be raised to 0.6, somewhat higher than the values ( $\leq 0.5$ ) for the chains used to date. Finally, the flow stress of the matrix material,  $\sigma_{my}$ , must be raised above current levels ( $\sim 100$  MPa for epoxy in compression) to raise the displacement stress,  $\sigma_d$ , to the maximum allowable for stronger links. With all these modifications and closely packed chains of the conventional racetrack shape, the energy absorbed per unit volume during link displacement alone can be raised to approximately 160 MJ/m<sup>3</sup>. This value has been indicated in Fig. 3 as a range attainable for "ideal" chain composites. It is a very attractive prospect.

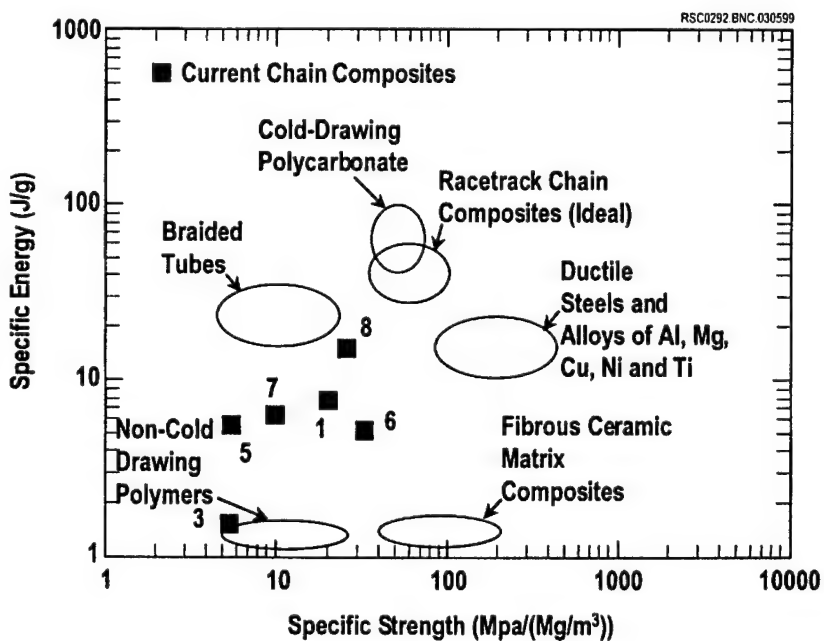
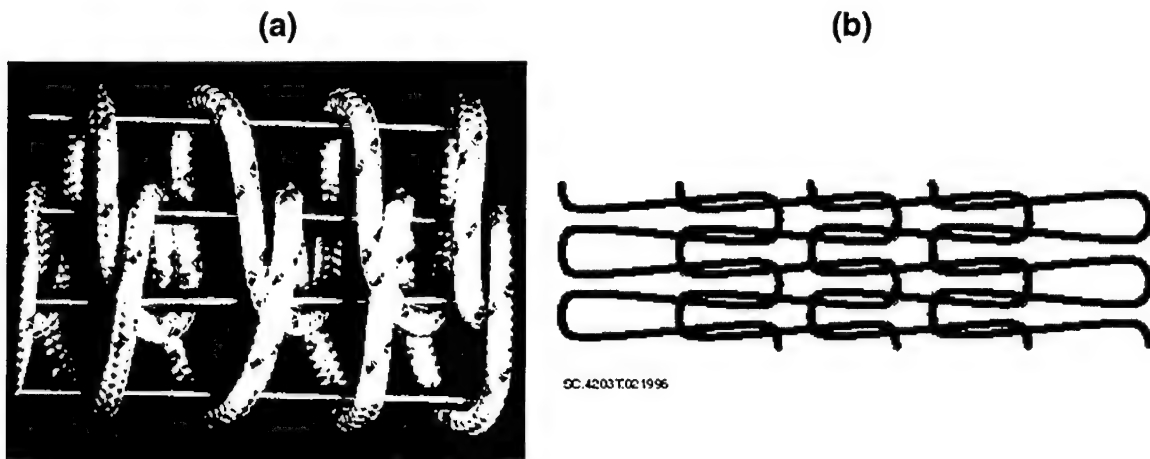


Fig. 4: The specific energy absorption,  $W_s$ , for chain composites (numbered data points), hypothetical, optimal chain composites, and other groups of materials, plotted against specific strength.

The specific energy absorption attainable for carbon steel chain composites with the same steps towards optimization is approximately 40 J/g. This is indicated in Fig. 4 by the "ideal" chain composite. It is again a very attractive goal.

## CONTINUOUS FIBER COMPOSITES

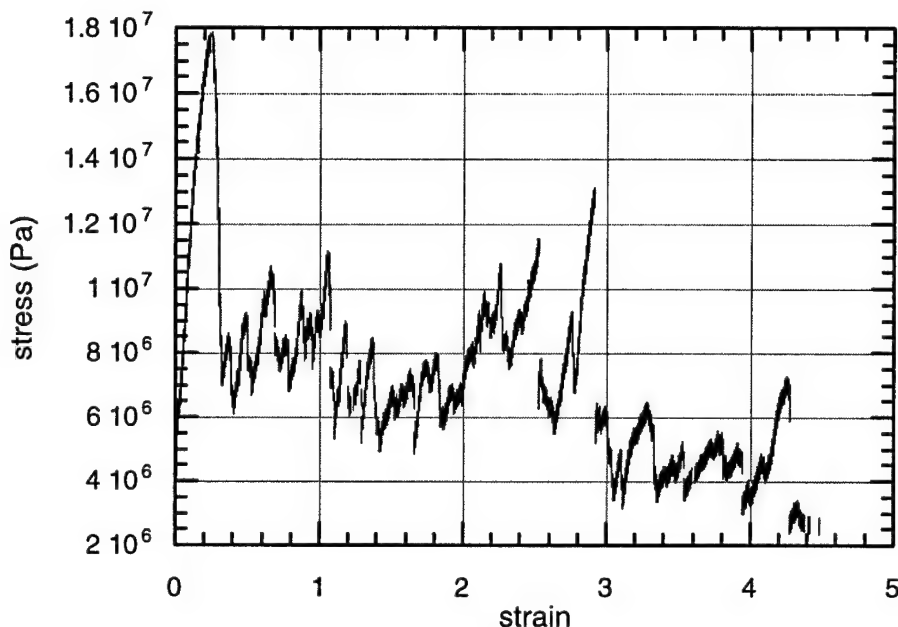
A lockup mechanism analogous to that in the chain composites can be achieved with continuous fiber reinforcement by novel arrangements of loops formed by braiding or knitting. In the textile process, interpenetrating loops are formed, which in analogy to the contracted configuration of links depicted in Fig. 1, are not in intimate contact until they have displaced towards one another after an applied load has created extensive matrix damage. Loops formed by braiding and knitting are shown in Fig. 5.



*Fig. 5: (a) Braided reinforcement configuration, formed on a series of rods to control loop separation. The tows have been spread into a loose arrangement to allow their interlacing pattern to be seen more easily. In the finished composite, they are tightly packed in the horizontal direction in the figure, but retain their elongation in the vertical direction (the intended direction of loading). (b) Schematic of weft knit in which loops have been separated so as not to be initially in intimate contact by knitting onto rods similar to those in (a) (not depicted). In (b), the intended loading direction is horizontal.*

Composites can be formed with the braided or knitted reinforcements by infiltrating with epoxy resin. Since there is no limit to the initial overlap of loops (the fraction of a loop's length by which interpenetrating loops are set apart on the positioning rods) in either design, there is no limit to the lockup strain,  $e_c$ . Braided composites fabricated to date have exhibited delocalized failure with ultimate strains to failure of 300% or more. The maximum loads during failure in braided composites are  $\sim 30$  MPa for the tow packing densities achieved so far. Figure 6 shows a typical stress-strain record for a braided composite achieving the somewhat lower maximum stress of 18 MPa and a plateau stress,  $\sigma_d \approx 10$  MPa, but extending to a strain exceeding 400%. The energy absorbed per unit volume in this test was approximately 30 MJ/m<sup>3</sup> and the specific energy absorbed approximately 24 J/g. With some fairly obvious improvements in the braiding technique to achieve higher fiber packing densities and some modifications to the matrix to avoid premature loss of matrix material during loop displacement, the plateau stress could be raised much higher. Quite interesting combinations of strain to failure, peak stress, and energy

absorption could then be achieved. The braided composites will clearly rival the best chain composites and outstrip other classes of material.



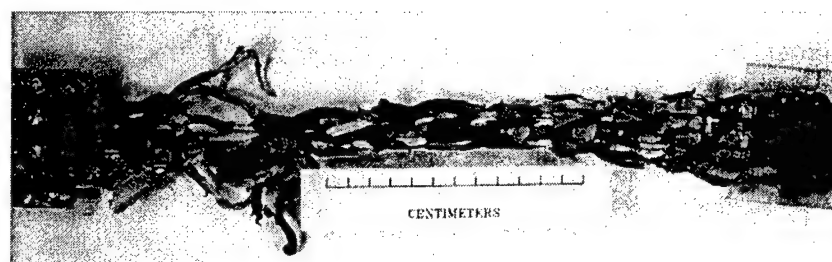
*Fig. 6: Stress-strain plot for braided specimen.*

Fig. 7 shows a knitted specimen before and after testing. The fabric is wrapped with a small amount of yarn to inhibit the loss of matrix during large sliding displacements. The wrapped fibers are only partly effective in this. A better method, not yet pursued, would be to toughen the matrix by incorporating chopped fibers in it, for example. Because of premature loss of resin, the stress during the initial stages of loop displacement is smaller than in the chain or braided composites. Figure 8 shows a case in which the initial stresses are especially low (they are  $> 10$  MPa in other cases, depending on the aspect ratios and initial overlap of the loops), but it illustrates another characteristic peculiar to the knitted structure. As the knitted loops (such as those in Fig. 5b) are drawn tight during loop displacement, they are pulled against one another laterally in an action similar to tightening a knot, resulting in increasing and ultimately very strong frictional forces between them. (The distinction between knitted loops and braided loops or chain links is in the topology of the interlacing of the loops. The braided loops and chain links approach one another after sliding displacement with the curved ends – e.g., the crowns of the chain links – orthogonal to one another and perhaps without lateral contact. Interpenetrating knitted loops approach one another obliquely with a tightening action.) Thus the knitted composites tend to exhibit gradual hardening during the loop displacement phase. The stress in the example of Fig. 8 rises by a factor of about three before tow rupture leads to specimen failure. In Fig. 8, the strain to failure is nearly 300%. If the initial overlap of the knitted loops is reduced, the stress during sliding displacement tends to rise (to approximately 20 MPa in cases tested to date), while the strain to ultimate failure decreases (to  $\sim 100$  % in the cases of highest sliding stress). The energy absorbed per unit volume in knitted composites made to date ranges up to about 25 MJ/m<sup>3</sup> and the specific energy absorbed is about 18 J/g. Substantial improvement could

be achieved by using a matrix, e.g., one reinforced by chopped fibers, that was not as easily ejected during loop displacement. Resin is more easily lost from the knitted loops than from braided loops or chain links, because it is not trapped as effectively in pockets in which large hydrostatic compression can develop.



a)



b)

*Fig. 7: (a) A knitted Kevlar/epoxy composite as fabricated. (b) Tested composite showing distributed damage.*

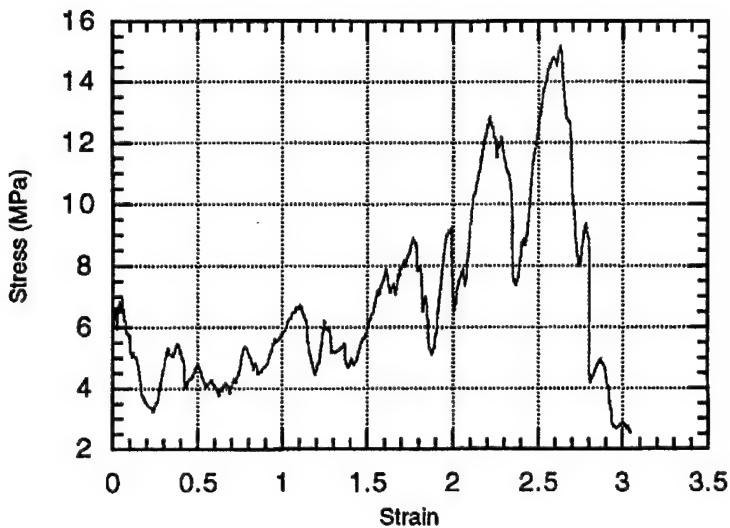


*Fig. 8: Stress-strain data for a composite of knitted Kevlar tows impregnated with student-friendly Epoxy resin.*

### SUMMARY REMARKS

By regarding the geometry of its reinforcement as a design variable, unusual failure mechanisms can be built into a composite, leading to damage delocalization and exceptionally high values of energy absorption. Values of energy absorbed per unit volume and per unit mass have been demonstrated that exceed those available from other current candidates for energy absorbing applications. Much higher values could be achieved in the next generation of all classes of these composites, according to estimates made with models of the damage processes.

The composites demonstrated here have been made with common constituents and by processes that appear amenable to automation and cheap mass production.

### Acknowledgment

Work supported by the U.S. Army Research Office, Contract No. DAAH04-95-C-0050.

### References

1. Cox, B. N., "Lockup, Chains and the Delocalization of Damage," *J. Mater. Sci.*, **31** (1996), 4871-81.
2. Gong, X.-Y., Zok, F. W., Cox, B. N. and Davis, J., "Chain Composites with High Energy Absorption: I. Theory of the Localization/Delocalization Transition," submitted to *Acta Materialia*.

3. Cox, B. N., Davis, J., Narayanaswamy, S., Zok, F., and Gong, X.-Y., "Chain Composites with High Energy Absorption: II Demonstrations and Potential," submitted to *Acta Materialia*.
4. Harte, A.-M., Ph. D. Thesis, Engineering Department, Cambridge University, 1998.
5. Suo, Z., Ho, S., and Gong, X.-Y., "Notch Ductile-to-Brittle Transition Due to Localized Inelastic Band," *J. Engng Mater. Technol.* **115** (1993), 319-26.
6. Ashby, M. F., *Cambridge Materials Selector*, Cambridge University Press, Cambridge, 1995.

# **Rockwell Science Center**

## **THE ENERGY ABSORPTION POTENTIAL OF CHAIN COMPOSITES**

**B. N. Cox, N. Sridhar, and J. B. Davis**

Rockwell Science Center  
1049 Camino Dos Rios  
Thousand Oaks, CA 91360  
U.S.A.

**X.-Y. Gong and F. W. Zok**

Materials Department  
University of California, Santa Barbara  
Santa Barbara, CA 93106  
U. S. A.

## ABSTRACT

Various chain composites designed to exhibit delocalized damage and high energy absorption have been fabricated and tested. The energy absorbed per unit volume ranges up to  $60 \text{ MJ/m}^3$  and the specific energy absorption up to  $14 \text{ J/g}$ , figures comparable to or exceeding the best current candidate materials for energy absorption. Observations of damage mechanisms are reported and related to a previously derived model appropriate to chain composites with matrices that are relatively weak in tension. Estimates are made of the energy absorption levels that could be achieved in the optimal case are then made based on modeling arguments. They are found to exceed  $160 \text{ MJ/m}^3$  or  $40 \text{ J/g}$ .

## 1. Introduction

Composites of chains in epoxy matrices in which the links are initially in a contracted configuration (Fig. 1) fail with damage spread over the whole stressed volume and absorb unusually large energy per unit volume during failure. The underlying phenomena were first discussed for composites with epoxy resin matrices in [1] and have now been analyzed quantitatively in [2]. Damage begins with extensive matrix cracking. Successive chain links slide towards contact with one another, crushing resin trapped between them in a state of near hydrostatic compression. The displacement of links through the resin absorbs most of the energy expended en route to ultimate failure. When two links come into direct contact, they are said to lock up: the material hardens locally, resisting further local displacement and triggering the displacement of links elsewhere in the same chain. Only when all links in a chain are in direct contact with their neighbors does the chain begin to fail by plastic deformation of the links followed by rupture of the weakest among them.

Such a delocalized progression of damage requires that the material strength,  $\sigma_{ch}$ , of the chain links be high enough that the links survive the stresses generated in them during their displacement through the matrix. As shown in [2], stress transfer into the links from the matrix can be partitioned conveniently into several contributions. 1) Hydrostatic compression in the resin trapped between two links as they approach one another exerts pressure over the inner surface of the crown of each link. 2) Shear tractions develop over the crown of a link as it slides through the matrix. 3) Tensile tractions act on the outer surface of the crown where the matrix is being pulled apart between the crowns of abutting links, at least until the matrix fails. 4) Shear stresses act over the legs as the link slides through the matrix. All four of these contributions, when resolved in the direction of motion of the links, must be balanced by tension in the legs, which takes its maximum value,  $\sigma_{max}^{(leg)}$ , at the centre of the legs; and all four are proportional to the matrix shear flow stress,  $\sigma_{my}$ , the constants of proportionality depending on the link geometry. A transition from delocalized to localized failure should occur if  $\sigma_{max}^{(leg)}$  exceeds  $\sigma_{ch}$  during

link displacement through the matrix. The criterion for delocalization may be expressed as [2]

$$\frac{\sigma_{ch}}{\sigma_{my}} > \beta \quad (1a)$$

$$\beta \equiv \frac{\sigma_{max}^{(leg)}}{\sigma_{my}} = \frac{2}{\pi} \left( C_1 + C_2 + 3.664 C_3 \right) \left( 1 + \frac{R}{r} \right) - \left( \frac{C_1 - C_2}{2} \right) + C_4 \frac{H}{r} \quad (1b)$$

where  $r$ ,  $R$ , and  $H$  are defined in Fig. 1 and  $C_1$ ,  $C_2$ ,  $C_3$ , and  $C_4$  are dimensionless constants of proportionality corresponding in order to the four contributions to tension in the legs that are listed above. The constants  $C_1$ ,  $C_2$ ,  $C_3$ , and  $C_4$  were evaluated in [2]. Equation (1b) is restricted to links consisting of semi-toroidal crowns connected by cylindrical legs, which is the standard geometry of commercially available chains. For perfectly bonded link/matrix interfaces, Eq. (1b) reduces to

$$\beta = 2.37 + 3.32 \frac{R}{r} + 0.5 \frac{H}{r} \quad (1c)$$

and for unbonded, frictionless interfaces to

$$\beta = 0.36 + 1.69 \frac{R}{r} \quad (1d)$$

If they are correct, such simple expressions will serve as very useful composite design rules.

In this paper, many more experiments are reported for composites of steel chains in various matrices, including epoxy, polycarbonate, aluminum alloys, and solder. Depending on the matrix, the mechanisms of failure sometimes differ from those previously observed,. The localization/delocalization transition is explored and the correctness of Eq. (1) is tested.

Pursuing the role of Eq. (1) as a design rule, new predictions are made of the greatest energy absorption per unit volume and per unit mass that could be achieved with chains of conventional geometry, assuming ideal dimensions and link and matrix materials. Predictions for chain composites in which the shape of the links can also be varied will be made elsewhere.

## 2. Material Systems

Steel chains with various strengths and link dimensions and matrices with diverse cracking behaviour and plasticity were selected, since these properties were identified in [2] as key factors affecting the transition from localized to delocalized failure. The degree of bonding between the reinforcement and matrix is also a critical factor, but it is difficult to control and was therefore not a focus of the study. All of the systems studied exhibited weak bonding between chains and matrix.

Steel chains (C1008 composition) with various link shapes (Table I) were obtained from a commercial vendor. The links will be distinguished by their sizes: large, medium, and small. All links were welded in the middle of one leg. Some variation in the strength of medium-link chains was obtained by annealing them at 800°C for 30 minutes.

Bare chains were tested in tension to establish their properties. Typical stress-strain curves show a distinct knee at the onset of yielding, beyond which significant hardening is obtained, followed ultimately by necking and failure of one of the chain links. The ultimate strength,  $\sigma_{ch}$ , the stress at the knee,  $\sigma_y$ , and the strain to ultimate failure,  $\varepsilon_{ch}$ , are summarized in Table I. The annealed chains have only a slightly changed ultimate strength, but an approximately two-fold increase in the strain to ultimate failure.

The chains were embedded in epoxy, polycarbonate, solder, and aluminum matrices, whose properties are shown in Table II. The chains were first cut to length, washed in

acetone, and arranged parallel to one another in a mold. They were configured in a contracted geometry in which each link overlapped the preceding and following links by half their lengths, as shown in Fig. 1b. Between six and ten chains were present in each specimen. Several processing techniques were developed for composite formation.

The aluminum matrix was an Al-4.5% Mg alloy, which was introduced into the chain preform by squeeze casting. The chains were arranged within a machined cavity in a porous  $\text{Al}_2\text{O}_3$  insulation mold. The assembly was then wrapped with ceramic felt to inhibit chain movement during subsequent processing steps. The mold and chains were pre-heated to approximately 400°C for 30 minutes prior to infiltration with molten alloy. After casting, the composites were machined into bars approximately 25 mm x 12 mm x 100 mm. All of the specimens contained significant excess aluminum matrix around the periphery as well as remnants of the  $\text{Al}_2\text{O}_3$  mold, now infiltrated with Al, which were difficult to remove mechanically without damaging the reinforcement. All aluminum alloy composites were made with small-link chains. Identical chains that were heat-treated to the processing temperature and tested in tension showed no change in properties.

The epoxy matrix was either Shell Epon 828 resin with Jeffamine D-230 hardener or Streurs Epofix Resin, which is a room temperature curing resin. Both resins have similar shear flow stresses in the cured state. The epoxy matrix composites were produced in a Teflon-coated aluminum mold. Chain preforms were built up within this mold and epoxy was added to fill the remaining volume. The assembly was then placed in an evacuation chamber to remove air bubbles from the resin prior to curing at room temperature (Epofix) or moderately elevated temperatures (80-90°C) (Epon 828). This procedure produced net-shape specimens with typical dimensions of 25 mm x 37 mm x 250 mm. After curing, the epoxy matrix was lightly ground with SiC paper to produce flat parallel surfaces for gripping in tests.

The polycarbonate matrix was introduced by heating powder in situ to approximately 300°C and removing bubbles by drawing a moderate vacuum. The polycarbonate composites were otherwise similar to the epoxy composites.

The solder was an electronic grade eutectic solder of nominal composition 63%Sn-37%Pb and melting temperature 185°C. Composites with solder matrices were also produced in Teflon-coated molds, but the ends of the specimens were first masked off so they could subsequently be filled with epoxy, since solder proved difficult to grip in tensile tests. Thus only the center of the preform was infiltrated with solder. Cold solder was placed on top of the chains and loaded with a small dead weight via a platen. The mold was then placed in an oven, evacuated, and heated to approximately 280°C. The solder melted and flowed into the preform. Specimens were produced with typical dimensions 25 mm x 20 mm x 250 mm.

A complete list of the chain and matrix combinations that were tested appears in Table III. The cited area fraction,  $A_c$ , is the area occupied by the chain legs on the plane A-A in Fig. 1b. In the cases of the epoxy and polycarbonate composites, excess peripheral matrix was deemed to contribute insignificantly to the total load in the specimen, since it suffered multiple cracking at low strains. Therefore, for the epoxy and polycarbonate composites,  $A_c$  has been defined taking into account only the central core region, where the chain links are tightly packed, using the formulae of the Appendix. Likewise the value shown for the volume fraction of reinforcement,  $V_r$ , is that in the core alone.

### 3. Experiments - Mechanisms and Results

The mechanical properties of the chain composites were evaluated in a screw-driven, universal testing machine with a 135 kN capacity. Wedge grips were used, machined to a rough surface finish to ensure adequate friction with the test piece. Typical displacement rates were 0.2 mm/s for epoxy, polycarbonate, and solder matrix specimens and 0.02 mm/s for the Al matrix specimens (strain rates  $10^{-3}$  and  $10^{-4}$  sec<sup>-1</sup>, respectively).

The average tensile engineering stress in the composite, the “composite stress”, denoted  $\sigma_c$ , was determined by dividing the load by the specimen cross-section (using the cross-section of the core region only for the epoxy and polycarbonate specimens). A representative tensile stress in the reinforcement, the “reinforcement stress”, denoted  $\sigma_r$ , was defined by dividing the composite stress by the area fraction,  $A_c$ :

$$\sigma_r = \frac{\sigma_c}{A_c} . \quad (2)$$

This is the average stress that must exist in the centre of the legs if the matrix carries zero stress on this plane (the plane A-A in Fig. 1b). If this condition is realized,  $\sigma_r$  must be less than the material strength of the chain links,  $\sigma_{ch}$ , for localized failure to be avoided. In the case of composites with an Al matrix, the matrix will be strong enough to carry significant load and the stress in the legs will be substantially less than  $\sigma_r$ . However, in all the other composites, the reinforcement stress defined by Eq. (2) is a fairly close upper bound to the maximum stress in the legs. It is presented in stress-strain plots as the right hand ordinate.

The aluminum matrix composites all suffered localized failure and the portions of the chain links that pulled out from the matrix exhibited considerable plasticity. In all cases, links failed at the weld. The chain/matrix interface appeared to debond cleanly so that little or no aluminum adhered to the links. A representative engineering stress/engineering strain curve is shown in Fig. 2. The initial part of the curve (up to  $\sim 4\%$  strain) closely resembles that of the Al alloy itself. Evidently the chains offer little constraint to plastic flow in this regime. A single matrix crack formed at the stress maximum ( $\sigma_c \approx 150$  MPa) and led to localized failure. The nominal reinforcement stress,  $\sigma_r$ , at the onset of cracking (estimated from Eq. (2)) was  $\sim 750$  MPa, which is well above the ultimate strength of the chains. This implies that much of the composite stress over the plane A-A in Fig. 1b was carried by the matrix when cracking occurred.

In each of the epoxy composite specimens, multiple rather than single cracks occurred in the matrix where the crowns of links abutted. This matrix cracking began at relatively low stresses ( $\leq 20$  MPa). By comparison, the reported ultimate strength of neat epoxies comparable to those used here is  $\approx 100$  MPa. The difference can be attributed to the high concentration of stress in the matrix where chain links abut, along with the low ductility and fracture toughness of the matrix. Matrix cracking also led to debonding of the chains from the matrix. Prior to chain lockup, the matrix exhibited plasticity as reported earlier by Cox [1]. In most instances, the composite stress prior to lockup was essentially constant at approximately 30 MPa.

In all cases shown, damage was delocalized in the epoxy composites.<sup>1</sup> A typical stress-strain curve for a small link chain composite is shown in Fig. 3.

The lines labeled " $\sigma_r = \sigma_{ch}$ " and " $\sigma_r = \sigma_y$ " in Fig. 3 (and subsequent stress-strain plots) mark where the nominal reinforcement stress equals either the ultimate strength of the bare chain,  $\sigma_{ch}$ , or its yield stress,  $\sigma_y$  (data of Table I). If the matrix is relatively weak, the condition  $\sigma_r = \sigma_{ch}$  should be near the ultimate strength of the composite. In fact, the composite strength is usually beneath this limit and a little above that implied by the condition  $\sigma_r = \sigma_y$ . The ultimate strength is indeed expected to be lower than implied by the ultimate strength of the chains, since the separate chains in a specimen tend to fail at slightly different strains because of minor inconsistency in their stacking.

The line labeled " $\varepsilon_c$ " marks the strain at which universal contact occurs between all the links in a chain after they have displaced through the matrix. This strain will be called the lockup strain. It is a simple function of the dimensions of the links:

---

<sup>1</sup> (One exception, not reported in detail, occurred in a composite fabricated with links welded on the crown, which failed on a single plane within the specimen. The crown-welded chains have only ~50% of the ultimate strength of the other chains, with each link failing at the weld. Because of the location of the failure, these composites were not considered a useful test of the criterion for delocalization, Eq. (1), and so results for them are not especially illuminating. However, they do illustrate the importance to energy absorption of delocalization: ultimate failure occurred at strains of only 0.3 and the energy absorbed per unit volume was a small fraction of that in specimens exhibiting delocalised failure.)

$$\varepsilon_c = \frac{H/r + 2R/r - 4}{H/r + 2R/r + 4} \quad (3)$$

In Fig. 3, the stress is approximately constant in a plateau region prior to the lockup strain and then rises significantly after lockup as the load transfers to the chains.

The line labeled “ $\sigma_r = \beta\sigma_{my}$ ” in Fig. 3 marks where the nominal reinforcement stress equals the maximum stress expected in the chains due to the resistance of the constrained matrix (Eq. (1)). The stress developed in the chain links also scales as the matrix yield stress,  $\sigma_{my}$ . In a relatively weak matrix, the line  $\sigma_r = \beta\sigma_{my}$  should coincide with the plateau stress measured for the composite prior to lockup. It tends to be higher in the epoxy composites, for reasons to be discussed below.

Stress-strain records for epoxy composites made with medium link chains, both as received and annealed, are shown in Fig. 4. Annealing the medium-link chains decreased the yield stress of the bare chains by ~50%, increased their strain to failure by ~100%, and left the ultimate strength relatively unchanged (Fig. 2). These changes did not effect a transition in failure mode: all composites exhibited delocalized damage. However, there were significant changes in mechanisms and the maximum stresses and strains achieved. Unannealed chains failed primarily in the legs (~ 90% of link failures) at the weld location. Annealed chains all failed by necking at the crown. The stress required for link displacement with the annealed chains is considerably lower. Perhaps because the links yield more readily, they stretch and narrow during link displacement, resulting in a lower effective ratio  $R/r$  and therefore a lower resistance to displacement (Eq. 1c). The higher ductility of the annealed links (Fig. 2) also partly accounts for the greater composite strain to ultimate failure. The relatively low value of ultimate composite stress attained with annealed chains (falling even below the condition  $\sigma_r = \sigma_y$ ) suggests that the separate chains in the composite were not equally loaded after the nominal lockup strain was reached, but how this relates to the modified chain properties is unclear.

Damage in the epoxy composite formed with unannealed, medium link chains developed in a particularly interesting way. Link sliding began in all chains at one end of the gauge section at about the same specimen displacement and then progressed steadily up the specimen as successive links locked up. This moving damage front was very similar to the self-similar damage propagation seen in cold-drawing polymers as the necked down region propagates along the specimen.

The epoxy composites with large-link chains exhibited delocalized damage and larger strains prior to lockup than epoxy composites with smaller chain dimensions (Fig. 5). However, the rather open link geometry of the large-link chains allowed relatively easy ejection of epoxy from the specimen, producing the large down-spikes in the stress. Matrix constraint was relatively poor.

The polycarbonate matrix composites all exhibited delocalized failure. The polycarbonate suffered less cracking and was more resistant to ejection during link displacement, resulting in a higher plateau stress level prior to lockup (Fig. 6).

The solder matrix composites also exhibited delocalized damage. The matrix in these composites flowed at very low stresses and was plastically extruded from areas of chain contact. The ease of matrix flow is evident in the low measured composite stresses during link displacement and the similarly low predicted stress,  $\sigma_r = \beta\sigma_{my}$  (Fig. 7).

#### **4. Assessment of the Model of Link Displacement**

The simple analysis of [2] led to predictions of the global stress during link displacement and the condition Eq. (1) for achieving delocalization in a chain composite. Here the validity of the model is assessed against the test results and newly observed mechanisms.

#### 4.1 Stress for Link Displacement

The model of [2] predicts the stress in the middle of the legs of the chain links that is generated by the resistance of the matrix to the displacement of the links. This is the stress marked  $\sigma_r = \beta\sigma_{my}$  in Figs. 3 – 7. If the matrix is relatively compliant, so that  $\sigma_r$  is close to the actual stress in the legs of the links, and is also elastic/perfectly plastic, as assumed in the model, then the prediction  $\sigma_r = \beta\sigma_{my}$  should lie close to the plateau stress, i.e., the stress prior to lockup,  $\varepsilon = \varepsilon_c$ . In fact, for all the epoxy matrix composites (Figs. 3 – 5), the predicted stress lies somewhat above the measured plateau stress. This is probably a consequence of matrix cracking and premature loss of resin fragments from the composite, which lowers the degree of constraint but is not included in the prediction of the constraint factor,  $\beta$ .

For the polycarbonate and solder matrix composites, there was less matrix cracking and much less loss of matrix (hardly any in the solder composites). For these cases, the model ought to be applicable and indeed the predicted stress agrees very well with the measured plateau stress (Figs. 6 and 7). The validity of the model is confirmed.

The plateau stress could be raised in the epoxy composites if matrix cracking and premature loss of matrix could be suppressed, e.g., by fiber reinforcement.

#### 4.2 Predictions of the Transition

The condition for link failure has been included in Figs. 3 – 7 as the line “ $\sigma_r = \sigma_{ch}$ ”. Prediction of the delocalization (the criterion of Eq. (1)) corresponds to this line lying above the predicted line for link displacement, “ $\sigma_r = \beta\sigma_{my}$ ”. The constraint factor,  $\beta$ , has been assigned the values of Eq. (1d), which correspond to the chain/matrix interfaces that are very weak and therefore transfer no load by normal tension or shear. This should be correct for all the composites tested: interface separation always occurred during tests and

remnants of matrix could always be easily detached from chain links. In all cases, delocalization is predicted and observed.

The constraint factor,  $\beta$ , depends quite strongly on the condition of the interfaces. For strongly bonded interfaces, Eq. (1c) predicts values of  $\beta$  that are 2 – 3 times greater than those of Eq. (1d) for the subject links, depending on whether the effects of tensile tractions around the crowns are included (they must be small if the matrix has already cracked between crowns). Such values of  $\beta$  would lead in every case to localized failure.

### 4.3 Composites with Strong Matrices

In the case of the Al matrix composite, the mechanisms of damage development are different to those on which the model of [2] was based. Most importantly, the onset of matrix cracking was delayed until relatively high stress levels had been achieved. At peak load, when the first matrix crack appears on one of the planes A-A of Fig. 1b, the matrix must be carrying significant load, because the upper bound reinforcement stress,  $\sigma_r$ , is, as noted above, well above the strength of the chains. Thus when the matrix does finally fail, the chains are severely overloaded at the failure plane. The model leading to Eq. (1) has been derived by assuming that the matrix is weak in tension and contributes to composite load bearing capacity only by constraining the displacement of links where it is in compression in the entrapped zones. A more complex model is required for composites with matrices that are strong in tension.

Delocalization could be achieved in a composite with a matrix that is strong in tension by introducing defects into the matrix. For example, if weak platelets, e.g., of ceramic, were introduced across the planes A-A of Fig. 1b, then matrix cracking on those planes would occur at relatively low composite stress and the reinforcement on those planes would not

be overloaded when the first matrix occurred. The high flow stress of the matrix would then serve to resist link displacement in the desired fashion.<sup>2</sup>

## 5. Energy Absorption

When failure is delocalized, the average energy absorbed per unit volume is determined by the total area under the engineering stress-engineering strain curve, where the strain refers to the average axial strain over the specimen gauge length. The total energy absorbed,  $W$ , can be partitioned into contributions from the displacement of links through the matrix prior to lockup and from the plastic stretching of the links. These contributions will be referred to as the displacement and chain contributions,  $W_d$  and  $W_{ch}$ , respectively. Since plastic deformation of the links is minimal until all the links in a chain are in direct contact with one another (locked up), the displacement contribution is the area under the stress-strain curve up to the strain at which universal contact occurs, i.e., up to the lockup strain,  $\varepsilon_c$ , of Eq. (3).

Energy absorption data are displayed in Table III. The values shown were computed using the area,  $A_c$ , of the so-called core region of each specimen in deriving the composite stress from the applied load. This yields values that would be expected if the specimens had been made with close packed chains and without any excess, peripheral matrix, which contributes negligibly to the stress-strain curves or the total energy absorption. In all the cases in which damage was delocalized, the displacement contribution exceeds the chain contribution. When delocalization occurs, the total energy absorbed ranges from 15 to 59 MJ/m<sup>3</sup>, the highest values being obtained for polycarbonate matrix composites.

---

<sup>2</sup> Despite the failure of the current effort to achieve delocalization in a metal matrix composite, there is still merit in all metal compositions. They may have significant advantages over polymeric composites in preventing penetration by sharp projectiles in armour applications, for example. A sharp projectile that strikes exactly into the cavity of a link filled with resin might pass through without loading the chains.

The energy absorption per unit volume of the chain composites is compared in Fig. 8 with data for other materials, including cold drawing polymers, monolithic alloys, and some recently developed braided composite tubes [3]. The cold drawing polymers are typified by monolithic polycarbonate, which sustains relatively low loads but can achieve strains of several hundred percent. The energy absorption of alloys is estimated as the area under typical tensile stress-strain curves prior to the formation of any necking instability. The energy absorption data are plotted in Fig. 8 against strength, which is projected to exceed 100 MPa for composites of close packed chains.

Barring idealized chain composites to be discussed below, monolithic alloys and cold-drawing polymers possess the highest values of  $W$ , but other aspects of behaviour must also be considered. The degree of global plasticity attained in both alloys and polymers is quite sensitive to the presence of notches or other stress concentrators, which might arise from part design or damage. Localized failure will occur in alloys if the notch size exceeds a few mm at most [4]. Polycarbonate, a typical cold-drawing polymer, is even more sensitive to notches. The presence of a sub-millimeter nick in the side of a polycarbonate sheet will lead to localized failure and pre-empt cold drawing [1].<sup>3</sup> Furthermore, cold drawing of polymers is also very rate sensitive, with failure at even moderately elevated strain rates reverting to brittle behaviour. The localization/delocalization transition in chain composites, by contrast, is very insensitive to notches, because the chains do not communicate stress concentrations effectively. They are mechanically decoupled early in the failure process. Delocalization in the chain composites is also relatively insensitive to strain rate, a point that will be demonstrated elsewhere.

The values of  $W$  found for the chain composites are usefully higher than those obtained for the braided composite tubes ( $\sim 30$  MJ/m<sup>3</sup>) developed by Harte and Fleck [3]. Furthermore, the chain composites do not need to be tubular; and their stiffness, strength,

---

<sup>3</sup> The polycarbonate matrix *in a chain composite* does not exhibit cold-drawing, because it suffers damage from stress concentrations. Only the chain composite as a whole can sometimes exhibit an analogue of cold-drawing, as an effect of the link lockup mechanism.

and energy absorbing capacity can be made even higher by a combination of material selection and redesign of the link geometry.

The attractiveness of the chain composites for applications demanding high energy absorption but low weight can be assessed in terms of the energy absorbed per unit mass or the specific energy absorption,  $W_s$ , which is defined as

$$W_s = \frac{W}{\rho_c} \quad (4)$$

with  $\rho_c$  the mean composite (or material) density. This property is plotted in Fig. 9 together with the specific composite strength,  $\sigma_s$ , given by

$$\sigma_s = \frac{\sigma_c}{\rho_c} \quad (5)$$

Once again, data for the chain composites has been adjusted to the values expected for closed packed chains with no excess peripheral matrix. The specific energy absorbed by the chain composites ranges up to 14 J/g (for the polycarbonate composite), which stands up very well against monolithic alloys and is not far from the best braided tubes. Cold drawing polymers have the highest specific energy absorption, but even these levels can be equaled for optimized chain composites, as discussed in the following section.

## 6. Potential of Ideal Cases

The ease with which delocalization can be achieved in chain composites and the values attained for energy absorption per unit volume or mass are very encouraging, but still the concept is far from being optimized. Here the modeling developed in [2] is used to predict the maximum energy absorption that could be achieved for idealized chain composites. The question is restricted to optimizing composites using links of the

conventional racetrack geometry (legs and crown of circular cross-section, Fig. 1). The argument is resumed elsewhere for links whose shape can be varied arbitrarily.

The energy absorbed during displacement of the links prior to lockup,  $W_d$ , exceeds the work done in stretching and rupturing the chain links after lockup and it is also the more easily increased by design. So attention will be restricted to enhancing  $W_d$ .

### 6.1 Energy Absorbed per Unit Volume

The displacement contribution to energy absorption,  $W_d$ , is bounded above by the product of the lockup strain,  $\varepsilon_c$ , and the ultimate strength of the composite,  $\sigma_c$ :

$$W_d \leq \varepsilon_c \sigma_c \quad (6)$$

It is therefore maximized by raising  $\varepsilon_c$  as close as possible to unity (the limit for chain composites), raising the ultimate strength and volume fraction of the chain material as high as possible, and raising the constraint and yield strength of the matrix as far as possible, subject to the condition that the criterion of Eq. (1) must remain satisfied to ensure delocalized failure.

For composites with a relatively compliant matrix or containing multiple matrix cracks, a useful approximation to the composite strength is

$$\sigma_c = A_c \sigma_{ch} \quad (7)$$

Both  $A_c$  and  $\sigma_{ch}$  must therefore be maximized. The area fraction,  $A_c$ , depends on the link geometry and the way the parallel chains are stacked together. As shown in the Appendix, the maximum value of  $A_c$  that can be achieved by close packing for racetrack links is

$$A_c \approx \frac{1}{2} \frac{\pi}{[1 + (1 + R/r)\sin \theta/2][1 + (1 + R/r)\cos \theta/2]} \quad (8)$$

This has the peak value 0.27, obtained when  $R/r = 1$ , independent of  $H/r$ .

Currently available commercial chains do not have very high ultimate strength,  $\sigma_{ch}$ , because relatively ductile alloys must be used for safety. A chain must not break before showing clearly visible evidence of plastic strain. In contrast, the links in chain composites do not need to be ductile. Even if the links are brittle, the composite will be very ductile, provided the chains are strong enough to sustain link displacement. Thus much higher strength alloys can be used. Here  $\sigma_{ch} = 1$  GPa will be taken to represent a feasible strong chain material, instead of the values  $\sigma_{ch} < 500$  MPa of Table I. Recalling the maximum achievable value of  $A_c$  (0.27), the maximum achievable composite strength is  $\approx 270$  MPa.

The maximum value of the lockup strain,  $\varepsilon_c$ , for chain composites is unity, a limit approached as the legs of the links become long ( $H \gg r$ ). However, Eq. (3) shows that  $H/r$  must be quite large when  $R/r = 1$  to achieve lockup strains much over 0.5. When  $R/r = 1$ ,

$$\varepsilon_c = \frac{H/r}{H/r + 8} \quad (9)$$

and thus, for example,  $H/r = 12$  is required to achieve  $\varepsilon_c = 0.6$ . The value  $\varepsilon_c = 0.6$  will be used here as a representative upper limit. Combining this with the estimated limit  $\sigma_c = 270$  MPa yields the maximum achievable energy absorption,  $W_d \approx 160$  MJ/m<sup>3</sup>.

Utilizing the ultimate composite strength during link displacement requires that Eq. (1a) be only just satisfied, i.e.,  $\sigma_{my} \approx \sigma_{ch}/\beta$ . Assuming that the constraint constants,  $C_1$ ,  $C_2$ ,  $C_3$ , and  $C_4$ , are unchanging, which might be reasonable if geometrical variations preserve the racetrack shape of the links, then Eq. (1d) yields  $\beta = 2.35$  for  $r = R$ , the condition for maximizing  $A_c$ . Thus optimization requires  $\sigma_{my} \approx 430$  MPa.

Achieving such a large matrix yield stress is itself a material selection challenge. Most materials with such a high yield stress are also fairly brittle and would be likely to fragment and escape from the chains rather than remaining entrapped during large sliding displacements. Loss of matrix was indeed a limiting phenomenon in the epoxy composites. However, the ejection of matrix can be controlled by modifying the geometry of the links and therefore a brittle matrix should not be discounted for this reason. Furthermore, low ductility promotes the onset of matrix cracking where the chain links abut, which averts localized composite failure due to the overloading of links at the first matrix cracking (as in the Al matrix composites). One possible solution might be to use a SiC particulate-reinforced Al alloy composite as the matrix phase, which can be tailored to produce the requisite flow stress (especially in the presence of hydrostatic compression) in combination with limited tensile ductility.

Since relatively long legs are sought ( $H/r \geq 12$ ), the desired matrix yield stress would be reduced if significant shear stress was transferred from the matrix to the chain legs, suggesting a quest for strong interfaces or interfaces with strong friction.

An alternative approach to achieving the desired resistance to link sliding is to raise the constraint factor,  $\beta$ , by modifying the reinforcement geometry. The constraint coefficients,  $C_1$ ,  $C_2$ ,  $C_3$ , and  $C_4$  were evaluated by numerical computation for the particular ratios  $R/r = 2.75$  and  $1.5$ . Although the degree of constraint was (rather remarkably) almost constant over this range, the constraint coefficients and thence  $\beta$  may well increase significantly as the optimal ratio for energy absorption per unit volume is

approached, namely  $R/r = 1$ . In a separate paper, arbitrarily high constraint factors will be demonstrated for chain composites in which the links are not constrained to have circular sections.

## 6.2 Energy Absorbed per Unit Mass

While the energy absorbed per unit volume increases in proportion to the cross-sectional area of the chain legs,  $A_c$ , the energy absorbed per unit mass follows different trends. To first order, both the energy absorbed per unit volume and the composite density are proportional to  $A_c$  and therefore the energy absorbed per unit mass is approximately independent of  $A_c$ .

Equation (4) for the energy absorbed per unit mass may be rewritten:

$$E = \frac{W}{\rho_{ch} V_f + \rho_m (1 - V_f)} \quad (10)$$

where  $\rho_{ch}$  and  $\rho_m$  are the density of the reinforcement and the matrix respectively and  $V_f$  is the reinforcement volume fraction. Focusing once again on the contribution arising during link displacement, assuming  $\rho_{ch} \ll \rho_m$ , recalling the bound Eq. (6), writing  $\sigma_c \approx A_c \sigma_{ch}$ , and substituting Eqs. (3) and (6) and Eqs. (A.2) and (A.4) for  $A_c$  and  $V_f$  for close packed chains, one finds

$$W_s = \frac{A_c \sigma_{ch} \varepsilon_c}{V_f \rho_{ch}} = \frac{\left[ \frac{H}{r} + 2 \frac{R}{r} - 4 \right] \sigma_{ch}}{\left[ \frac{H}{r} + \pi \frac{R}{r} + \pi \right] 2 \rho_{ch}} \quad . \quad (11a)$$

This expression is maximized by the limits  $R = r$  and  $H/r \rightarrow \infty$ . For  $R = r$  and the practical limit  $H/r = 12$ , Eq. (11a) yields

$$W_s \approx 0.3 \frac{\sigma_{ch}}{\rho_{ch}} \quad . \quad (11b)$$

With  $\sigma_{ch} = 1$  GPa and  $\rho_{ch} = 8$  Mg/m<sup>3</sup>, which are representative values for a strong steel alloy,  $W_s \approx 40$  J/g. This energy per unit mass compares very favourably with values for other classes of materials (Fig. 9).

## 7. Conclusions

Experiments for a series of chain composites have confirmed the validity of the model derived in [2] for composites with relatively weak matrices. Provided premature matrix ejection is limited, as in the polycarbonate composite, the stress required for link displacement is accurately predicted. The model can therefore serve as a simple guide to optimizing the chain composites. Its predictions suggest that the energy absorption per unit volume can be raised from 20 – 60 MJ/m<sup>3</sup> for the current chain composites to approximately 160 MJ/m<sup>3</sup> by optimizing the proportions of the chain links (without changing their circular cross-sections) and making optimal choices of chain and matrix materials. By similar optimization, the energy absorbed per unit mass could be raised from the present 14 J/g to approximately 40 J/g.

However, the matrix required for optimization must have a flow stress  $\sim 450$  MPa if chains of circular cross-section are used in combination with weak chain/matrix interfaces, which may be difficult to realize. In other words, for the degree of constraint attainable with chains of circular cross-section, the chain material is probably superfluously strong relative to commonly attainable matrices. A better approach may be

to raise the geometrical constraint factor by modifying the chain shape, so that matrices with more moderate flow stress values,  $\sim 100$  MPa, will suffice.

The chain composites are very attractive relative to other candidate materials for energy absorption. They have the additional advantage that the near independence of separate chains in a chain composite makes the composite very insensitive to notches and other stress concentrators.

### **Acknowledgments**

Work funded by the U.S. Army Research Office, Contract No. DAAH04-95-C-0050. Noemi Altamirano, Christian Berg, Jenny Garredo, Rachel Goldberg, Gloria Rios, Annalise Keen, Amber Sands, and James Yang provided invaluable assistance in fabricating and testing specimens.

## APPENDIX - Area and Volume Fractions for Chains.

Here the problem of stacking chains whose links consist of straight cylindrical legs and semi-toroidal crowns is analyzed. The simplest way to visualize arrangements of chains is to consider projections of links along the axis of the chain (the  $y$ -axis of Fig. 1). The projections of two interpenetrating links are shown in Fig. A.1. The coordinate system in Fig. A.1 is consistent with that in Fig. 1b, where the  $x$ -axis lies in the plane of view. The highest volume fraction of reinforcement will be achieved if the links are allowed to press against one another by rotation about the axis of the chain, as shown in the figure. The contact angle can be deduced from the condition that the projections of the crowns of one link should just meet the projections of the legs of the other link in the pair (Fig. A.1). In the notation of the figure, the contact angle  $\theta$  is given by

$$\theta = \sin^{-1} \left[ \frac{2r}{R+r} \right] \quad (A.1)$$

Area and volume fractions follow after a unit cell (or stacking arrangement) is assigned to the link configuration. One simple unit cell that gives a packing density that is not far from maximized is the rectangular outline shown in Fig. A.1. This unit cell corresponds to chains stacked in the same orientation as those in Fig. A.1 in a tetragonal array similar to that shown in Fig. 1b. The area fraction,  $A_c$ , of the legs on a plane such as A-A in Fig. 1b is

$$A_c = \frac{2\pi r^2}{l_1 l_3} \quad (A.2)$$

where the cell sides  $l_1$  and  $l_3$  are given by

$$\begin{aligned}
l_1 &= 2r + 2(r+R)\cos\frac{\theta}{2} \\
l_3 &= 2r + 2(r+R)\sin\frac{\theta}{2}
\end{aligned} \quad . \quad (A.3)$$

Equations (A.2) and (A.3) lead immediately to Eq. (8).

The volume fraction,  $V_f$ , of the chains in the same stacking arrangement is obtained by dividing the volume of two links,  $2[2\pi r^2 H + 2\pi(R+r)\pi r^2]$ , by the volume of the unit cell,  $l_1 l_2 l_3$ , where  $l_2 = H + 2R + 4r$  is the length of the unit cell (one link) in the direction of the axis of the chain (the  $y$ -axis). Thus

$$\begin{aligned}
V_f &= \frac{\pi \left( \pi + \pi \frac{R}{r} + \frac{H}{r} \right)}{\left[ 4 + 2 \frac{R}{r} + \frac{H}{r} \right] \left[ 1 + \left( 1 + \frac{R}{r} \right) \sin\left(\frac{\theta}{2}\right) \right] \left[ 1 + \left( 1 + \frac{R}{r} \right) \cos\left(\frac{\theta}{2}\right) \right]} \\
&= \frac{\pi + \pi \frac{R}{r} + \frac{H}{r}}{4 + 2 \frac{R}{r} + \frac{H}{r}} \cdot 2A_c
\end{aligned} \quad (A.4)$$

This function depends only very weakly on  $H/r$  and its limit when  $H/r \rightarrow \infty$ , i.e,

$$V_f^{(\infty)} = \frac{\pi}{\left[ 1 + \left( 1 + \frac{R}{r} \right) \sin\left(\frac{\theta}{2}\right) \right] \left[ 1 + \left( 1 + \frac{R}{r} \right) \cos\left(\frac{\theta}{2}\right) \right]} = 2A_c \quad (A.5)$$

gives a lower bound that is close to  $V_f$  for any case.

In the special case,  $r = R$  and  $\theta = \pi/2$ , which is favoured for high constraint, Eq. (A.2) reduces to

$$A_c = \frac{\pi}{2(1+\sqrt{2})^2} \quad (R = r) \quad (\text{A.6})$$

and Eq. (8) to

$$V_f = \frac{\pi}{(1+2\sqrt{2})^2} \frac{2\pi + H/r}{6 + H/r} \quad (R = r) \quad (\text{A.7})$$

When  $r = R$ , geometry imposes the bounds  $2 \leq H/r \leq \infty$ . Over this entire range, Eq. (A.7) varies only from 0.558 to 0.539.

When  $R/r \rightarrow \infty$ , the less useful limit of chains made from fine wires, Eq. (A.2) reduces to

$$A_c = \frac{\pi}{4} \frac{r}{R} \quad (R/r \rightarrow \infty) \quad (\text{A.8})$$

and Eq. (A.4) to

$$V_f = \left(\frac{\pi}{2}\right)^2 \frac{r}{R} \quad (R/r \rightarrow \infty), \quad (\text{A.9})$$

the latter result being independent of  $H/r$ .

## References

- (1) Cox, B.N., "Lockup, Chains and the Delocalization of Damage," *J. Mater. Sci.*, **31** (1996), 4871-81.
- (2) Gong, X.-Y., Zok, F.W., Cox, B.N. and Davis, J., "The mechanics of delocalization and energy absorption in chain composites," submitted to *Acta Materialia*.
- (3) Harte, A.-M., "The Mechanics of Braided Composites," Thesis for Ph.D., Engineering Department, Cambridge University, 1998.
- (4) Suo, Z., Ho, S., and Gong, X.-Y., "Notch Ductile-to-Brittle Transition Due to Localized Inelastic Band," *J. Engng Mater. Technol.* **115** (1993), 319-26.
- (5) Ashby, M. F., *Cambridge Materials Selector*, Cambridge University Press, Cambridge, 1995.

**Table I. Chain Specifications and Properties**

	$H$ (mm)	$R$ (mm)	$r$ (mm)	ultimate strength $\sigma_{ch}$ (MPa)	ultimate strain $\epsilon_{ch}$	yield strength $\sigma_y$ (MPa)	density $\rho_{ch}$ (Mg/m <sup>3</sup> )
<b>Small link</b>	8.67	1.79	0.955	480	0.09	300	7.9
<b>Medium link</b>	7.75	3.00	1.5	480 <sup>(a)</sup> 440 <sup>(b)</sup>	0.13 <sup>(a)</sup> 0.27 <sup>(b)</sup>	300 <sup>(a)</sup> 180 <sup>(b)</sup>	7.9
<b>Large link</b>	21.75	3.00	1.5	460	0.045	300	7.9

<sup>(a)</sup> Pristine

<sup>(b)</sup> Annealed

**Table II. Matrix Properties**

	density $\rho_m$ (Mg/m <sup>3</sup> )	yield stress $\sigma_{my}$ (MPa)
<b>Al alloy matrix</b>	2.83	100 <sup>(a)</sup>
<b>epoxy matrix</b>	1.60	100 <sup>(b)</sup>
<b>polycarbonate</b>	1.2 <sup>(c)</sup>	100 <sup>(d)</sup>
<b>63Sn-37Pb eutectic solder</b>	12.6	37 <sup>(e)</sup>

<sup>(a)</sup> Measured tensile flow stress.

<sup>(b)</sup> Ultimate compressive strength at room temperature – *Engineered Materials Handbook, Vol. 1., Composites*.

<sup>(c)</sup> *Engineering Materials Handbook, Desk Edition*, ASM International.

<sup>(d)</sup> Ultimate compressive strength at room temperature (range 85 – 110 MPa) – *Engineering Materials Handbook, Vol. 2., Engineering Plastics*, ASM International.

<sup>(e)</sup> Tensile yield stress at room temperature and displacement rate 0.003/sec. – *ASM Handbook Vol. 6, Welding, Brazing and Soldering*.

**Table III. Characteristics and Energy Absorption of Chain Composites**

Specimen number	1	2	3	4	5	6	7
<b>Chain</b>	small link (Fig. 3)	small link (Fig. 2)	small link (Fig. 7)	medium link (Fig. 4a)	medium link/annealed (Fig. 4b)	large link (Fig. 5)	small link (Fig. 6)
<b>Matrix</b>	epoxy	Al alloy	solder	epoxy	epoxy	epoxy	polycarbonate
<b>Area fraction of chains<sup>(a)</sup> <math>A_c</math></b>	0.21	0.21	0.21	0.20	0.20	0.20	0.20
<b>Volume fraction of chains<sup>(a)</sup> <math>V_f</math></b>	0.46	0.46	0.46	0.44	0.44	0.42	0.46
<b>Failure Mode<sup>(b)</sup></b>	Del.	Loc.	Del.	Del.	Del.	Del.	Del.
<b>Ultimate strength <math>\sigma_{ult}</math> (MPa)</b>	85	150	45	80	23	70	85
<b>Energy/volume <math>W</math> (MJ/m<sup>3</sup>)</b>	44	11	15	28	19	38	59(?)
<b>Energy from displacement <math>W_d</math> (MJ/m<sup>3</sup>)</b>	26	0	9	18	8	29	43
<b>Energy from chains <math>W_{ch}</math> (MJ/m<sup>3</sup>)</b>	18	11	6	10	11	9	16
<b>Energy/mass <math>W_s</math> (J/g)</b>	9.8	2	1.4	6.4	4.3	8.9	13.8

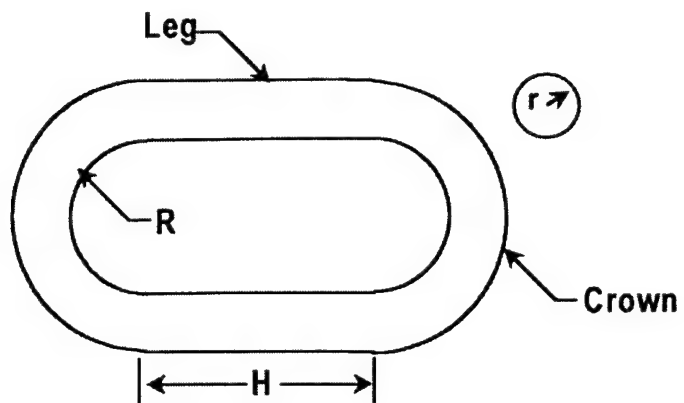
<sup>(a)</sup> Area and volume fractions for epoxy and polycarbonate composites computed from the formulae of the Appendix excluding excess matrix outside the core region of tightly packed chains.

<sup>(b)</sup> "Del" = delocalised; "Loc" = localised.

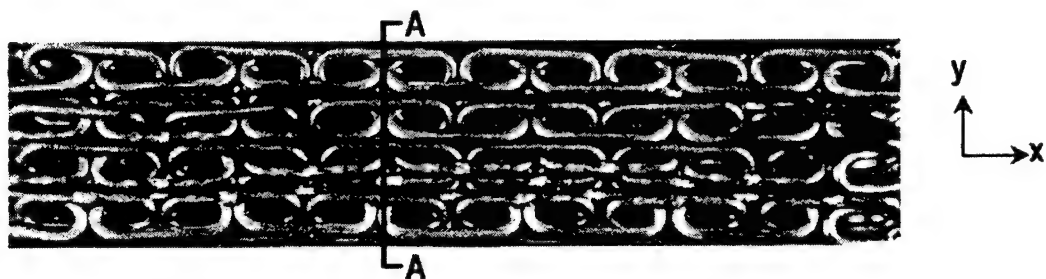
## Figures

- 1 (a) Geometry of a standard chain link (a racetrack link). (b) Contracted chain configuration used in composites. The line  $A-A$  indicates a plane over which the area fraction,  $A_c$ , is computed.
- 2 Stress-strain response of Al matrix/chain composite. The stress-strain response of unreinforced Al alloy has been superimposed.
- 3 Stress-strain record for a small-link chain/epoxy composite.
- 4 Stress-strain records of (a) unannealed medium-link chain/epoxy composites and (b) annealed medium-link chain/epoxy composites.
- 5 Stress-strain record for large-link chain/epoxy composite.
- 6 Stress-strain record for small-link chain/polycarbonate composite.
- 7 Stress-strain record for small-link chain/solder composite.
- 8 The energy absorption,  $W$ , for the tested chain composites, identified by numbers of Table III; hypothetical, optimal chain composites; and other groups of materials. Typical scatter is represented by elliptical domains, following the style of the materials selection charts of Ashby [5]. The energy data are plotted against composite or material strength.
- 9 The specific energy absorption,  $W_s$ , for the tested chain composites, identified by numbers of Table III; hypothetical, optimal chain composites; and other groups of materials. Plotted against specific strength.

A.1 Projection of two interpenetrating links onto a plane normal to the axis of the chain. The projections of the straight cylindrical legs appear as circles. The projections of the semi-toroidal crowns appear as rectangles joining the legs in pairs.



(a) Chain Link Geometry



(b) Contracted Chain Configuration

Figure 1

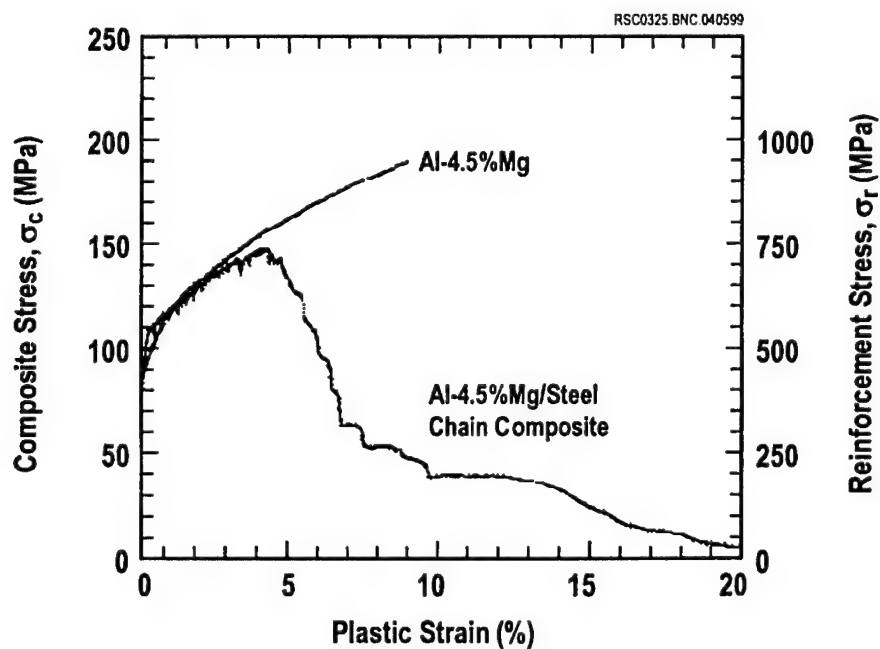


Figure 2

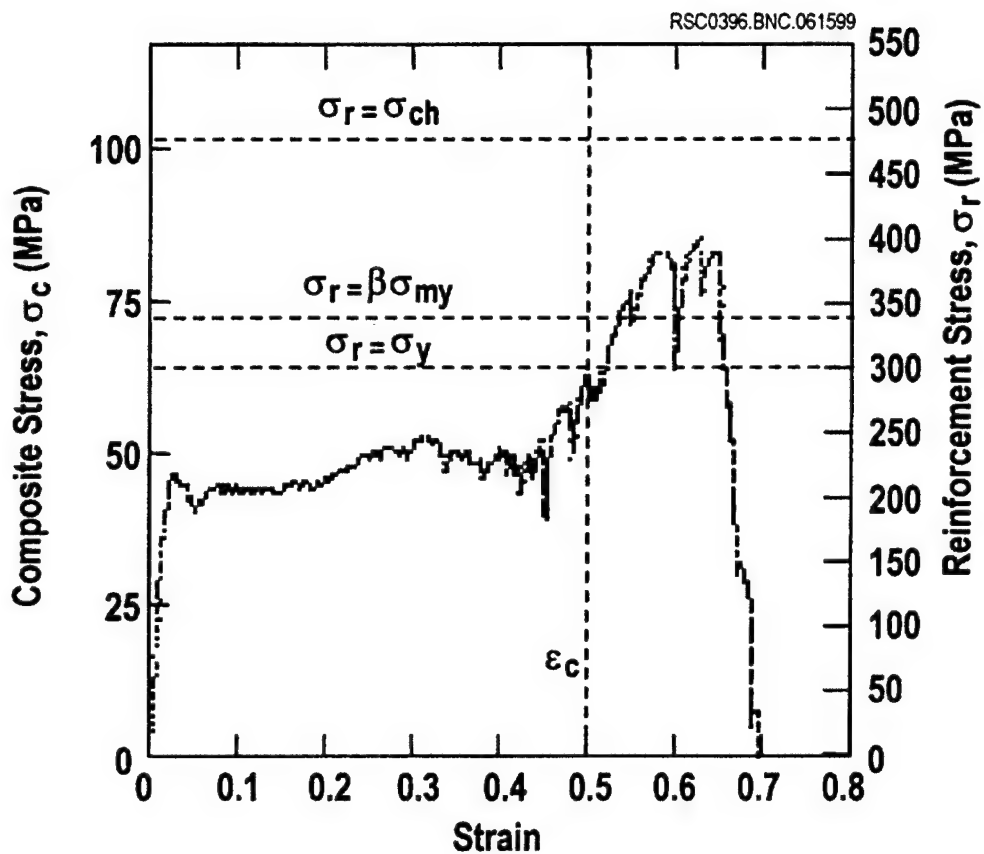


Figure 3

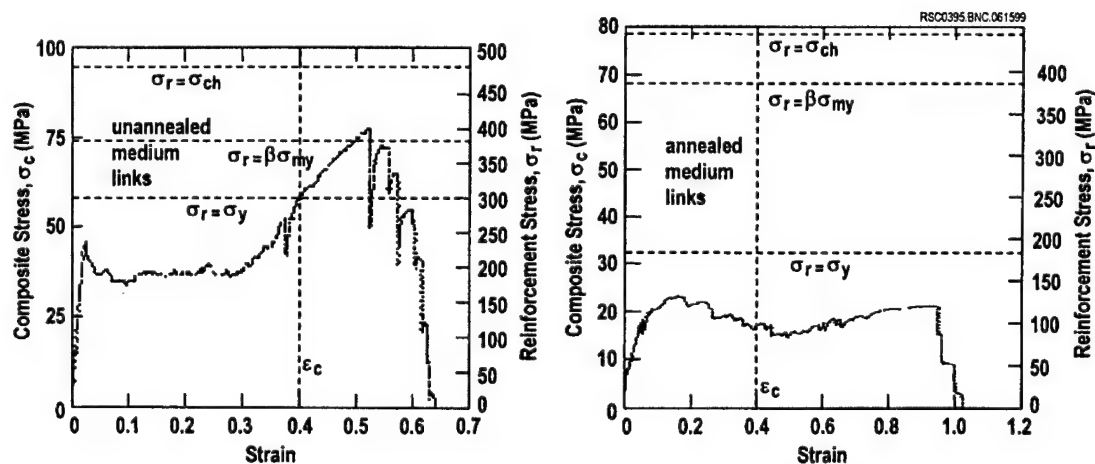


Figure 4a

Figure 4b

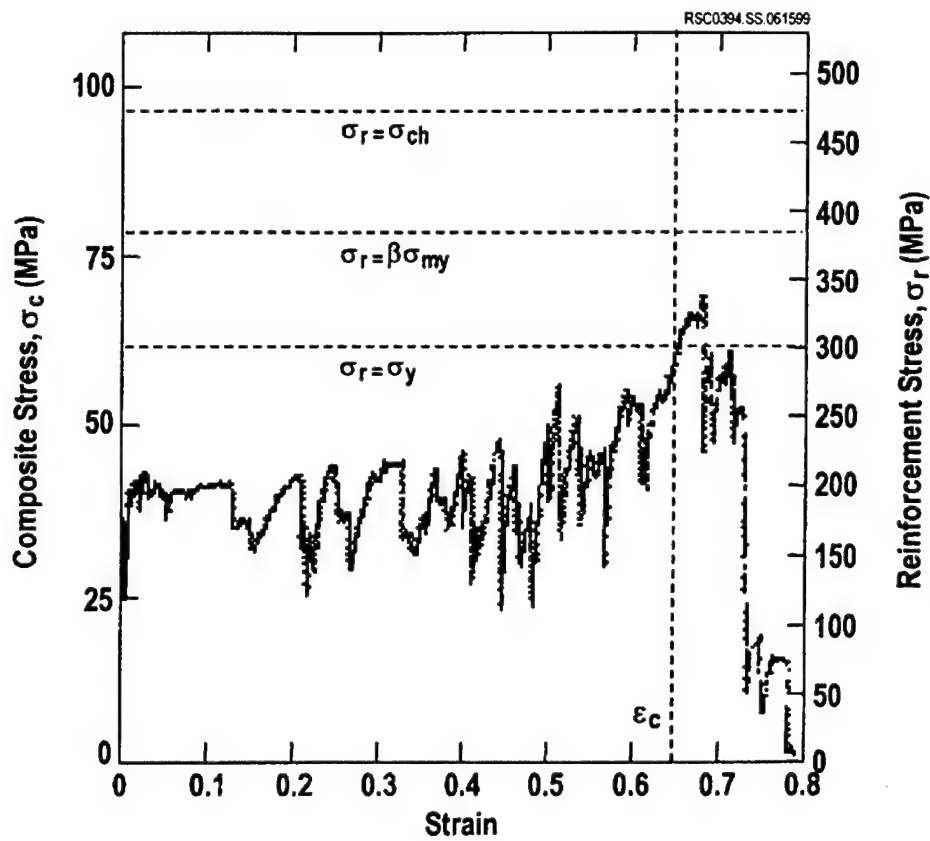


Figure 5

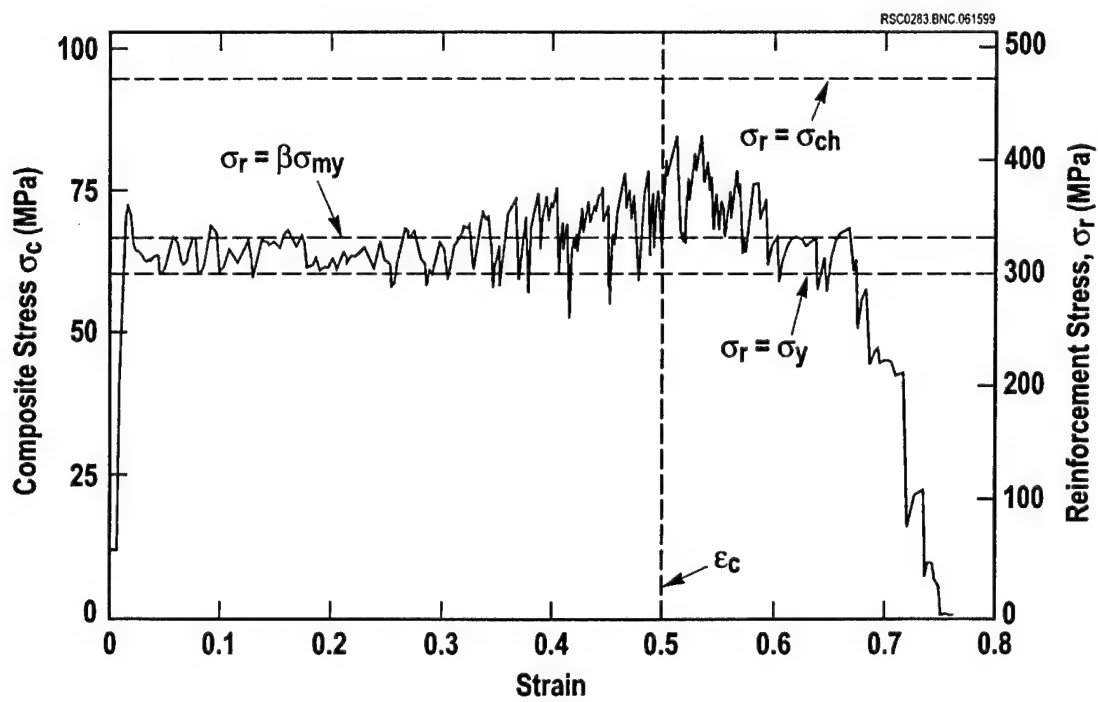


Figure 6

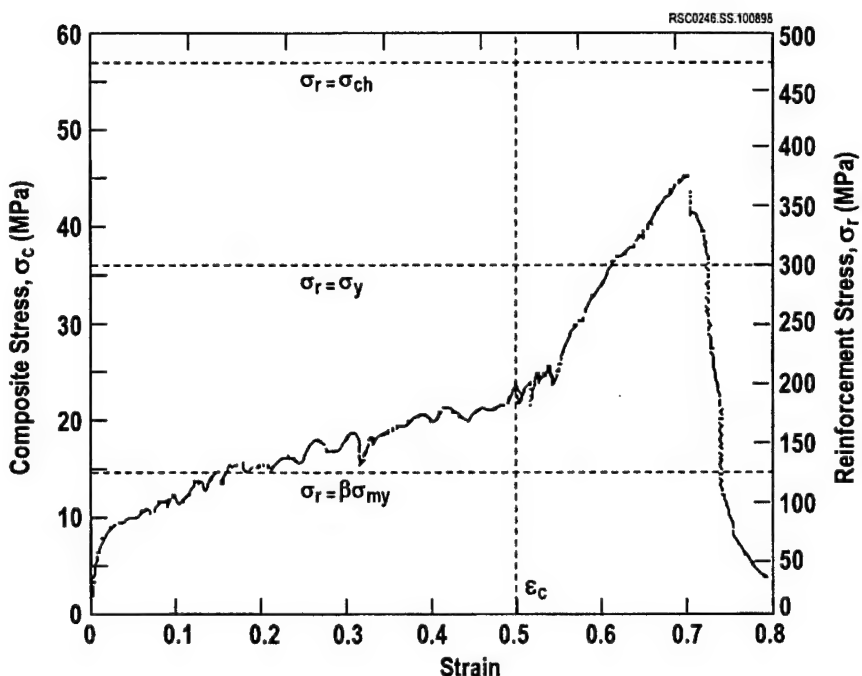


Figure 7

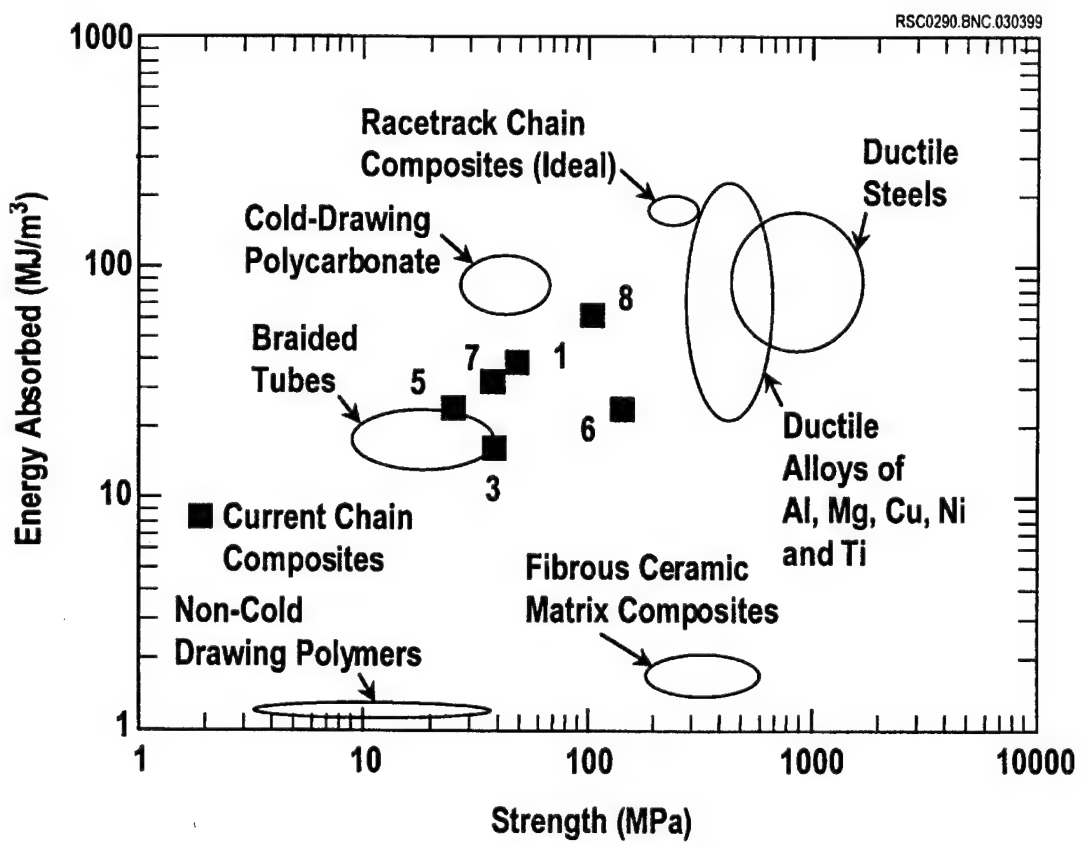


Figure 8

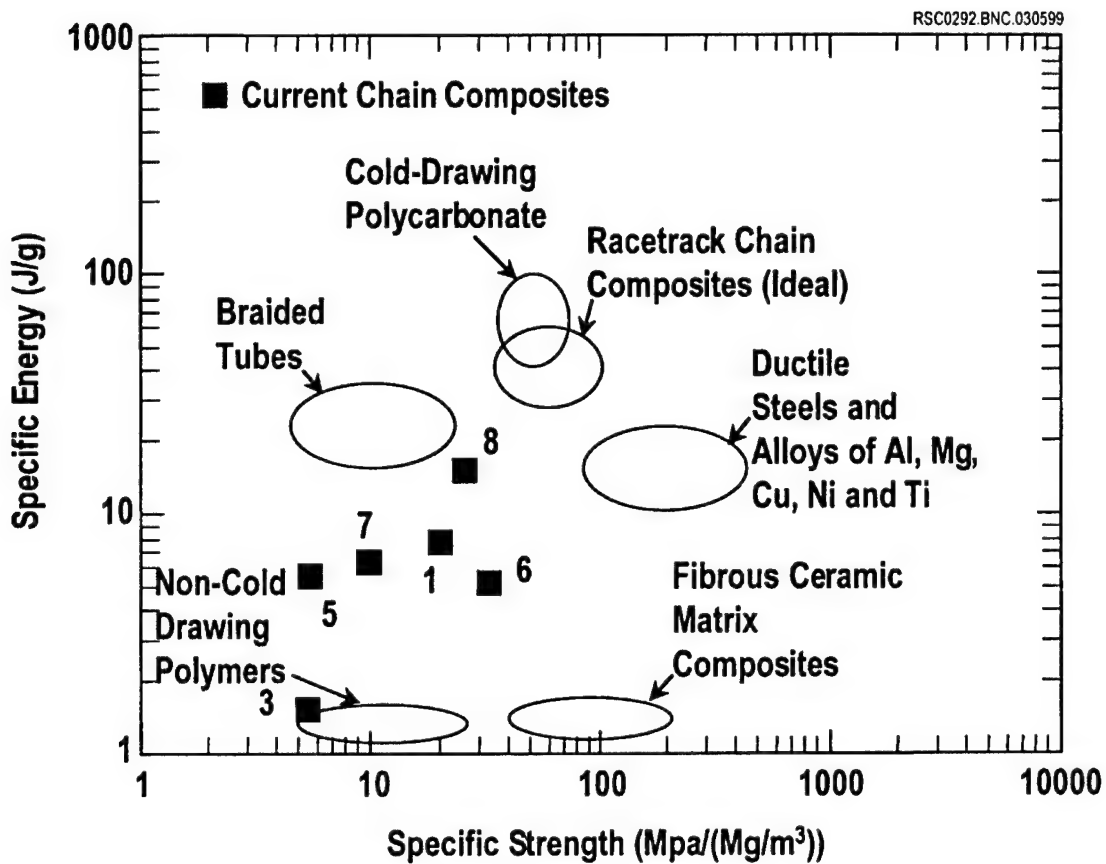


Figure 9

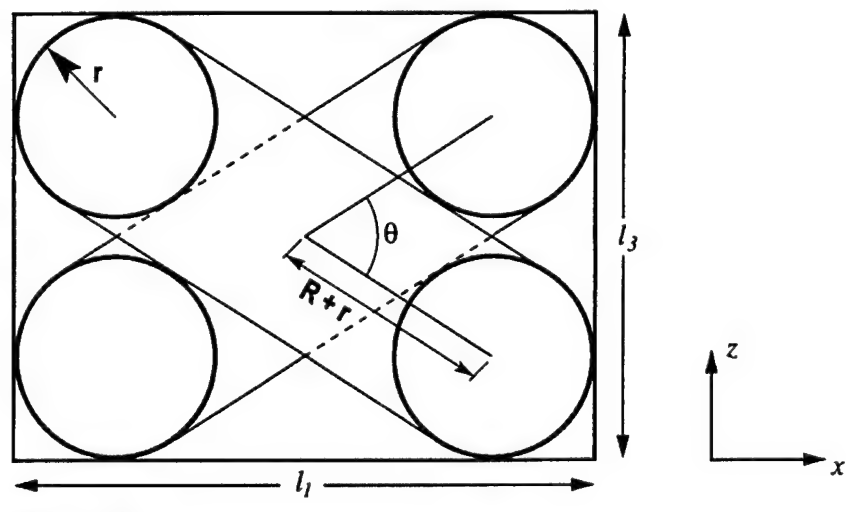
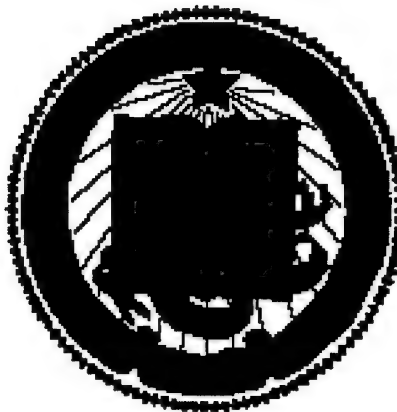


Figure A.1



# **THE MECHANICS OF DELOCALIZATION AND ENERGY ABSORPTION IN CHAIN COMPOSITES**

X.-Y. Gong and F.W. Zok

Materials Department  
University of California  
Santa Barbara, California 93106

B.N. Cox and J. Davis  
Rockwell Science Center  
Thousand Oaks, CA 91360

*Submitted to Acta Materialia*

March, 1999

*Revised June, 1999*

## ABSTRACT

The mechanics of chain composites that can exhibit delocalized failure and very large values of energy absorbed per unit volume during failure are analyzed. The composites absorb energy because they are configured in such a way that chain links must displace through large distances before coming into intimate contact with one another, doing work continuously against the matrix. An approximate analytical model for the stresses within the chain links during link displacement is formulated and the results validated by finite element analyses. The condition that the maximum stress within the links be less than the link strength leads to a criterion for transition from localized failure (involving failure of the links at small strains) to delocalized failure (with distributed damage and large plastic strains occurring via link displacement). The model is also proposed as a design rule for optimizing the energy absorption of this class of composites.

## 1. INTRODUCTION

Mechanical energy is absorbed by solids through irreversible (plastic) deformation. The extent of the absorption depends on the nature of the deformation mechanism, the density of sites at which the mechanism is activated, and the stability of the deformation.

In metals, the deformation occurs by dislocation glide. This mechanism provides very high energy absorption because of the high density of available sites (characterized by the dislocation density) and the rapid hardening that occurs as the dislocations multiply and interact with one another. However, under uniaxial tensile loading, stability of the deformation is lost when the geometric softening associated with area reduction overcomes the intrinsic hardening due to dislocation interactions. This plastic instability is a consequence of the volume-conserving nature of dislocation plasticity. Failure progresses via necking, damage becomes localized to the necked region, and the total work expended per unit volume falls with increasing specimen size. Typically, the global energy absorption in a uniaxial tensile test of a ductile metal alloy is in the range,  $E_v \bullet 20-100 \text{ MJ/m}^3$ .

Some linear polymers exhibit similar energy absorption capacity at temperatures slightly above their glass transition temperature. Flow and hardening occur by sliding of the molecules past one another and their subsequent straightening and alignment along the loading direction. Necking initiates under conditions similar to those in metals, but the neck is stabilized by the high hardening rate associated with molecular alignment. The necked zone then enlarges by self-similar expansion in the process of cold drawing [1]. All the material in even large specimens is eventually deformed to large strains in the failure process and the energy absorbed per unit volume is a constant, independent of specimen size, and may take large values. In cold-drawing polymers such as polyethylene and polycarbonate,  $E_v \bullet 10-80 \text{ MJ/m}^3$ . Network

polymers (e.g., epoxy) deform by similar mechanisms, but cross-linking precludes large-scale molecular alignment and limits the tensile fracture strain to only a few percent. Consequently, the energy absorption capacity is low ( $E_v \sim 1 \text{ MJ/m}^3$ ).

Most monolithic ceramics do not exhibit any global inelastic deformation under tensile loads. Some may undergo distributed microcracking, but this mechanism does not lead to hardening in tension and invariably leads to catastrophic fracture before the attainment of any measurable inelastic strain. In contrast, under compressive loading with a superimposed hydrostatic pressure, microcracks can develop and propagate stably as the load increases. The subsequent frictional sliding along the crack surfaces can result in substantial levels of energy absorption ( $E_v \sim 100 \text{ MJ/m}^3$ ) [2]. Ceramic matrix composites with continuous fiber reinforcement can exhibit global damage under tension in the form of matrix microcracking. Again, the energy is absorbed by friction, in this case when the cracked matrix segments slide over the fibers. However, the energy absorbed per unit volume in tensile tests is modest,  $\sim 1 - 3 \text{ MJ/m}^3$  [3], one or two orders of magnitude less than in ductile metals or cold-drawing polymers.

Recently, a novel composite was devised to demonstrate how the geometry of a reinforcement can be tailored to give remarkably high energy absorption in a uniaxial tensile test (Fig. 1) [4]. The composite comprises steel chains in an epoxy matrix. The chains are embedded in a collapsed condition so that they must be stretched by  $\bullet 40\%$  before the successive links make contact with one another and the load is transferred directly along the length of the chains. The chains *compress* the epoxy matrix entrapped between the links. In compression, the epoxy is capable of absorbing an extremely large amount of energy through plastic work, despite its very low tensile ductility. Indeed, the energy absorbed before the chain links make contact is  $\sim 10 \text{ MJ/m}^3$ . Since the compressed resin pockets constitute only  $\sim 10\%$  of the total composite volume, the energy absorbed in the compressed resin alone is  $\sim 100 \text{ MJ/m}^3$ . Additional energy of  $\sim$

10-15 MJ/m<sup>3</sup> is dissipated in the composite once the chain links make contact with each other and they deform plastically as the strain is increased further.

This paper presents a model for the tensile deformation of chain composites. The primary goal is to identify the material and geometrical factors that determine whether the chains can be drawn through the matrix without failure of the links. The critical condition at which the maximum link stress reaches the link strength represents a transition from delocalized damage and deformation (which is required for high global energy absorption) to one of localized damage and catastrophic failure of the chains with minimal energy absorption. The scope of the model is limited to materials in which the matrix is capable of plastic deformation under compressive loading.

A further experimental investigation of the energy absorption potential of chain composites is presented in Ref. [5]. The latter paper also assesses the ability of the present model to predict the conditions for delocalized damage.

Viewed generally, the chain composites consist of interlocking loops of strong reinforcement arranged to allow large strains before they transfer load directly to one another (by normal contact) and to envelop a ductile matrix which will be loaded in compression. These characteristics can be realized by other loop configurations and with non-metallic, fibrous reinforcements. Novel knitted and braided composites exhibiting delocalized damage and high energy absorption capacity will be reported elsewhere.

## 2. DAMAGE SEQUENCE IN CHAIN COMPOSITES

The model of the localization/delocalization transition is based on the sequence of damage events observed in composites of steel chains in epoxy or soft metal matrices during tensile straining [4, 5]. There are three regimes of interest.

(i) At small strains (up to 1-2%), matrix cracks form in regions where the crowns of links abut, because of the high tensile stress in these regions (Fig. 2). Once cracked, the matrix sheds load to the legs of adjacent links that span the cracks. The planes containing the first matrix cracks are also the planes in which the area fraction of chains is at a minimum.

(ii) Provided the chains are sufficiently strong, further straining is accommodated by plastic deformation of the matrix material entrapped between successive links in the same chain as they move past one another; otherwise (if the chains are weak), the chains fail along the plane of a matrix crack, leading to localization of the deformation. In order for delocalized damage to continue through to large plastic strain, the load needed to effect the plastic deformation must not exceed the load needed to break the chain links. The global straining process may continue until all the matrix material has split or been extruded out of the entrapped volume and the chain links make contact with one another. When the link length is much greater than the link diameter, this contact may require strains approaching 100%.

(iii) Once the chain links are in contact with one another, the matrix contributes negligibly to the load-bearing capacity and the subsequent stress-strain response is dictated by the chains alone. Therefore, the ultimate composite strength and the further strain to failure are equivalent to the strength and failure strain of a dry bundle of chains.

In essence, when the matrix yield stress and reinforcement geometry conspire to transfer high loads to the chain legs at the onset of the full plastic yielding, failure occurs by chain rupture at low strains, thereby limiting the work done by matrix deformation. Conversely, when the stress in the chain leg remains below the chain strength, composite deformation continues until the chain links make contact and considerable work is done through the accompanying deformation. The transition from

localized to delocalized deformation thus represents the critical point at which high energy absorption may be obtained.

To determine the conditions under which delocalized damage is obtained, an analysis has been performed on a 3-dimensional unit cell of the composite. The cell comprises two chain segments between two co-planar matrix cracks, along with the intervening matrix material, as shown in Fig. 2. Because of symmetry, only one quarter of each of the two chain segments is considered. The stresses within the chains have been calculated using both an approximate analytical model and a finite element analysis. For simplicity, the chains are assumed to be elastic and the matrix elastic-perfectly plastic.

### 3. APPROXIMATE ANALYTICAL MODEL

Broadly, the stresses within the chains can be attributed to the interactions between the chains and the matrix as the chains move past one another and the matrix plastically deforms. The nature of these interactions is distinctly different near the crown and the leg segments. Near the crown, matrix deformation is heavily constrained by the chain, resulting in large hydrostatic stresses. In contrast, the matrix regions near the legs are subjected to a relatively uniform tensile stress and load transfer to the legs occurs by a shearing process parallel to the legs. Because of these differences, the two regions are analyzed separately.

The notation for dimensions and the coordinate systems used in the modeling are shown in Fig. 3. The crown sections are assumed to be half-toroids of sectional radius  $r$ . The legs are assumed to be straight cylinders of the same radius. The curvature of the crowns is defined by the inner radius,  $R$ , of the toroid. The inside separation of the two legs of the same link is therefore  $2R$ . The length of each leg is denoted  $H$ . The remote load is applied along the Y-axis of the Cartesian coordinates (X, Y, Z). The

surface of the crown can also be conveniently represented by the angular coordinates  $(\theta, \phi)$ . The  $\rho$ -axis in Fig. 3 will be used to define one component of force acting on the crown segment. The coordinate  $y$  will be used to discuss stress distributions in the leg of the chain.

### 3.1 Stress Distribution Within Crown

Within this region, the tractions acting on the chain surface can be partitioned into three components: the normal pressure,  $P$ , acting along the "inner" surface of the crown ( $-\pi/2 \leq \phi \leq \pi/2$ ); the normal tension,  $T$ , acting along the "outer" surface ( $\pi/2 \leq \phi \leq 3\pi/2$ ); and the maximum shear traction,  $\underline{S}$ , tangential to the interface. Because macroscopic flow within the matrix near the crown occurs predominantly along paths in the Y-Z plane, the vector  $\underline{S}$  is expected to lie within this plane. (The latter hypothesis is confirmed by the finite element calculations, presented in Section 4.)

The quantities  $P$ ,  $T$  and  $\underline{S}$  scale with the matrix yield strength,  $\sigma_{my}$ , in accordance with

$$P = C_1(\theta, \phi)\sigma_{my} \quad (1(a))$$

$$T = C_2(\theta, \phi)\sigma_{my} \quad (1(b))$$

$$S = \left| \underline{S} \right| = C_3(\theta, \phi)\sigma_{my} \quad (1(c))$$

where  $C_1$ ,  $C_2$  and  $C_3$  are functions of location and the interface properties. The incremental forces,  $dF_\rho$  and  $dF_\theta$ , acting in the radial and hoop directions on the surface of the crown at a prescribed value of  $\theta$  can be written in terms of  $P$ ,  $T$  and  $S$  as

$$\begin{aligned}\frac{dF_p}{d\theta} &= \int_{-\pi/2}^{\pi/2} P r(R + r - r \cos \phi) \cos \phi d\phi - \int_{\pi/2}^{3\pi/2} T r(R + r - r \cos \phi) \cos \phi d\phi \\ &+ \int_{-\pi}^{\pi} S_\phi r(R + r - r \cos \phi) \sin \phi d\phi\end{aligned}\quad (2(a))$$

and

$$\frac{dF_\theta}{d\theta} = \int_{-\pi}^{\pi} S_\theta r(R + r - r \cos \phi) d\phi \quad (2(b))$$

where  $r(R + r - r \cos \phi) d\phi d\theta$  is an increment of area on the crown surface; and  $S_\phi$  and  $S_\theta$  are the components of  $S$  acting in the  $\phi$  and  $\theta$  directions, given by

$$S_\phi = \frac{S \sin \theta}{\sqrt{1 - \cos^2 \phi \cos^2 \theta}} \quad (3(a))$$

$$S_\theta = \frac{S \sin \phi \cos \theta}{\sqrt{1 - \cos^2 \phi \cos^2 \theta}} \quad (3(b))$$

The average tensile stress,  $\sigma_o$ , at the leg-crown junction ( $\theta = 0$ ) is obtained by resolving the forces  $dF_p$  and  $dF_\theta$  in the loading direction  $Y$ , integrating over the surface of the crown, and dividing by the cross-sectional area,  $\bullet r^2$ . This yields the result:

$$\frac{\sigma_o}{\sigma_{my}} = \frac{2}{\pi} \left[ I_1 \left( 1 + \frac{R}{r} \right) - I_2 \right] \quad (4)$$

where  $I_1$  and  $I_2$  are the integrals

$$\begin{aligned}
 I_1 &= \left[ \int_0^{\pi/2} [C_1(\theta, \phi) \cos \phi + C_2(\theta, \phi) \sin \phi] d\phi \right] \\
 &\quad + \frac{\pi}{2} \left[ \int_0^{\pi} \frac{C_3(\theta, \phi) \sin \phi}{\sqrt{1 - \cos^2 \theta \cos^2 \phi}} d\phi \right]
 \end{aligned} \tag{5(a)}$$

$$\begin{aligned}
 I_2 &= \left[ \int_0^{\pi/2} [C_1(\theta, \phi) \cos^2 \phi - C_2(\theta, \phi) \sin^2 \phi] d\phi \right] \\
 &\quad + \frac{\pi}{2} \left[ \int_0^{\pi} \frac{C_3(\theta, \phi) \sin \phi \cos \phi}{\sqrt{1 - \cos^2 \theta \cos^2 \phi}} d\phi \right]
 \end{aligned} \tag{5(b)}$$

To proceed simply,  $C_1$ ,  $C_2$  and  $C_3$  are assumed to be independent of  $\theta$  and  $\phi$ .

Then, upon integration, Eqns. 5(a) and 5(b) reduce to

$$I_1 = C_1 + C_2 + 3.664 C_3 \tag{6(a)}$$

$$I_2 = (C_1 - C_2) \pi / 4 \tag{6(b)}$$

and the average tensile stress at the crown-leg junction (from Eqns. 4 and 6) becomes

$$\frac{\sigma_o}{\sigma_{my}} = \left( \frac{2}{\pi} \right) (C_1 + C_2 + 3.664 C_3) \left( 1 + \frac{R}{r} \right) - \frac{(C_1 - C_2)}{2} \tag{7}$$

Estimates of the coefficients  $C_i$  are made in the following way. The coefficient  $C_1$  represents the constraint of the chain on the compressive strength of the matrix. It is expected to be similar to the constraint factor associated with the indentation of a flat-bottomed punch into a semi-infinite plastic medium:  $C_1 \approx 1 + \pi/2 \approx 2.57$  [6]. The coefficient  $C_2$  represents the corresponding constraint on the outer surface of the crown where the matrix is predominantly in tension. Here the constraint is significantly lower

because of the presence of the matrix cracks along the upper and lower cell boundaries. It is expected that  $C_2 \sim 1$  for well-bonded interfaces, and  $C_2 = 0$  for debonded, frictionless interfaces. Finally, the coefficient  $C_3$  represents the normalized sliding resistance of the interface:  $C_3 = S/\sigma_{my}$ . If the interface is perfectly-bonded, this resistance is equal to the shear yield stress of the matrix. That is,  $S = \tau_{my} \cdot \sigma_{my}/2$ , and consequently  $C_3 \cdot 0.5$ . At the other extreme, if the interface is debonded and frictionless,  $C_3 = 0$ .

As shown by the subsequent finite element analysis, the stress in the link at the leg-crown junction ( $\theta = 0$ ) is distributed nonuniformly across the diametral plane. Because of the way in which load is transferred from the crown to the leg, the problem is closely analogous to the distribution of stress across the wall of a thick cylindrical shell loaded by internal pressure. Consequently, the solution for the pressurized shell can be used to estimate the distribution across the diametral plane of the crown-leg junction. The stress distribution in a cylindrical shell of inner radius  $R$  and wall thickness  $2r$ , subject to an internal pressure that gives an average shell stress  $\sigma_0$  is given by:

$$\frac{\sigma}{\sigma_0} = \frac{R}{2(R+r)} \left[ 1 + \left( \frac{R+2r}{X} \right)^2 \right] \quad (8)$$

This solution is compared with the finite element results in Section 4. Upon applying this solution to the chains, the predicted minimum and maximum stresses across the crown-leg junction,  $\sigma_{min}^{(jun)}$  and  $\sigma_{max}^{(jun)}$ , obtained at  $X = R + 2r$  and  $X = R$ , respectively, are given by

$$\frac{\sigma_{min}^{(jun)}}{\sigma_0} = \frac{1}{1 + r/R} \quad (9(a))$$

and

$$\frac{\sigma_{\max}^{(\text{jun})}}{\sigma_o} = 1 + \frac{r}{R} + \frac{(r/R)^2}{1+r/R} \quad (9(b))$$

### 3.2 Stress Distribution Along Leg

Further stresses arise in the legs by direct load transfer from the matrix along the surface of the legs, which is effected through interfacial shear tractions acting parallel to the loading direction, Y. In the shear lag approximation, the axial stress,  $\sigma_y$ , within the leg builds up with the distance  $y$  from the crown end (Fig. 3) according to

$$\frac{d\sigma_y}{dy} = \frac{2S'}{r} \quad (10)$$

where  $S'$  is the shear stress, which scales with the matrix yield stress through

$$S = C_4 \sigma_{my} \quad (11)$$

with  $C_4 \approx 0.5$  for perfectly-bonded interfaces and  $C_4 = 0$  for debonded, frictionless interfaces. Integrating Eqn. 9 along the leg (assuming  $S'$  to be constant) and superimposing the average stress,  $\sigma_o$ , transferred from the crown yields the maximum stress,  $\sigma_{\max}^{(\text{leg})}$ , at the center of the leg ( $y = H/2$ ):

$$\frac{\sigma_{\max}^{(\text{leg})}}{\sigma_{my}} = \left(\frac{2}{\pi}\right) (C_1 + C_2 + 3.664 C_3) \left(1 + \frac{R}{r}\right) - \frac{(C_1 - C_2)}{2} + C_4 \frac{H}{r} \quad (12)$$

To re-iterate, the approximate values of the relevant coefficients are:  $C_1 \bullet 2.57$ ; while  $C_2 \sim 1$  and  $C_3 = C_4 \bullet 0.5$  for perfectly-bonded interfaces; and  $C_2 = C_3 = C_4 = 0$  for debonded, frictionless interfaces.

### 3.3 Composite Stress and Energy Absorption Capacity

Because the matrix is cracked at the center of the leg, the axial matrix stress along this plane is zero. Consequently, from equilibrium, the average composite stress,  $\bar{\sigma}_c$ , is dictated by the area fraction of chains and the stress in the leg along this plane. It can be readily shown from the geometry that the pertinent area fraction  $A_f$  is related to the volume fraction,  $V_f$ , through [5]

$$A_f = \frac{V_f}{2} \left[ \frac{4 + 2R/r + H/r}{\pi + \pi R/r + H/r} \right] \quad (13)$$

Thus the average composite stress when delocalized damage is obtained is given by:

$$\bar{\sigma}_c = \sigma_{\max}^{(\text{leg})} A_f = \frac{\sigma_{\max}^{(\text{leg})} V_f}{2} \left[ \frac{4 + 2R/r + H/r}{\pi + \pi R/r + H/r} \right] \quad (14)$$

Assuming the composite stress to be roughly constant during this phase of the deformation, the energy absorption capacity prior to chain lock-up is given approximately by  $\sigma_{\max}^{(\text{leg})} \varepsilon_c$  where  $\varepsilon_c$  is the tensile strain at the onset of chain lock-up.

## 4. FINITE ELEMENT ANALYSIS

The analytical model was assessed by comparison with a series of finite element calculations based on the cell model and mesh shown in Fig. 2(b). For most simulations, the link dimensions were selected to be  $R/r = 2.75$  and  $H/r = 8.5$ . Some calculations

were performed also for  $R/r = 1.50$  and  $H/r = 8.5$ . These values were selected to be representative of the steel chains used in the companion study [5]. The two geometries yielded essentially the same results for the various coefficients,  $C_i$ , and consequently only the results of the former geometry are presented here. The cell dimensions in the  $X$ ,  $Y$ , and  $Z$  dimensions were  $l_x = l_z = R + 2r$  and  $l_y = R + 2r + H/2$ . The Young's modulus of the chain was taken to be 210 GPa (representative of steel). The matrix was assumed to be elastic-perfectly plastic, with a Young's modulus of 70 GPa and a yield stress of 100 MPa (representative of low-strength Al alloys). It should be noted, however, that at strains much greater than the matrix yield strain, the stresses within the chains depend only on the matrix yield stress and the geometry. Consequently, the numerical results obtained from the present calculations with the specified material properties can be applied to other materials systems, through a re-scaling factor that is simply the ratio of the respective matrix yield strengths; the elastic moduli are largely irrelevant.

Axial displacements were applied uniformly to the chain legs at the top and bottom of the unit cell. The matrix regions on these surfaces were taken to be traction-free. Along the symmetry planes of the cell ( $Z = 0$  and  $X = 0$ ), the normal displacements were fixed at zero. The two other surfaces ( $Z = l_z$  and  $X = l_x$ ) were assigned one of two conditions: either traction-free (to simulate a composite containing a single chain); or symmetric, with uniform normal displacements (to simulate a composite containing an infinite array of parallel chains). These boundary conditions will be referred to as single chain and array boundary conditions, respectively. The interface between the matrix and the chains was assumed to be either perfectly-bonded or unbonded and frictionless. The two interface conditions and the array and single chain conditions constitute a total of four distinct simulations for each chain geometry. The simulations were performed using the ABAQUS<sup>1</sup> finite element code.

---

<sup>1</sup> Hibbit, Karlsson, and Sorensen, Inc., 1080 Main St., Pawtucket, RI 02860.

The calculated stress-strain curves for  $R/r=2.75$  and  $H/r=8.5$  are shown in Fig. 4.

The left ordinate shows the stress,  $\sigma_y$ , averaged over the section of the leg, which is denoted  $\langle\sigma_y\rangle$ , at the middle of the leg ( $y = H/2$ ); the right ordinate shows the average composite stress. The single chain and array boundary conditions yield similar results, with the array condition giving a flow stress that is ~5% higher than that of the single chain condition. In contrast, the two interface conditions yield large differences in strength: the perfectly-bonded material being ~3 times stronger than the unbonded, frictionless material. In all cases, the hardening rate diminishes rapidly with increasing strain as the flow stress approaches a plateau level: the tangent modulus typically reaching a value of <1% of the original elastic modulus at a strain of 3%. This plateau is expected because of the assumed elastic-perfectly plastic nature of the matrix material. Analogous steady-state behavior is obtained in other metal-matrix systems, including unidirectional fiber composites loaded perpendicular to the fibers [7] and particulate-reinforced composites [8].

The stresses obtained from the finite element simulations were used to calculate the various constraint factors. This was accomplished by calculating the pertinent average stress and normalizing the result by the matrix yield stress. For instance,  $C_1$  was determined from the average pressure along the inner surface of the crown, in accordance with Eqn. 1(a). These results are summarized in Table I. The coefficient  $C_1$  is almost identical to the one obtained from the analytical model (2.57), varying only slightly with the imposed boundary condition (2.52 vs. 2.65). As expected,  $C_2 = 0$  for the unbonded, frictionless interface. For the perfectly-bonded interface,  $C_2 = 0.71-0.74$ , depending on the boundary conditions. The low value of  $C_2$  in relation to  $C_1$  is expected, because the matrix cracks along the upper and lower boundaries of the cell reduce constraint on plastic flow. The values of the coefficients  $C_3$  and  $C_4$  are essentially

identical to those obtained from a shear lag analysis for the well-bonded interface (0.5). They are zero for the unbonded, frictionless interface.

The finite element simulations were also used to validate the assumption in the analytical model that the shear traction  $\underline{S}$  acting on the crown surface lies in the Y-Z plane. Figure 5 shows the components of this shear traction acting both within this plane and normal to it as a function of the angular coordinate,  $\theta$ . Clearly, the latter component is about an order of magnitude smaller than the former one, validating the assumption that matrix flow occurs predominantly along the Y-Z plane.

The variation of the average axial chain stress,  $\langle \sigma_y \rangle$ , with position along the leg, obtained from both the finite element calculations and the analytical model, is plotted in Fig. 6. The analytical model works very well provided  $C_2$  is selected appropriately ( $\bullet$  0.6-0.8 for the well-bonded interface). These correlations justify using the analytical model to explore the localization/delocalization transition.

The distribution of the maximum principal stress over the bisecting plane of the crown and leg combination (one quarter of a whole link) is plotted in Fig. 7(a) for a composite with perfectly-bonded interfaces. A notable feature is the stress concentration along the inner surface both near the leg-crown junction and the center of the leg. The distributions in the axial stress across the leg-crown junction computed using the finite element analysis are shown for both strongly bonded and unbonded materials in Fig. 7(b). Also shown for comparison is the corresponding prediction for the stress gradient based on the pressurized shell analogy (Eqn. 8). Remarkably good agreement is obtained.

In the example of the perfectly-bonded interface (Fig. 7(a)), the maximum principal stress at the leg-crown junction is  $\blacktriangle 18 \sigma_{my}$ : significantly higher than the average axial stress across this section, which is  $11.4 \sigma_{my}$ . Moreover, the maximum stress in this region is slightly higher than the average axial stress at the center of the leg ( $\blacktriangle 16 \sigma_{my}$ ). Thus, using the average stress at the leg center to predict the onset of chain

failure may be nonconservative (unduly favoring link survival and delocalized failure of the composite), because the peak stress may be located elsewhere. The differences in these stresses are pronounced in instances where either the chain legs are short (providing less build-up of axial stress at the leg center via interfacial shear) or when the interfaces are unbonded and frictionless. However, the effect of the stress concentration at the leg-crown junction will be important only when the chains are brittle. When the chains are ductile (as were the steel chains in the experiments in Refs. [4] and [5]), the stress concentrations will be blunted and the average stresses at the middle of the leg will be adequate for calculating the critical condition for the onset of chain failure.

## 5. LOCALIZATION/DELOCALIZATION TRANSITION

The preceding analysis can be used to identify the conditions associated with the transition from localized damage (when the maximum chain stress exceeds the chain strength,  $\sigma_{ch}$ ) to delocalized damage. The transition is determined by setting  $\sigma_{max}^{(leg)} = \sigma_{ch}$  in Eqn. 11. The results are plotted as normalized strength,  $\sigma_{ch}/\sigma_{my}$ , against a parameter,  $\beta$ , that characterizes both the chain geometry (through  $H/r$  and  $R/r$ ) as well as the constraints on matrix deformation (through the coefficients  $C_i$ ). Following Eqn. 12, this parameter is defined as

$$\beta = \frac{2}{\pi} (C_1 + C_2 + 3.664 C_3) \left( 1 + \frac{R}{r} \right) - \left( \frac{C_1 - C_2}{2} \right) + C_4 \frac{H}{r} \quad (15)$$

For the array boundary condition, the parameter reduces to

$$\beta = 2.37 + 3.32 R/r + 0.5 H/r \quad (16(a))$$

for perfectly-bonded interfaces, and to

$$\beta = 0.36 + 1.69 R/r \quad (16(b))$$

for unbonded, frictionless interfaces. Quantitatively similar results are obtained for the single chain configuration. It is interesting that, in the former case, the weighting of the ratio  $R/r$  is  $\sim 6$  times that of the ratio  $H/r$ , i.e., most load transfer into the link is via the crown unless the link is exceptionally long; in the latter case, the dependence on  $H/r$  vanishes altogether because of the absence of load transfer along the chain legs.

At large plastic strains, the volume of matrix material entrapped between adjacent crowns decreases as it is extruded outwards. As a consequence, the extent of load transfer diminishes accordingly, especially if the interfaces are well bonded and hence a significant fraction of the chain stress is derived from shear transfer along the legs. The result will be a decreasing composite stress with increasing strain (prior to lock-up). Since the criterion for the localization/delocalization transition has been based on the peak chain stress, it is expected to yield a conservative estimate of the conditions required for delocalized behavior.

## 6. SUMMARY

Analysis of the mechanics of deformation in the chain composites following matrix cracking has resulted in a simple criterion for the transition from localized to delocalized failure in terms of the chain geometry and the strengths of the chain and the matrix. The criterion essentially expresses the balance between raising the resistance to link sliding by strengthening the matrix and increasing the degree to which it is

constrained and not exceeding the strength of the links themselves. The validity of the criterion is appraised in Ref. [5].

The underlying model should be quantitatively correct for links of various proportions, providing they consist of cylindrical legs and semi-toroidal crowns. It is used accordingly in Ref. [5] to predict optimal specifications for chain composites with cylindrical legs and semi-toroidal crowns. But it also provides insight into the essential physics of the delocalization phenomenon, which is relevant to much more general cases that arise when links of other shapes or reinforcements with different topology are considered. This topic will be considered in turn elsewhere.

The model assumes that the chain links are arranged on a perfectly periodic array and the matrix crack spacing is uniform. If periodicity is disrupted either by imperfect composite processing or inhomogeneous damage (both the usual case), the model might be questioned. However, the closeness of computed results for the single chain and array boundary conditions (Figs. 4 and 6) removes this doubt. The motion of one chain is largely independent of its environment.

The model further assumes that the matrix remains perfectly-plastic and then predicts that a constant stress is required for displacement through large displacements. Both the assumption and its consequence will be shown in [5] to be valid to remarkable accuracy provided pieces of the matrix are not ejected prematurely from the region of confinement between links (the most desirable situation). Even when matrix is lost, the stress required for displacement is approximately independent of strain and not far below the prediction of the model.

## ACKNOWLEDGMENTS

Funding was provided by the ARPA University Research Initiative Program at UCSB under ONR contract No. N00014-92-J-1808 and at Rockwell by the U.S. Army Research Office under Contract No. DAAH04-95-C-0050.

## REFERENCES

1. I.M. Ward, *Mechanical Properties of Solid Polymers*, Wiley Interscience, London (1971).
2. M.S. Patterson, *Experimental Rock Deformation - The Brittle Field*, Springer-Verlag, Berlin (1978).
3. D.S. Beyerle, S.M. Spearing and A.G. Evans, "Damage Mechanisms and the Mechanical Properties of a Laminated 0°/90° Ceramic Matrix Composite," *J. Am. Ceram. Soc.*, **75** (1992), 3321-30.
4. B.N. Cox, "Lockup, Chains and the Delocalization of Damage," *J. Mater. Sci.*, **31** (1996), 4871-81.
5. B.N. Cox, J. Davis, N. Sridhar, F.W. Zok and X.-Y. Gong, "The Energy Absorption Potential of Chain Composites," submitted to *Acta Mater.*
6. R. Hill, *The Mathematical Theory of Plasticity*, Clarendon Press, Oxford 1989, pp. 254-61.
7. D.B. Zahl, S. Schmauder and R.M. McMeeking, *Acta Metall. Mater.*, **42** (1994), 2983-2997.
8. G. Bao, J.W. Hutchinson and R.M. McMeeking, *Acta Metall. Mater.*, **39** (1991), 255.

**Table I** Coefficients obtained from finite element analysis

Interface Condition	Boundary Condition	Constraint factors				Integrals (Eqn. 5)	
		C <sub>1</sub>	C <sub>2</sub>	C <sub>3</sub>	C <sub>4</sub>	I <sub>1</sub>	I <sub>2</sub>
Perfectly bonded	Array	2.65	0.74	0.50	0.50	5.22	1.50
	Single chain	2.52	0.71	0.48	0.48	4.99	1.42
Unbonded, frictionless	Array	2.65	0	0	0	2.65	2.08
	Single chain	2.52	0	0	0	2.52	1.98

## FIGURE CAPTIONS

Figure 1 Engineering stress-strain curve of a steel chain/epoxy matrix composite (from Cox *et al.* 1999).

Figure 2 (a) Macrophotograph of the steel chain/epoxy matrix composite. The first matrix cracking occurs between abutting crowns, e.g., at point A. Stress is then concentrated in the legs of the links that span the matrix cracks, e.g., at point B. (b) The representative 3-D unit cell and finite element mesh.

Figure 3 Dimensions and coordinate systems.

Figure 4 Tensile response of chain composite, calculated using the finite element method.

Figure 5 Components of the shear traction  $\underline{S}$ , on the crown surface acting in the Y-Z plane (denoted  $S_{\text{par}}$ ) and perpendicular to this plane ( $S_{\text{perp}}$ ). The results are normalized by the shear yield strength of the matrix.

Figure 6 Distributions in the average axial stress along the leg of the chain.

Figure 7 Distributions of (a) maximum principal stress through the chain cross-section, and (b) the axial stress across the diameter at the leg-crown junction ( $\theta = 0$  or  $y = 0$  in Fig. 3). In (b), the symbols are from the finite element analysis, the solid lines are the analytical model (Eqn. 8), and the dashed lines are the average stress levels across the section.

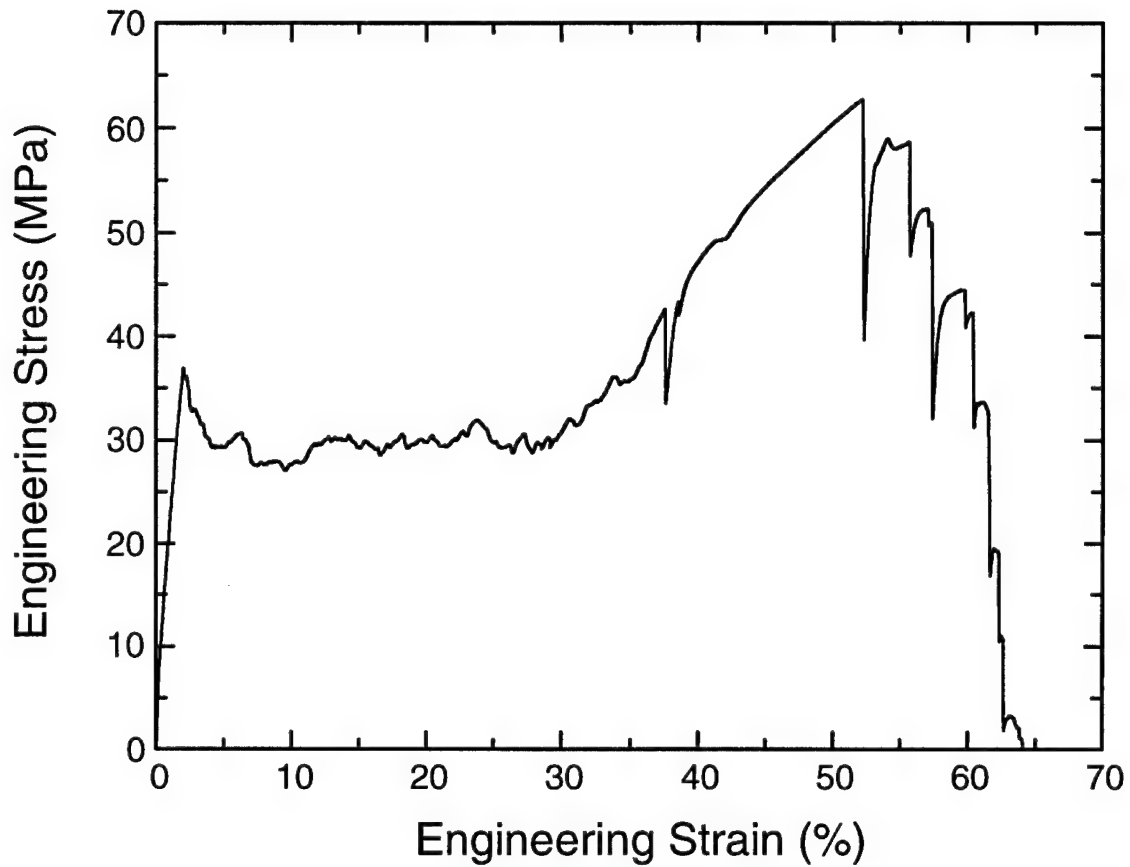


Figure 1 Engineering stress-strain curve of a steel chain/epoxy matrix composite (from Cox *et al.*, 1999).

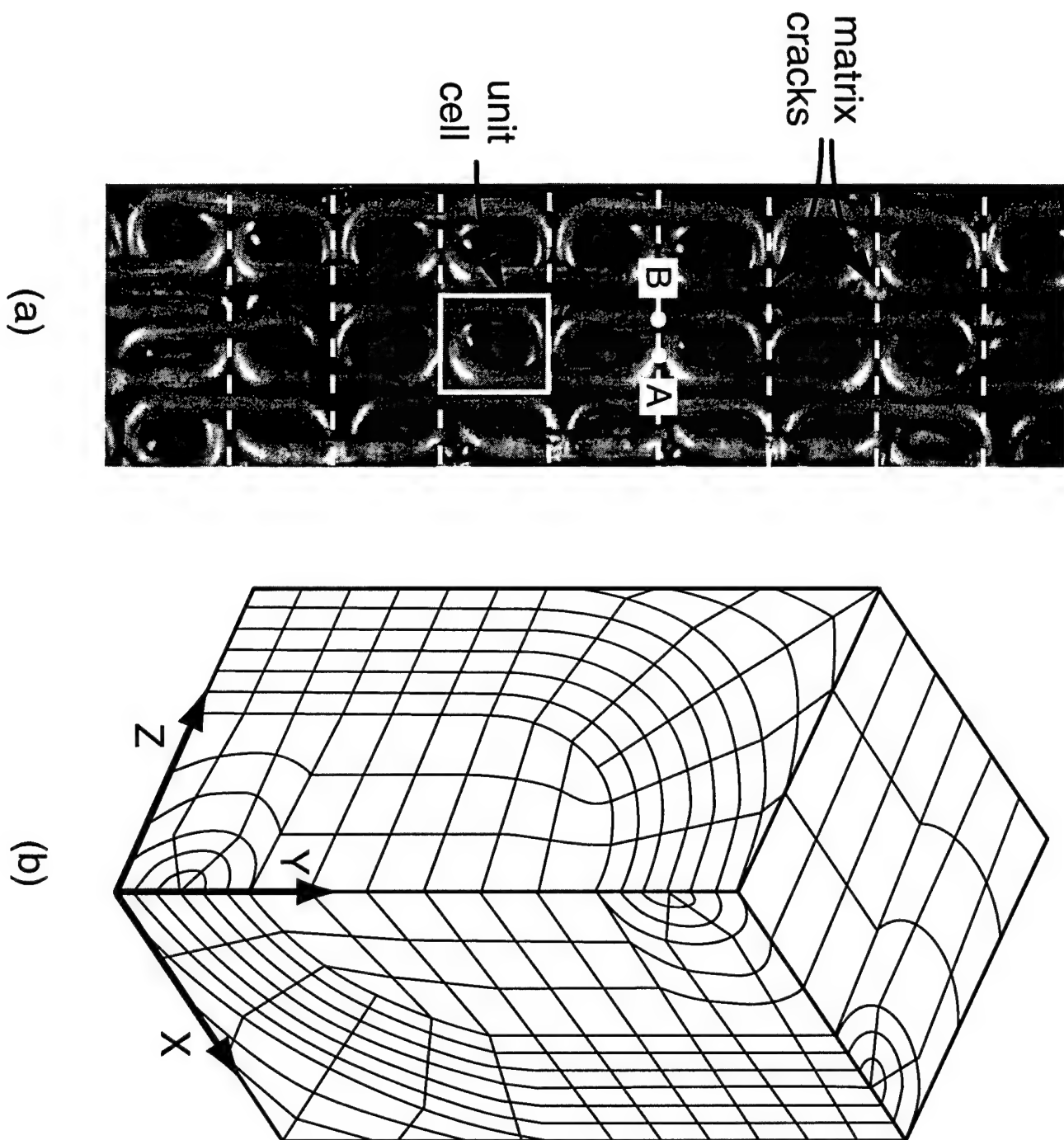


Figure 2 (a) Macrophotograph of the steel chain/epoxy matrix composite. The first matrix cracking occurs between abutting crowns, e.g., at point A. Stress is then concentrated in the legs of the links that span the matrix cracks, e.g., at point B. (b) The representative 3-D unit cell and finite element mesh.

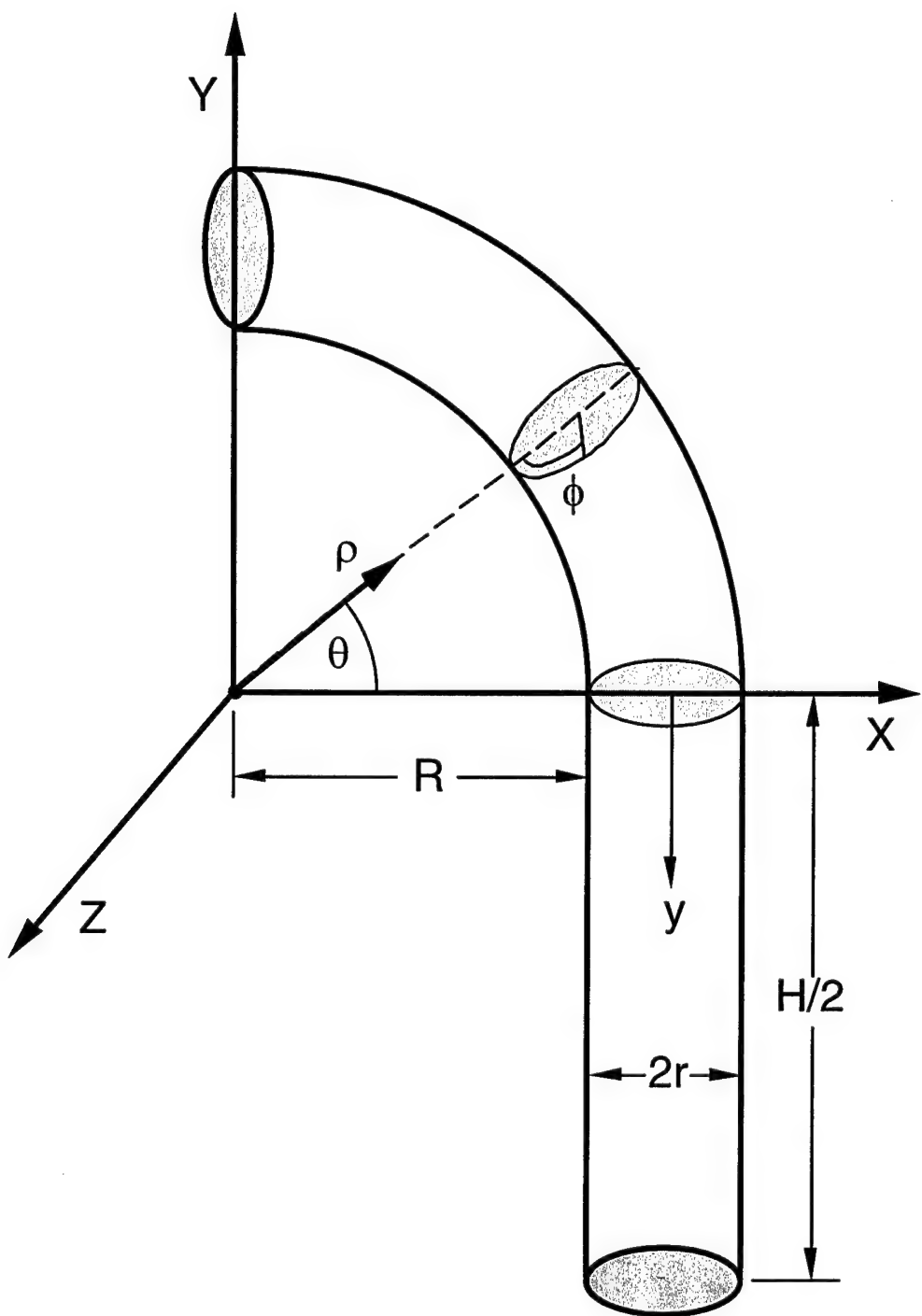


Figure 3 Dimensions and coordinate systems.

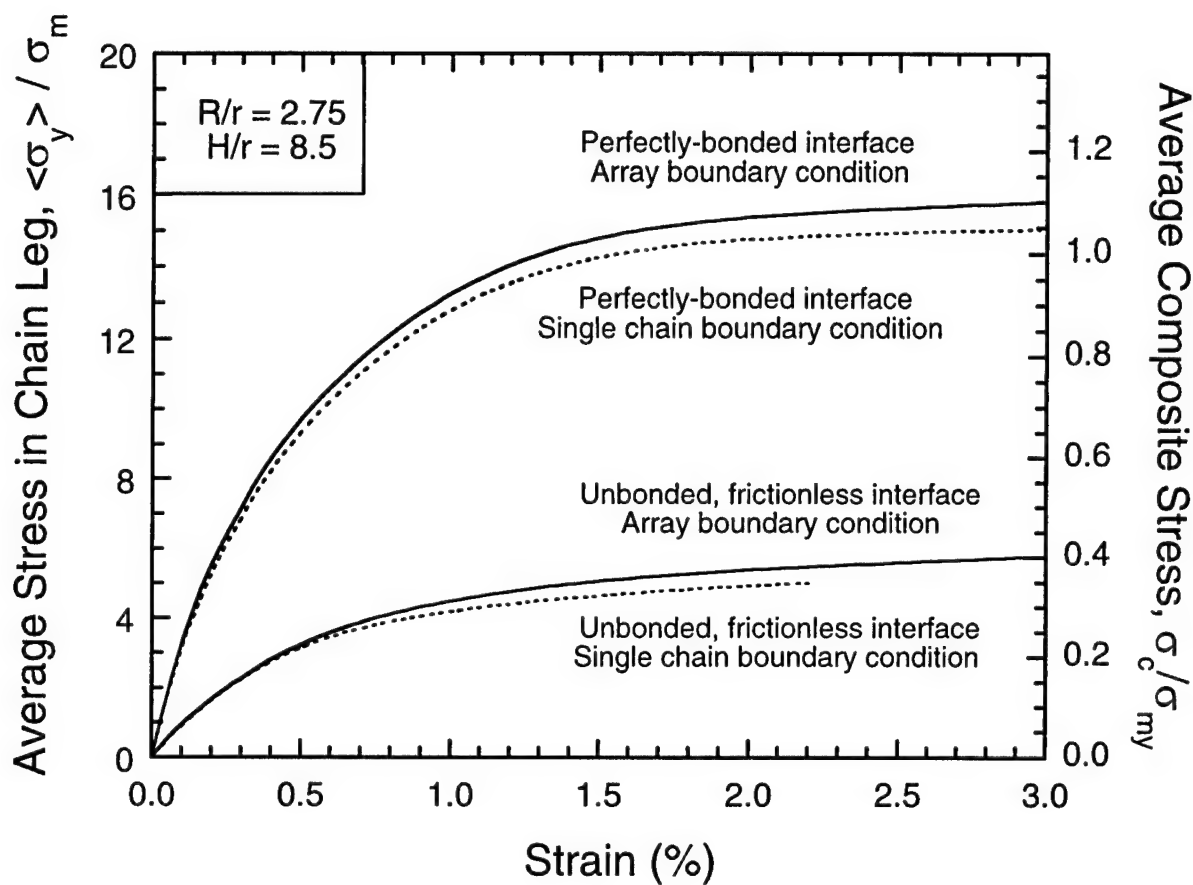


Figure 4 Tensile response of chain composite, calculated using the finite element method.

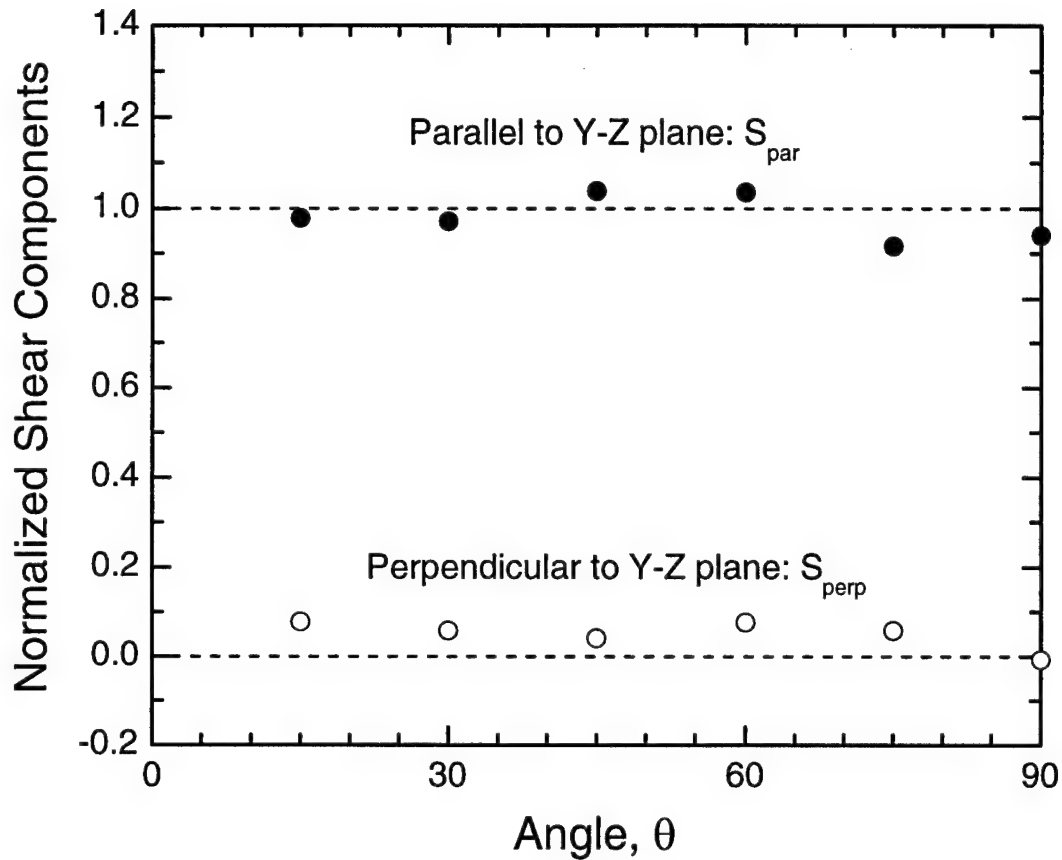


Figure 5 Components of the shear traction  $\underline{S}$ , on the crown surface acting in the Y-Z plane (denoted  $S_{\text{par}}$ ) and perpendicular to this plane ( $S_{\text{perp}}$ ). The results are normalized by the shear yield strength of the matrix.

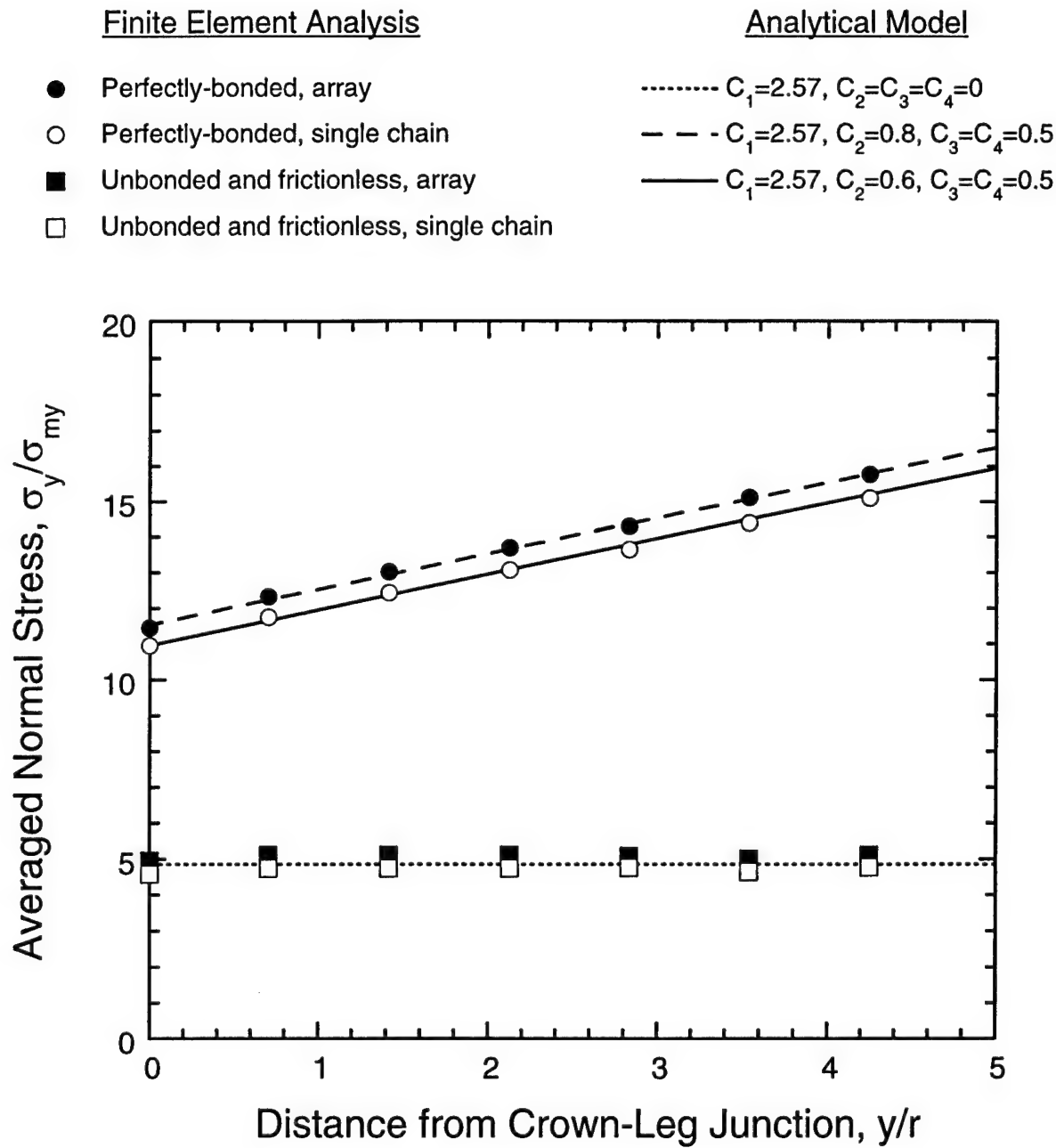


Figure 6 Distributions in the average axial stress along the leg of the chain.

Maximum Principal Stress,  $\sigma_p/\sigma_{my}$

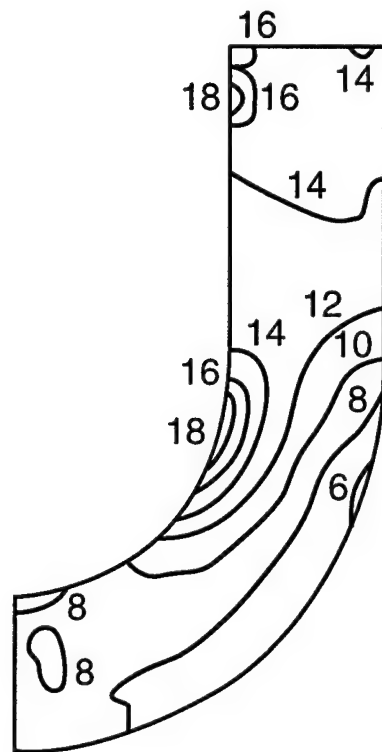


Fig. 7(a)

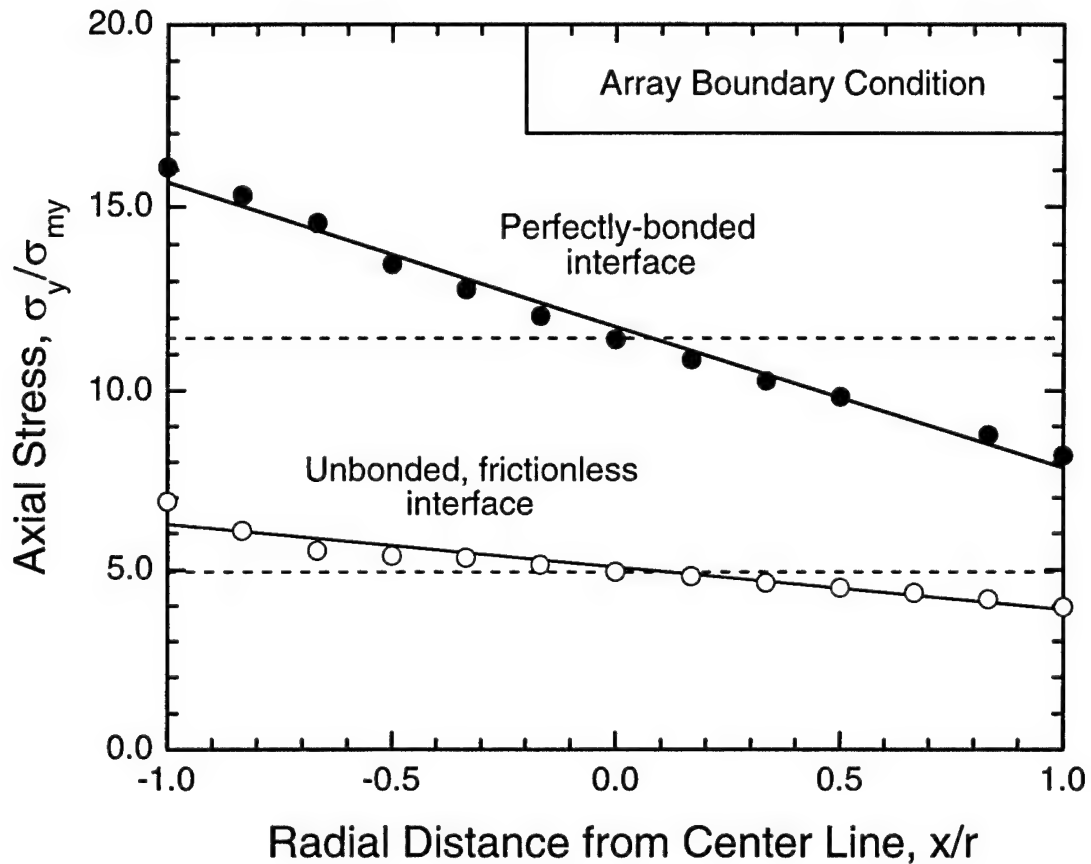


Fig. 7(b)

Figure 7 Distributions of (a) maximum principal stress through the chain cross-section, and (b) the axial stress across the diameter at the leg-crown junction ( $\theta = 0$  or  $y = 0$  in Fig. 3). In (b), the symbols are from the finite element analysis, the solid lines are the analytical model (Eqn. 8), and the dashed lines are the average stress levels across the section.

# **Rockwell Science Center**

## **CHAIN COMPOSITES UNDER BALLISTIC IMPACT CONDITIONS**

**B. N. Cox, N. Sridhar, and J. B. Davis**

Rockwell Science Center  
1049 Camino Dos Rios  
Thousand Oaks, CA 91360  
U.S.A.

**A. Mayer, T. J. McGregor, and A. G. Kurtz**

Wright-Patterson Air Force Base  
Dayton, OH 45433  
U.S.A.

For possible submission to *J. Materials Science*, June, 1999

---

## ABSTRACT

An existing family of composites of steel chains in resin matrices that exhibit delocalised failure and high levels of energy absorption under static tensile loading have been tested under high velocity impact conditions. Panels of chain composites were shot with anti-personnel rounds in an instrumented test range. The tests demonstrate that the lockup mechanism operates at strain rates approaching  $10^4$  sec, with delocalised damage extending in several cases from the impact site to the edge of the test panel. Estimates of the energy absorbed per unit volume under impact conditions range from 30 to 75 MJ/m<sup>2</sup>, approximately 50 – 60% higher than values measured in static tension for the same composites. The enhancement of energy absorption is tentatively attributed to strengthening of the resin at high strain rates. Implications of the tests for designing ballistic protection are discussed.

## INTRODUCTION

Many energy absorption problems involve loads that are tensile, for example, casings designed to contain bursting rotors, turbines, or flywheels; backing plates in armour systems; and containers subject to internal explosions. Here some results of ballistic tests are shown for a new class of chain composites with unusually high-energy absorption capacity under tensile loading.

The chain composites incorporate mechanisms for ensuring that damage is broadly distributed throughout the body of a specimen or structure before the instability associated with ultimate failure sets in [1]. Damage delocalization is promoted by the presence of a so-called lock-up mechanism, in which chain links are arrested by physical contact with one another after displacing through the matrix. The extent of the displacement allowed before the lock-up of two links determines the global engineering strain up to which damage will remain delocalized, which is denoted  $\varepsilon_c$ . The total energy absorbed per unit volume is bounded from below by the product of  $\varepsilon_c$  and the magnitude of the global composite engineering stress required for reinforcement displacement,  $\sigma_d$ . Measured levels of total energy absorbed per unit volume by chain composites in static tests range up to  $60 \text{ MJ/m}^3$ . The potential has been demonstrated by modeling the micromechanics of link displacement for levels up to  $180 \text{ MJ/m}^3$  in optimized chain composites.

Here static tests are extended to the dynamic regime (local strain rates  $\sim 10^4 \text{ sec}^{-1}$ ) by a series of ballistic tests on flat panels of chain composite. The essential questions addressed in the tests are whether lockup and the delocalization mechanism will be activated at high strain rates and what levels of energy absorption per unit volume can be achieved under dynamic conditions.

## COMPOSITES OF CHAINS UNDER STATIC LOADING

Composites of chains in epoxy matrices in which the links are initially in a contracted configuration (Fig. 1) fail under static loading with damage spread over the whole stressed volume. The underlying phenomena were first discussed in [1] and have now been analyzed quantitatively by analytical and computational methods [2,3]. Damage begins with extensive matrix cracking. Successive chain links slide towards contact with one another, crushing resin trapped between them in a state of near hydrostatic compression. The displacement of links through the resin absorbs most of the energy expended en route to ultimate failure. When two links come into direct contact, they are said to lock up: the material hardens locally, resisting further local displacement and triggering the displacement of links elsewhere in the same chain. Only when all links in a chain are in direct contact with their neighbors does the chain begin to fail by plastic deformation of the links followed by rupture of the weakest among them.

A typical stress-strain curve from a static test is shown in Fig. 2. During link displacement, the applied engineering stress is approximately constant in most chain/polymer composites (strain less than 0.5 in Fig. 2). Its magnitude can be estimated by modeling the matrix as a rigid/perfectly plastic medium through which the links must move. Stress transfer into the links from the matrix during the displacement can be partitioned conveniently into several contributions. 1) Hydrostatic compression in the resin trapped between two links as they approach one another exerts pressure over the inner surface of the crown of each link (the curved end). 2) Shear tractions develop over the crown of a link as it slides through the matrix. 3) Tensile tractions act on the outer surface of the crown where the matrix is being pulled apart between the crowns of abutting links, at least until the matrix fails (e.g., along line A-A in Fig. 1). 4) Shear stresses act over the legs (the straight portions) as the links slide through the matrix. The sum of the four contributions, when resolved in the direction of the motion of the links, must be balanced by tension in the legs, which takes its maximum value,  $\sigma_{\max}^{(leg)}$ , at the centre of the legs; and all four are proportional to the matrix shear flow stress,  $\sigma_{my}$ , the

constants of proportionality depending on the link geometry. Summarizing the results of finite element calculations [2]

$$\sigma_{\max}^{(leg)} = \beta \sigma_{my} \quad (1)$$

$$\beta \equiv \frac{2}{\pi} \left( C_1 + C_2 + 3.664 C_3 \right) \left( 1 + \frac{R}{r} \right) - \left( \frac{C_1 - C_2}{2} \right) + C_4 \frac{H}{r}$$

where  $r$  is the radius of the wire in the link,  $R$  is the inner radius of the crown segment, and  $H$  is the length of the leg segment (Fig. 1a); and  $C_1$ ,  $C_2$ ,  $C_3$ , and  $C_4$  are dimensionless constants of proportionality corresponding in order to the four contributions listed above. The constants  $C_1$ ,  $C_2$ ,  $C_3$ , and  $C_4$  were evaluated in [2]. Equation (1) is restricted to links consisting of semi-toroidal crowns connected by cylindrical legs, which is the standard geometry of commercially available chains. For perfectly bonded link/matrix interfaces, the proportionality factor  $\beta$  reduces to the even simpler result

$$\beta = 2.37 + 3.32 \frac{R}{r} + 0.5 \frac{H}{r} \quad (2)$$

and for unbonded, frictionless interfaces to

$$\beta = 0.36 + 1.69 \frac{R}{r} \quad . \quad (3)$$

Equation (3) represents the case that the dominant resistance to link displacement arises from the matrix trapped under hydrostatic compression acting on the crown of the link. This is the situation in the epoxy/steel chain composites fabricated to date [3].

If the matrix is relatively compliant, then Eq. (1) multiplied by the area fraction occupied by the legs of the links on a plane through their centres (e.g., the plane A-A in Fig. 1) should be approximately equal to the composite stress during link displacement,  $\sigma_d$ . This is shown in Fig. 2 by the line marked “ $\sigma_r = \beta \sigma_{my}$ . It is a little above the measured plateau

stress. The discrepancy is attributed to loss of matrix from the composite, which reduces the resistance to link displacement and was not included in the model. In static tests, the matrix fractures into fairly small pieces, which are ejected from the specimen at intermediate strains.

A transition from delocalized to localized failure should occur if  $\sigma_{\max}^{(leg)}$  exceeds the strength of the chain material,  $\sigma_{ch}$ , during link displacement. This was not the case in the test of Fig. 2. However, when the composite stress divided by the area fraction of the links, which is denoted  $\sigma_r$ , exceeds  $\sigma_{ch}$  following link lockup, the chains must fail. This condition is indicated by the line marked “ $\sigma_r = \sigma_{ch}$ ” in Fig. 2. The line lies somewhat above the measured peak stress, a discrepancy attributed to slightly unequal loading among the chains.

## BALLISTIC IMPACT TESTS OF CHAIN COMPOSITE PANELS

### Test Panels

Specimens were made with carbon steel chains of two sizes, whose specifications are listed in Table I. The listed static ultimate strengths of the chains were measured as the load to failure divided by the cross-sectional area of the two legs of a link. Square panels were fabricated with lateral dimensions approximately 127 x 127 mm. The chains were laid up in two layers in the contracted configuration illustrated by Fig. 1b, with the chain orientation alternating between 0° and 90° from layer to layer. Four panels, whose specifications are listed in Table II, were tested. The chains were set in Epofix epoxy resin.

The listed volume fraction of the chains were deduced from the measured total panel mass and the known densities of carbon steel and epoxy resin. They are higher for the panels made with small links because the links were packed more skillfully in these panels. The areal densities of the chain composites were approximately 0.032 g/mm<sup>2</sup> for

the small link panels and  $0.047 \text{ g/mm}^2$  for the large link panels. Plates of monolithic steel of the same areal density as the small and large link panels would be 4 mm and 6 mm thick respectively.

### Ballistic Test Procedure and Observations

The panel specimens were tested under impact by 0.30 and 0.50 calibre armour piercing (AP) rounds fired from a gun. The rounds are made of lead with a copper jacket and are pointed. Each specimen was clamped around its periphery in a square gripping arrangement. The panels were milled in the gripped region to expose chain links for better load transfer.

The incident velocity for which the probability of penetration for the chain composites would be expected to be 0.5 was estimated by testing with mild steel plates of similar areal density. Tests of the chain composites were then conducted at around this incident velocity.

The round achieved penetration in every test, with incident and exit velocities,  $v_{\text{in}}$  and  $v_{\text{out}}$ , and kinetic energy lost from the round,  $\Delta K$ , as listed in Table II. The rounds were not severely damaged by the tests, implying that most of the lost kinetic energy went into deformation of the chain composite rather than of the round itself.

Representative states of damage of a chain composite panel following a test are shown in Fig. 3. On both faces, chains have failed and the failed links and perhaps the next links have been displaced to the point of lockup. This process is generally much more widespread on the exit face, being confined to the environs of the impact site on the incident face. In the specimen shown, more distant damage on the front face consists solely of distributed matrix cracks and accounts for a minor contribution to energy absorption. On the rear (exit) face, links are significantly displaced all the way to the edge of the plate. In one case, specimen CA#4, two chains were pulled completely out of the gripping area at the specimen's edge.

High-speed photography showed resin ejected from both the incident and exit faces. Links were seen flopping quite freely against the exit face once they had been freed from the resin.

## DEFORMATION OF THE CHAIN COMPOSITE DURING IMPACT

Energy absorption in the chain composites is associated primarily with the very high levels of local damage associated with link displacement to lockup. This is evidenced by the stress-strain record under static loading. Multiple matrix cracking similar to that in Fig. 3 occurs in static tests at quite low strains ( $\sim 0.01 - 0.05$ ), yet the global stress during this phase is no higher than during the subsequent displacement of links to lockup (Fig. 2). The displacement phase of damage lasts from strains of near zero to strains of approximately 0.5. Thus the plastic work done against the matrix during link displacement is much larger than the energy associated with distributed matrix cracking; and it will also be much larger than the energy dissipated in elastic wave propagation. The most important issue is therefore to quantify the process of link displacement. Links that have been displaced significantly towards lockup will be said to have been activated. In the following, some estimates of loads and energy absorption in the activated chains are made, based on the assumption that all of the kinetic energy lost from the round has gone into displacing activated links.

The energy absorbing damage in a panel can be summarized as the distribution of displacements of individual links. This distribution was measured by inspection of the panels after ballistic testing. The displacement of any link was recorded as a fraction,  $\phi_d$ , of the displacement required for its lockup against the next link in the chain. If all resin was missing between the two links,  $\phi_d$  was recorded as unity: lockup was assumed to have been achieved. If two links had displaced significantly but not to lockup, they were assigned a fractional displacement  $\phi_d = 0.5$ . This two-valued approximation for  $\phi_d$  is adequate for estimating the total energy absorbed. The recorded numbers of links with  $\phi_d = 0.5$  or 1 are shown for each specimen in Table III. Two-thirds to three-quarters of the activated links lay in the rear layer of chains.

The round will be assumed to drag the chains it contacts out away from the panel (Fig. 4). To accommodate this chain displacement, the links within the chains must displace towards lockup. Since activation sometimes extends only part of the way to the specimen boundaries in some specimens, activation is inferred to begin at the site of impact and propagate away from it, with successive links locking up fully before the next link begins to be displaced. Because the chains are held into the composite by resin only, which is brittle and weak in tension, the activated links will rotate relatively easily between the activation front and the impactor, as shown in Fig. 4. The rotation will be assumed to occur within a relatively small interval. Links and resin in this curved section could be represented as a beam, in which large membrane tension exists, along with such bending moments and shear as are required to support the curvature. When the links have displaced fully to lockup, the resin will have been ejected from their vicinity, leaving bare links in contact to sustain load. These bare links must lie on a straight line, as indicated in Fig. 4. The angle of the straight line to the back face of the plate,  $\theta$ , is related to the strain to lockup,  $\varepsilon_c$ . It is constant during propagation of the activation zone if the curved segment is small.

## Kinematics

Attention will be focused on the interaction of the round with the rear layer of chains, since that is where most energy absorption occurred. The kinetic energy lost by the round (Table II) can be partitioned into energy absorbed by the front and rear layers of chains in proportion to the number of activated links in the layers. The ratio of the energy absorbed in the rear layer to the total energy absorbed,  $\Delta K_{\text{rear}}/\Delta K$ , is listed in Table III. It lies between 2/3 and 3/4. From this energy partition, a representative incident velocity for the round upon the rear layer of chains,  $v_2$ , can be estimated as

$$\frac{v_2^2 - v_{\text{out}}^2}{v_{\text{in}}^2 - v_{\text{out}}^2} = \frac{\Delta K_{\text{rear}}}{\Delta K} \quad . \quad (4)$$

Let  $t_0$  denote the time of contact between the round and the activated chains in the rear layer,  $d$  the interval of the round's flight through which contact exists,  $m$  the mass of the round, and  $F$  the force acting on the round. If the loads in the locked-up chains and the angle  $\theta$  are constant during propagation of the activation zone, then  $F$  and  $a$  must also be constant. By elementary kinematics

$$t_0 = \frac{2d}{v_2 + v_{\text{out}}} \quad . \quad (5)$$

Denote by  $n$  the greatest number of links in any chain that are activated and attain lockup, counting from the impact site in one direction only. The initial length of the  $n$  links in the pristine composite is

$$s_1 = \frac{n}{2} [H + 2(2r + R)] \quad (6a)$$

and the final length (after displacement to lockup) is

$$s_2 = n[H + 2R] \quad (6b)$$

where  $H$ ,  $R$ , and  $r$  are defined in Fig. 1. Thus the engineering strain to lock-up is

$$\varepsilon_c = \frac{s_2 - s_1}{s_1} = \frac{H/r + 2R/r - 4}{H/r + 2R/r + 4} \quad . \quad (7)$$

The interval of contact is

$$d = n[s_2^2 - s_1^2]^{\frac{1}{2}} \quad (8)$$

while the angle of deflection of the activated chains is

$$\theta = \cos^{-1} \left[ \frac{s_1}{s_2} \right] \quad . \quad (9)$$

The activation front advances with a velocity,  $v_f$ , that is in direct proportion to the velocity of the round,  $v_r$ , during contact:

$$v_f = \frac{v_r}{\sqrt{(1 + \varepsilon_c)^2 - 1}} \quad . \quad (10)$$

Thus  $v_f$  has its maximum value,  $v_0$ , at the initiation of contact and decreases linearly thereafter.

Inspection of impacted specimens suggests that the progression of a link from first entering the activation zone to being free of resin and therefore fully locked up occurs when the activation front moves over a distance comparable to the length of one link. In that case, the average strain rate during this process must be

$$\dot{\varepsilon} = \frac{\varepsilon_c v_f}{[H + 2(R + 2r)]} \quad (11)$$

which again has its maximum value at the initiation of contact.

The maximum number of locked up links,  $n$ , observed in any chain on the exit side of the panel (where most locked up links are found) is listed in Table III along with ensuing estimates of various kinematic parameters. The interval of contact and the contact time are inferred directly from  $n$ . The maximum (initial) velocity of the activation front and the maximum strain rates depend mainly on the velocity data of Table II and only weakly on the count of activated links, through the energy partitioning step.

## Energy Absorption

If all the kinetic energy lost by the round,  $\Delta K$ , is assumed to be taken up by work done in displacing all activated links (front and rear layers), then the energy absorbed per unit volume by the chain composite in the activated zone,  $W$ , is just the ratio of  $\Delta K$  to the initial volume of the activated zone,  $V_a$ . In a tightly packed array of chains, each chain occupies an area perpendicular to its axis given by [3]

$$A = \left[ 2r + 2(r+R)\cos\frac{\alpha}{2} \right] \left[ 2r + 2(r+R)\sin\frac{\alpha}{2} \right] \quad (12a)$$

where

$$\alpha = \sin^{-1} \left[ \frac{2r}{r+R} \right] \quad (12b)$$

and, in the initial contracted chain configuration, each link accounts for a length

$$l_1 = \frac{1}{2} [H + 2(2r+R)] \quad (12c)$$

Thus

$$W = \frac{\Delta K}{V_a} = \frac{\frac{m}{2} (v_{in}^2 - v_{out}^2)}{NA[H + 2(2r+R)]} \quad (12c)$$

with the assignment

$$N = n_1 + n_{0.5}/2 \quad . \quad (13)$$

Equation (13) will give a fair representation of the apportioning of energy absorption to fully and partially activated volumes. Values of  $W$  estimated for the four tests are listed in

Table IV, along with the equivalent quantity,  $W^{(st)}$ , from static tests [3]. The energy absorbed per unit volume is approximately 50 – 60 % higher in dynamic tests than in static tests for all but specimen CA#4, where the static value is slightly the higher. In this test, activated chains pulled free from the grip region of the specimen, which may have aborted energy absorption.

### **Peculiarities of Dynamic Damage Propagation**

Possible reasons for the energy absorption levels inferred for dynamic loading being higher than for static loading include the following. 1) At high strain rates, the yield stress of the epoxy resin matrix could under conditions of hydrostatic compression (resin trapped between links) rises. Simultaneously, the ultimate strength of the steel links will rise with strain rate, so that the links remain strong enough to be dragged through the increasingly resistant resin. 2) At high strain rates, the time required for resin fragments to be ejected from the region of entrapment between links may be comparable to the time of the link displacement ( $< 10^{-4}$  sec for a single link to reach lockup). 3) In the static tests cited for comparison, the applied load was uniaxial. In the impact experiments, activated chains rotate as well as extending. Additional work might be expected to be absorbed during link rotation.

Thus optimal design of chain composites for impact resistance must be based on material properties and mechanisms that may be significantly different from those found for static loading. Tests that are more amenable to analysis than the ballistic tests reported here, both in regard to mechanisms and stress distributions, need to be developed to acquire the necessary data.

### **CONCLUDING REMARKS**

Ballistic tests show that the mechanisms of link displacement, lockup, and damage delocalization persist in chain composites at strain rates approaching  $10^4$  sec<sup>-1</sup>. Activation zones of links that have displaced to lockup can extend to the edge of the tested plate.

Energy absorption is thus spread over a much larger volume of material than in ballistic impact upon monolithic materials or conventional composites. Estimates of the energy absorbed per unit volume in the activated zones yield levels 50 – 60 % higher than measured in static tension tests of similar chain composites. The difference is attributed tentatively to reduction of the effects of ejected resin under dynamic conditions and a higher flow stress in the resin at high strain rates under conditions of nearly hydrostatic compression.

The tests reported here should be regarded as a demonstration of the lockup mechanism at high strain rate and not as a quantitative measurement of the performance of chain composites as ballistic protection. In their current configuration, the chain panels have several obvious limitations. Contact between the round and the activated chains tends to be interrupted by the round breaking the contacted links or slipping through or past them. This terminates propagation of the activated zone and the deceleration of the round. Activation is also restricted mainly to the rear layer of chains, which have the freedom to extend into the free space behind the plate, allowing an activated zone to develop. Chains in the front layers are constrained by the layers behind them and exhibit far smaller activation zones.

These problems can be remedied by simple redesign. For example, persistent contact between links and the round can be achieved by using smaller links, with smaller holes and a higher density of chains per unit width of the panel. To first order under static loading, the lockup strain and the stress required for link displacement are invariant under changes of scale that preserve similarity [2], since both depend only on ratios of dimensions (Eqs. (1) and (7)). Therefore the energy absorption per unit volume or mass must be invariant too. Round penetration can also be combated by generalizing the shape of the links. Space filling links, topologically equivalent to racetrack links but presenting gapless, prismatic outer surfaces, can be found [4]. Alternatively, a hard plate or a set of hard tiles can be placed in front of the chains to flatten the projectile and spread it over a larger area of the chain panel, ensuring greater activation of links.

Better use of multiple layers of chains will presumably be achieved if the layers are separated in space, so that each layer can be activated without constraint from succeeding layers. The spacing of layers should be enough to accommodate the chain deflection. Multiple layers separated by layers of light polymer foam would seem an attractive option.

### **Acknowledgment**

Work supported by the U.S. Army Research Office, Contract No. DAAH04-95-C-0050.

### **References**

1. Cox, B. N., "Lockup, Chains and the Delocalization of Damage," *J. Mater. Sci.*, **31** (1996), 4871-81.
2. X. Gong, F. Zok, B. N. Cox, and J. Davis, "The Mechanics of Delocalization and Energy Absorption in Chain Composites," submitted to *Acta Materialia*.
3. B. N. Cox, J. Davis, S. Narayanaswamy, F. Zok, and X. Gong, "The Energy Absorption Potential of Chain Composites," submitted to *Acta Materialia*.
4. B. N. Cox, "Space-Filling Chain Composites for Energy Absorption," invention disclosure, Rockwell Science Center, *June 1998*.

**Table I. Chain and Resin Specifications.**

	$H$ (mm)	$R$ (mm)	$r$ (mm)	static ultimate strength $\sigma_{ch}$ (MPa)	static yield strength $\sigma_y$ (MPa)	density $\rho$ (Mg/m <sup>3</sup> )
small link	8.67	1.79	0.955	480	300	7.9
large link	21.75	3.00	1.5	460	300	7.9
epoxy resin					100 <sup>(a)</sup>	1.60

<sup>(a)</sup> Ultimate compressive strength at room temperature – *Engineered Materials Handbook, Vol. 1., Composites.*

**Table II. Data from Ballistic Tests.**

specimen label	chain link size	panel thickness $t$ (mm)	volume fraction of chains	impactor mass $m$ (gm)	incident velocity $v_{in}$ (m/sec)	exit velocity $v_{out}$ (m/sec)	energy loss $\Delta K$ (Joules)
CA#1	small	9.4	0.30	10.5	344	15	620
CA#2	small	9.4	0.30	10.5	332	102	523
CA#3	large	16.3	0.20	44.9	337	152	2033
CA#4	large	16.0	0.22	45.2	236	52	1197

**Table III. Estimates of Kinematic Characteristics of Impact.**

specimen label	CA#1	CA#2	CA#3	CA#4
number of links with $\phi_d = 1$ $n_1$	12	13	13	15
number of links with $\phi_d = 0.5$ $n_{0.5}$	0	12	2	3
maximum number of locked up links in one chain $n$	3	3	2	2
interval of contact $d$ (mm)	28	28	44	44
angle $\theta$ (deg.)	49	49	53	53
energy partition $\Delta W_{\text{rear}}/\Delta W$	0.74	0.74	0.71	0.64
time of contact $t_0$ (msec)	0.18	0.14	0.20	0.36
lockup strain $\varepsilon_c$	0.52	0.52	0.64	0.64
max. velocity of front $v_f$ (m/sec)	257	252	227	146
max. strain rate $\dot{\varepsilon}$ ( $\text{sec}^{-1}$ )	8380	8220	4330	2790

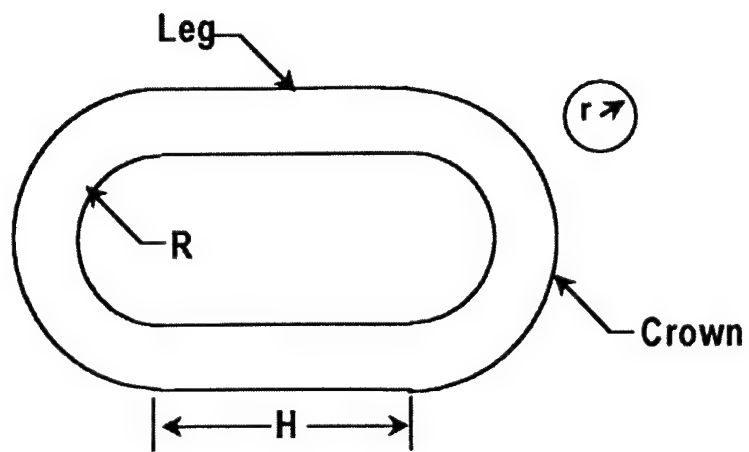
**Table IV. Energy Absorption and Macroscopic Stresses in Activated Chains**

	energy absorption in activated zone $W$ (MJ/m <sup>3</sup> )	energy absorption in static loading $W^{(st)}$ (MJ/m <sup>3</sup> )	force on impactor $F$ (kN)	load in chains when $\theta' = \theta$ $F_{ch}$ (kN)	area of chain $A$ (mm <sup>2</sup> )	composite stress in activated zone $\sigma_c$ (MPa)	plateau stress in static loading $\sigma_c^{(st)}$ (MPa)
CA#1	73	44	11.2	3.71	27.8	133	40
CA#2	62	44	14.2	4.70	27.8	169	40
CA#3	61	38	52.9	12.67	70.9	179	35
CA#4	30	38	31.2	7.47	70.9	105	35

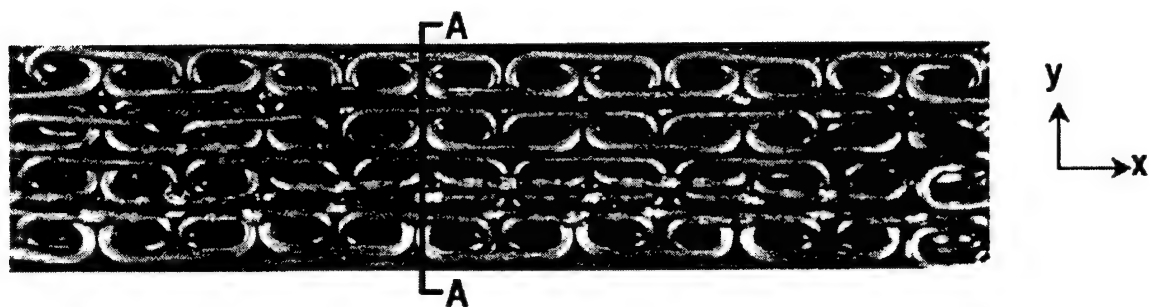
---

## Figures.

1. (a) Notation for the geometry of a common racetrack shaped link. (b) Links laid up in a chain composite in the contracted configuration, viewed through a transparent epoxy matrix.
2. Stress-strain record from a static test of a composite of carbon steel chains in an epoxy matrix (small links; data from [3]).
3. Chain panel made from small link chains after passage of a round. (a) Incident face. (b) Exit face.



(a) Chain Link Geometry



(b) Contracted Chain Configuration

Figure 1.

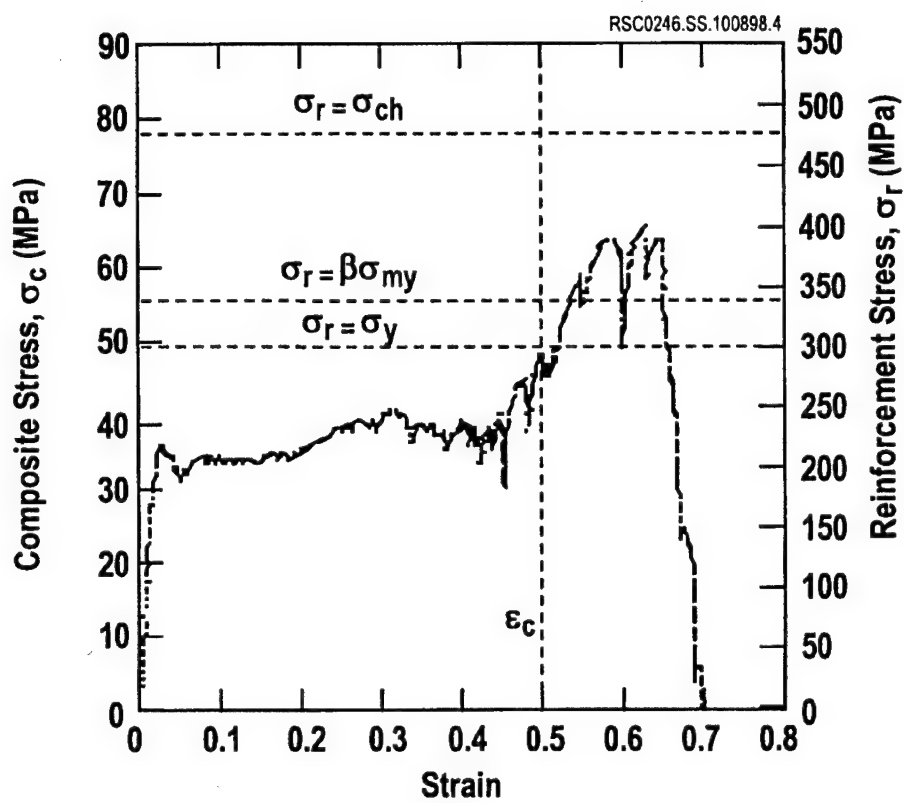


Figure 2.

RSC0409.BNC.070299

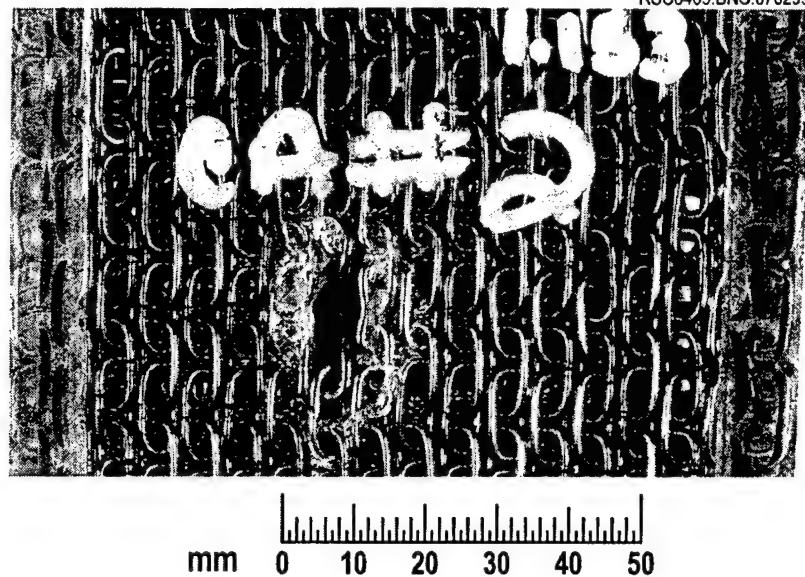


Figure 3a.

RSC0408.BNC.070299

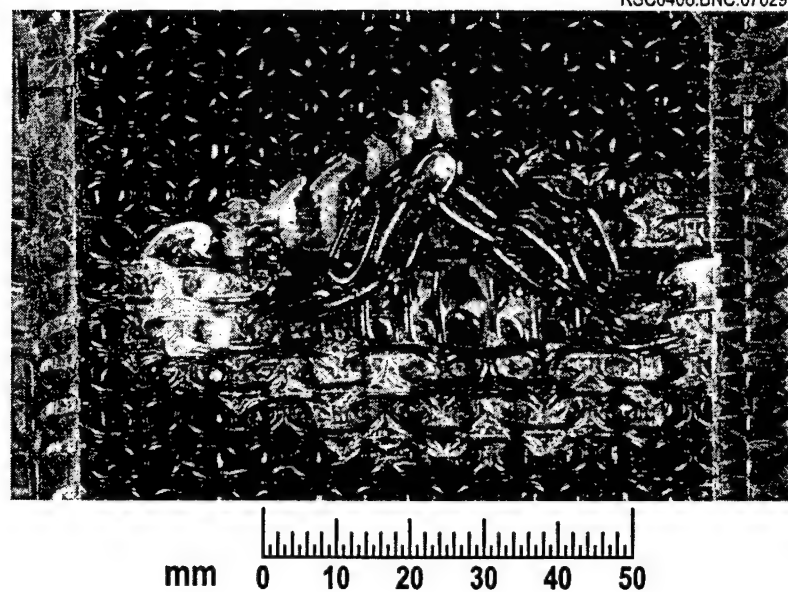


Figure 3b.

PP 99-??

# **Rockwell Science Center**

## **BRAIDED COMPOSITES FOR ENERGY ABSORPTION UNDER TENSILE LOADING**

**B. N. Cox and J. B. Davis**

Rockwell Science Center, LLC  
1049 Camino Dos Rios  
Thousand Oaks, CA 91360  
U.S.A.

---

For possible submission to *J. Mater. Sci.*

## ABSTRACT

A new class of braided composites has been designed to maximize the total energy absorbed during tensile failure. Braided loops of light, continuous fiber tows are configured in such a way that they must be drawn through relatively large displacements before they come into direct contact with one another. Upon loop contact, the material hardens locally, forcing further damage to develop by the same process elsewhere. In this way the entire gauge section absorbs energy before ultimate failure. Levels of energy absorption per unit volume reach  $30 \text{ MJ/m}^3$  and, per unit mass,  $18 \text{ J/g}$ . The mechanisms involved in damage delocalization and failure are detailed and modeled at a very simple level. While the current values of energy absorption are already attractive, much higher values are indicated by the simple models for composites that have been optimized.

## 1. INTRODUCTION

Many energy absorption problems involve loads that are tensile, for example, casings designed to contain bursting rotors, turbines, or flywheels; backing plates in armour systems; and containers subject to internal explosions. Here a new class of textile composites is introduced with unusually high-energy absorption capacity under tensile loading.

The new composites incorporate mechanisms for ensuring that damage is broadly distributed throughout the body of a specimen or structure before the instability associated with ultimate failure sets in. Damage delocalization is promoted by incorporating a so-called lockup mechanism, in which components of the reinforcement are arrested by physical contact with one another after displacing through the matrix. The extent of the displacement allowed before the lockup of two elements of the reinforcement determines the global strain up to which damage will be delocalized, denoted  $\varepsilon_c$ . The total energy absorbed per unit volume is bounded from below by the product of  $\varepsilon_c$  and the magnitude of the global stress required for reinforcement displacement,  $\sigma_d$ . Both  $\sigma_d$  and  $\varepsilon_c$  can be varied over quite wide ranges by selecting materials and the geometry of the reinforcement, so that composites can be designed, for example, to avoid large stresses during energy absorption; or for maximum total energy absorption without constraint on the stress level. The levels of total energy absorbed per unit volume or per unit mass by members of the new class of composites are potentially very high.

The textile composites are variants of a concept first demonstrated with composites of carbon steel chains in a polymer or other matrix [1-3]. The chains are laid up so that the links are initially in a contracted configuration (Fig. 1a). Under tensile loading, damage begins with extensive matrix cracking, which allows neighbouring chain links to slide towards one another, crushing resin trapped between them in a state of near hydrostatic compression. The displacement of links through the resin absorbs most of the energy expended en route to ultimate failure. When two links come into direct contact, they are said to lock up: the material hardens locally, resisting further local displacement and triggering the displacement of links elsewhere in the same chain. Only when all links in a chain are in direct contact with their neighbors does the chain begin to fail by plastic deformation of the links followed by rupture of the weakest among

them. The stress-strain response is typified by Fig. 1b. A plateau stress is sustained out to large strains, during the phase of link displacement. When the links are all in contact (strain  $\varepsilon \approx 0.5$ ), the stress drops as the links begin to fail. The total energy absorbed per unit volume for chain composites fabricated to date ranges up to approximately  $60 \text{ MJ/m}^3$  and the specific energy absorption (energy absorbed per unit mass) up to approximately  $13 \text{ J/g}$ . The former figure is superior to alternative candidates for energy absorption under tension. The latter figure is also very competitive, but the high density of the steel in chains suggests that higher specific energy absorption could be achieved if analogous composites could be made with light, strong continuous fibers.

In this paper, analogues of the chain composites are demonstrated by braiding continuous fibers. Braiding creates a reinforcement geometry that is most closely analogous to the geometry of interpenetrating links in chains. Large displacement capacity and a lockup effect can also be achieved by variants of weft knitting, but the mechanics of load transfer and lockup are different [4].

## 2. FABRICATION OF BRAIDED COMPOSITES FOR ENERGY ABSORPTION

The braided composites are fabricated using common continuous fibers in common matrices. The essence of the approach is to achieve the desired behavior by tailoring the reinforcement geometry, not by using exotic high-performance materials.

### 2.1 Braided Loops

Figure 2 illustrates the principal idea of how fiber bundles or cords can be assembled by braiding onto a set of dowel pins to simulate the contracted arrangement of links in a chain.<sup>1</sup> The cords have been spread in Fig. 2 to allow their interlacing pattern to be seen more easily. In the

---

<sup>1</sup> The cords in Fig. 2 consist of a core of lightly twisted, nearly aligned Kevlar fibers in a single tow, around which a sheath of additional Kevlar fibers has been braided with a braid angle of approximately  $45^\circ$ . This commercial product is not optimal. Tows that achieve superior results are described below.

finished composite, they are tightly packed in the horizontal direction in the figure, but retain their elongation in the vertical direction, which is the intended direction of loading.

As Fig. 2 shows, the presence of the pins allows the braided loops to interpenetrate without initially being in intimate contact. When loaded, the loops will slide and eventually make contact on the insides of their curved ends, just like the links in chain composites.

By varying the pin spacing and the choice of pins around which the cords are looped, fabric with virtually any sliding strain capacity and loop aspect ratio (loop length to loop width) can be fabricated.

## 2.2 Tooling for Composite Formation

After the braided fabric has been formed, it must be released from the dowel pins without relaxation of the desired geometry, infiltrated with a matrix, and consolidated. A laboratory-scale apparatus that accomplishes these tasks quite effectively is shown in Fig. 3. It consists of the array of dowel pins and their base plate (the “braiding frame” in Fig. 3) and several other components, all of which are Teflon-coated for easy release after curing of the finished composite. A plate (the “lid”) containing holes slightly larger than the pin diameter is placed over the pins and against the base plate prior to braiding. The braid is then built above the lid. When the braiding is complete, the pins and fabric are inverted into a female mold (Fig. 3). Then the lid is clamped to the mold, generating sufficient compression to fix the cords in place by friction. The pins can then be withdrawn through the holes in the lid by drawing away the base plate, with minimal movement of the cords. Pistons whose heads run the length of the fabric are then pushed between the lid and the female mold by rods extending out of the mold cavity through ports, so that the fabric is further compacted by side pressure. Applying pressure in two directions assists in maximizing volume fraction. It also reduces any undesirable distortions created in the fabric when the pins are removed. Epoxy matrix is added in an uncured, inviscid state by vacuum infiltration. The epoxy is cured and the specimen is released by breaking the lid and female mold apart.

The cords to be braided are fastened initially onto the base plate, typically one at each dowel pin. The interlacing pattern is then created by passing the cords in sequence around the pins to the right and left of the pin to which they are first fastened, so that the fabric is built up continuously along a front that moves away from the base plate. During braiding, idle cords are held in tension by a system of cleats, to assist in compacting the braided fabric to an acceptably high volume fraction. It is not necessary to pass a cord end through a loop that has already been formed when producing the interpenetrating pattern. Thus one key advantage is the ease with which this process could be adapted to large scale manufacturing.

Because of the topology of the braiding process, loose ends of cords must remain when specimen fabrication is halted at the prescribed layer size. During loading to high strains, the loose ends tend to slide through the composite, unraveling the fabric. Unless the fabric is quite wide, the unraveling can propagate through an entire specimen. This premature failure mechanism can be averted by splicing the loose ends together to close the last row of loops. The splice must be strong enough to transmit the large loads experienced by individual cords. After considerable experimentation, the best splice that could be made by hand was found to consist simply of two cord ends laid side by side and glued together with epoxy while held fast by a wrapping of Teflon. When carefully formed, these splice joints are nearly as strong as a single straight cord.

Since the pins are coplanar, the braid built up on them will consist of a single flat layer. Laminates can be formed by stacking together layers with desired fiber orientations.

### **2.3 Optimal Cords for Braiding**

The first generation of braided composites were made with loose rovings of Kevlar (or glass or carbon) fibers, which were held together relatively weakly by a small quantity of uncured polymer sizing. These tows tended to splay during braiding, especially at the crowns of loops (where tows turn around pins), which weakened them and gave them a flat, tape-like aspect. The flatness of the crowns inhibits their displacement through the matrix in the composite. As a result, failure of the reinforcement tends to precede matrix failure and reinforcement sliding,

resulting in localized rather than delocalized failure; and therefore poor energy absorption characteristics.

Obtaining twisted or wrapped fiber tows that retain strength and cross-sectional aspect ratio during braiding was a major challenge. Commercial Kevlar cord was tried next, which consisted of moderately large denier tows (approximately 20k denier) sheathed in a braided skin. The commercial cord is easily handled without obvious damage and suffers a relatively small change of aspect ratio where it is bent around pins. However, the commercial cord is disappointingly loose in its packing and the majority of its fibers lie in its braided sheath, rather than in its core. The overall volume fraction of aligned Kevlar fibers achievable in the final composite is therefore low. Since the tensile strength of the cord and thus of the composite arises mainly from the aligned fibers, with the sheath contributing minimally, the ability of the cord to sustain loop displacement is severely degraded.

As an alternative to sheathed cord, a three-strand rope was fabricated by plaiting tows of sized Kevlar together before using them for braiding. This plaited rope also exhibits reduced fiber damage and change of aspect ratio during braiding. However, because it is braided, its fibers are not aligned with the axis of the rope and therefore it cannot yield the same ultimate strength as a well compacted, sheathed cord of mainly aligned fibers.

Two solutions to the problem of forming adequate cords were eventually found. The first was to revisit the concept of sheathing axial fibers in a braided wrap. This process was done to preferred specifications using a hand-winding machine.<sup>2</sup> Large denier Kevlar tows were wrapped by a light rayon yarn wound in a fairly open pattern. Thus the ratio of axial to wrapped fibers was maintained at a high level. In spite of some variance in the skill of the operator of the hand winder, reasonably high packing densities of the aligned fibers were achieved (40 – 50%), which survived the braiding process quite well.

The second solution was to encase the Kevlar tows in lengths of shrink-wrap plastic tubing. When the tubing was subsequently warmed with a hair dryer, it formed a tight sheath around the

---

<sup>2</sup> Courtesy Dr. Chris Pastore, Philadelphia College of Textiles and Science.

fibers. This method achieved the highest packing densities and had the further advantage of protecting the fibers during braiding. A typical braided preform made with tows in shrink-wrap tubing and partially finished with Teflon bound splices is shown in Fig. 4.

Specifications of the cords used in specimen fabrication are listed in Table I. The cord radius,  $r$ , is defined as

$$r = \sqrt{\frac{1}{\pi f \rho y}} \quad (1)$$

where  $f$  is the fiber packing factor in the cord, taken to be 0.7,  $\rho$  is the density of the fibers (0.00145 gm/mm<sup>3</sup> for Kevlar), and  $y$  is the yield of the axial fibers in the cord.

When shrink-wrap tubing is used, resin is prevented almost entirely from entering the interior of the cord during infiltration. The only polymer present amongst the fibers of the cords during curing of the composite is the small amount of sizing on the Kevlar tows as supplied. It is not known whether the net strength of individual tows is higher or lower because of this after braiding and composite consolidation. The absence of resin may facilitate turning of the cords around nails during braiding, minimizing residual strains and physical damage in the fibers. It also changes the mechanics of load transfer between fibers in the tow as they begin to break during failure of the composite.

## 2.4 Geometrical Characteristics of the Braided Composites

Figure 5 shows schematics of two different patterns of braiding around pins, which will be called cases (a) and (b). Cord segments drawn as solid lines pass in front of the pins, while those drawn as dashed lines pass behind. The cords are drawn stretched out in the  $y$  direction for easier visualization of their interlacing. The braid pattern is periodic, with convenient unit cells as indicated by dotted lines in Fig. 5. In case (b) (Fig. 5b), pins are provided in pairs, with the left pin in each pair used exclusively for reversals of the direction of a cord to the left, and the right pin for reversals to the right. This allows abutting crowns of loops (e.g., marked  $C_1$  and  $C_2$  in the

figure) to slide down opposite one another when the fabric is beaten up (compacted) in the  $y$  direction. The compacted fabric can therefore collapse into a configuration where the straight tow segments are horizontal (parallel to the  $x$ -axis). In case (a), crown  $C_1$  must remain above crown  $C_2$ . The straight segments of the cords will therefore remain at some angle  $\theta$  to the  $x$ -axis.

Figure 6 shows the loci of two cords in the collapsed configuration in a perspective drawing. The lines correspond to the axes of the cords.

Simple analysis of the geometry of the composites and their mechanical behaviour can be made by idealizing the braid geometry. Each cord is assumed to consist of a sequence of straight segments (legs) alternating with curved segments (crowns) where the cord passes around a pin, as suggested by Figs. 5 and 6. The crowns follow helical paths with radius of curvature  $R$  and legs and crowns both have circular cross-sections with radius  $r$ . Predictions for the area and volume fractions of fibers for this idealization are presented in Appendix A.

### 3. PROPERTIES OF BRAIDED COMPOSITES

#### 3.1 Tests on Single Tows

Indicative strengths,  $\sigma_{cd}^{(ult)}$ , were determined for the braiding cords by testing single tows of dry Kevlar fibers, each with a yield of 554 mm/g (16.2k denier). The tests were conducted by potting the ends of tow segments approximately in resin blocks and loading in uniaxial tension by gripping the blocks. The tested gauge length was approximately 120 mm. Failure by fiber rupture generally occurred away from the blocks. The strength was recorded as the failure load divided by the total cross-sectional area of fibers in the tow,  $1.24 \text{ mm}^2$ .

The first series of tests determined the strengths of splice joints. The lap joints eventually preferred for specimen fabrication showed values of  $\sigma_{cd}^{(ult)}$  between 1.8 and 2.2 GPa. Even

though failure usually occurred in or adjacent to the splice, the sliced tows were comparable in strength to pristine Kevlar fiber bundles of the same gauge length.

The second series of tests were conducted on looped specimens, which were formed by bending two tow segments into half loops and linking them together in the same way as two interpenetrating half loops would be linked in the composite (Fig. 5). Thus each end of the specimen comprised two tow ends, potted together in a resin block. The reported strengths from these tests were defined as the failure load divided by the cross-sectional area of the fibers in two tows,  $2.48 \text{ mm}^2$ . Values of  $\sigma_{cd}^{(\text{ult})}$  for these tests ranged from 550 to 700 MPa. Thus the strength of a cord can be expected to be reduced by a factor of about three by the stress concentration associated with loop intersection.

### 3.2 Specimens and Tests

All specimens were fabricated in the pattern of case (a) (Fig. 5a) on a frame with uniformly spaced pins with  $d_x = 12.7 \text{ mm}$  and with processing as described in Section 2. Other specimen details are summarized in Table II. Braiding was terminated after 4, 6, or 10 courses of loops had been formed, each course corresponding to two turns of a cord in the  $y$  direction of Fig. 5 or 6. All specimens were approximately 200 mm long, with lateral dimensions,  $l_y$  and  $l_z$ , as tabulated. The lateral dimensions refer to a so-called core region, which contained all the fiber reinforcement but excluded any peripheral zones of pure resin. Peripheral resin extends to the dimensions of the mold, whereas the reinforcement is compacted into a smaller volume. The peripheral resin cracks many times very early in the failure process and does not affect the composite behaviour.

The fiber volume fractions reported in Table I were calculated by measuring the total length of cords incorporated into the braids during braiding, multiplying by the cross-sectional area of fibers expected for a cord of the given yield, and dividing by the volume of the core region. The area fraction,  $A_{cd}$ , refers to the fraction of planes A – A in Fig. 5a occupied by the legs of cords (including internal resin or void), calculated according to

$$A_{cd} = \frac{2n_{course}\pi r^2}{l_y l_z} = \frac{2n_{course}}{l_y l_z f\rho y} \quad (2)$$

where  $n_{course}$  is the number of courses of loops.

The matrix in all specimens consisted of student-friendly Epofix resin, cured at 150°C for two hours. Various measures were sometimes built into the composite to resist matrix loss during loading to large strains. In some cases, additional Kevlar tows were wrapped by hand around the specimen while it was still on the braiding frame. The wrapping tows were sometimes drawn in helices around the outside of the fabric, working along an axis parallel to the  $x$ -direction. In other cases, the wrapping tows were threaded in the  $y$  direction through the channel-like cavities of the braided loops. In one specimen, the resin was reinforced with chopped  $\text{Al}_2\text{O}_3$  fibers approximately 10 – 20 mm long, stuffed by hand into the loop cavities.

Uniaxial tension tests were carried out in a screw-driven machine at low strain rates. All specimens were straight bars, as formed in the mold. To enhance gripping, steel pins were sometimes inserted into the ultimate loop cavities of the braid before resin infiltration, with their ends left protruding from the specimen. The pins were then inserted into slots in the grips. This eliminated slippage in the grips, which otherwise can be a difficult problem. Even at high grip pressures, disintegration of the specimen near the grips at high strains can cause loss of shear load transfer.

### 3.2 The Achievement of Delocalized Failure.

In four of the reported tests, completely delocalized failure was achieved. Figure 7 shows the appearance of two such specimens after testing. The braided loops have been drawn out into intimate contact over the whole gauge length without reinforcement failure. (The less damaged regions at either end were in the grips.) The black shrink-wrap tubing has been torn in many places, but the fibers within the tubing have suffered minimal damage. In Fig. 7b, wrapping Kevlar yarns can still be seen in the less damaged regions. Ultimate failure ensues by rupture of the cords, not usually at splices.

The first damage observed in all specimens at relatively low strains consists of matrix cracking. The cracks are at first predominantly normal to the load axis, but develop into cracks of complicated shape with some segments parallel to the load axis at higher strains. When failure is delocalized, resin fragments are lost from the composite at strains exceeding approximately 0.1, but some resin remains out to much higher strains.

In the two specimens exhibiting localized failure, damage was confined to a limited region of the gauge section. In the case of specimen BR6298b, this band still extended over approximately one third of the gauge length and included substantial loop displacement and resin ejection. In this specimen, splice failure was observed well before ultimate failure, leading to the conjecture that the splice was unusually weak. Reasons for the delocalized failure in specimen BR6298a will be discussed below.

### 3.3 Stress-Strain Response and Energy Absorption

Records of engineering stress,  $\sigma_a$ , vs. engineering strain,  $\varepsilon_a$ , are presented in Fig. 8. Each record shows an initial phase of monotonically increasing stress, reaching a peak stress,  $\sigma_p$ , at some strain,  $\varepsilon_p$ . Values of  $\sigma_p$  range from 30 MPa to 140 MPa and values of  $\varepsilon_p$  from 0.1 to 0.4 (Table II). Stress variations following the peak vary from specimen to specimen. In one specimen that suffered localized failure (specimen BR6298a), the load plummeted almost to zero following the peak, although it remained nonzero out to moderately large strains during a phase of unraveling and pullout of ruptured cords. In other specimens, the stress dropped to levels in the range 20 – 40 MPa, remaining there to strains not far from the ultimate strain,  $\varepsilon_{ult}$ , listed in Table II. The region following the peak load is often punctuated by numerous drops and spikes in the load, corresponding to periods of resin fracture and ejection of resin fragments.

In all specimens, damage tends not to develop uniformly over the whole gauge section, even though, in cases of delocalized failure, the whole gauge section is uniformly damaged and strained prior to ultimate failure. Large strains usually develop in one region of the specimen, in a band involving two to three loops or, in other words, an interval of length approximately  $2d_x$

(25 mm) along the  $x$ -axis. When the damage in the band is mature (loops in direct contact with one another or local strain  $\varepsilon \approx \varepsilon_{\text{ult}}$ ), damage spreads to neighbouring material. Peak load usually corresponds to maturation of the damage in the initial band. In cases where the stress following the peak is considerably lower than the peak stress, one infers that the development of similar damage in neighboring material is facilitated by the pre-existing damage in the initial band. A mechanism for this effect will be suggested in the next section.

The energy absorbed per unit volume of the original gauge section,  $W_v$ , is given by the area under the engineering stress-strain curve<sup>3</sup>:

$$W_v = \int \sigma_a d\varepsilon_a \quad . \quad (3)$$

When damage is delocalized, values range from 15 to nearly 30 MJ/m<sup>3</sup> (Table II). The specific energy absorption,  $W_m$ , i.e., the energy absorbed per unit mass, is related to  $W_v$  by

$$W_m = \frac{W_v}{\rho} \quad (4)$$

with  $\rho$  the composite density. Values of  $W_m$  range from 10 to 18 J/g.

## 4. MECHANISMS

### 4.1 Prediction of the Displacement Stress

Some insight into the mechanics of delocalization and damage progression in the braided composites can be inferred from a model developed by Gong and Zok [2] for chain composites

---

<sup>3</sup> For Eqs. (3) and (4) to yield material constants, damage must be uniform over the gauge length and the stress to displace loops must be independent of location in the gauge length. This is not the case for all the specimens tested. Damage was nonuniform in the two specimens suffering localised failure and the stresses were not universally constant in the others. However, the conditions are at least approximately satisfied if delocalization is achieved and therefore the figures quoted for energy absorption in these cases ought to be reasonably indicative of material properties.

such as that depicted in Fig. 1. The model predicts the tensile stress component in the centers of the legs of the links (on the plane A – A in Fig. 1) as the links are dragged through the matrix.

The matrix is modeled as a rigid/perfectly plastic medium. Stress transfer into the links from the matrix during the displacement can be partitioned into several contributions. 1) The resin trapped in near hydrostatic compression between two links as they approach one another exerts pressure over the inner surface of the crown of each link. 2) Shear tractions develop over the crown as it slides through the matrix. 3) Tensile tractions act on the outer surface of the crown where the matrix is being pulled apart between the crowns of abutting links, at least until the matrix fails along the line A – A. 4) Shear tractions act over the legs as the links slide through the matrix. The sum of the four contributions, when resolved in the direction of the motion of the links, must be balanced by tension in the legs, which takes its maximum value,  $\sigma_{\max}^{(leg)}$ , at the centre of the legs. All four are proportional to the matrix shear flow stress,  $\sigma_m$ , the constants of proportionality depending on the link geometry.

The model is developed by considering the interaction of just two interpenetrating half-links. But, this is exactly the geometry of two interpenetrating half-loops in a braided composite, at least in the geometrical idealization introduced in Section 2. Therefore, the problems of dragging two braided loops or two chain links towards one another can be expected to have many similarities. The chain model is a good starting point for discussing the braided composites.

The results obtained in [2] can be summarized as follows, using the notation of this paper (note especially that  $R$  has different definitions in [2] and here). The stress in the centre of the leg of a braided loop is related to the matrix flow stress by

$$\begin{aligned}\sigma_{\max}^{(leg)} &= \beta \sigma_m \\ \beta &\equiv \frac{2}{\pi} \left( C_1 + C_2 + 3.664 C_3 \left( 1 + \frac{R-r}{r} \right) - \left( \frac{C_1 - C_2}{2} \right) + C_4 \frac{2d_x}{r} \right)\end{aligned}\quad (5)$$

where  $C_1$ ,  $C_2$ ,  $C_3$ , and  $C_4$  are dimensionless constants of proportionality corresponding in order to the four contributions listed above. Equation (5) is restricted to links consisting of semi-toroidal

crowns connected by cylindrical legs, which is the standard geometry of commercially available chains and a reasonable approximation for the braided loops. For unbonded, frictionless cord/matrix interfaces<sup>4</sup>, all load transfer from matrix to cord occurs on the compressive side of the crown and the proportionality factor  $\beta$  reduces to the even simpler result

$$\beta = 0.36 + 1.69 \frac{R-r}{r} \quad (6)$$

Values are shown for  $\beta$  in Table II. They range approximately from 2 to 5. If the cord/matrix interfaces are strong, then much higher values result for  $\beta$ , ranging approximately from 10 to 20 for the cases of interest here (using results for  $C_1$ , etc., from [2]). For either strong or weak interfaces, if the matrix is much more compliant than the reinforcement, as is epoxy resin relative to Kevlar, then Eq. (5) multiplied by the area fraction,  $A_{cd}$ , should be approximately equal to the composite stress during link displacement. This is shown in Fig. 8 by the line marked " $\sigma_{cd} = \beta\sigma_m$ ", where  $\sigma_{cd}$  is the value of  $\sigma_{max}^{(leg)}$  predicted by Eq. (5) in the limit of Eq. (6) (weak cord/matrix interfaces – lowest values of  $\beta$ ).

Also marked in Fig. 8 is the expected strain to lockup,  $\varepsilon_c$ , which is (Appendix A)

$$\varepsilon_c = \frac{1}{2} + \frac{R-r}{d_x} \quad (7)$$

Loop displacement through the matrix might be expected to occur mainly at strains below  $\varepsilon_c$ .

#### 4.2 Mechanisms underlying the Stress-Strain Curves

Consider first the three specimens other than the specimens that suffered localized failure and the specimen whose matrix was strengthened with chopped  $Al_2O_3$  fibres, i.e., the specimens of Figs. 8a, 8b, and 8c. For these specimens, the strain to peak stress,  $\varepsilon_p$ , is quite high – in the range 0.1 to

---

<sup>4</sup> The interfaces in question are not those between individual fibers and resin. Fiber/resin interfaces are usually relatively strong and do not commonly fail during composite failure. The relevant interfaces are instead those between entire cords and the surrounding matrix. When these debond, they do so by means of a peripheral matrix crack that separates the cord as an entity from its environment.

0.4. The peak stress therefore occurs when substantial damage has already pervaded the specimen. The damage must include significant link displacement, at least in the initial damage band. Yet the peak stress far exceeds the stress for loop displacement,  $\beta\sigma_m$  (Figs. 8a, 8b, and 8c). This implies that, in spite of the extensive damage to the matrix at peak stress, there is still sufficient coupling between the cords and the matrix that the constraint factor,  $\beta$ , has a value somewhat larger than its value for weak (debonded) cord/matrix interfaces. Observations were not sufficiently detailed to confirm this conjecture (details are difficult to see in the midst of widespread damage), but one would expect that the additional load transfer to the legs probably comes through strong friction around the legs, which is assumed zero in Eq. (6).

Since premature cord rupture or splice failure was not observed in these cases, the load drop following peak stress in Figs. 8a, 8b, and 8c is probably associated with loss of matrix material and loss of frictional contact with the legs of the displacing cords. Since the difference in values of  $\beta$  for debonded, stress-free interfaces and interfaces with some load transfer is quite pronounced, the fall in stress can be large.

In the case of the specimen with  $\text{Al}_2\text{O}_3$  reinforced fibres (Fig. 8f), the strain to peak stress is relatively small ( $\varepsilon_p = 0.02$ ) and the peak stress is very near the predicted displacement stress for weak interfaces. One can speculate that the  $\text{Al}_2\text{O}_3$  fibres have embrittled the matrix, so that it could not follow the displacements of the cords and broke away from them much earlier.

For the four cases of delocalized failure, the stress in the period following the peak stress and up to or somewhat beyond the expected lockup strain,  $\varepsilon_c$ , is not far from the prediction of  $\sigma_{cd}$  for weak interfaces. Here the chain link model seems to work quite well. With corroborating observations from tests, the validity of the description of the mechanics of link displacement embodied in Eq. (5) is confirmed.

In the two specimens fabricated with cords contained in shrink-wrap tubing, relatively large stresses were sustained well beyond the nominal lockup strain,  $\varepsilon_c$  (Figs. 8a and 8b). The shrink wrap tubing creates a fairly stiff cord that does not turn around the dowel pins during braiding as easily as the served cords. Consequently, the shrink-wrapped cords tend to bow out more in the

braided fabric, with crowns of larger radius of curvature and shorter legs (Appendix A). Under the high loads of a test, the loops can stretch by changing their shape, raising the effective strain to lockup. This effect could account for test strains approaching 1. Even higher recorded strains correspond to the last gasps of a specimen's strength after one or more cords has ruptured and is unraveling through the fabric. This process can sustain appreciable stress levels and also accounts for the tail of the curve ( $\varepsilon_a > 0.6$ ) for the specimen with  $\text{Al}_2\text{O}_3$  reinforced matrix (Fig. 8f). The presence of the  $\text{Al}_2\text{O}_3$  fibers inhibits unravelling.

In all the specimens exhibiting delocalized failure, a minor peak can be identified at about the lockup strain (or somewhat beyond it for the shrink-wrap tubing specimens) beyond which the stress declines fairly steeply and monotonically to zero. These points have been labeled  $P_u$ . While direct observations were inconclusive (because of the high level of damage accrued prior to such strains), this peak can reasonably be conjectured to correspond to the failure of a cord. The stress in the cords at  $P_u$  (right hand ordinate of Fig. 8) ranges from 200 to 350 MPa (Figs. 8a, 8b, 8c, and 8f), which corresponds, for a fiber packing factor of 0.7, to fiber stresses ranging from 340 to 500 MPa. This is somewhat lower than  $\sigma_{cd}^{(ult)}$  determined from loop tests (550 – 700 MPa), suggesting that the cords are weakened by the damage sustained during loop displacement.

The delocalized failure observed in the specimen fabricated with thin cords (Fig. 8d) is now easily understood. For a thin cord, the ratio  $(R-r)/r$  is large, the factor  $\beta$  is therefore large, and the stress required to displace loops ( $\sigma_{cd} = 550$  MPa) is larger than the cord strength.

In several cases, the stress for loop displacement following peak stress is markedly lower than the predicted displacement stress (Figs. 8b and 8f). This probably signifies loss of matrix material that was previously trapped between two loops, which will lower the effective constraint factor,  $\beta$ . A similar effect occurs in chain/epoxy composites [3]. In braided composites, it can be exacerbated by separation of the legs of loops in the  $y$ -direction, which can be wedged apart by the entrapped matrix as they are drawn towards one another. This can happen relatively easily in the braided composites, because the legs are highly anisotropic unidirectional composites that are strong in tension but weak in axial shear.

Loop displacement prior to peak stress commonly (but not always) occurs at significantly higher stresses than loop displacement following peak stress. This and the fact that damage prior to the peak stress occurs mainly in the initial damage band implies that pre-existing damage to large strains in adjacent loops facilitates loop displacement. It is possible that loop spreading in the previously damaged material promotes matrix cracking in neighbouring regions, facilitating matrix loss and the reduction of the constraint factor,  $\beta$ .

## 5. POTENTIAL FOR ENERGY ABSORPTION

The values of energy absorption for the braided composites are very encouraging, but substantially higher values could be obtained by better design and processing. The energy absorption will be maximized by 1) raising the fiber volume fraction; 2) using the strongest possible reinforcing fibers; 3) choosing a matrix with a flow stress,  $\sigma_m$ , for which the product  $\beta\sigma_m$  is as great as possible without exceeding the reinforcement strength,  $\sigma_{cd}^{(ult)}$ ; and 4) preventing the premature loss of matrix from between loops by brittle matrix fracture and fragment ejection.

The fiber volume fraction,  $V_f$ , can be raised in several ways. Fabricating composites in which crowns abut without overlapping, such as in Case (b) of Fig. 5, will immediately raise  $V_f$  by up to 50%. Benefit will also come from starting with a supply of fiber cords, such as fibers wrapped in wound yarns, that have been prepared in an automated serving apparatus to high consistency and therefore higher fiber packing factors; and further developments of compacting apparatus will enable a tighter fabric arrangement in the mold.

The effective fiber strength can be improved by minimizing fiber damage during loop displacement, which currently degrades cord strength by approximately 40%. A more effective protective sheath than the shrink wrap tubing could be developed; and matrices such as elastomers that are more ductile than the epoxy resin might be less abrasive.

In this work, reinforcing the matrix with  $\text{Al}_2\text{O}_3$  fibers was tried as a method of resisting matrix loss during loop displacement. An alternative route that may work better would be to use an elastomeric matrix, such as natural rubber.

With such modifications, goals of  $100 \text{ MJ/m}^3$  for the energy absorbed per unit volume and  $50 \text{ J/g}$  for the specific energy absorption would seem to be attainable.

## 6. SCALE CHANGES

As far as the model of loop displacement embodied in Eq. (5) is correct, the stress required for loop displacement will be unchanged by changes in the scale of the reinforcement that maintain similarity. The displacement stress depends only on the ratios  $R/r$  and  $d_x/r$ , not on their absolute values. Likewise, the area fraction,  $A_{cd}$ , depends only on ratios of lengths (Eqs. (A.4) and (A.9)) and so the global stress required for cord rupture will be invariant under changes in scale (apart from possible size effects in the statistics of fiber bundle strength). Thus there may be neither advantage nor disadvantage for energy absorption in producing finer or coarser braids.

If the cords can decouple relatively easily from the matrix, as in all the composites reported here, then the stress for loop displacement will also be neutral with respect to changes in the loop aspect ratio,  $d_x/r$ . If, however, the cords can remain coupled to the matrix through large displacements, then the stress in the legs of the cord can rise quite dramatically. The constraint factor,  $\beta$ , is much higher when load transfer along the legs is significant [2]. Where this occurs, the efficacy of the matrix in resisting loop displacement, and therefore in taking best advantage of the strength of the cords, is enhanced. Furthermore, the surface area of the legs varies as  $d_x r$  while  $A_{cd}$  varies as  $r^2$ , so the matrix resistance will rise if the aspect ratio rises under conditions where the matrix and legs remain mechanically coupled.

Reduction of the scale of the reinforcement will be very important in reducing the sensitivity of the composite to intrinsic flaws, including unusually weak splices, or damage from an external source. The specimens tested here contained only a few loops across their width and were

therefore especially vulnerable to a weak flaw. If hundreds of courses of loops were present in the same volume, which would seem a reasonable achievement for an automated braiding process, then one poor splice would have little effect.

## **7. SUMMARY REMARKS**

A new class of braided composites has been presented that exhibit lockup mechanisms following loop displacement, thus delocalizing damage and achieving high levels of energy absorption. The energy absorbed per unit mass is especially attractive.

The mechanisms of the progression to failure appear to be similar in many regards to those observed previously in chain composites. In particular, the stress required for loop displacement can be predicted to a useful approximation by a model developed for the chain composites. This allows some simple inferences about design optimization.

Further prospects for optimization lie in improving the volume fraction of reinforcing fibers, towards which automating the braiding process should be a major step, and selecting a tougher matrix to avoid premature loss of matrix during damage to large strains.

### **Acknowledgments**

Work supported by the U.S. Army Research Office, Contract No. DAAH04-95-C-0050. The authors are very pleased to record the enthusiastic, patient, and skilful handicraft of Noemi Altamirano, Christian Berg, Jenny Garredo, Rachel Goldberg, Gloria Rios, Annalise Keen, and Amber Sands in supplying the numerous specimens consumed in this study. Helpful discussions with Drs. Sridhar Narayanaswamy and Frank Zok are also acknowledged.

## REFERENCES

1. B. N. Cox, "Lockup, Chains, and the Delocalization of Damage," *J. Mater. Sci.*, **30**, 4871-4881 (1996).
2. X. Gong, F. Zok, B. N. Cox, and J. Davis, "The Mechanics of Delocalization and Energy Absorption in Chain Composites," *Acta Materialia*, in press.
3. B. N. Cox, J. Davis, N. Sridhar, F. Zok, and X. Gong, "The Energy Absorption Potential of Chain Composites," *Acta Materialia*, in press.
4. B. N. Cox and J. B. Davis, "Knitted Composites for Energy Absorption under Tensile Loading," submitted to *J. Mater. Sci.*

**Table I. Specifications of Cords Used**

cord label	containment	yield <sup>(d)</sup> (mm/g)	cord radius <sup>(e)</sup> (mm)
S1 <sup>(a)</sup>	none	1056	0.545
S2 <sup>(b)</sup>	shrink wrap	277	1.064
S7 <sup>(c)</sup>	wound polyester	151	1.44

<sup>(a)</sup> formed from a single Kevlar tow with approximately 3 weight percent resin binder<sup>(b)</sup> formed from two dry Kevlar tows<sup>(c)</sup> formed from seven Kevlar tows with approximately 3 weight percent resin binder<sup>(d)</sup> yield of all axial fibers taken together<sup>(e)</sup> for core of axial fibers only, assuming a fiber packing factor of 0.7**Table II. Composite Specifications and Properties**

specimen	BR5798a	BR5798b	BR5798c	BR6298a	BR6298b	BR6298c
<b>cord</b>	S2	S2	S7	S1	S7	S7
<b>features<sup>(a)</sup></b>	interlaced wrap		interlock wrap	interlock wrap	interlock wrap	$\text{Al}_2\text{O}_3$ in matrix
<b>courses</b>	4	4	8	10	4	4
$l_y$ (mm)	26.7	29.7	28.7	15.2	28.4	30.0
$l_z$ (mm)	13.7	15.0	18.5	9.7	12.2	11.1
$A_{cd}$ (meas <sup>d)</sup> )	0.078	0.064	0.147	0.127	0.151	0.156
$V_f$ (meas <sup>d)</sup> )	0.22	0.18	0.36	0.30	0.38	0.42
$\beta$	2.9	2.9	2.2	5.3	2.2	2.2
<b>failure<sup>(b)</sup></b>	del	del	del	loc	loc	del
<b>peak stress</b>						
$\sigma_p$ (MPa)	78	32	91	84	146	33
<b>strain at peak stress</b>						
$\epsilon_p$	0.4	0.25	0.4	0.07	0.08	0.02
<b>strain at ultimate</b>						
$\epsilon_{ult}$	1.4	2.0	1.0	0.3	0.8	1.3
<b>W/volume</b>						
$W_v$ (MJ/m <sup>3</sup> )	27.5	18	28.5	4.5	22	15
<b>W/mass</b>						
$W_m$ (J/g)	17.5	11.5	18.5	3	14.5	10

<sup>(a)</sup> see text for details<sup>(b)</sup> "del" = delocalized; "loc" = localized

## Appendix A. Model of the Composite Geometry

A simple model of the geometry of the braided loops aids material design and the analysis of stress distributions and mechanisms. The model shown here begins with the assumptions stated in Section 2.4, that the braided cords comprise straight legs and helical crowns with circular cross-sections of radius  $r$ . Their positions can be represented by the loci of their axes. The junctions of leg and crown segments are assumed to lie exactly at the  $x$ -coordinate of the centre of the pin around which the crown bends. The axis of the helical crown segment passes around a cylindrical surface of radius  $R$ . Thus  $R = r_{\text{pin}} + r$ , where  $r_{\text{pin}}$  is the radius of one of the pins.

Case (b) of Fig. 5, which has a slightly simpler geometry because of the avoidance of overlap of abutting crowns, will be dealt with first.

*Case (b):* Let  $d_x$  and  $d'_x$  denote the centre-to-centre separations of the pins, as indicated in Fig. 5b. Following compaction in the  $y$  direction, the legs in case (b) are horizontal. Since the cords rest directly on one another, the apexes of successive crowns such as those marked E in Fig. 5b must be separated by  $4r$  (the diameter,  $2r$ , of one leg plus twice the half-thickness,  $r$ , of one crown.) Therefore, the helix followed by each crown must have pitch  $4r$  in one complete turn. The length of the axis of one representative half loop,  $s_1$ , such as that highlighted by bold lines in Fig. 5b, is the arc length of the helix over a half-turn plus the length of one leg, i.e.,

$$s_1 = \pi R \sqrt{1 + \left( \frac{2r}{\pi R} \right)^2} + 2d_x + d'_x \quad . \quad (\text{A.1})$$

There are four such half-loops in one unit cell. The dimensions of the unit cell are  $2(d_x + d'_x)$ ,  $4r$ , and  $2(R + r)$  in the  $x$ ,  $y$ , and  $z$  directions, respectively, where the  $z$ -axis points into the page of Fig. 5 (see additional note below). Since the cross-sectional area of a cord is  $\pi r^2$ , the fraction of the composite occupied by the cords,  $V_{\text{cd}}$ , follows as

$$V_{cd} = \frac{\pi \left[ \pi \bar{R} \sqrt{1 + (2/\pi \bar{R})^2} + 2\bar{d}_x + \bar{d}'_x \right]}{4(\bar{d}_x + \bar{d}'_x)(\bar{R} + 1)} \quad (\text{case (b)}) \quad (\text{A.2a})$$

where

$$\bar{R} \equiv \frac{R}{r} \quad \bar{d}_x \equiv \frac{d_x}{r} \quad \bar{d}'_x \equiv \frac{d'_x}{r} \quad . \quad (\text{A.2b})$$

If the packing density of the axial fibers in the cords is  $f$ , then the volume fraction of the axial fibers in the composite,  $V_f$ , is given by

$$V_f = f V_{cd} \quad . \quad (\text{A.3})$$

A useful parameter for analyzing stress distributions is the area fraction,  $A_{cd}$ , of a plane such as that marked A – A in Fig. 5a or 5b occupied by the legs of the cords. Since there are two legs crossing such a plane in each unit cell,

$$A_{cd} = \frac{\pi}{4} \frac{1}{\bar{R} + 1} \quad (\text{case (b)}). \quad (\text{A.4})$$

The strain capacity,  $\varepsilon_c$ , which is the engineering strain expected before interpenetrating loops come into direct contact with one another, is

$$\varepsilon_c = \frac{\bar{d}_x + 2[\bar{R} - 1]}{2[\bar{d}_x + \bar{d}'_x]} \quad (\text{case (b)}). \quad (\text{A.5})$$

*Case (a):* In case (a), the legs do not compact to loci parallel to the  $x$ -axis, but remain inclined to it at an angle  $\theta$ . The right end of each leg segment sits higher than the left by the thickness,  $2r$ , of one crown (Fig. 5a), so that

$$\theta = \tan^{-1} \left[ \frac{2r}{d_x} \right] \quad (\text{case (a)}). \quad (\text{A.6})$$

Inclination of the legs to the  $x$ -axis is visible in the specimen shown in Fig. 4. The pitch of the helical crowns is the same as in case (b), so the path length of a half-loop becomes

$$s_1 = \pi R \sqrt{1 + \left( \frac{2r}{\pi R} \right)^2} + 2\sqrt{d_x^2 + (2r)^2} \quad (\text{case (a)}). \quad (\text{A.7})$$

The dimensions of the unit cell of Fig. (5a) are  $2d_x$ ,  $6r$ , and  $2(R + r)$  in the  $x$ ,  $y$ , and  $z$  directions, respectively. The volume fraction occupied by the cords is thus

$$V_{cd} = \frac{\pi \left[ \pi \bar{R} \sqrt{1 + (2/\pi \bar{R})^2} + 2\sqrt{\bar{d}_x^2 + 4} \right]}{6 \bar{d}_x (\bar{R} + 1)} \quad (\text{case (a)}). \quad (\text{A.8})$$

The area fraction of the plane marked A – A in Fig. 5a occupied by the legs is

$$A_{cd} = \frac{\pi}{6} \frac{1}{\bar{R} + 1} \quad (\text{case (a)}). \quad (\text{A.9})$$

The stain capacity is given by

$$\varepsilon_c = \frac{1}{2} + \frac{\bar{R} - 1}{\bar{d}_x} \quad (\text{case (a)}). \quad (\text{A.10})$$

In both cases (a) and (b), the following restriction must hold for cords of circular cross-section:

$$\bar{d}_x \geq 2(\bar{R} + 1) \quad (\text{A.11})$$

In practice, the lower bound  $\bar{R} \geq 2$  also holds, equality corresponding to a pin of radius equal to  $r$ .

The results for  $V_{cd}$  for cases (a) and (b) are plotted in Fig. A.1 for representative values of parameters. The fiber volume fraction,  $V_f$ , will typically be  $\approx 70\%$  of  $V_{cd}$ . Some improvement over the estimates shown in Fig. A.1 can be achieved by compacting the composite, which reduces the gaps between legs in the  $y$  direction and achieves closer packing of both legs and crowns by squashing them into square rather than circular cross-sections.

Figure A.2 shows a cross-sectional view of two interlacing half-loops in a compacted braid projected onto an  $x - z$  plane. A similar figure appears in an appendix of [3] for two links in a steel chain composite. Inspection of Fig. A.2 reveals that, if the legs are assumed to sit directly on one another as shown (and as assumed in calculating the volume of the unit cells in Fig. 5) and the crowns remain toroidal, then the crowns of the two half-loops must interpenetrate. In dealing with steel chain links, this must be taken into account and the legs must remain separated. The fibrous cords, in contrast, can deform fairly easily under lateral loads. Thus they will reshape themselves as suggested in Fig. A.2 and the legs will come into contact. Indeed, since the legs can also change fairly easily from a circular cross-section, they can be pressed even closer together in practice than indicated by a centre-to-centre separation of  $2r$ .

Table A.1 shows various parameters as predicted by the model and measured in specimens. For predictions of  $V_f$ , a packing factor  $f = 0.7$  was assumed. The predictions and measurements agree quite well generally, with some significant variances. The dimension,  $l_z$ , is underestimated in several cases, especially for those specimens made with cords contained in shrink-wrap (BR5798a and BR5798b). This implies that the cords are too stiff to follow the radius of the dowel pins during braiding. For specimens made with served Kevlar tows where  $l_z$  is underpredicted (BR5798c and BR6298a), the probable cause is compaction in the  $x$ -direction in the mold, which causes bulging in the  $z$ -direction. Note that  $l_y$  is over-predicted for these two composites, whereas it is predicted correctly for the composites with shrink-wrapped cords.

**Table A.1. Measured and predicted dimensions and fiber volume fractions.**

	$l_y$ expt (mm)	$l_z$ expt (mm)	$l_y$ model (mm)	$l_z$ model (mm)	$V_f$ expt	$V_f$ model
BR5798a	26.7	13.7	25.5	9.6	0.22	0.28
BR5798b	29.7	15.0	25.5	9.6	0.18	0.28
BR5798c	28.7	18.5	51.8	11.8	0.36	0.34
BR6298a	15.2	9.7	32.7	6.5	0.30	0.19
BR6298b	28.4	12.2	34.6	11.8	0.38	0.34
BR6298c	30.0	11.2	34.6	11.8	0.42	0.34

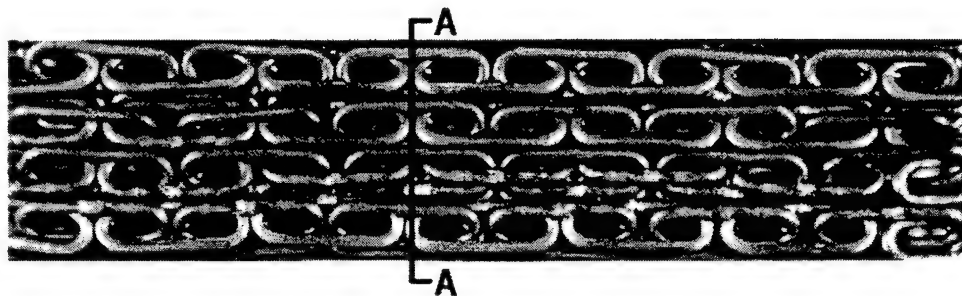
## Figure Captions

1. (a) Contracted chain configuration viewed through a transparent epoxy matrix. (b) Measured stress-strain curve for a chain/polycarbonate composite (from [3]).
2. Cords on a set of pins with loop interlacing analogous to links of a chain.
3. Apparatus for forming braided composites with high sliding strain capacity.
4. Braid reinforcement on nail bed showing Kevlar fiber tows (wrapped in black shrink-wrap plastic tubes to enhance fiber packing) and Teflon wrapped splices.
5. Two braid configurations. (a) Single pin system in which opposing crowns overlap above and below one another. (b) Dual pin system that can separate abutting crowns.
6. Schematic of two interpenetrating cords in a braided composite.
7. Failed composites showing lock up of loops following delocalized damage.
8. Engineering stress – engineering strain records for the specimens of Table I.

A.1 The volume fraction of the composite occupied by cords in case (a) of Fig. 5.

A.2 Schematic of the cross-sections of two half-loops compacted in the  $y$ -direction. The plus and minus symbols indicate the direction in which the legs progress in or out of the page towards their crowns.

(a)



(b)

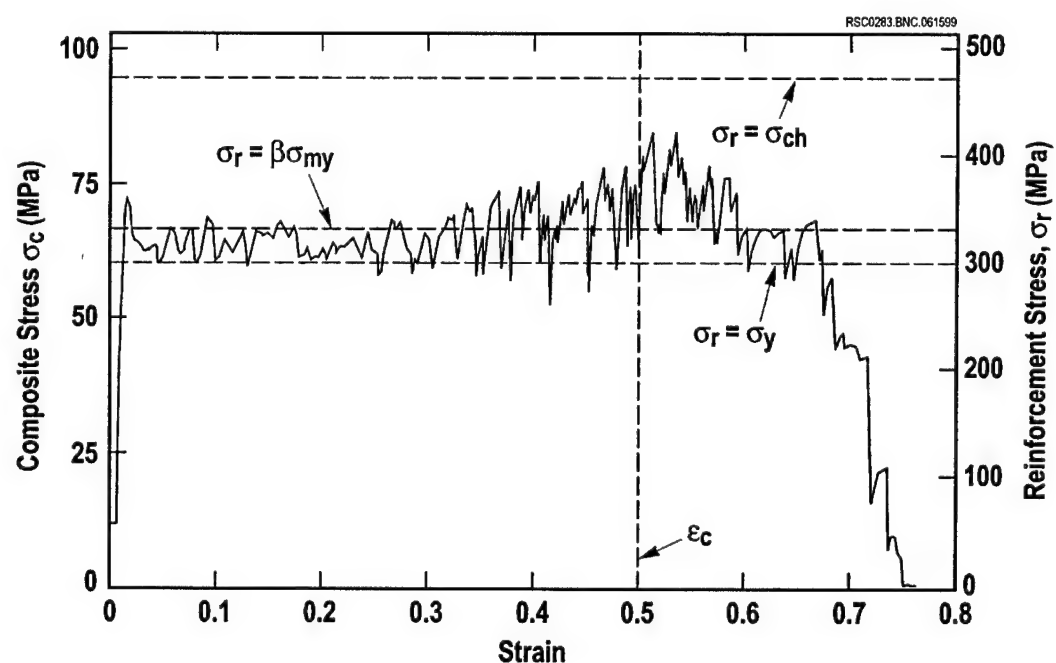


Figure 1

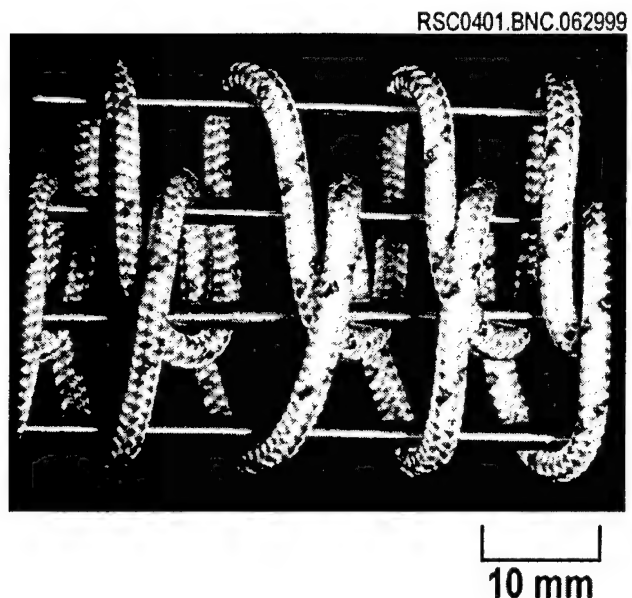


Figure 2

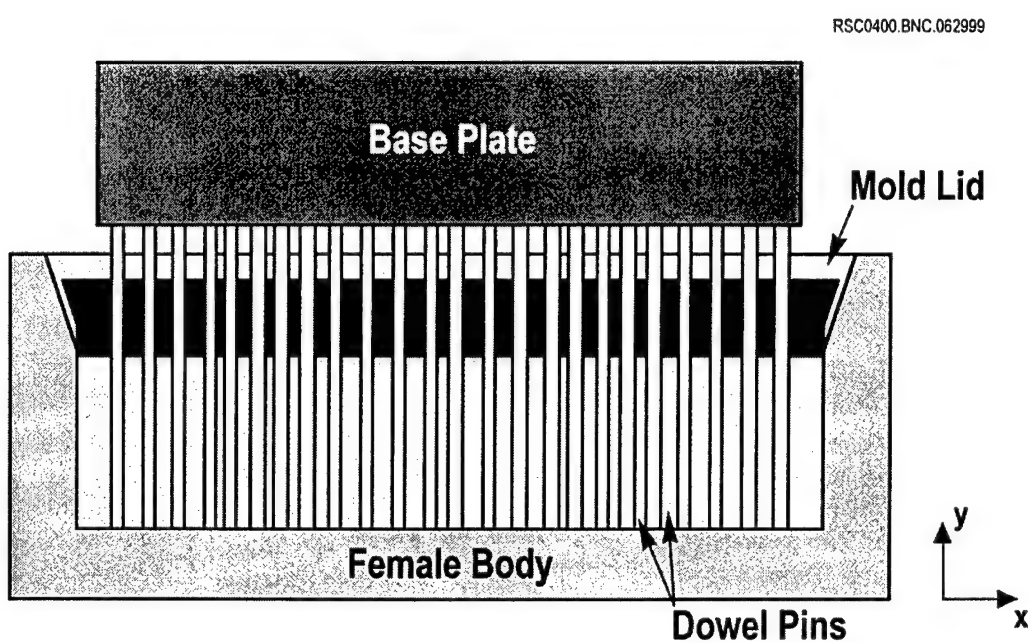


Figure 3

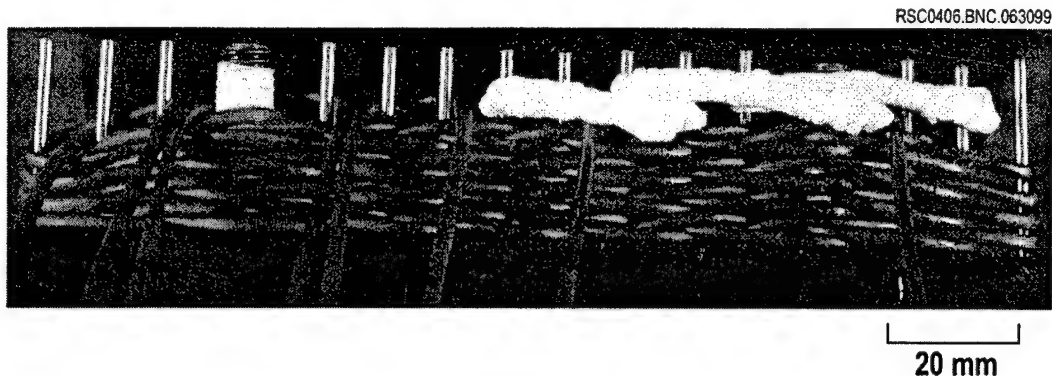


Figure 4

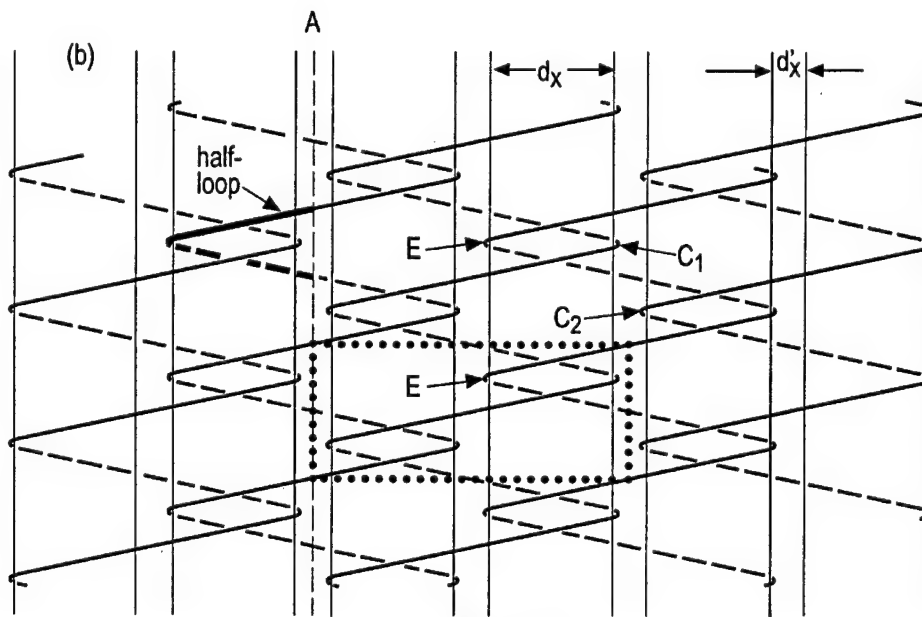
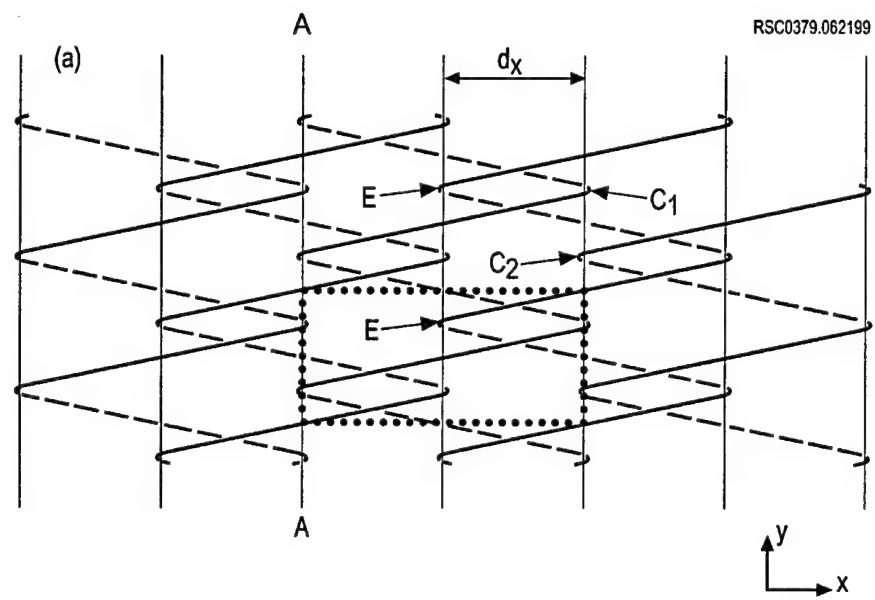


Figure 5

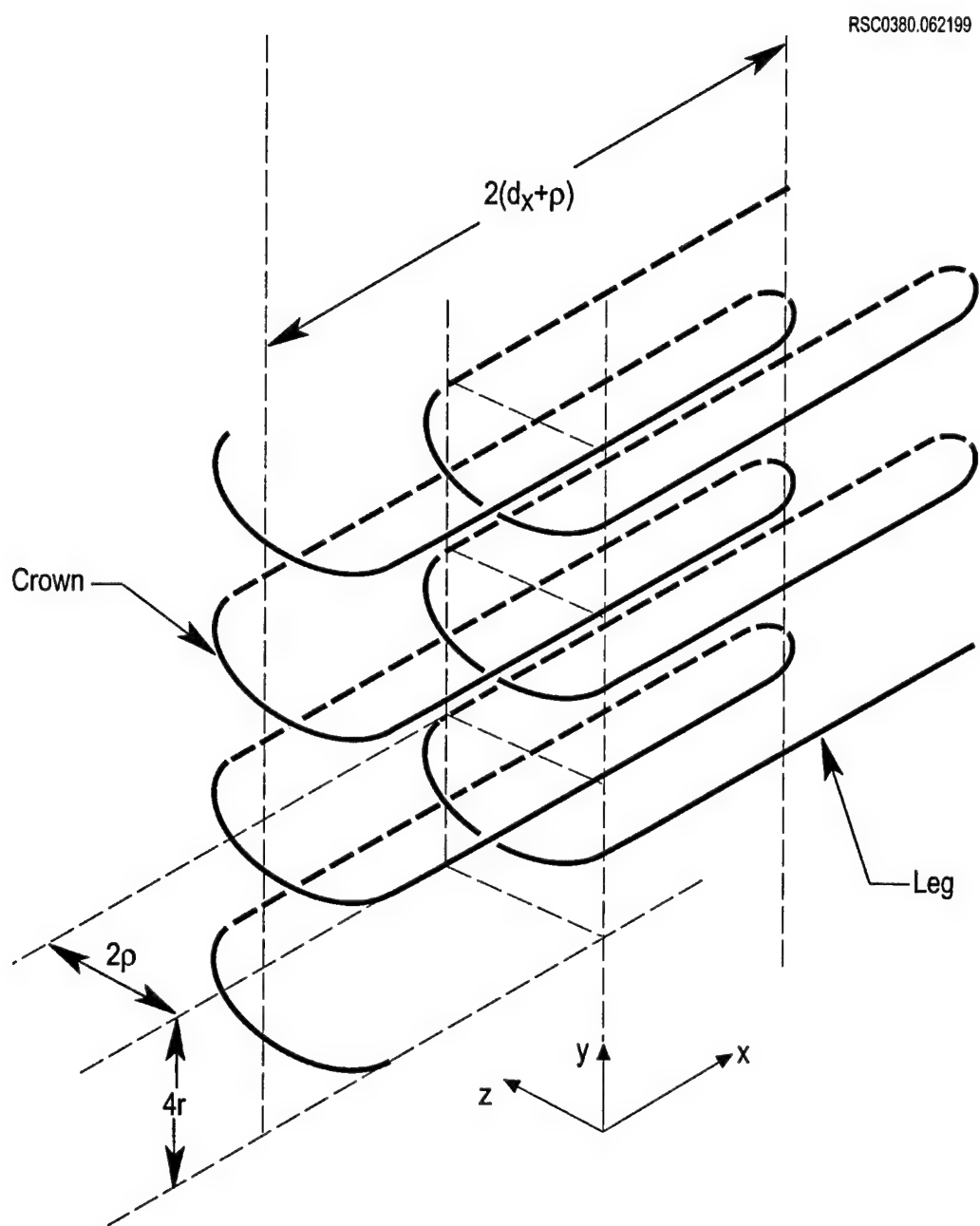
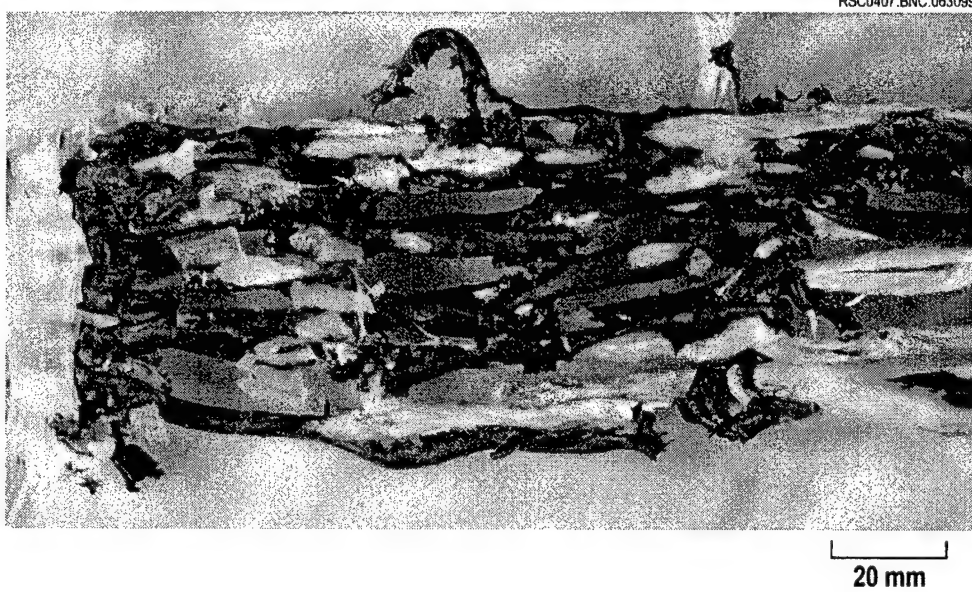


Figure 6

(a)



(b)

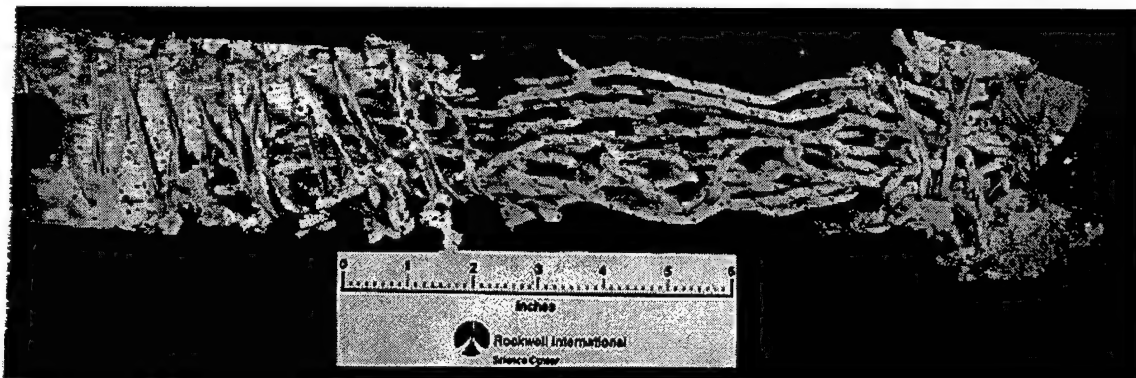


Figure 7

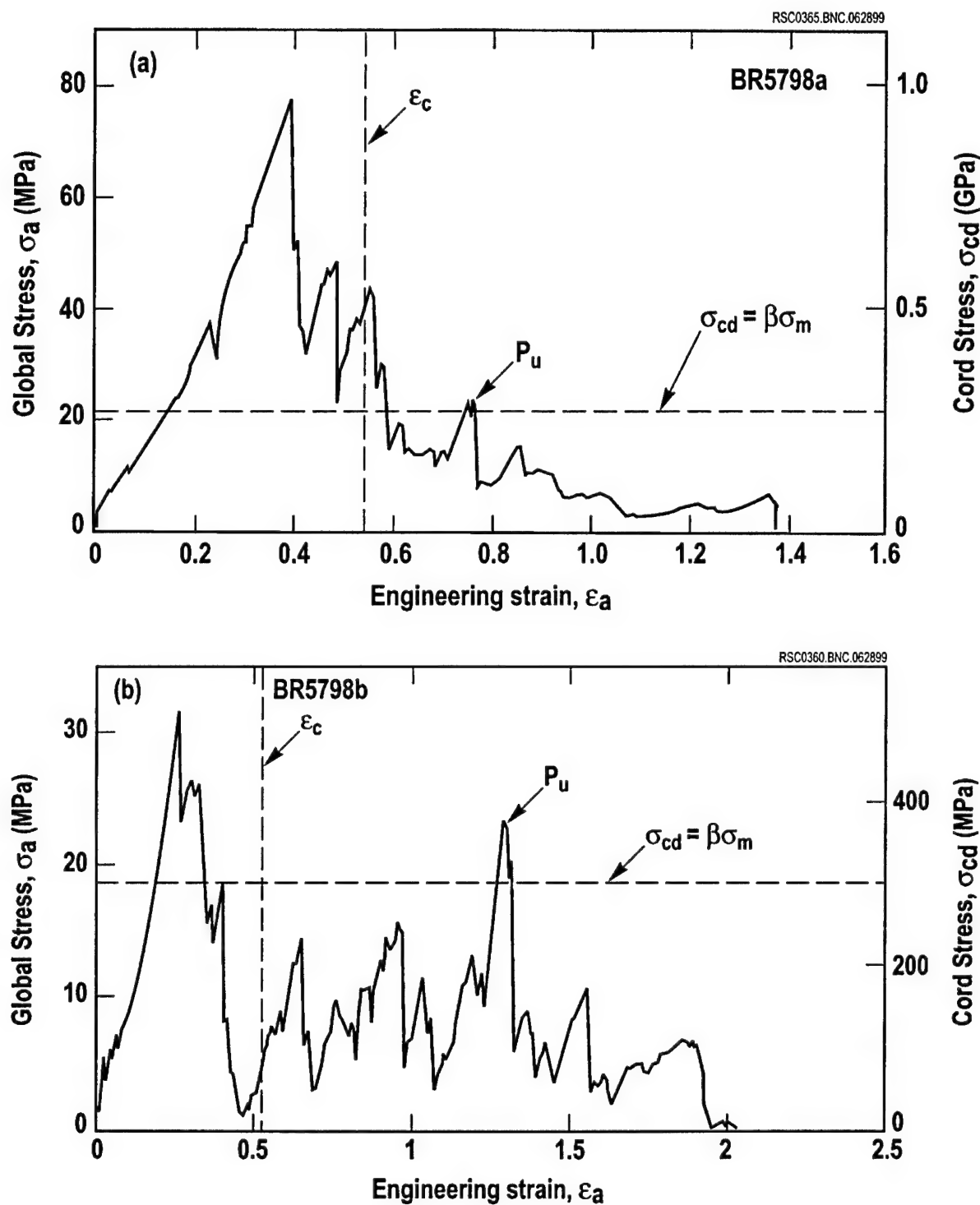


Figure 8

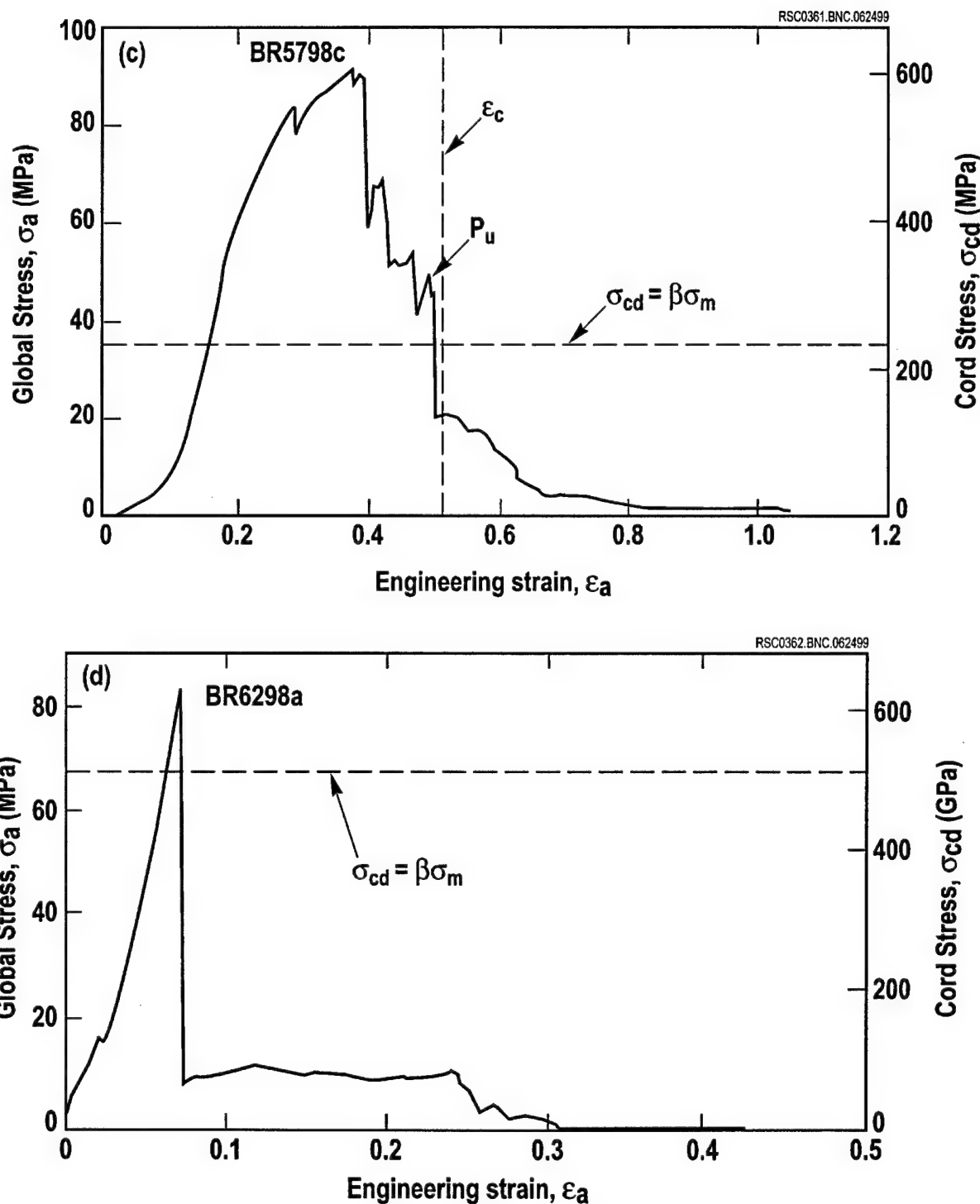


Figure 8 (Contd.)

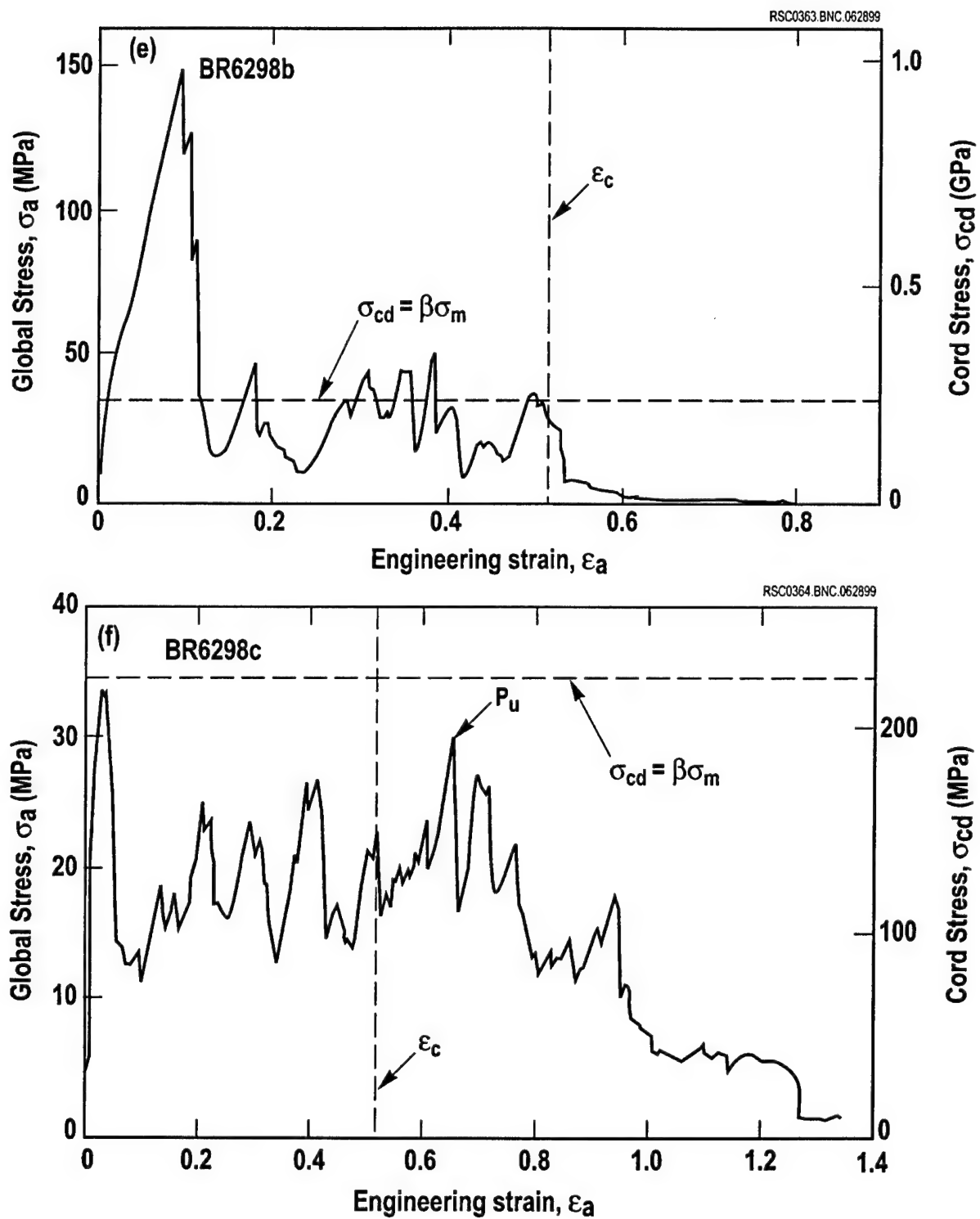


Figure 8 (Contd.)

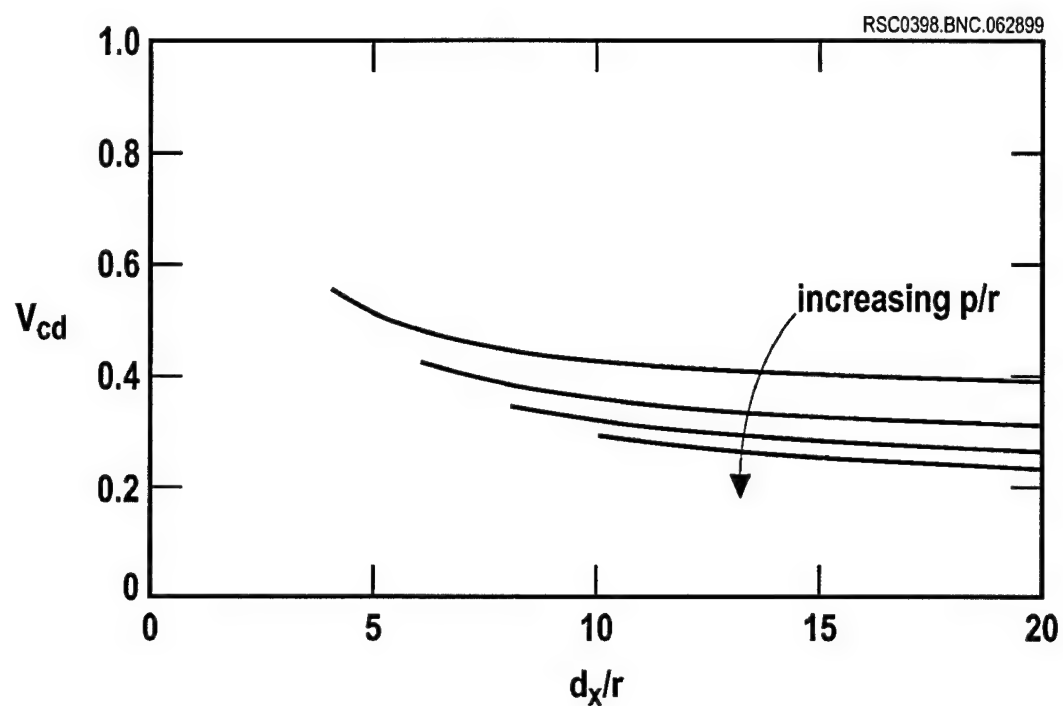


Figure A.1

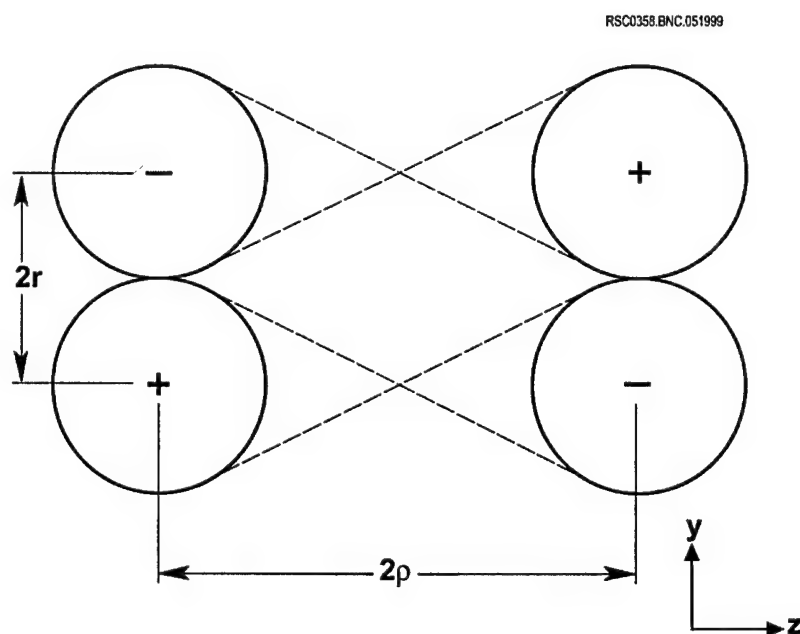


Figure A.2

# **Rockwell Science Center**

## **KNITTED COMPOSITES FOR ENERGY ABSORPTION UNDER TENSILE LOADING**

**B. N. Cox and J. B. Davis**

Rockwell Science Center, LLC  
1049 Camino Dos Rios  
Thousand Oaks, CA 91360  
U.S.A.

---

For possible submission to *J. Mater. Sci.*

---

## ABSTRACT

A new class of knitted composites has been designed to maximize the total energy absorbed during tensile failure. Knitted loops of light, continuous fiber tows are configured in such a way that they must be drawn through relatively large displacements before they come into direct contact with one another. Upon loop contact, the material hardens locally, forcing further damage to develop by the same process elsewhere. In this way the entire gauge section absorbs energy before ultimate failure. Levels of energy absorption per unit volume reach  $40 \text{ MJ/m}^3$  and, per unit mass,  $25 \text{ J/g}$ . The mechanisms involved in damage delocalization and failure are detailed and modeled at a very simple level. While the current values of energy absorption are already attractive, the simple models indicate much higher values for composites that have been optimized.

## 1.0 INTRODUCTION

This paper continues a series on methods of creating composites in which unusually high levels of energy absorption under tensile loading have been incorporated by novel arrangements of the reinforcement geometry. Potential applications for such composites include casings designed to contain bursting rotors, turbines, or flywheels; backing plates in armour systems; and containers subject to internal explosions.

Prior work has reported composites of steel chains in various matrices, including polycarbonate and epoxy, and braided continuous fiber composites that are based on the presence of geometrical units that are directly analogous to interpenetrating chain links [1-4]. The chain links or braided loops are configured so that they are not initially in direct contact. When matrix damage commences during tensile loading, the links or loops are drawn through the matrix, which requires significant plastic work. When two links or loops do come into direct contact, the material hardens locally, driving further damage and link or loop displacement to occur elsewhere. Thus, damage is delocalized, to the extent that in a successfully designed composite, the entire material must undergo substantial damage before ultimate failure. The proper measure of energy absorption becomes the energy absorbed per unit volume (or per unit mass), which can be expected to be independent of specimen size. In contrast, the energy absorbed by a localized fracture event depends on the cross-sectional area of the specimen. Although the fracture process may create a fairly wide band of damage, for large enough specimens the energy absorbed per unit volume declines to relatively low values.

In the chain composites, energy absorption levels of nearly  $60 \text{ MJ/m}^3$  or  $14 \text{ J/g}$  have been achieved, while reasonable extrapolations to idealized chain and matrix materials suggest that levels of  $160 \text{ MJ/m}^3$  or  $40 \text{ J/g}$  are feasible [3]. By generalizing the shape of the links of the chains, even higher values of the energy per unit volume are attainable [5].

Braided composites have been developed with Kevlar reinforcement in epoxy matrices. The braided loops are similar to the interlacing in common chain-link fencing. The loops are arranged in an initially non-contacting configuration by braiding them onto a row of dowel pins [4]. The

non-contacting configuration is preserved even when the pins are removed before consolidation by holding the braided fabric in a clamped mold. Energy absorption levels of approximately 30 MJ/m<sup>3</sup> or 18 J/g have been achieved so far with the braiding concept [4]. Significantly higher levels should be attainable with stronger matrices and amendment of the braiding configuration to achieve higher volume fractions of reinforcement, with specific energy absorption levels perhaps exceeding 50 J/g.

The chief advantages of the braiding method are that it allows the use of strong, light fibers, thus assuring specific energy absorption results superior to those achievable with steel chains; and that braiding ought to be amenable to automation and cheap production. However, the method also suffers from two potentially limiting characteristics. The topology of the braiding process makes inevitable the presence of loose ends of braided tows or cords when the desired amount of fabric has been braided. If they are left unsecured, the loose ends tend to draw through the composite at moderate strains during loading, causing premature failure. They must be secured by splicing them together prior to composite consolidation, which can be done with repeatable success, but is an awkward and time-consuming operation, at least in hand-scale fabrication in the laboratory. Second, the braided loops, being weaker in the transverse direction than steel links, tend to spread out sideways during composite damage to large strains. This tends to release matrix entrapped between braided loops, allowing the loops to approach one another too easily. Energy absorption is compromised.

While solutions to the challenges of the braiding method are available, there is also reason to explore alternative textile processes in which the problems are entirely avoided. Here an approach to high-energy absorption based on weft knitting is presented. The knitting process can be executed with a single continuous tow or cord, so that loose ends are never present. The geometry of the interlacing of the knitted loops leads to potentially advantageous force distributions during loop displacement, with loops drawn tightly against one another to resist lateral separation. The knitted and braided composites yield similar energy absorption levels in their current states of development, but offer alternative manufacturing routes.

The general objective of the new composite development is to create a material that undergoes large tensile strains at an approximately constant stress before failure. The strain to failure is limited by the extent of the displacement allowed before the lock-up (strong contact) of knitted loops, which occurs at a critical global engineering strain denoted  $\varepsilon_c$ . The total energy absorbed per unit volume is approximately the product of  $\varepsilon_c$  and the magnitude of the global engineering stress required for loop displacement,  $\sigma_d$ . Both  $\sigma_d$  and  $\varepsilon_c$  can be varied over quite wide ranges by choosing different materials and geometrical parameters for the knitted fabric.

## 2. FABRICATION OF KNITTED COMPOSITES FOR ENERGY ABSORPTION

Like the braided composites of [4], the knitted composites are fabricated using common continuous fibers in common matrices. The spirit of the approach is to achieve the desired behavior by tailoring the reinforcement geometry, not by using exotic high-performance materials.

### 2.1 Knitting on a Bed of Nails

The geometry of the knitted composites is schematized in Fig. 1. Topologically, the tow arrangement is exactly the same as in a simple weft knit. Courses of loops are formed from a single, continuous cord, with successive courses interlaced as shown. The novel feature introduced here is that the loops have been elongated normal to the courses (i.e., in the  $x$ -direction in Fig. 1). Under load in the  $x$ -direction, any loop can slide a considerable distance before coming into intimate contact with the loop on the next course into which it is interlaced. In a conventional knit, in contrast, all interlacing loops (loops in successive courses) are already drawn into intimate contact by yarn tension during knitting and the whole system can strain under load only if the loops change their shape.

To create high sliding strain capacity in a knit, the loops are assembled on a 2D bed of nails (Fig. 2). The knit of Fig. 1a is formed by repeating the maneuver illustrated in Fig. 3. The cord labeled 2 is initially straight (dashed line) and lies under the loop labeled 1, which has been stretched around nails as shown. The nails all possess free ends that stand up out of the page. A new loop,

labeled 3, is formed by bringing cord 2 up through loop 1 using a hooked tool and drawing it out and over the nail labeled A. As it is drawn out, the lower portions of loop 3 (in the sense of the figure) are pulled up against the nails labeled B, completing the formation of a new loop exactly similar to loop 1. By stretching the knitted loops over the nails, the loops are formed in a configuration that will initially transfer tensile loads in the  $x$  direction by shear only. Load transfer by normal contact tractions will occur only after the loops have slid relative to one another by a distance comparable to the nail spacing.

The photograph of Fig. 2 further illustrates the method of forming a knit. The fabric shown comprises courses of three loops each. Only two loops have been formed in the last course (towards the top of the picture). The third loop will be formed by drawing the straight cord out from under the right hand loop in the penultimate course and lifting it over the vacant nail at the top right of the last course. The working cord is being supplied continuously from a large spool. It is always laid down under the course of loops that is about to be formed in readiness for the drawing of the next course.

Figure 1b shows a variant of the process in which loops have been drawn out over three nail spacings in the  $x$  direction, instead of two. The repeated knitting motion is otherwise the same as described above and in Fig. 3. To achieve the desired pattern of interlacing, the straight cord labeled 2 in Fig. 3 must be laid down at such a stage in the process that when it is drawn out it will penetrate only the most recently formed course of loops, as in Fig. 1b.

The knits sketched in Figs. 1a and 1b have sliding strain capacities,  $\varepsilon_c$ , that appear to be approximately 1.0 and 2.0, respectively, but will be somewhat less in practice, because the sliding loops are drawn into knots within which friction increases rapidly.

All the preceding description refers to the formation of one layer or ply of knitted fabric. Thicker parts comprising many layers may be made by repeating the process over the same bed of nails.

## 2.2 Optimal Cords for Knitting

Specimens have been fabricated with carbon, glass, and Kevlar fiber tows in various epoxy matrices. While carbon fibers ought in principle to be an excellent choice, since they are stiff, strong, and light, in practice they are difficult to knit without severe damage. Consequently, reinforcement failure precedes loop sliding at unsatisfactorily low loads. Kevlar has proven to be the best fiber tried so far, because of the relative insensitivity of its strength to lateral loads.

As with the braided composites of [4], knitting with loose rovings of Kevlar (or glass or carbon) fibers that are held together relatively weakly by a small quantity of uncured polymer sizing does not work well. These tows are difficult to grasp with the knitting hook. Partial grasping results in severe fluffing of the tow, the risk of creating an irreversible mess before knitting is complete, and inadequate strength even when a composite is successfully finished. Loose rovings also tend to flatten out at the crowns of loops (where they turn around pins), which damages and weakens them.

Different methods of serving predominantly axial fiber bundles so that they cannot easily split apart or suffer damage in handling were developed during work on the braided composites [4]. The resulting products are called cords, although they may not necessarily contain wound or braided fibers, as might be expected when the word cord is used to describe a light rope. The most successful cords were straight tows of Kevlar threaded through shrink-wrap tubing, which has the dual benefit of compressing the tows into a state of high compaction when the tubing is heated and shrunk [4], and protecting them during knitting. Successful knits were also made with cords consisting of straight Kevlar tows wound with light polyester yarn [4].

Specifications of the cords used in specimen fabrication are listed in Table I. The cord radius,  $r$ , is defined as

$$r = \sqrt{\frac{1}{\pi f \rho_y}} \quad (1)$$

where  $f$  is the fiber packing factor in the cord, taken to be 0.7,  $\rho$  is the density of the fibers (0.00145 gm/mm<sup>3</sup> for Kevlar), and  $y$  is the yield of the axial fibers in the cord.

As remarked in [4], when shrink-wrap tubing is used, resin is prevented almost entirely from entering the interior of the cords during infiltration to form a composite. The only polymer present amongst the fibers of the cords during curing is the small amount of sizing on the Kevlar tows as supplied. It is not known whether this condition raises or lowers the net strength of individual cords after knitting and composite consolidation. The absence of resin may facilitate turning of the cords around nails during knitting, minimizing residual strains and physical damage in the fibers. It also changes the mechanics of load transfer between fibers in the cord as they begin to break during failure of the composite.

Tow strengths were assessed in [4] by testing single tows under uniaxial tension, which are representative of the strengths of legs, and pairs of tows interlaced in loops. The loops were chosen to mimic the geometry of the braided composites of [4], but they will also give some indication of the strength reduction caused in the knits of this paper by the stress concentrations associated with looping. The strength is defined as the stress in the fibers (far from the loop in the looped specimens) at ultimate failure and is denoted  $\sigma_{cd}^{(ult)}$ . The straight tows are characterized by  $1.8 < \sigma_{cd}^{(ult)} < 2.2$  GPa, whereas for the looped tows  $550 < \sigma_{cd}^{(ult)} < 700$  MPa. The stress concentration of the loop lowers strength by about a factor of three. These strengths will be taken as representative for the cords of Table I.

### **2.3 Tooling for Composite Formation**

The bed of nails comprises two moveable parts, one being the nails themselves together with the base plate into which they are anchored; and the other a second plate, called the lid, through which the nails can slide via an array of holes. The lid is first placed over the nails and allowed to rest against the base plate and the knitted fabric is then formed on the nails above the lid. When the knitting is completed, the bed assembly is inverted and lowered into a female mold, with the fabric still stretched over the nails. The lid and female molds are clamped together,

compressing the fabric. If the compression is sufficient (modest levels suffice), the base plate can be removed by withdrawing the nails through the holes in the lid, without the fabric moving. At this point, lateral pressure can also be applied to the long sides of the fabric (motion along the  $y$  axis) to raise the overall fiber volume fraction. This is effected by pistons mounted on arms protruding through slots in the walls of the mold (slots shown in Fig. 2, but not the pistons). Applying pressure in two directions helps maximize volume fraction. It also reduces any undesirable distortions created in the fabric when the nails are removed. Epoxy matrix is added in an uncured, inviscid state by vacuum infiltration. The epoxy is cured in a vacuum furnace and the specimen is released by breaking the lid and female mold apart. Release of the cured specimen from the mold is facilitated by a Teflon coating applied to all mold surfaces.

Photographs of typical knitted composite specimens are shown in Fig. 4. The composite in Fig. 4a had been formed with commercially available cords consisting of straight Kevlar tows in a braided sheath of further Kevlar fibers. The braided sheath contains an undesirably high percentage of all fibers, so that the aligned fiber volume fraction is too low for achieving delocalised failure (see also [4]). Nevertheless, the untested specimen in Fig. 4a shows the knitted pattern very clearly. The composite in Fig. 4b has been formed with the preferred cords consisting of Kevlar tows in black shrink-wrap tubing. Further Kevlar tows have been wound around the specimen and drawn tight by hand to maximize the fiber volume fraction, a method of compaction that predates the development of a mold containing lateral pistons. The lid plate is also visible in Fig. 4b, in this case with long slots rather than holes through which the nails in the bed can pass. The holes or slots in the lid must fit the nails fairly tightly, since otherwise the cords have a tendency to bulge back out through them during compaction, which introduces weak points in the composite.

Screws can also be seen in the ends of the specimen of Fig. 4b. The knitted loops have been formed around them. The screws improve load transfer from the grips during testing. Metal pins, whose ends can be slotted into the grips, can serve the same purpose.

## 2.4 Geometrical Characteristics of the Knitted Composites

Analysis of the mechanics of damage in the knitted composites requires a simple model of the geometry of the knitted reinforcement. Appendix A presents a model based on the idealization depicted in Fig. 1, with the following assumptions. The fabric is assumed to consist of a periodic arrangement of loops, which will be considered to consist of semicircular crown segments connected by piecewise straight leg segments. Both legs and crowns will be assumed to have circular cross-sections of radius  $r$ . Let  $\rho$  denote the radius of curvature of the axis of the crown segments and  $h$  the projected length of the legs in the  $x$  direction. Let  $d_x$  denote the centre-to-centre spacing of the nails on which the knit is formed in the  $x$  direction and  $d_y$  their spacing in the  $y$  direction (Fig. 1). Let  $n_{\text{loop}}$  denote the number of nail spacings over which loops are drawn ( $n_{\text{loop}} = 2$  or 3 in Fig. 1).

The model yields analytical estimates of the volume fraction,  $V_{\text{cd}}$ , occupied by the cords (including internal resin or void) in the final composite. These predictions do not compensate for fabric compaction after its removal from the bed of nails, which can raise  $V_{\text{cd}}$ , substantially, but they nevertheless correctly demonstrate trends with important design parameters. Figure 5 shows representative plots of  $V_{\text{cd}}$  vs.  $d_x$  for fixed  $d_y$  (evaluated by substituting Eqs. (A.9) and (A.5) into Eq. (7)). The nail radius has been assumed equal to the cord radius,  $r_n = r$ , which is typical of the composites reported in this paper. The radius of curvature of the crowns has been assigned the values,  $\rho = r_n + 2r$  or  $\rho = r_n + 3r$ . Results for the two cases  $n_{\text{loop}} = 2$  and 3 are shown together. Figure 5 shows no significant dependence of  $V_{\text{cd}}$  on  $\rho$  at any value of  $d_x$  or  $d_y$ . For large  $d_x$ ,  $V_{\text{cd}}$  tends towards a constant value,  $\pi/2d_y$ , which is the same for either loop length. For moderate  $d_x$ ,  $V_{\text{cd}}$  is only mildly dependent on loop length.

The enhancement achieved in  $V_{\text{cd}}$  during compaction depends mainly on the change in the cord spacing in the  $y$ -direction, which may be represented in the geometrical model as a reduction in the effective value of  $d_y$ . (Of course, the nails themselves have already been removed from the mould before the compaction process.) The nail spacing is generally chosen to be relatively large to facilitate knitting. Under compaction, the gaps between legs in the  $y$  direction are reduced and closer packing of both legs and crowns is achieved by squashing them towards square rather than

circular cross-sections, effectively reducing  $d_y$ . In current experience,  $3r \leq d_y \leq 4r$  is a typical result. Figure 5 suggests  $V_{cd} \approx 0.5 - 0.6$  when  $3r \leq d_y \leq 4r$ . The spacing of layers of fabric in the  $z$  direction may also be reduced from the estimate of the model (Eq. (A.11)), but to a degree that depends on the order in which through-thickness and lateral compacting loads are applied. For the architecture of Fig. 1b, compaction in the  $z$  direction can be significantly aided by offsetting successive layers of knitted fabric so that the high points (labeled Q in Fig. A.1) are displaced from one another. As tooling is improved, volume fractions  $V_{cd} \approx 0.7$  are probably a reasonable goal.

Achievable levels of fiber packing within cords are probably represented by values of the fiber packing factor,  $f \approx 0.7$ . Therefore achieving  $V_{cd} \approx 0.7$  will lead to overall volume fractions for the axial fibers in the knitted cords of  $V_f \approx 0.5$ .

### 3. PROPERTIES OF KNITTED COMPOSITES

#### 3.1 Specimens and Tests

Table II lists the specifications of the five specimens to be reported below. The primary axial fibers in all knitted cords were Kevlar fibers, served as described in Table I. Every specimen was reinforced by a single layer of knitted fabric containing three courses of loops formed on a bed of nails seven pins wide ( $y$  direction). Table II lists the dimensions  $l_y$  and  $l_z$  in the  $y$  and  $z$  directions respectively of a so-called core region that contained all the reinforcement in the consolidated composite but excluded any peripheral regions of pure resin. Peripheral resin fills the cavity of the mould, whereas the reinforcement is compacted into a smaller volume. Peripheral resin cracks in many places at low strains and has negligible effect on the response of the specimen to large strains. Each specimen was approximately 200 mm long. The nail spacings in all cases were  $d_x = 12.7$  mm and  $d_y = 6.35$  mm. The nail radius was 1.5875 mm (1/16 in).

The volume and area fractions quoted in Table II are experimental measurements obtained as follows. The fiber volume fraction,  $V_f$ , was calculated by measuring the total length of cord

knitted into each specimen, multiplying by the volume of fibers per unit length expected for the number of tows served in the cord, and dividing by the volume of the core region. The area fraction of cords,  $A_{cd}$ , represents the fraction of planes such as 2 – 2 in Fig. 1 that is occupied by leg segments of cords. It is given by

$$A_{cd} = \frac{(n_{loop} - 1)n_{course}n_{layer}\pi r^2}{l_y l_z} \quad (2)$$

where  $n_{course}$  is the number of courses of loops in each of  $n_{layer}$  layers. For the case  $n_{loop} = 3$ , only one pair of legs cut by the plane 2 – 2 has been included in the definition of  $A_{cd}$ . When the local strain exceeds unity, loops originating from alternate (rather than successive) rows of nails will cease to overlap. Therefore, for most of the strain history of the composite, the definition of Eq. (2) is more representative of the geometry. These definitions of experimentally determined volume and area fractions yield numbers that are not far from those predicted by the geometric idealization of the previous section (see Appendix A).

The matrix in all specimens consisted of student-friendly Epofix resin,<sup>1</sup> cured at 150°C for two hours. In an attempt to reduce premature loss of matrix during loading to high strains, additional Kevlar tows were wrapped by hand around one specimen while it was still on the knitting nails (e.g., Fig. 4b). The wrapping tows were drawn in helices around the outside of the fabric, working along an axis parallel to the  $x$ -direction.

Uniaxial tension tests were carried out in a screw-driven machine at low strain rates. All specimens were straight bars, as formed in the mold. To enhance gripping, steel screws were sometimes inserted into the loop cavities of the knit near the ends of the specimen before resin infiltration, with their ends left protruding from the specimen (Fig 4b). This eliminated slippage in the grips, which otherwise can be a difficult problem. Even at high grip pressures, disintegration of the specimen near the grips at high strains can cause loss of shear load transfer.

---

<sup>1</sup> Co. name and address.

### 3.2 The Achievement of Delocalized Failure

Delocalization is not easily achieved with knitted composites unless certain measures are taken. Specimens knitted with bare carbon, glass, and even Kevlar tows all exhibited localized failure. This was attributed to a combination of damage to the fibers during knitting and the low packing factors of loose rovings, which lead to unacceptably low fiber volume fractions. Delocalization is also more difficult to achieve if the knitted loops are too short. Specimens made in the configuration of Fig. 1a ( $n_{loop} = 2$ ) even with the preferred cords were liable to localized failure. This appears to be associated with strong friction effects, as discussed in the next section. Delocalization was achieved in all but one case for the specimens for which tests are reported here, which were all fabricated in the configuration  $n_{loop} = 3$  (Table I).

When delocalization was achieved, the first damage observed at relatively low strains consists of matrix cracking. Cracks appear both normal to the load axis and parallel to it between the legs of neighbouring loops. Resin fragments are lost from the composite at strains exceeding approximately 0.1, but some resin remains out to much higher strains. At the highest strains, where the cords are nearly bare, interpenetrating loops are drawn straight and knot against one another very tightly (e.g., Fig. 6). Load transfer must occur primarily by friction.

### 3.3 Stress-Strain Response and Energy Absorption

Engineering stress-engineering strain records are presented for the five specimens in Fig. 7. All of the specimens exhibited delocalized failure, but the stress-strain response varies significantly in shape. The left-hand ordinate in Fig. 7 shows the applied stress,  $\sigma_a$ , which is the load divided by the cross-sectional area of the core region,  $l_y l_z$ . The right hand ordinate shows the stress estimated in the centres of the legs of loops,  $\sigma_{cd}$ , under conditions where the legs alone are supporting stress across the plane 2 – 2 of Fig. 1.

Specimens made with cords consisting of Kevlar tows in shrink-wrap tubing tended to support modest stress levels (5 – 8 MPa) during most of the load history (Figs. 7a – 7d). As the strain increased towards the value at which lock-up of loops was expected, the stress rose to a peak of

15 – 30 MPa, which was achieved near the lockup strain. The specimen around which Kevlar tows were wound (Fig. 4b) showed somewhat improved but still modest stress levels over the strain interval  $0 \leq \varepsilon \leq 2$ .

The specimen made with Kevlar tows served with wound polyester exhibited a local peak in the applied stress at low strain ( $\varepsilon \approx 0.05$ ), which was almost equal to the ultimate peak engineering stress,  $\sigma_u = 28$  MPa, which occurred at  $\varepsilon \approx 2$ . This specimen supported a stress exceeding 15 MPa over most of the intervening life.

All the stress-strain curves are punctuated by numerous drops and spikes in the load, very similar in appearance to those observed with steel chain and braided fiber composites [1,3,4]. These features correspond to instances of resin fracture and ejection of resin fragments.

In all specimens, damage tends not to develop uniformly over the whole gauge section, even though, in cases of delocalized failure, the whole gauge section is uniformly damaged and strained prior to ultimate failure. Large strains tend to develop in one region of the specimen and then spread along the rest of the gauge section.

The energy absorbed per unit volume of the original gauge section,  $W_v$ , is given by the area under the engineering stress-strain curve:

$$W = \int \sigma d\varepsilon \quad . \quad (3)$$

Values range from 15 to nearly 40 MJ/m<sup>3</sup> (Table II). The specific energy absorption,  $W_m$ , i.e., the energy absorbed per unit mass, is related to  $W_v$  by

$$W_m = \frac{W_v}{\rho} \quad (4)$$

with  $\rho$  the composite density. Values of  $W_m$  range from 8 to 25 J/g.

#### 4. MECHANICS OF LOOP DISPLACEMENT

Insight into the mechanics of delocalization and energy absorption in the knitted composites can be inferred from simple micromechanical considerations. Because of the difference in the topology of the interlacing of loops in knits, braids, and chains, the mechanisms of damage in the knitted composites are quite distinct from those in the braided and chain composites. Therefore, the model used so successfully for those prior composites [2] is not pertinent here.

However, although the mechanisms are distinct, a useful modeling goal remains predicting the tensile stress component in the centers of the legs of knitted loops (on the plane 2 – 2 in Fig. 1) as the loops are displaced relative to one another. Figure 8 shows a schematic of the contacting portions of two interlaced knitted loops. This unit is representative of a whole composite of the type illustrated in Fig. 1a: the entire pattern of knitted loops can be constructed from it by operations of reflection and translation. It is also similar to the basic load-transferring unit in the configuration of Fig. 1b.

Load transfer from one loop to the other involves contact between the knitted cords, which may be mediated by intervening matrix (resin) or may be direct, following fragmentation and ejection of the matrix. Here consideration is restricted to direct contact, since the current generation of knitted composites all suffered substantial matrix loss early in the load life. This is a major distinction from the chain and braided composites, where matrix remains trapped between interpenetrating loops through large relative loop displacements. The loops in chains or braids form nearly enclosed cavities, which are relatively effective in confining the matrix. In the knitted composites, loop segments such as those depicted in Fig. 8 split any intervening matrix in a scissoring action as they slide past one another, rather than confining it.

Contact between the interpenetrating loops can be divided for convenient analysis into two kinds of zone, as illustrated in Fig. 8. One is a zone of contact,  $S_c$ , between one crown and one leg and lying approximately in the  $x - y$  plane; the other a domain of contact,  $S_l$ , between the two legs and lying approximately in the  $z - x$  plane. If the crowns and legs are squashed towards square sections during processing, then they will make contact along bands of width somewhat less than

$2r$ . Here the width  $r$  will be considered representative, so that the dimensions of the zones will be as follows. Zone  $S_c$  will extend distances of  $r$  in the  $x$  direction and  $r$  in the  $y$  direction. Zone  $S_l$  will extend distances of  $r$  in the  $z$  direction and  $l_f$  in the  $x$  direction, where  $l_f$  will be reduced as the loops slide towards lockup. In the geometrical idealization of Fig. 1,  $l_f$  must initially satisfy

$$l_f = (n_{\text{loop}} - 1)d_x + 2(r_n + r - \rho) \quad (5a)$$

which reduces, for the typical case  $\rho = r_n + 3r$  to

$$l_f = (n_{\text{loop}} - 1)d_x - 4r \quad (5b)$$

As the engineering strain of the composite,  $\varepsilon_a$ , increases,  $l_f$  will be reduced by the relative displacement of interlocking loops, which, by reference to Fig. 1, is the amount

$$\delta l_f = \varepsilon_a d_x \quad (6)$$

The condition  $l_f = 0$  provides a lower bound to the strain to lockup, which would be realized if the crowns retain their initial curvature, given by

$$\varepsilon_c^{(\text{lb})} = n_{\text{loop}} - 1 - \frac{4r}{d_x} \quad (7)$$

where the assignment of Eq. (A.10) has been used. If, however, the crowns are stretched into arcs of reduced radius of curvature, which is the general observation late in the stress-strain history, then the total initial path length of a loop can become drawn out along the  $x$  axis. Thus an upper bound estimate to the lockup strain,  $\varepsilon_c^{(\text{ub})}$ , follows from Eq. (A.5) for the initial path length. The result is cumbersome and not written out in full here. Instead, numerical results are shown in Table II along with predictions from Eq. (7). The bound estimates are also marked on the parts of Fig. 7. The peak corresponding to ultimate failure always lies between the bounds,

but usually closer to the upper bound, implying that the crowns are indeed pulled down into tight radii.

The ends of the leg segments shown in Fig. 8 correspond to the planes 2 – 2 in Figs. 1a and 1b. For the configuration of Fig. 1a ( $n_{\text{loop}} = 2$ ), the stress,  $\sigma_{\text{cd}}$ , in the leg at that point should be its maximum, by symmetry, throughout loop displacement. For the configuration of Fig. 1b ( $n_{\text{loop}} = 3$ ), the same will be true once the loops have displaced sufficiently that overlap no longer occurs between loops that were originally knitted on alternate, rather than successive, rows of nails. Overlap ceases for  $n_{\text{loop}} = 3$  at a strain of  $\varepsilon_a \approx 0.5$ . For  $n_{\text{loop}} = 3$ , consideration will be restricted here to strains higher than this. Assume that axial tension is transferred from loop to loop by friction alone and that the frictional tractions have magnitude  $\tau_c$  on zone  $S_c$  and  $\tau_l$  on zone  $S_l$ . Assume further that  $l_f = d_x$ , corresponding to strains  $\varepsilon_a \approx 1$ . Then, taking a cross-sectional area of  $\pi r^2$  for the leg, one finds by force equilibrium in the  $x$  direction that

$$\pi r^2 \sigma_{\text{cd}} = 2S_c \tau_c + S_l \tau_l \quad (8a)$$

or, if  $\tau_c = \tau_l = \tau$ ,

$$\sigma_{\text{cd}} = \left[ \frac{2}{\pi} + \frac{d_x}{\pi r} \right] \tau \quad (8b)$$

The geometrical factors in this expression are obviously approximate, but useful numbers are suggested nonetheless. The horizontal dashed lines in Fig. 7 indicate representative stress levels during loop displacement at moderately large strains. Substituting these values into Eq. (8b) along with values of  $r$  from Table I and the known nail spacing,  $d_x$ , leads to the estimates of the friction stress,  $\tau$ , shown in table III. The friction stress is not far from 30 MPa in all but one case, where it is approximately 45 MPa. These values have no direct verification for the current composites, but they are reasonable values in view of previous measurements of the friction stress during pullout of tows of similar diameter from 3D textile composites with epoxy matrices [6].

In all cases, the stress required for loop displacement rises as the strain increases (apart from a possible dip following a brief peak at very low strain). Since the contact area between interlaced loops decreases with strain ( $l_f$  decreasing), the friction stress must be rising quite dramatically. This should be expected, since the contact pressure between loops is likely to rise as they are drawn more tightly together. , However, the mechanics of this contact problem, in which the loops can change shape significantly with increasing strain because they are relatively weak in shear, are by no means trivial. A complete analysis is not attempted here.

A transition from delocalized to localized failure should occur if  $\sigma_{cd}$  exceeds the strength of the cords in the composite,  $\sigma_{cd}^{(ult)}$ , during loop displacement against friction. This does not appear to have the case in any composite that survived past the onset of significant local damage. Once the matrix has been broken up, the cords are amply strong to work against frictional loads. Where localised failure occurred (specimens not in Table II), it happened early in the damage sequence, when the matrix still had sufficient integrity to transfer load itself.

The cord stress,  $\sigma_{cd}$ , at ultimate failure is listed in Table II. It ranges from 185 to 375 MPa. This is significantly lower than the ultimate strengths,  $\sigma_{cd}^{(ult)}$ , deduced from tests on looped single tows, which range from 550 – 700 MPa (Section 2 and [4]). A similar discrepancy was found for braided composites [4]. This implies that the cords are damaged during loop displacement.

## 5. POTENTIAL FOR ENERGY ABSORPTION

The values of energy absorption for the knitted composites are very encouraging, but substantially higher values could be obtained by better design and processing. The energy absorption will be maximized by 1) raising the fiber volume fraction or the area fraction of cords,  $A_{cd}$ ; 2) raising and preserving the strength of the reinforcing fibers; and 3) preventing the premature loss of matrix from between loops by brittle matrix fracture and fragment ejection. Choosing a knit geometry that increases the strain before lockup,  $\varepsilon_c$ , will also raise the energy absorbed, but many applications may require that  $\varepsilon_c$  not rise beyond the high values already achieved.

The fiber volume fraction,  $V_f$ , can be raised in several ways. First, the pacing factor within cords must be maximized. An automated serving apparatus for winding a light thread around axial tows will achieve better packing and higher consistency than hand winding. Second, further developments of compacting apparatus will enable a tighter fabric arrangement in the mold.

Fiber strength can be increased by selecting fibers that are stronger than Kevlar, although any fiber used must be tough enough not to be damaged during the knitting process. Fiber strength might be preserved during deformation by developing a tough sheath for cords to protect the axial fibers from sharp resin fragments. The shrink-wrap tubing used here is relatively easily torn. A coating of rubber over the cords might work much better. Damage to cords can also be reduced by selecting a matrix that is less brittle and therefore less likely to fragment into sharp, abrasive pieces. Polycarbonate and elastomeric matrices, for example, are worth consideration.

Even with the fiber volume fractions and fiber strengths achieved in the present composites, loop displacement was not sufficiently resisted to maximize energy absorption. Ideally, loop displacement should require a global stress not far below that required for loop rupture, so that the stress-strain response is flat. For this to occur in the knitted composites, a tougher, stronger matrix is required to resist loop displacement before strong friction effects develop. Again, more ductile matrices such as polycarbonate and elastomers appear attractive, perhaps reinforced with short fibers.

Displacement resistance may also be raised by rescaling the reinforcement. Friction forces probably scale with the contact area between interlocking loops,  $S_l + S_c$ . While  $S_c \propto r^2$ , which is the same proportionality as the cross-sectional area of the cords (and therefore their strength),  $S_l \propto rl_f$ , where  $l_f$  might remain constant if the cord radius is reduced while the loop length is fixed. If this is true, then the stress required for loop displacement in the regime dominated by friction will rise relative to that required for ultimate failure. However, the mechanics of frictional contact between two flexible cords are quite complex and further analysis is required to explore the effect of varying the aspect ratio. Furthermore, loop displacement at relatively low stresses involves load transfer through the matrix and will scale in a different way. The resistance to loop

displacement for loops of the shape of chain links, for example, is dominated by nearly hydrostatic compression formed in the matrix inside the crown of the loop and this stress is approximately scale invariant and independent of the loop aspect ratio [4].

By maximizing fiber volume fraction and protecting cords during loop displacement, global stress levels of 60 – 100 MPa at ultimate failure (cord rupture) ought to be achievable. With a strong and tough enough matrix to exploit such strength during loop displacement to the same lockup strain that has been demonstrated here ( $\varepsilon_c \approx 2$ ), energy absorption levels of 120 – 200 MJ/m<sup>3</sup> would be achieved; or 75 – 130 J/g. Such levels would be very useful in many applications.

## 6. SUMMARY REMARKS

Delocalized damage can be achieved by a variant of weft knitting, leading to high values of energy absorbed per unit volume and per unit mass in static uniaxial tension tests. The essential mechanisms are loop displacement accompanied by extensive matrix cracking and plastic deformation, friction between interlaced loops at higher strains where the matrix has been ejected, and lockup at a critical value of the local strain, which triggers displacement elsewhere in the specimen.

Levels of energy absorption currently achieved reach approximately 40 MJ/m<sup>3</sup> or 25 J/g. With optimization, levels of 120 – 200 MJ/m<sup>3</sup> or 75 – 130 J/g seem feasible.

The knitting process is straightforward and ought to be amenable to automation and low-cost production.

### Acknowledgments

Work supported by the U.S. Army Research Office, Contract No. DAAH04-95-C-0050. The authors are very pleased to record the enthusiasm, patience, and skilful handicraft of Noemi Altamirano, Christian Berg, Jenny Garredo, Rachel Goldberg, Gloria Rios, Annalise Keen, and

Amber Sands, who made and tested a large number of specimens for this study. Helpful discussions with Drs. Sridhar Narayanaswamy and Frank Zok are gratefully acknowledged.

## REFERENCES

1. B. N. Cox, "Lockup, Chains, and the Delocalization of Damage," *J. Mater. Sci.*, **30**, 4871-4881 (1996).
2. X. Gong, F. Zok, B. N. Cox, and J. Davis, "The Mechanics of Delocalization and Energy Absorption in Chain Composites," *Acta Materialia*, in press.
3. B. N. Cox, J. Davis, N. Sridhar, F. Zok, and X. Gong, "The Energy Absorption Potential of Chain Composites," *Acta Materialia*, in press.
4. B. N. Cox and J. B. Davis, "Braided Composites for Energy Absorption under Tensile Loading," submitted to *J. Mater. Sci.*
5. B. N. Cox and N. Sridhar, "Space Filling Chain Composites for Energy Absorption," to be submitted to *Acta Materialia*.
6. B. N. Cox, M. S. Dadkhah, and W. L. Morris, "On the Tensile Failure of 3D Woven Composites," *Composites* **27A**, 447-58 (1996).

**Table I. Specifications of Cords Used**

cord label	containment	yield <sup>(d)</sup> (mm/g)	cord radius <sup>(e)</sup> (mm)
S2 <sup>(a)</sup>	shrink wrap	277	1.064
S4 <sup>(b)</sup>	shrink wrap	264	1.089
S7 <sup>(c)</sup>	wound polyester	151	1.44

<sup>(a)</sup> formed from two dry Kevlar tows<sup>(b)</sup> formed from four Kevlar tows with approximately 3 weight percent resin binder<sup>(c)</sup> formed from seven Kevlar tows with approximately 3 weight percent resin binder<sup>(d)</sup> yield of all axial fibers taken together<sup>(e)</sup> for core of axial fibers only, assuming a fiber packing factor of 0.7**Table II. Composite Specifications and Properties**

specimen	KD112097	KN32598a	KN32598b	KN32598c	KN51198a
<b>cord</b>	S2	S4	S4	S4	S7
<b>features<sup>(a)</sup></b>					
<b>courses</b>	3	3	3	3	3
<b>layers</b>	2	2	2	2	2
<i>l<sub>y</sub></i> (mm)	35.6	31.5	38.1	30.5	32.3
<i>l<sub>z</sub></i> (mm)	9.1	8.4	9.4	8.1	8.4
<i>A<sub>cd</sub></i> (meas <sup>d)</sup> )	0.066	0.085	0.063	0.090	0.145
<i>V<sub>f</sub></i> (meas <sup>d)</sup> )	0.17	0.26	0.20	0.23	0.42
<b>failure<sup>(b)</sup></b>	del	del	del	loc	del
<b>peak stress (MPa)</b>	15	32	18	22	27
<b>peak cord stress (MPa)</b>	225	375	285	245	185
<b>strain at peak stress</b>	2.7	2.4	2.2	2.2	2.1
$\varepsilon_c^{(lb) (c)}$	1.66	1.66	1.66	1.66	1.55
$\varepsilon_c^{(ub) (c)}$	2.91	2.93	2.93	2.93	3.15
<b>strain at ultimate</b>	3.0	2.7	3.3	2.4	2.4
<b>W/volume</b> <i>W<sub>v</sub></i> (MJ/m <sup>3</sup> )	≈ 20	≈ 15	≈ 21	≈ 13	39
<b>W/mass</b> <i>W<sub>m</sub></i> (J/g)	13	10	13	8	25

<sup>(b)</sup> "del" = delocalized; "loc" = localized<sup>(c)</sup> Lower and upper bounds estimated in the text

**Table III. Estimates Friction Stress**

specimen	KD112097	KN32598a	KN32598b	KN32598c	KN51198a
$A_{cd}$ (displ <sup>t</sup> ) <sup>(a)</sup>	0.066	0.085	0.063	0.090	0.145
$\sigma_a$ (displ <sup>t</sup> ) (MPa)	8	17	8	10	17
$\sigma_{cd}$ (MPa)	120	200	125	110	120
$\tau_l = \tau_c$ (MPa) <sup>(b)</sup>	27	46	29	25	34

<sup>(a)</sup> Defined as the area fraction of the legs of cords after sufficient displacement has occurred to remove overlap of loops formed on alternate nails.

<sup>(b)</sup> From Eq. (8).

## Appendix A – Geometric Model of the Knitted Reinforcement

Here a geometric idealization of the knitted reinforcement is proposed and analytical estimates of fiber volume fractions and specimen dimensions are derived from it. The notation used was introduced in Section 2, with the additional assignment that  $d_z$  denotes the spacing of the knitted layers in the  $z$  direction or through-thickness direction (out of the plane of Fig. 1). If negligible excess resin is left after consolidation above and below the knitted fabric, then

$$d_z = \frac{t}{n} \quad (\text{A.1})$$

where  $t$  is the specimen thickness in the  $z$  direction and  $n$  is the number of layers..

The loci of the axes of the loops shown in Fig. 1 (e.g., those highlighted in bold) will be assumed to be as follows.

$n_{\text{loop}} = 2$ : In Fig. 1a, the axes of the crowns will be assumed to lie in the  $x - y$  plane ( $z = 0$ ). The axes of the legs will be assumed to rise linearly to  $z = 2r$  between the marked points P and Q and then return linearly to  $z = 0$  in a symmetric fashion (Fig. A.1). Thus one half of a leg makes an angle

$$\theta = \tan^{-1} \left[ \frac{4r \cos \alpha}{h} \right] \quad (n_{\text{loop}} = 2) \quad (\text{A.2})$$

where  $\alpha$  is the angle subtended by the  $x$ -axis and the projection of the leg on the  $x - y$  plane:

$$\alpha = \tan^{-1} \left[ \frac{2\rho - d_y}{2h} \right] . \quad (\text{A.3})$$

$n_{\text{loop}} = 3$ : In Fig. 1b, the axis of the crown at the top of the highlighted loop will be assumed to lie in the  $x - y$  plane ( $z = 0$ ). The adjoining leg segment will be assumed first to rise linearly to  $z = 4r$  between the points marked P and Q and then return linearly to  $z = 2r$  at point R. The crown

segment at the bottom of the highlighted loop will be assumed to lie in the plane  $z = 2r$ . Thus the upper and lower halves of the leg segment make angles

$$\left. \begin{aligned} \theta_1 &= \tan^{-1} \left[ \frac{8r \cos \alpha}{h} \right] \\ \theta_2 &= \tan^{-1} \left[ \frac{4r \cos \alpha}{h} \right] \end{aligned} \right\} \quad (n_{\text{loop}} = 3) \quad (\text{A.4})$$

to the  $x - y$  plane, respectively, with  $\alpha$  still given by Eq. (3).

With the geometry of the loops thus specified, the path length of the axis of one loop is given by

$$s = \begin{cases} 2\pi\rho + \frac{2h}{\cos \alpha \cos \theta} & (n_{\text{loop}} = 2) \\ 2\pi\rho + \frac{h}{\cos \alpha \cos \theta_1} + \frac{h}{\cos \alpha \cos \theta_2} & (n_{\text{loop}} = 3) \end{cases} \quad (\text{A.5})$$

Since the knitted structure is periodic, a representative volume,  $V$ , can be associated with each loop as its share of the total volume of the composite. The loops are separated by one nail spacing,  $d_x$ , in the  $x$  direction and two nail spacings,  $2d_y$ , in the  $y$  direction. Therefore,

$$V = 2d_x d_y d_z \quad . \quad (\text{A.6})$$

The total volume fraction of the composite occupied by the knitted cords (including the matrix or void space within them) is given by

$$V_{\text{cd}} = \frac{\pi r^2 s}{V} \quad . \quad (\text{A.7})$$

The volume fraction of the aligned reinforcing fibers alone can be written

$$V_f = fV_{cd} \quad (A.8a)$$

where the packing factor,  $f$ , can be written

$$f = \frac{\pi r^2}{y_f \rho_f} \quad (A.8b)$$

with  $y_f$  the yield (length per unit mass) of the aligned fiber tows in the cord and  $\rho_f$  the density of the fibers.

It remains to specify  $\rho$ ,  $h$ , and  $d_z$ . From inspection of Fig. 1

$$n_{loop} d_x = 2(\rho - r - r_n) + h \quad (A.9)$$

where  $r_n$  is the radius of a nail. A practical estimate of  $\rho$  is

$$\rho \approx r_n + 3r \quad (A.10)$$

which follows from assuming that a crown must encompass a nail and two legs of an interpenetrating loop. Equation (1) provides a value for  $d_z$ , but requires a measurement of the final composite thickness. When this is unavailable,  $d_z$  can be estimated from Fig. A.1:

$$d_z \approx 2n_{loop}r \quad (n_{loop} = 2 \text{ or } 3). \quad (A.11)$$

This expression assumes no compaction in the  $z$  direction and, all else being equal, will lead to underestimates of the volume fraction of the reinforcement.

Specimen dimensions and volume and area fractions predicted by the above results are compared with experimental measurements in Table A.1. The model fares reasonably well. Discrepancies in the lateral dimensions reflect the degree of compaction achieved following removal of the

knitted fabric from the bed of nails. In most cases, the fabric is compacted in the  $y$  direction and swells in the  $z$  direction in compensation. The discrepancies in the predicted and measured area fractions are in direct proportion to the differences in the product  $l_y l_z$ . Further differences arise in the volume fractions, because of the manner in which the experimental volume fraction was determined. This was by measuring the total length of cord that was knitted into the specimen. However, the distribution of cord is not uniform along the specimen, because the knitting pattern is disrupted at the specimen ends. Additional non-knitted loops are added there to build up the fabric thickness, but these may consume a greater or lesser proportion of cord, depending on their details.

**Table A.1. Predicted and measured dimensions and area and volume fractions.**

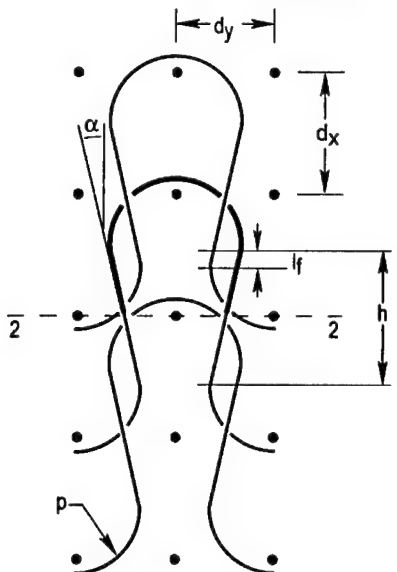
<b>specimen</b>	KD112097	KN32598a	KN32598b	KN32598c	KN51198a
$l_y$ (mm) (meas <sup>d.</sup> )	35.6	31.5	38.1	30.5	32.3
$l_z$ (mm) (meas <sup>d.</sup> )	9.1	8.4	9.4	8.1	8.4
$l_y$ (mm) (model)	45.5	45.6	45.6	45.6	47
$l_z$ (mm) (model)	6.4	6.5	6.5	6.5	8.6
$A_{cd}$ (meas <sup>d.</sup> )	0.066	0.085	0.063	0.090	0.145
$A_{cd}$ (model)	0.073	0.076	0.076	0.076	0.097
$V_f$ (meas <sup>d.</sup> )	0.17	0.26	0.20	0.23	0.42
$V_f$ (model)	0.24	0.25	0.25	0.25	0.35

## FIGURE CAPTIONS

1. Schematics of weft knits with large strain capacity. (a) Loop length twice loop spacing.  
(b) Loop length three times loop spacing.
2. Bed of nails (viewed from above) and mold components (male under fabric; female to right) for forming and consolidating knitted composites.
3. Schematic of the motion by which a weft knit fabric is formed over a bed of nails.
4. Typical knitted composite specimens. (a) untested knit made from commercial sheathed Kevlar; (b) untested knit made with cord S4 of Table I and wound around with additional Kevlar tows to inhibit matrix loss.
5. Variation of the volume fraction of knitted cords,  $V_c$ , with nail spacings,  $d_x$ , and  $d_y$ , for  $r_n = r$  and two choices of the radius of curvature of crowns,  $\rho$ .
6. A knitted specimen after ultimate failure following delocalized damage to a high strain level. The undamaged cords are locked up and drawn tightly together in knots.
7. Engineering stress-engineering strain data for the specimens of Table I.
8. Contact between segments of two interpenetrating knitted loops.

A.1. Idealization of the locus of a loop projected onto the  $x - z$  plane: (a)  $n_{loop} = 2$  and (b)  $n_{loop} = 3$ .

(a)



(b)

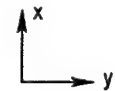
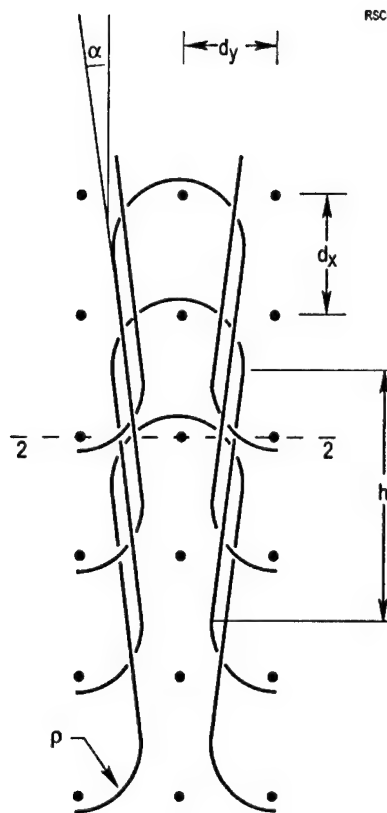


Figure 1

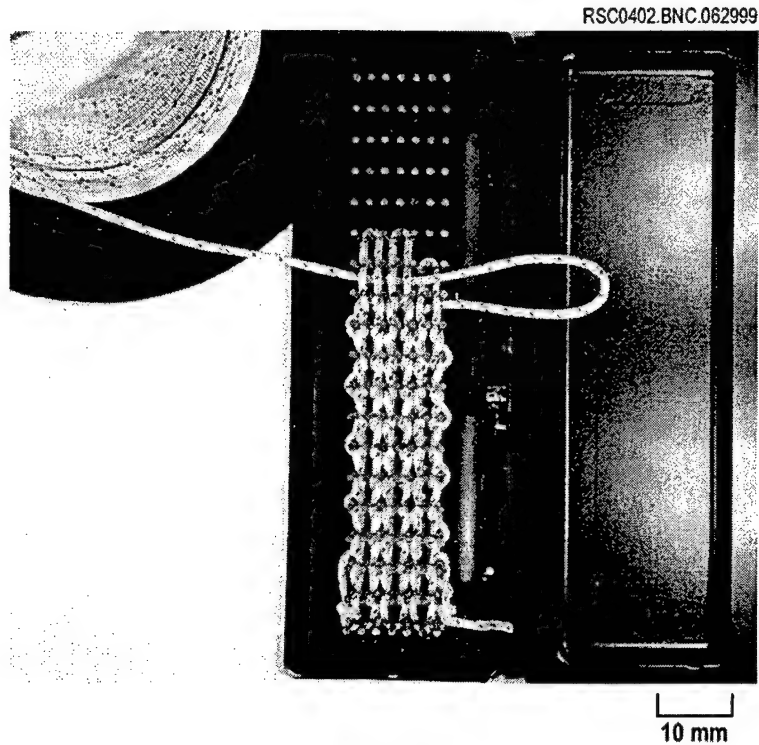


Figure 2

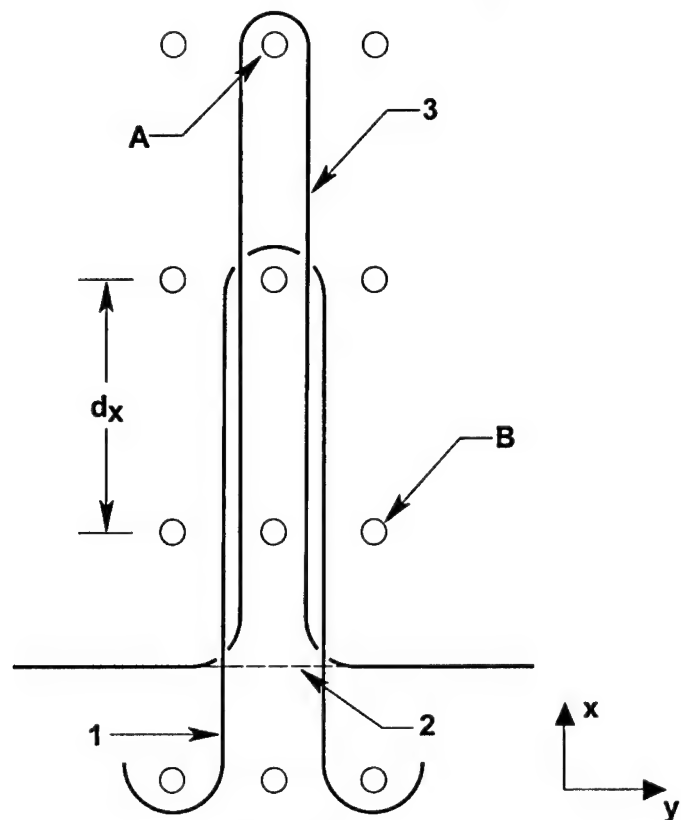
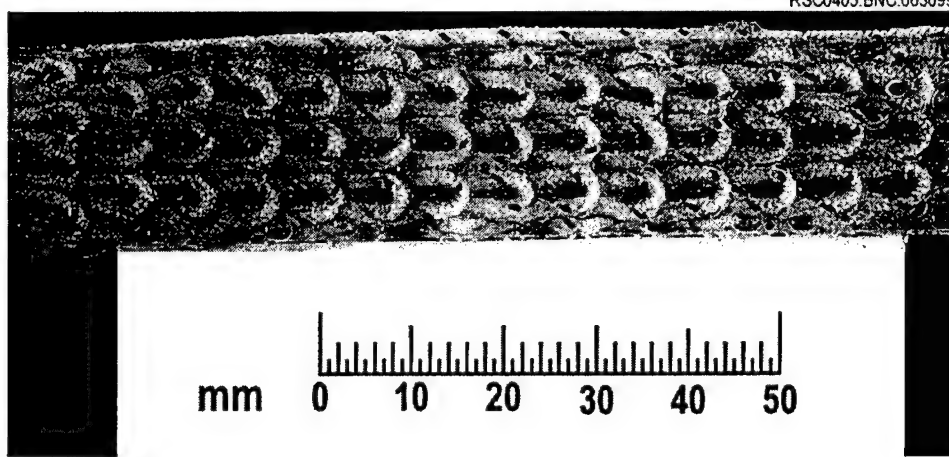


Figure 3

(a)



(b)

RSC0404.BNC.062999

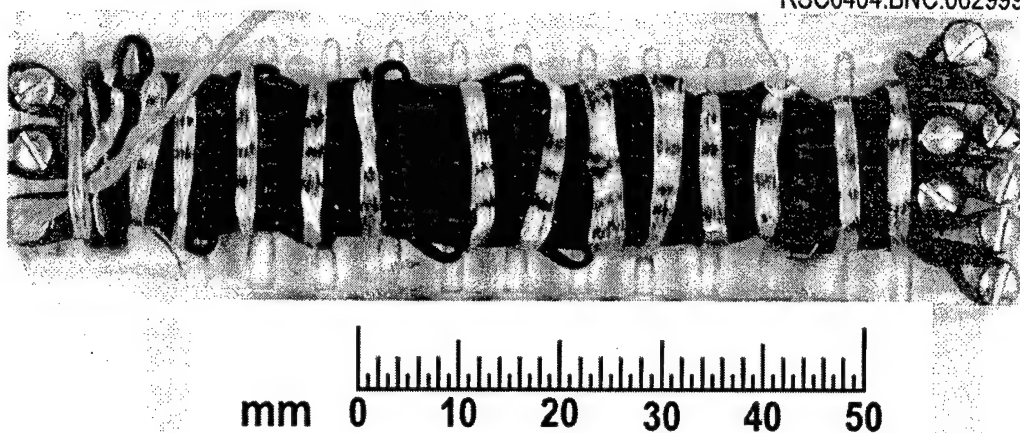


Figure 4

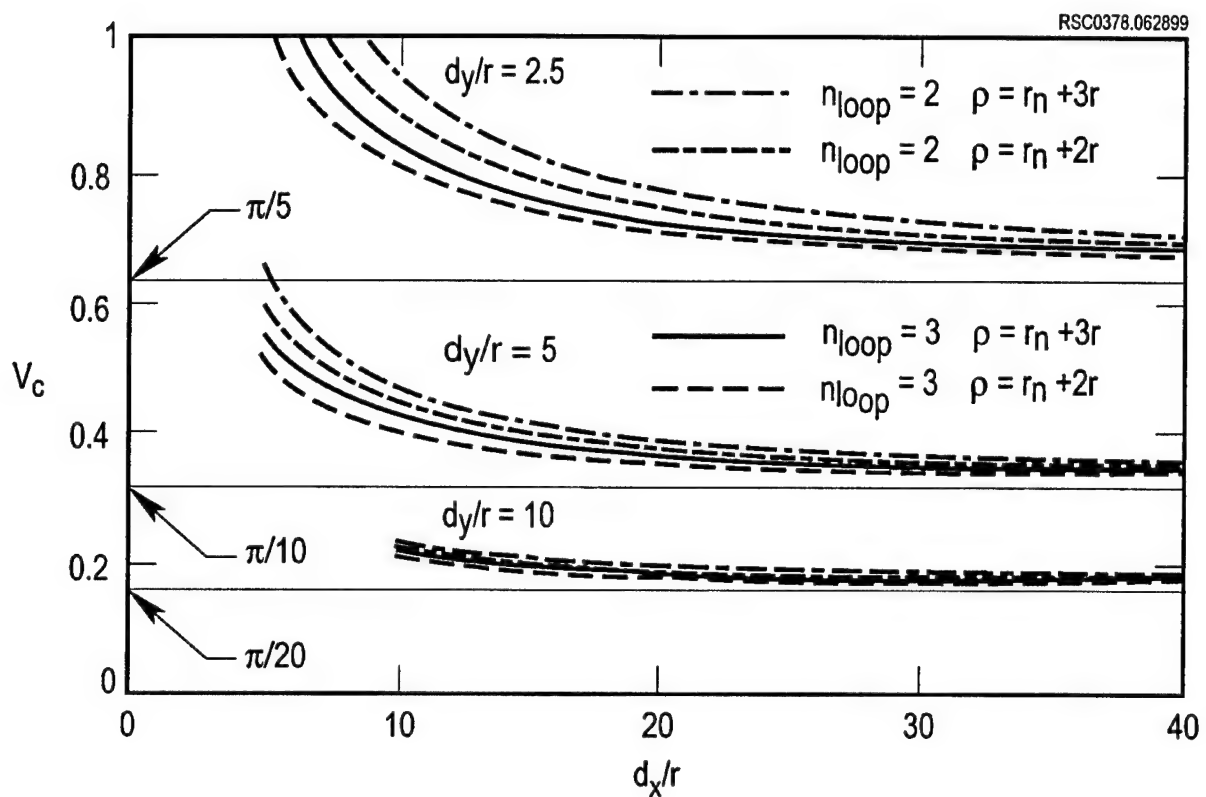


Figure 5

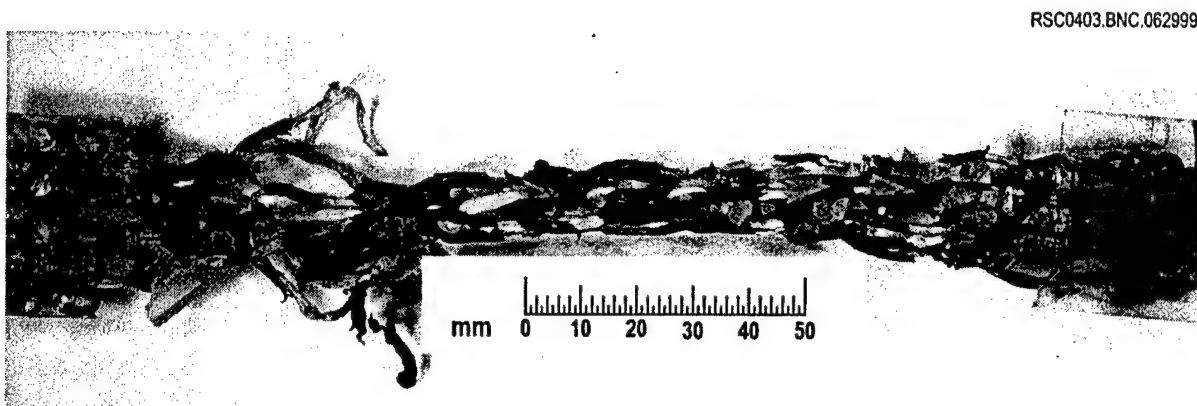


Figure 6

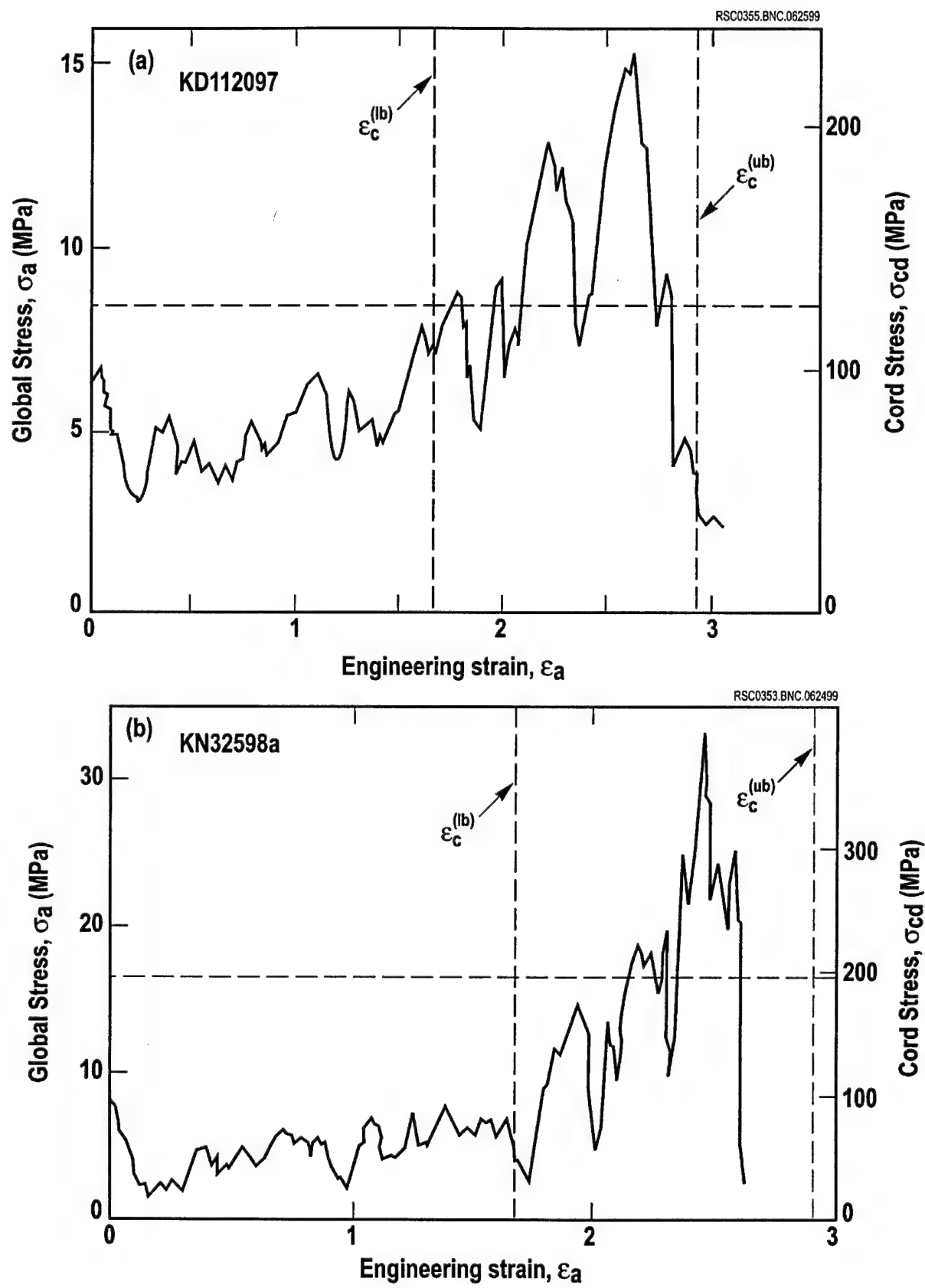


Figure 7

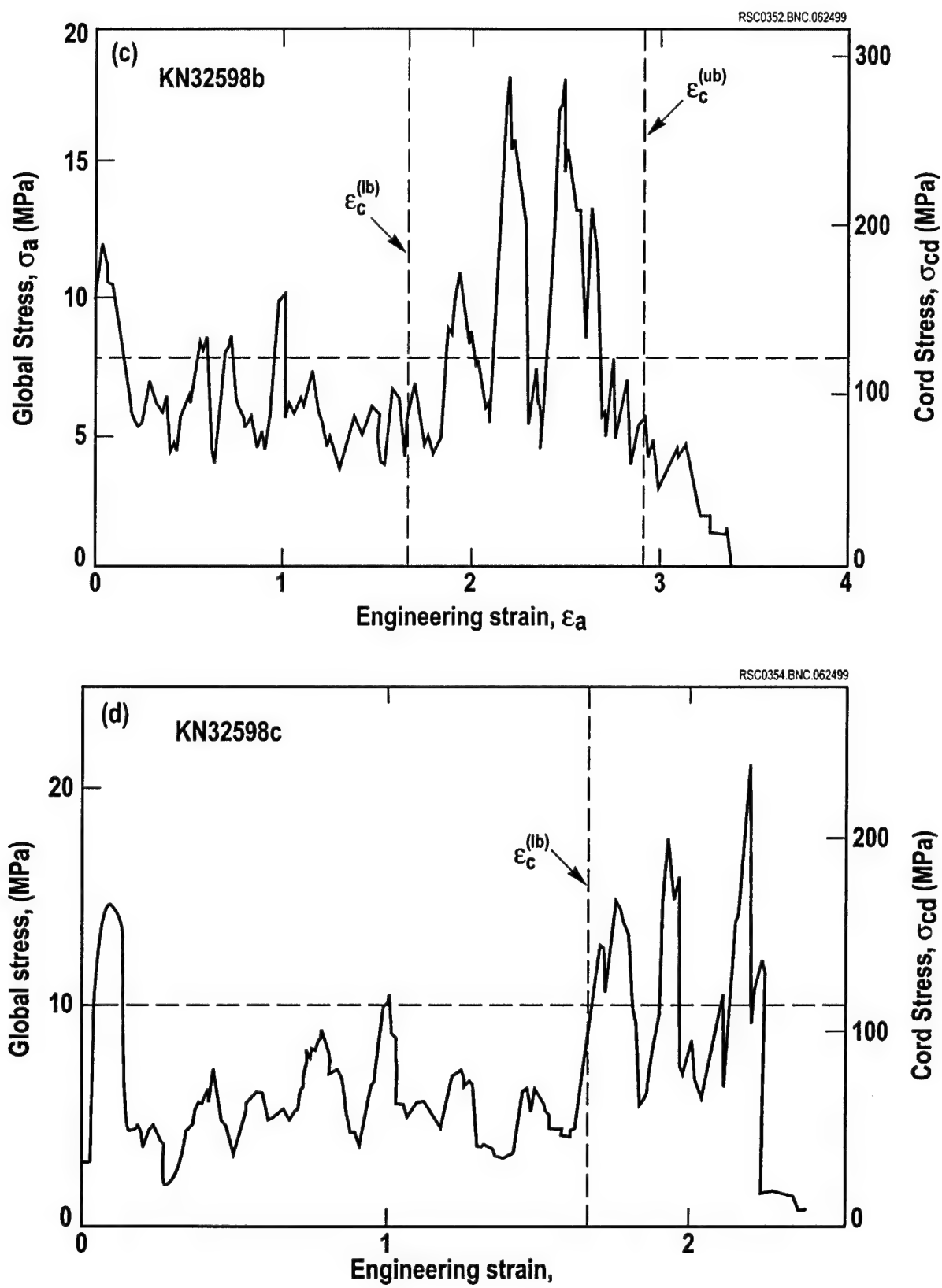


Figure 7 (continued)

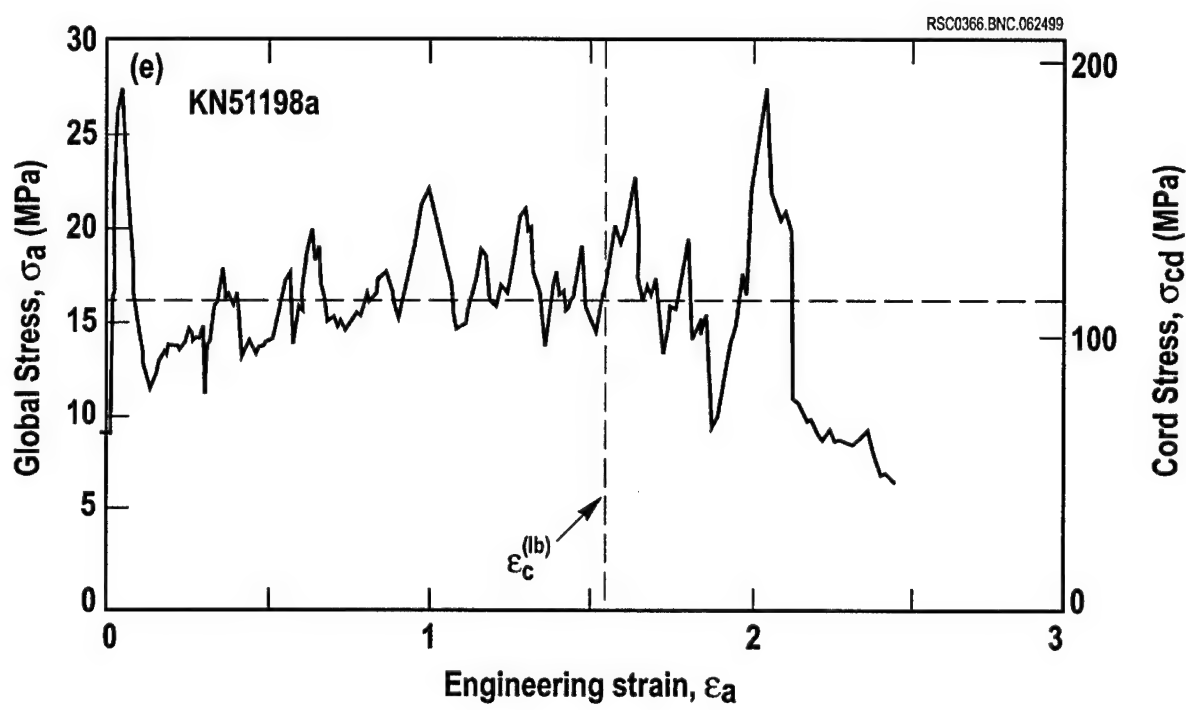


Figure 7 (completed)

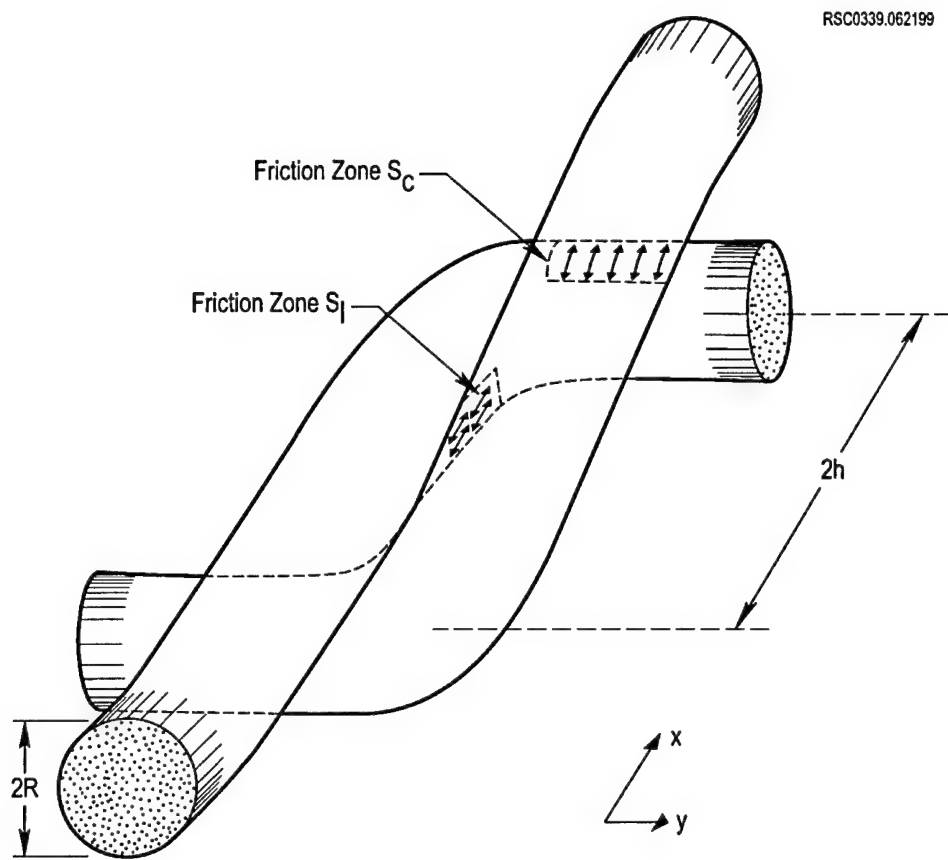


Figure 8

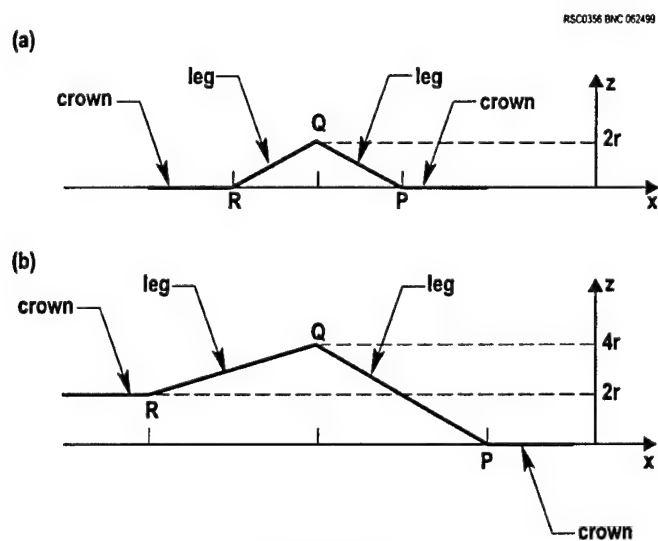


Figure A.1

# **Rockwell Science Center**

## **THE BINARY MODEL – A COMPUTATIONAL APPROACH TO TEXTILE COMPOSITES**

**B. N. Cox**

Rockwell Science Center, LLC  
1049 Camino Dos Rios  
Thousand Oaks, CA 91360  
U.S.A.

**R. M. McMeeking and M. A. McGlockton**

Department of Mechanical Engineering  
University of California, Santa Barbara  
Santa Barbara, CA 93106  
U.S.A.

# THE BINARY MODEL – A COMPUTATIONAL APPROACH TO TEXTILE COMPOSITES

B. N. Cox <sup>1\*</sup>, R. M. McMeeking <sup>2</sup>, and M. A. McGlockton <sup>2</sup>

<sup>1</sup>Rockwell Science Center, 1049 Camino Dos Rios, Thousand Oaks, CA 91360, U.S.A.

<sup>2</sup>Department of Mechanical and Environmental Engineering, University of California, Santa Barbara, Santa Barbara, CA 93106, U.S.A.

**SUMMARY:** This paper describes the development of a computer code called the Binary Model for modeling textile composites. The model has the features that it needs no assumption of periodicity in the textile structure, can deal with significant volumes of a structure (typically  $\sim 10^3 - 10^4 \text{ mm}^3$ ), treats arbitrary external loads including loads with large spatial gradients, invokes arbitrary nonlinear constitutive laws, and, in its most recent version, computes thermal strains and temperature distributions as well as stress distributions. Here the formulation of the model is reviewed and some of its capabilities are illustrated by computations of the effects of random disorder in the textile structure on stress distribution in the elastic regime and simulations of the progression to ultimate failure in a textile composite in which some unusual failure phenomena are known to occur.

**KEYWORDS:** textiles, computational models, nonlinearity, failure, structural modeling

## INTRODUCTION

One of the most challenging and interesting problems in textile composites is calculating in a tractably efficient scheme the distribution of loads among the constituent fiber tows. Because of the geometrical complexity of the tow arrangements, the structure is generally nonperiodic; or, if it is periodic, the unit cell (repeating unit) typically contains tens or hundreds of tow segments [1]. It is not feasible to represent each of these tow segments by a large number of finite elements to ensure accuracy of local stresses in all their detail and then solve for the whole system. Therefore, conventional finite element gridding methods are not applicable. On the other hand, many of the failure mechanisms in textile composites involve the failure of single tows, so the

---

\* Currently EPSRC Visitor, Engineering Department., Cambridge University, Trumpington Street, Cambridge CB2 1PZ, England.

physics of failure cannot be represented faithfully if stresses are averaged over distances larger than a tow diameter; i.e., the material cannot be homogenized over gauge lengths exceeding the tow diameter.

Models of the interaction of observed local failure mechanisms must be based on the most efficient finite element formulation possible that distinguishes individual tows while representing their three-dimensional pattern of interlacing correctly. One such model, called the Binary Model, has been developed for work on polymer and ceramic composites. The Binary Model is a finite element formulation in which the geometry of the 3D textile architecture is represented in one-to-one correspondence, while the element size is chosen to be sufficiently coarse to enable experimentally significant volumes of a 3D textile to be simulated [2,3]. By careful definition of the elements' constitutive properties, the mechanics of deformation can be made approximately independent of the choice of element size.

The Binary Model assigns a string of one-dimensional elements to each tow, which represent the tow's axial stiffness. The tow elements are embedded in solid, so-called effective medium elements, which represent matrix dominated composite properties, including transverse stiffness, shear stiffness, and Poisson's effect. Figure 1 shows tow elements representing stuffers, fillers, and warp weavers in a through-the-thickness angle interlock weave. The tow elements are located along a path corresponding to the axis of the tow they represent in the actual composite. A single stuffer or filler element extends a distance equal to the centre-to-centre separation of neighbouring tows. The warp weavers are idealized as following saw-tooth paths in the model depicted, with a single element extending through the thickness.

As shown in Fig. 1, an effective medium element also usually extends in any direction from the centre of one tow to the centre of one of its neighbours. It therefore represents a volume of material containing fragments of more than one tow, usually with different orientations. In interlock weaves, effective medium elements are conveniently defined as eight-noded cuboidal elements containing eight Gaussian quadrature points and whose vertices coincide in the elastic regime with the nodes of either stuffer or filler tow elements.

In its most general formulation, the Binary Model can deal with nonlinearity due to distributed damage, such as microcracking and plasticity, as well as tow rupture, shear load transfer around tow breaks, and tow pullout. These are all essential mechanisms in the ultimate tensile failure of interlock weaves. The model is often used to execute Monte Carlo simulations of specimens or structures, with the strength and spatial distribution of a large number of flaws assigned according to various trial distribution laws. Such simulations offer considerable insight into the statistical nature of damage development in textile composites.

## THE ELASTIC REGIME

A short segment of a tow in a textile composite is effectively a unidirectional composite. Therefore, constitutive laws for tow and effective medium elements in the elastic regime can be defined in terms of the properties expected for a unidirectional composite [3], which can be calculated a priori from the properties of the constituent fibers and matrix using micromechanical models available in the literature. In assigning volumes to tow segments and fiber volume

fractions in this process, the most important constraint is that the total count of fibers in the entire composite and their orientations should be correct. The assignments should therefore usually involve an experimental measurement of the total fiber volume fraction as a check on weaver's specifications, which are often an inaccurate representation of the processed composite [3].

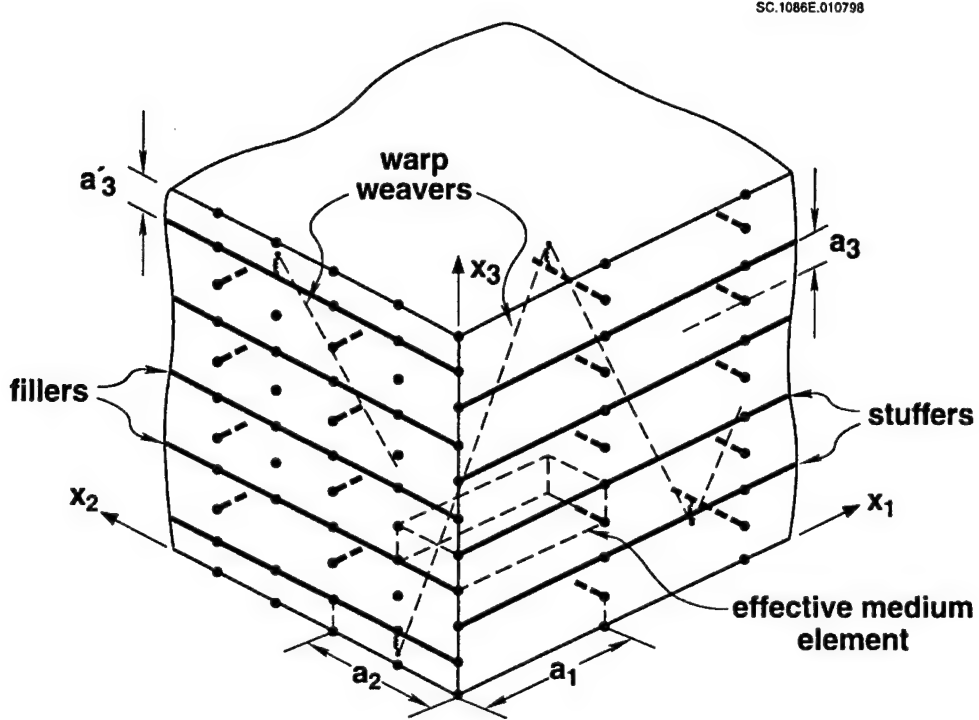


Fig. 1: Small part of a Binary Model element array for a simulation of a through-the-thickness angle interlock weave. All tow elements are shown but only one representative effective medium element.

Since effective medium elements usually extend from the centre of one tow to the centres of its neighbors in the textile composite (e.g., Fig. 1), each effective medium element represents fragments of different tows with generally different orientations. Nevertheless, since the effective medium elements represent only those components of elasticity that are matrix dominated (shear and transverse stiffness and local Poisson's effects), their properties may be assigned by approximate rules without compromising predictions for the textile composite. For example, with  $(x, y, z)$  a local coordinate system aligned so that the  $x$ -axis is parallel to the fiber direction in a unidirectional composite segment and  $(x_1, x_2, x_3)$  a global coordinate system defined as shown in Fig. 1, the engineering elastic constants of effective medium elements can be defined for the interlock weave of Fig. 1 by

$$E_1^{(m)} = E_2^{(m)} = E_3^{(m)} = E_y^{(UD)}$$

$$G_{12}^{(m)} = G_{xy}^{(UD)}; G_{23}^{(m)} = \frac{(p_f G_{xy}^{(UD)} + p_s G_{yz}^{(UD)})}{p_s + p_f}; G_{31}^{(m)} = \frac{(p_s G_{xy}^{(UD)} + p_f G_{yz}^{(UD)})}{p_s + p_f}$$

$$\nu_{12}^{(m)} = \nu_{xy}^{(UD)}; \nu_{23}^{(m)} = \frac{(p_f \nu_{xy}^{(UD)} + p_s \nu_{yx}^{(UD)})}{p_s + p_f}; \nu_{13}^{(m)} = \frac{(p_s \nu_{xy}^{(UD)} + p_f \nu_{yx}^{(UD)})}{p_s + p_f} \quad (1)$$

where  $p_s$  and  $p_f$  are the proportions of the effective medium element comprised of stuffer and filler tows and the superscripts “m” and “UD” denote properties of the effective medium element and unidirectional composite respectively. The component of stiffness for the UD composite chosen to define the contribution of a stuffer or filler to a component of elasticity for the effective medium element depends on the orientation of the stuffer or filler fragment with respect to the global coordinate system.<sup>1</sup> In angle interlock composites, the warp weaver tows occupy a relatively small fraction of the composite volume and may be neglected in defining the effective medium elements. The spring constants for stuffer and filler tow elements are prescribed by

$$k_s = D_s (E_x^{(UD)} - E_y^{(UD)}); k_f = D_f (E_x^{(UD)} - E_y^{(UD)}); k_w = D_w (E_x^{(UD)} - E_y^{(UD)}) \quad (2)$$

where  $D_s$ ,  $D_f$ , and  $D_w$  are the effective cross-sectional areas of the stuffer, filler and warp weaver tows, computed so as to preserve total fiber volume counts. Since the effective medium elements fill all space while the tow elements are one-dimensional line elements (zero volume), the term  $E_y^{(UD)}$  must be subtracted to avoid double counting of stiffness.

In the example of the angle interlock weave depicted in Fig. 1, in-plane composite moduli and Poisson’s ratios will be dominated by the axial extension of fibers in the stuffers and fillers and therefore by the properties of the tow elements. Thus the definition of in-plane shear moduli and Poisson’s ratios for the effective medium elements cannot be too critical to overall in-plane properties. In a well-designed composite, a significant fraction of all fibers will be aligned with any anticipated large load and therefore the Binary Model is assured to give reasonable estimates of the composite response to such loads. However, other loads, which may be minor but still important as design limits, such as through-thickness loads in the interlock composite of Fig. 1, may not be aligned with large numbers of fibers. Details in the assignment of the effective medium element properties are then more important.

Extensive comparisons have been made of the predictions of the Binary Model for interlock weaves with experimental measurements of stiffness components and the predictions of a simple, analytical model based on assuming isostain conditions throughout the composite [4]. The Binary Model agrees well with the experimental data in all elasticity components. It also agrees well with the isostain model for the in-plane stiffness components, which is to be expected since these correspond to aligned loading, where near isostain conditions will hold to a good approximation. But significant differences with the isostain model are found for the through-thickness modulus and other stiffness components.

If the tows in the textile composite are assumed in the models to be ideally straight (as depicted in Fig. 1), then there are also consistent discrepancies with experiment due to the fact that tows in

---

<sup>1</sup> Eq. (1) corresponds to assuming that isostain conditions hold within a single effective medium element. For shear, one might prefer to assume isostress and Eq. (1) would be replaced by capacitance type laws (proportions of inverses).

the real composites are wavy and otherwise irregular. Irregularity is an inevitable feature of textile composites, due to the rigours of textile manufacturing processes. The effects of irregularity can easily be studied using the Binary Model.

Large scale irregularity in the positioning of tows can be replicated in the Binary Model by offsetting tow element nodes. The offsets can be chosen in a Monte Carlo simulation according to any prescribed distributions. The effects of small-scale irregularities (over scales less than the tow element length) can be incorporated by modifying the constitutive laws for tow elements. Some illustrations of the effects of large-scale irregularities in the elastic regime are shown in Fig. 2. This figure shows statistical inferences presented as cumulative probability distributions from large numbers of Monte Carlo simulations of specimens of dimensions approximately 10x 15 x 50 mm. In the simulations, the positions of the nodes of stuffer elements were offset in the direction  $x_3$  to mimic the waviness observed in the through-thickness direction in angle interlock composites. The nodal offsets were chosen at random so that the stuffer elements deviated in alignment from the direction  $x_1$  by an angle  $\xi$  that followed a normal distribution with mean zero and deviance  $\sigma_\xi$ . Figure 2a shows how the axial stress in tow elements was distributed for different values of  $\sigma_\xi$ . There is some variance in the axial stress even when  $\sigma_\xi = 0$  (ideal geometry), because the warp weaver tows break the symmetry of the composite. But much greater variance exists when irregularity typical of that observed in interlock weaves is present ( $\sigma_\xi$  up to approximately 5° [4]).

Information is also available about stress variations in the effective medium elements, which can be interpreted as representing stress components in particular tows in the composite. For example, the shear stress component  $\sigma_{13}$  evaluated at the Gaussian quadrature points in the effective medium elements that surround a particular stuffer tow element and are closest to the stuffer tow element reveals the axial shear stress in the corresponding stuffer segment in the composite. Figure 2b shows cumulative probability distributions for this axial shear stress component for the simulations in which stuffer nodes were offset to mimic irregularity. Once again there is variance even when  $\sigma_\xi = 0$  (ideal geometry), due to the effect of warp weavers, but far higher variance ensues from irregularity, as tow elements become more or less aligned with the load axis. The axial shear stress in a tow segment is especially important in compressive failure, since it triggers kink band formation, which is the dominant compressive failure mechanism [5]. Figure 2b demonstrates that initial tow misalignment dominates the determination of compressive strength, rather than load-sharing interactions between tows of different type (represented by the results for  $\sigma_\xi = 0$ ), in angle interlock weaves.

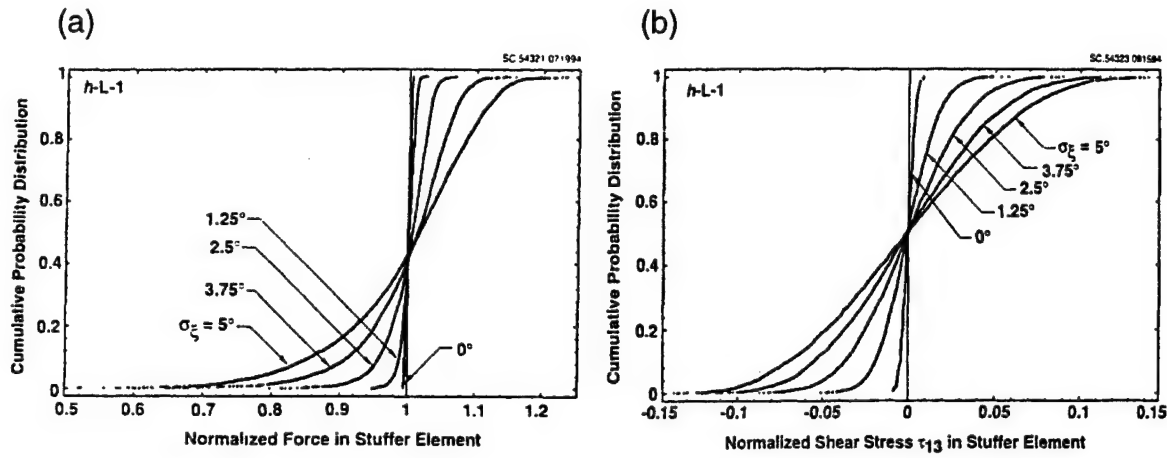


Fig. 2: Distributions of local stresses in an angle interlock weave in which stuffer segments are randomly misaligned (from [3]). (a) The axial stress and (b) the axial shear stress in stuffer segments.

## SIMULATIONS OF ULTIMATE FAILURE IN POLYMER COMPOSITES

Under tensile loads, 3D interlock weaves fail by the rupture of the aligned, primary load-bearing tows. The ultimate strengths are satisfactory from the point of view of engineering applications, with 1 GPa easily attained with fairly balanced proportions of stuffers and fillers. But the most remarkable property is the work of fracture in tension, which has been measured in the range  $0.4 - 1.1 \text{ MJm}^{-2}$  [6]. This is considerably higher than values for the toughest metal alloys ( $< 200 \text{ kJm}^{-2}$ ) or tape laminates ( $< 150 \text{ kJm}^{-2}$ ) [7]. Such large values of work of fracture point to many applications for 3D interlock weaves where high damage tolerance is demanded, including armour and explosion containment.

The high work of fracture is associated with the ability of specimens to bear loads near the peak load,  $\sim 1 \text{ GPa}$ , at strains of up to  $3 - 4\%$ , which significantly exceed the nominal failure strain of the tows ( $\approx 1.5\%$ ) [6]. Destructive examination of specimens at strains exceeding  $1.5\%$  reveals that all or at least most of the primary load bearing tows are ruptured, even though the composite stress at the time of interrupting the test was  $\sim 1 \text{ GPa}$ . Thus some unusually effective mechanism exists for transferring load from one end of a specimen to the other past sites of tow rupture. The mechanism of load transfer was conjectured in prior work to involve the locking up of sliding, load-bearing tows against one another. The effectiveness of the lockup could be enhanced by the contact of asperities on tows under the constraining influence of the warp weaver tows [6].

Along with lockup, the spatial distribution of the sites of tow rupture must also have an important role. If, for example, all load-bearing tows rupture on a single plane, then the specimen must fail catastrophically at modest strain. Spatially distributed tow breaks will in contrast favour ductility and high work of fracture.

The Binary Model can be generalized to deal with nonlinearity due to distributed damage, such as microcracking and plasticity, as well as tow rupture, shear load transfer around tow breaks, and tow pullout [8]. These are the essential mechanisms in the ultimate tensile failure of

interlock weaves. The generalized model can be used to execute Monte Carlo simulations of the entire gauge sections of the specimens that were previously tested. Within each Monte Carlo simulation, the strengths and locations of flaws are assigned according to various trial distribution laws. The simulation then predicts the full test life of the specimen.

Sliding and load transfer effects around a broken stuffer are simulated in the Binary Model by allowing the stuffer tow elements near a break to displace relative to the surrounding effective medium nodes and applying opposing friction forces to the displaced nodes (Fig. 3). When the broken tow slides in the real composite, its irregular features push the composite apart in the through-thickness direction. This effect is reproduced in the model by introducing a dilation strain,  $\varepsilon_s$ , in the through-thickness direction that is proportional to the computed sliding displacement,  $u_1$ , of the  $i^{\text{th}}$  stuffer element:

$$\varepsilon_3^{(i)} = \eta u_1^{(i)} \quad (3)$$

where  $\eta$  is a geometrical factor proportional to the misalignment of the stuffer segment. The constitutive law for the neighbouring effective medium elements is then modified to introduce  $\varepsilon_s$  as a stress-free eigenstrain:

$$\sigma_{ij}^{(m)} = C_{ijkl}^{(m)} (\varepsilon_{kl}^{(m)} - \varepsilon_s^{(i)} \delta_{k3} \delta_{l3}) \quad (4)$$

where  $\sigma^{(m)}$ ,  $\varepsilon^{(m)}$ , and  $C^{(m)}$  are the stress, strain, and stiffness tensors for the effective medium element, the last defined consistently with Eq. (1). In the next step of the simulation, the Binary Model computes the local stress component,  $\sigma_3$ , in the through-thickness direction in the effective medium elements surrounding the sliding stuffer element. Because the warp weavers constrain dilation in the through-thickness direction (until they break), the computed stress will usually be compressive, with a magnitude that increases with the sliding displacement. Friction forces will imply a stress differential,  $\Delta\sigma_1$ , between the two ends of a sliding stuffer element, which is introduced into the model as a force,  $Q_s$ , imposed at one end of the stuffer element and to the corresponding effective medium element (Fig. 3). Assuming Coulomb friction, the friction force will have the magnitude

$$Q_s^{(i)} = r \mu |\sigma_3^{(i)}| \quad (5)$$

where  $\mu$  is a friction coefficient and  $r$  is a geometrical factor that can be so defined as to make the outcome independent of the choice of the stuffer element size [2,8].

Simulated stress-strain curves and other fracture characteristics have been reported in detail elsewhere for various distributions of the strength and location of flaws in stuffers [8]. Generally, stuffer rupture events occur over a range of applied strains, which increases in breadth when flaws are more broadly distributed in strength. At some critical strain, every stuffer is broken and the slip zones emanating from the rupture sites all cross a single plane normal to the load axis. At this point, further global load increase is impossible: the rupture sites define the ultimate failure surface and there is typically a large drop in the applied load, the so-called primary load drop, as seen in experiments. Only small loads remain, corresponding to the pullout of stuffers in the

absence of the constraining influence of the warp weavers, which are always broken following the primary load drop.

If the stuffer flaws are distributed in space according to a Poisson process, then the large strains measured in some experiments after stuffer rupture but before the primary load drop cannot be replicated, whatever the distribution of flaws in strength. Neither can large strains before primary load drop be achieved if flaws are associated with particular sites in the interlock architecture (such as stuffer segments adjacent to the turning points of warp weavers) if these sites are also fairly uniformly distributed throughout the composite.

However, if flaws are located preferentially on two or more planes normal to the load direction, then a failure sequence arises that is very similar to that observed experimentally. Stuffers tend to fail alternately first on one plane, then on the other, with no more than three or four successive failure events occurring on the same plane. Long slip zones and strong lockup effects develop, so that even after every stuffer has failed, the total load remains near the ultimate strength. A typical stress-strain curve for such a simulation is shown in Fig. 4a. The primary load drop follows the last point for which the load has been calculated.

In the simulation, the primary load drop occurs when the warp weavers reach their assigned failure strains. Thereupon, constraint is lost, the clamping stress around sliding stuffers falls to a small value, and the friction forces become much smaller. Experimental evidence supports this depiction of the controlling role of the warp weavers [6]. At small composite strains, prior to stuffer rupture, the composite is observed to contract in the through-thickness direction. After stuffer rupture, in contrast, it begins to swell and soon exhibits a negative Poisson's effect. In specimens sectioned before the primary load drop, the warp weavers are always found to be intact, whereas following the primary load drop, they have always failed [6]. The evolution of Poisson's ratio,  $\nu_{13}$ , through the simulation of Fig. 4a is shown in Fig. 4b. It corresponds well with experiment.

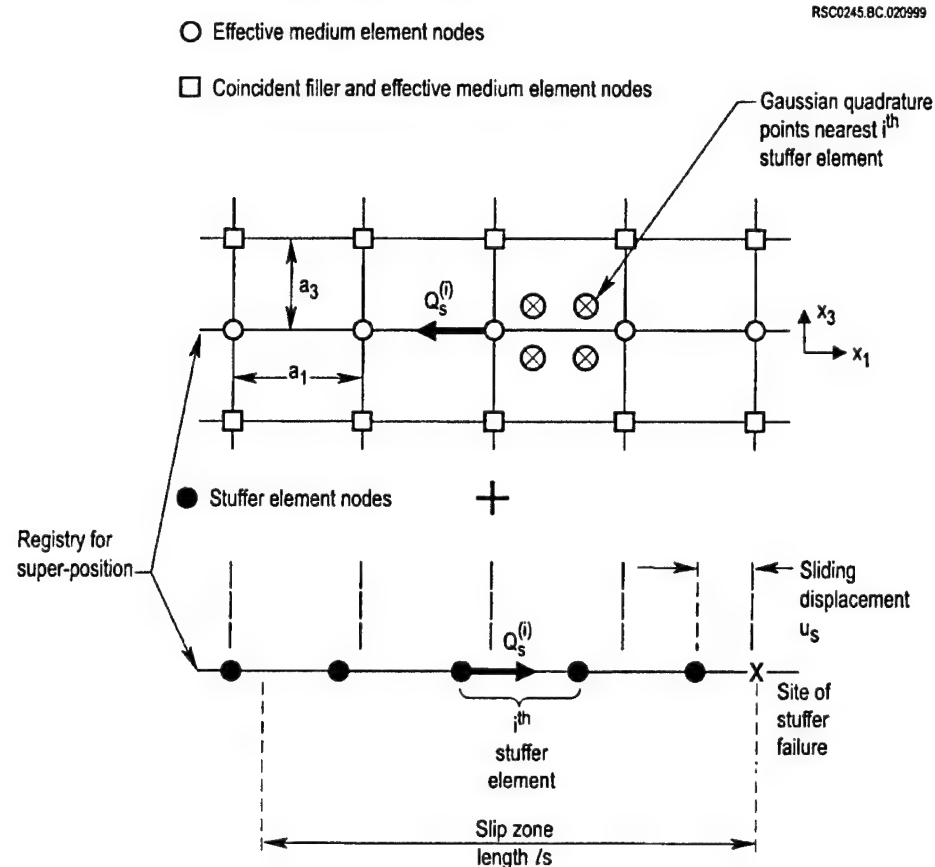


*Fig. 3: Schematic showing the separation of stuffer and effective medium nodes when a stuffer slides following rupture. The effective medium and stuffer elements are drawn separately but are superimposed in the model. The stuffer elements are sliding to the left away from the rupture. The sliding displacement disappears at the left end of the slip zone. Friction forces couple the displaced stuffer and effective medium nodes.*

While falling short of a rigorous proof, the Binary Model simulations quantify the roles of various material and geometrical factors in determining the work of fracture of the 3D interlock weaves. The highest values of work of fracture arise when high loads endure significantly beyond the failure strain of individual tows. This phenomenon has been shown to require an unusual spatial distribution of flaws in stuffers, as well as a strong lockup effect during the sliding of ruptured stuffers through the surrounding composite. The required spatial distribution of flaws is that planes of flaws should exist separated by 10 – 20 mm. The mechanism for the creation of such planes during the manufacture of a textile composite is unknown, but their existence is certainly feasible. For example, variations in tensioning or in the beating up of weft yarns during the weaving process can lead to bands of shear or buckling defects in the dry fiber preform. Furthermore, post-mortem studies of the specimens tested in [6] suggest that flaws populated planes or near-planes. For designing materials with the highest possible work of fracture, a systematic method of introducing flaws of known strength at preferred locations would be very useful.

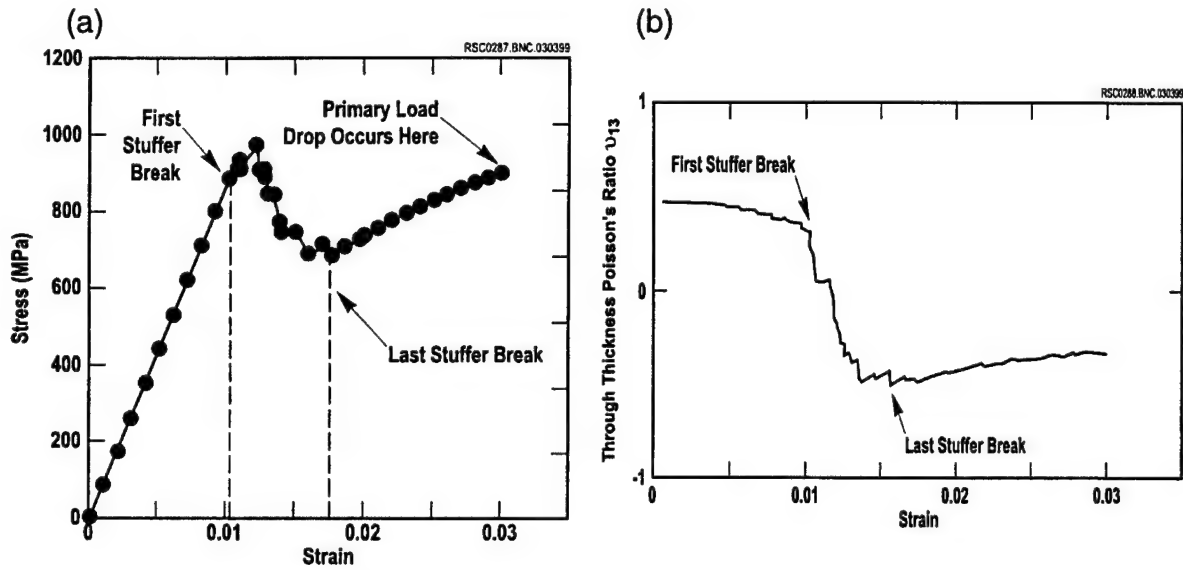


*Fig. 4: A simulation of the tensile rupture of an angle interlock composite, showing the effects of distributed flaws and a frictional lockup mechanism. (a) Tensile stress-strain curve up to the point of warp weaver failure. (b) Poisson's effect in the through-thickness direction.*

Regardless of the spatial distribution of flaws, the three-dimensional nature of the reinforcement in angle interlock weaves has a profound influence on the work of fracture through the lockup mechanism or enhanced friction. Even when high loads extend only slightly beyond the failure strain of individual tows, usefully large values of the work of fracture are obtained, which are attributable to high friction prior to the primary load drop and lesser but still substantial pullout loads following it.

## CONCLUDING REMARKS

The Binary Model has evolved through a number of research tasks carried out over the last six years into a powerful research tool. Grid generation routines are now available to set up complex textile architectures, including integrally formed structures created by weaving or other textile processes. The model appears currently to be unique in its ability to treat complex structures in which load distributions are nonuniform and either no periodicity exists or the repeating unit is very large.

Significant current effort exists in developing constitutive laws and model formulations to simulate ceramic composite structures that operate at high temperature. Constitutive laws are now available to deal with nonlinearity due to matrix microcracking, thermal strains, and damage modified thermal conductivity to solve coupled heat transfer and stress problems. The preferred approach to certifying the accuracy of the model in such complex material/structure problems is to validate results by direct comparison with full field measurements, for example of displacements and temperature fields.

## Acknowledgments

BNC was supported in the work on failure simulations by the Army Research Office, contract number DAAH04-95-C-0050.

## References

1. Cox, B. N., and Flanagan, G., "Handbook of Analytical Methods for Textile Composites," *NASA Langley Contractor Report*, 1996.
2. Cox, B. N., Carter, W. C., and Fleck, N. A., "A Binary Model of Textile Composites: I Formulation," *Acta Metall. Mater.*, 1994, **42**:3463-79.
3. Xu, J., Cox, B. N., McGlockton, M. A., and Carter, W. C., "A Binary Model of Textile Composites: II Elastic Regime," *Acta Metall. Mater.*, 1995, **43**:3511-24.
4. Cox, B. N., and Dadkhah, M. S., "The Macroscopic Elasticity of 3D Woven Composites," *J. Comp. Mater.* **29**[6], 785-819 (1995).
5. Argon, A. S., Fracture of composites, in *Treatise of Materials Sciences and Technology*, Vol. 1, Academic Press, New York, 1992.
6. Cox, B. N., Dadkhah, M. S., and Morris, W. L., "On the Tensile Failure of 3D Woven Composites," *Composites* **27A**, 447-58 (1996).
7. Ashby, M. F., *Cambridge Materials Selector*, Cambridge University Press, Cambridge, 1995.
8. McGlockton, M. A., Cox, B. N., and McMeeking, R. M., "A Binary Model of Textile Composites: III High Failure Strain and Work of Fracture in 3D Weaves," submitted to *J. Mech. Phys. Solids*.

# **Rockwell Science Center**

## **A BINARY MODEL OF TEXTILE COMPOSITES: III. HIGH FAILURE STRAIN AND WORK OF FRACTURE IN 3D WEAVES**

**M. A. McGlockton<sup>1</sup>, B. N. Cox<sup>2</sup>,  
and R. M. McMeeking<sup>1</sup>**

<sup>1</sup>Materials Department  
University of California, Santa Barbara  
Santa Barbara, CA 93106  
U. S. A.

<sup>2</sup>Rockwell Science Center, LLC  
1049 Camino Dos Rios  
Thousand Oaks, CA 91360  
U.S.A.

## ABSTRACT

Prior experiments have revealed exceptionally high values of the work of fracture (0.4 – 1.1 MJm<sup>-2</sup>) in carbon/epoxy 3D interlock woven composites. Detailed destructive examination of specimens suggested that much of the work of fracture arose when the specimens were strained well beyond the failure of individual tows yet still carried loads ~ 1 GPa. A mechanism of lockup amongst broken tows sliding across the final tensile fracture surface was suggested as the means by which high loads could still be transferred after tow failure. In this paper, the roles of weave architecture and the distribution of flaws in the mechanics of tow lockup are investigated by Monte Carlo simulations using the so-called Binary Model. The Binary Model was introduced previously as a finite element formulation specialized to the problem of simulating relatively large, three dimensional segments of textile composites, without any assumption of periodicity or other symmetry, and faithfully preserving the architecture and topology of the tow arrangement. The simulations are very successful in reproducing all aspects of measured stress-strain curves. They reveal that lockup can indeed account for high loads being sustained beyond tow failure, provided flaws in tows have certain spatial distributions. The importance of the interlock architecture in the phenomenon is highlighted.

## 1. Introduction

Woven composites with three-dimensional reinforcement have for some time been favored as candidates for applications requiring high in-plane stiffness with built-in delamination resistance. In 3D interlock weaves, warp tows (stuffers) and weft tows (fillers) are intended to be the primary load bearing tows for in-plane loads. In the interlock architecture, the stuffers and fillers form a coarse 0/90° laminate in which they can in principle be noncrimped, since they do not interlace with one another (Fig. 1). This confers the important advantage that the stuffer and filler fibers can be well aligned with in-plane loads, so that stiffness and strength are not compromised by fibers being misaligned at tow cross-over points, as they are, for example, in a two dimensional weave such as a plain or satin weave. The stuffers and fillers are approximately rectangular in cross-section in a consolidated composite, so that they can provide quite high total volume fractions of in-plane fibers. They are held together by warp weaver tows, which traverse from top to bottom of the stack of stuffer and filler layers, wrapping around fillers and so binding the whole stack together (Fig. 1). The warp weaver tows in a well fabricated interlock weave suppress delamination during compressive failure very effectively by resisting the deflection of delaminated stuffer and filler layers [Cox et al., 1992; Cox et al., 1994a; Cox, 1994].

While interlock weaves might be noncrimp weaves in principle, in practice all three sets of tows are distorted to some degree by the weaving process and subsequent consolidation into a composite. The geometric irregularity of the stuffers and fillers, in particular, has a measurable effect on the in-plane Young's moduli [Cox and Dadkhah, 1995] and a dominant effect on compressive strength [Cox et al., 1992; Cox et al., 1994a] and compression-compression fatigue life [Dadkhah et al., 1995]. Young's modulus is knocked down by up to 10% by the fact that segments of fiber bundles in a matrix are significantly softer when they are misaligned with the applied load so that the matrix experiences shear loading. The knockdown can be estimated quite well by averaging the effect of the misalignment of stuffers (for loading in the stuffer direction, for example)

over the whole composite via simple analytical approximations. Thus stiffness is sensitive to volume-averaged misalignments and insensitive to extremes of misalignment.

With delamination suppressed, compressive strength is determined by the mechanics of kink band formation, which occurs in isolated segments of the primary load bearing tows that happen to be unusually highly misaligned. The critical in-plane compressive load for kink formation in any tow segment depends inversely on the degree of its misalignment. Measurements of misalignment distributions lead to encouragingly accurate predictions of compressive strength [Cox et al., 1994a; Dadkhah et al., 1995]. Compression-compression fatigue failure also occurs via kink band formation and involves very similar micromechanics [Dadkhah et al., 1995]. Compressive strength and fatigue life are governed by extremes in the distribution of misalignments.

While stiffness, compressive strength, and compression-compression fatigue life are important and very interesting topics, perhaps the most striking and unexpected quality of 3D interlock weaves is their performance under tensile loads. Under tensile loads, 3D interlock weaves fail by the rupture of the aligned, primary load-bearing tows. The ultimate strengths are satisfactory from the point of view of engineering applications, with 1 GPa easily attained with fairly balanced proportions of stuffers and fillers. The strengths are approximately 30% less than might be expected from a tape laminate with a similar proportion of aligned fibers, suggesting some damage from the weaving process, but not an unacceptable degree. But the most remarkable property is the work of fracture in tension, which has been measured in the range  $0.4 - 1.1 \text{ MJm}^{-2}$  [Cox et al., 1996]. This is considerably higher than values for the toughest metal alloys ( $< 200 \text{ MJm}^{-2}$ ) or tape laminates ( $< 150 \text{ MJm}^{-2}$ ) [e.g., Ashby, 1995]. Such large values of work of fracture point to many applications for 3D interlock weaves where high damage tolerance is demanded, including armour and explosion containment, among others.

The high work of fracture has already been associated with very unusual mechanisms observed in experiments. The most important is the ability of specimens to bear loads near the peak load,  $\sim 1 \text{ GPa}$ , at strains of up to  $3 - 4\%$ , which significantly exceed the

nominal failure strain of the tows ( $\approx 1.5\%$ ) [Cox et al., 1996]. Destructive examination of specimens at strains exceeding 1.5% reveals that all or at least most of the primary load bearing tows are ruptured, even though the composite stress at the time of interrupting the test was  $\sim 1$  GPa. Thus some unusually effective mechanism exists for transferring load from one end of a specimen to the other past sites of tow rupture. The mechanism of load transfer was conjectured in prior work to involve the locking up of sliding, load-bearing tows against one another. The effectiveness of the lockup could be enhanced by the contact of asperities on tows under the constraining influence of the warp weaver tows [Cox et al., 1996].

Along with lockup, the spatial distribution of the sites of tow rupture must also have an important role. If, for example, all load-bearing tows ruptured on a single plane, then the specimen must fail catastrophically at modest strain. Spatially distributed tow breaks will in contrast favor ductility and high work of fracture. Unfortunately, unlike the problem of kink formation in compression, no micromechanical model exists to predict the critical load for tow rupture in tension. It is therefore not yet resolved how to relate weak spots (flaws) in tows under tension to characteristics of the textile reinforcement. Nevertheless, the misalignment of tow segments is probably once again an important factor, along with the presence a priori of fiber breaks. The misalignment of tow segments and clusters of fiber breaks are likely (but not yet proven) to be correlated in textile composites, since both are often caused by the pressing together of tows during the weaving process. Flaws are therefore quite likely to be correlated with geometrical irregularity in load-bearing tows and found at or near sites of tow contact. While the flaws can be expected to be random in strength, their locations will correlate with the tow spacing.

Complete examination of the mechanism of lockup during tensile failure and its relation to weave architecture and the distribution of flaws is the purpose of this paper. While the mechanism of lockup seems strongly indicated by experiments, its proper exposition requires a computational model that deals in detail with the distribution of stress and strain throughout a specimen as damage accumulates in it during the failure sequence. The so-called Binary Model will be used for the analysis. The Binary Model is a finite

element formulation in which the geometry of the 3D textile architecture is represented faithfully, while the element size is chosen to be sufficiently coarse to enable experimentally significant volumes of a 3D textile to be simulated [Cox et al., 1994b; Xu et al., 1995]. By careful definition of the elements' constitutive properties, the mechanics of deformation can be made approximately independent of the choice of element size.

The definition of the Binary Model is extended here to deal with nonlinearity due to distributed damage, such as microcracking and plasticity, as well as tow rupture, shear load transfer around tow breaks, and tow pullout. These are all essential mechanisms in the ultimate tensile failure of interlock weaves. The model is then used to execute Monte Carlo simulations of the gauge sections of specimens similar to those previously tested. Within each Monte Carlo simulation, the strength and spatial distribution of a large number of flaws are assigned according to various trial distribution laws. The simulation then predicts the full test life of a particular specimen, with a particular set of flaws. In this way, the form of distribution that is necessary to reproduce experimental data is determined.

The Binary Model simulations do indeed yield much insight into the factors that determine work of fracture. Implications for designing textiles with optimal work of fracture will be discussed.

## **2. Failure Mechanisms in 3D Interlock Weaves**

Here some details of the test data and mechanisms reported in an earlier experimental study [Cox et al., 1996] of tensile failure in interlock weaves are reviewed. In those experiments, the load was aligned with the stuffers (warp tows) and so in all the description and simulations in this paper, the stuffers will be considered the primary load-bearing tows and the fillers normally-loaded tows.

## 2.1 Weave Architecture and Constituent Materials

In the interlock weaves under study, layers of stuffers and fillers alternate through the thickness of the plate, with the outermost layers being layers of fillers. Warp weaver tows bind the stack of fillers and stuffers together by traversing through the thickness and wrapping around individual fillers. The warp weavers may traverse the stack at an angle of approximately  $45^\circ$  (Figs. 1a and 1b), in a variant called “angle interlock”; or perpendicularly (Fig. 1c) in a variant called “orthogonal interlock”. The warp weavers may turn only around the outermost layers of fillers (Figs. 1a and 1c), in which case the weave is called “through-the-thickness”; or around the fillers in successive filler layers, in which case the weave is called “layer-to-layer”. Thus the weaves in Fig. 1 will be called “layer-to-layer angle interlock” (Fig. 1a), “through-the-thickness angle interlock” (Fig. 1b), and “through-the-thickness orthogonal interlock” (Fig. 1c). The last will also be abbreviated to “orthogonal interlock weave”, since layer-to-layer orthogonal interlock weaves are not considered (and are not commonly manufactured). The warp weavers usually form a complex pattern, each being offset from its predecessors in progression through the composite in the direction of the fillers.

The composites are usually formed by first weaving the tows together into a preform of nearly net thickness and then infiltrating an uncured resin by resin film infusion or resin transfer molding and curing in a pressurized mold.

Geometrical irregularities are generally associated with the contact of tows. Segments of misaligned stuffers, for example, which are known to act as defects or flaws in compression and are very likely to do so in tension, are often found adjacent to sites where a warp weaver wraps around a filler and pushes the filler into a neighbouring stuffer (Fig. 2). Since tows are commonly  $\sim 1$  mm thick, the spacing of misalignment flaws is typically  $\sim 1 - 2$  mm or greater, depending on the warp weaver pattern.

The particular weave patterns studied by Cox et al. [1996] and simulated here are described in detail in Appendix A (see also [Cox and Dadkhah, 1995; Xu et al., 1995]). All types displayed in Fig. 1 were included.

The most important irregularity for tensile failure is believed to be waviness in the aligned tows, i.e., the stuffers, and the largest component of that waviness is in the through-thickness direction. The misalignment angle for stuffers on through-thickness sections parallel to the stuffer direction will be denoted  $\xi$ . Typical distributions of  $\xi$  measured in previous work possessed mean absolute misalignment angle  $\mu_\xi = 2.5^\circ$  and variance  $\sigma_\xi = 1.7^\circ$ , with the 90<sup>th</sup> percentile falling near  $5^\circ$ . The extremes tend to occur with spacing in multiples of the tow separation (1 – 2 mm). Smaller scale undulations of lesser magnitude may also be present.

Cox et al. [1996] reported tests and observations for composites of AS4 carbon fibers in a Shell 1895 resin. The fibers have an axial Young's modulus of 235 GPa, while Young's modulus for the resin is 3.7 GPa. Straight segments of tows in the woven composite can be regarded at least in the elastic regime as approximately unidirectional composites. For typical local fiber volume fractions in a tow, the axial Young's modulus of such a tow segment (which is fiber dominated) is  $\approx 150$  GPa and its transverse modulus (resin dominated) is  $\approx 8$  GPa. Thus, the anisotropy ratio of the tows is  $\approx 20$ . This high degree of anisotropy dictates the nature of many of the observed failure mechanisms and has strong implications for valid modeling assumptions. Full listings of the constitutive parameters used for the subject composites and their constituents are given in Appendix B.

## 2.2 Observations during Tensile Rupture

Representative stress-strain curves from [Cox et al., 1996] are shown in Fig. 3. The strain quoted refers to an average over the length of the gauge section, approximately 23 mm.

The first signs of nonlinearity in tests appear at strains of 0.5% to 1% and are believed to be due to plastic straightening of the waviness in stuffers. The onset of plastic

straightening can be estimated well by equating the axial shear stress expected in a tow segment of a given misalignment to the critical shear flow stress,  $\tau_c$ , measured for similar composites [Cox et al., 1996; Mouritz et al., 1999]. The shear flow stress here is that of an approximately unidirectional fiber composite under axial shear. It reflects the onset of large plastic strains in the resin due to the formation of arrays of microcracks, which in a unidirectional composite or ply will form under macroscopic shear between pairs of fibers (scale  $\sim 1 \mu\text{m}$ ) [Fleck, 1991; Xia and Hutchinson, 1994; Cox et al., 1994a]. Experiments in cross-plied AS4/1895 laminates yield  $\tau_c = 75 \text{ MPa}$  [Cox et al., 1994a]. Denote the nominal axial stress in a stuffer  $\sigma_1^{(s)}$  (in the coordinate system of Fig. 1), the composite stress in the stuffer direction  $\sigma_1$ , and the fraction of all fibers that lie in stuffers  $f_s$ . Since the fibers in stuffers dominate the bearing of load in that direction, the plasticity condition can be written

$$f_s \sigma_1 \xi = \sigma_1^{(s)} \xi = \tau_c \quad (\xi \text{ in radians; } \xi \text{ small}). \quad (1)$$

For  $\xi = 5^\circ$  and  $f_s = 0.5$ , plastic straightening will commence at  $\sigma_1^{(s)} = 1 \text{ GPa}$ ; or a composite stress  $\sigma_1 = 500 \text{ MPa}$ . The total strain possible by plastic straightening can be estimated from the measured misalignment distributions. It is found to be  $\sim 0.1\%$ .

Matrix cracks appear between fillers, which are loaded transversely, at strains near 1% and then become widespread at higher strains. These cracks are analogous to transverse cracks in the  $90^\circ$  plies of a  $0/90^\circ$  laminate, but their spacing is dictated by the width of the fillers. Cracks within the fillers themselves are rare. Since approximately 96% of the stiffness of the interlock weave is attributable to the stuffers, interfiller cracks have a small effect on the stress-strain curve.

At some critical strain that varies between 2.5 and  $> 3\%$ , a sudden, large load drop occurs, which is called the primary load drop. Beyond the primary load drop, the ultimate tensile fracture surface is clearly defined. Small loads persist to very large displacements (up to 25 mm or the entire gauge length) as stuffers are pulled out across the fracture

surface. The regime prior to the primary load drop is denoted the hardening phase and that following it the pullout phase. The appearance of the tensile crack and the extent of pullout are typified by Fig. 4.

Even allowing for plastic straightening of stuffers, which on average permits an axial plastic strain of  $\sim 0.1\%$  and for unusually wavy tows perhaps  $0.2\%$ , there remains a remarkable disparity between the failure strain of AS4 fiber composites, which is approximately  $1.6\%$ , and the composite strains at which the primary load drop occurs ( $2 - >3\%$ ). The stuffers should have ruptured well before the primary load drop. And indeed destructive inspection of specimens taken to loads near  $1\text{ GPa}$  and strains *prior* to the primary load drop reveals that most and possibly all of the stuffers have ruptured [Cox et al., 1996]. Yet those rupture sites are believed to define the ultimate fracture surface, because specimens taken to ultimate failure tend to exhibit a single rupture in any stuffer, the exceptions mainly being stuffers damaged by machining the free surfaces of the gauge section. Thus the observations imply that the sliding of ruptured stuffers through the specimen accommodates the large strains before the primary load drop, but that the mechanics of the sliding allow the continued transfer of loads not far diminished from the ultimate strength of the composite.

Stereoscopic observations show that stuffer sliding occurs over distances  $l_s = 1 - 5\text{ mm}$  on either side of a rupture site in the hardening phase (prior to the primary load drop) [Cox et al., 1996]. Since the load in the stuffer must be restored to its remote value,  $\sigma_1^{(s)}$ , by shear interactions (friction) with the surrounding composite over the length  $l_s$ , shear lag analysis implies that

$$\sigma_1^{(s)} = \frac{sl_s}{A_s} \tau_f \quad (2)$$

where  $s$  is the circumference of the stuffer,  $A_s$  is its cross-sectional area, and  $\tau_f$  is the friction stress, assumed for the moment to be uniform (non-uniform friction will be a feature of the modeling to follow). For typical stuffer geometry, Eq. (2) yields  $\tau_f = 100 -$

500 MPa. In contrast, analysis of the pullout phase (after the primary load drop), indicates  $\tau_f \approx 10$  MPa.

The high values of  $\tau_f$  prior to the primary load drop are a direct result of stuffer irregularity and the 3D nature of the reinforcement architecture. On the upper and lower surfaces of a sliding stuffer, irregular features on the stuffer are pressed against neighboring fillers as the tow slips, while on lateral surfaces, the stuffer contacts warp weavers and matrix debris. The features on the stuffer are found damaged but not straightened on pulled-out tows following failure, implying that they have been dragged through the composite in their distorted shapes. In the pull-out regime, mild oscillations in the load level occur with a period commensurate with the centre-to-centre spacing of fillers ( $\approx 2$  mm).

The crucial role of the three-dimensionality of the reinforcement is indicated by several observations. Prior to the onset of stuffer rupture (strains  $< 1.5\%$ ), there is universal contraction in the through-thickness direction, of magnitude consistent with Poisson's effect in the elastic regime for the applied level. At 2.3 % strain, in contrast, the specimen has expanded in the through-thickness direction, an apparent manifestation of irregular stuffers pushing one another apart as shape features slide out of registry. This through-thickness dilation must be opposed by the warp weavers, which are always found to be intact during destructive inspection of specimens from tests interrupted before the primary load drop, even after stuffers have ruptured. Increasing tension in the warp weavers will generate increasing compressive contact forces on the surfaces of sliding stuffers, leading to enhanced friction or lockup. On the other hand, warp weavers never survive the primary load drop. Thus, the primary load drop may indeed be triggered by warp weaver failure, upon which the stuffers, no longer constrained, can slip against greatly reduced frictional resistance.

In summary, high work of fracture is conjectured to derive from very high friction following stuffer rupture, which results from irregularities on the stuffers locking up against features on the surrounding composite under the constraining effect of the warp

weavers. The remainder of this paper is devoted to testing this hypothesis by simulations using the Binary Model. The simulations will also explore the role of the spatial distribution of flaws in the stuffers (or the distribution of stuffer rupture sites). The unusually long pullout lengths observed in failed specimens (e.g., Fig. 4) imply that the failure sites are broadly distributed. Broadly distributed rupture sites will be seen to be a second prerequisite of high work of fracture.

### 3. Formulation of the Binary Model

The Binary Model is an efficient finite element representation of a textile composite. The axial stiffness of tows is represented by one-dimensional line elements, which are concatenated in the model to recreate a close approximation to the actual loci of the tows in the real composite (Fig. 5). The tow elements are coupled to a space filling array of solid effective medium elements, which represent all stiffness contributions other than the axial stiffness of tows, *viz.*, the transverse and shear stiffness of tows and Poisson's effect. The decomposition into axial stiffness (tow elements) and all other stiffness contributions is especially effective when the degree of anisotropy of the tows is high, as in a polymer composite. But it is also useful in ceramic matrix composites, which have only modest anisotropy. Representing an entire tow by a single chain of line elements is also appropriate on physical grounds, because tows fail as discrete entities in textile composites. A ruptured tow can be represented as a single failed tow element in the Binary Model (along with modifications of the coupling of the ruptured tow to the rest of the model) without losing any significant detail of the local failure event.

Figure 5 shows tow elements representing stuffers, fillers, and warp weavers in a through-the-thickness angle interlock weave. The tow elements are located along a path corresponding to the axis of the tow they represent in the actual composite. A single stuffer or filler element extends a distance equal to the centre-to-centre separation of neighboring tows. The warp weavers are idealized as following saw-tooth paths in the model depicted, with a single element extending through the thickness.

As shown in Fig. 5, an effective medium element also usually extends in any direction from the centre of one tow to the centre of one of its neighbors. It therefore represents a volume of material containing fragments of more than one tow, usually with different orientations. In interlock weaves, effective medium elements are conveniently defined as eight-noded cuboidal elements containing eight Gaussian quadrature points and whose vertices coincide initially with the nodes of either stuffer or filler tow elements.

In this work, warp weavers are ignored in the definition of effective medium elements. Their influence is sufficiently incorporated in the model by the effect of the warp weaver tow elements. The warp weaver tow elements are coupled to the rest of the composite solely via coupling springs connecting their ends to nodes in the fillers around which they turn. The value of the spring constant assigned to the coupling springs is known from prior work to have very little effect on the stress distribution in the model [Xu et al., 1996].

Stuffer and filler nodes remain coincident with effective medium nodes during elastic deformation and also during nonlinear response corresponding to plasticity and distributed microcracking. However, when a stuffer element fails, the nodes of the failed stuffer are allowed to displace relative to the neighboring filler and effective medium elements to simulate debonding and sliding. During sliding, coupling forces are applied to the displaced nodes to represent friction (Fig. 6).

Large scale irregularity in the positioning of tows can be replicated in the Binary Model by offsetting tow element nodes. The offsets will be chosen in a Monte Carlo simulation according to prescribed distributions, as described below. The effects of small-scale irregularities (over scales less than the tow element length) can be incorporated by modifying the constitutive laws for tow elements. The most important example of this in the current study is the reduction of the random strength assigned to a tow element where a misaligned tow segment exists within the interval represented by the element.

Stuffers and fillers have typical widths in the plane of the specimen of 2 mm. A typical weave pattern contains nine stuffer and filler layers and a specimen gauge section is typically  $25 \times 10 \times 6$  mm. Thus a simulation in the Binary Model might contain  $\sim 1000$  tow elements and  $\sim 10^4$  degrees of freedom. Larger models are also sometimes executed.

Definition of the model is completed by specifying the constitutive properties of tow and effective medium elements that describe the elasticity of elements, their plastic response and strength, and their mechanical coupling following localized failure events (friction following stuffer rupture events). Constitutive models are based on micromechanical models that are computed beforehand, but may contain parameters evaluated by sampling displacements and stresses at certain nodes or quadrature points during the execution of the simulation. The following sections describe these details.

### 3.1 Element Dimensions and Random Irregularity

The element dimensions  $a_1$ ,  $a_2$ ,  $a_3$ , and  $a_3'$  defined by Fig. 5 were evaluated in this work from manufacturer's specifications for the weaves studied experimentally in [Cox et al., 1996] in combination with measurements of the total fiber volume fractions. The formulae used are reproduced in Appendix A. By involving the measured total fiber volume fraction, the formulae are assured to lead to correct fiber volume counts and therefore accurate predictions of macroscopic stiffness. Indeed, the whole macroscopic stiffness matrix has been proven to be well estimated by the Binary Model [Xu et al., 1996].

Large-scale irregularity in the alignment of stuffers can be simulating by offsetting the stuffer element nodes in the initial, stress-free model configuration. Measurements show that misalignment is greatest in the through-thickness direction,  $x_3$ , and node offsets were therefore considered in this direction only. The offset,  $\delta$ , of any stuffer node was prescribed by

$$\frac{\delta}{a_3} = \beta g_s \quad (3)$$

where  $\beta$  is a normally distributed random variable with zero mean and standard deviation one. Thus the parameter  $g_s$  sets the degree of misalignment, with  $0 \leq g_s \leq 0.2$  in the cases considered. The main effect of stuffer node offset is to introduce local fluctuations in the effective stiffness of stuffer elements under aligned macroscopic loads and therefore fluctuations in the sharing of loads among nominally similar stuffers; and greater shear stresses in effective medium elements adjoining misaligned stuffer segments [Xu et al., 1996].

### 3.2 Elasticity, Microcracking, and Plasticity

Formulae for the spring constants assigned to tow elements and the elasticity of effective medium elements are listed in Appendix B. The tow element spring constants are related trivially to the axial stiffness of the tow represented, which is dominated by the fibers, and its cross-sectional area. The stiffness of the effective medium elements is evaluated using micromechanical models in the literature from the properties of the fibers and the resin. Account is taken of the different orientations of tow fragments represented by a single effective medium element. Because of symmetry considerations, the effective medium elements are assumed transversely isotropic, with planes of isotropy lying in the plane of the laminate. However, the response of the Binary Model, including estimates of local stress components, is not sensitive to how the elasticity of the effective medium elements is defined, provided the definition is reasonable [Xu et al., 1996]. Stress distributions are dominated by the tow elements.

The full set of element dimensions, spring constants, and elasticity components is shown in Table 1, along with typical values for a layer-to-layer angle interlock weave. The spring constants are defined in terms of strain and therefore have units of force. The units can also be written as stress-area (GPa-mm<sup>2</sup>). Since tows have cross-sectional areas  $\sim 1$

mm<sup>2</sup>, the values in GPa-mm<sup>2</sup> give a quick indication of the tow stiffness relative to the far more compliant effective medium elements.

The first matrix cracking observed in an interlock weave loaded under tension aligned with the stuffers consists of interfiller cracks orthogonal to the load axis. Interfiller cracks are represented in the Binary Model by knocking down Young's modulus in effective medium elements that represent volumes containing such cracking. Because of the orientation of the interfiller cracks, a reasonable criterion for their onset is that the strain in the stuffer direction in an effective medium element,  $\varepsilon_1^{(m)}$ , should exceed some critical value:

$$\varepsilon_1^{(m)} \geq \varepsilon^{(mc)} \quad . \quad (4)$$

Because of the element size in the Binary Model, the effect of interfiller cracking on stiffness must be represented as uniform over distances similar to the centre-to-centre filler separation. The ramifications of this for the mechanics of load transfer will only be reasonable if stuffers slip over distances that are at least several times the width of a filler. But experiments show that this is indeed the case at loads near ultimate failure, which is the focus of this study, even when friction is high [Cox et al., 1996]. The response of an effective medium element to the onset of matrix (interfiller) cracking is defined to be that its Young's modulus in the stuffer direction is reduced to zero. Its Young's moduli in other directions and shear moduli remain unaffected.

A condition similar to Eq. (4) can be imposed for interstuffer cracking when tensile strains develop in the direction  $x_2$ ; or cracking between stuffers and fillers under tension in the direction  $x_3$ . But, this is not critical in the overall failure process and was not always done in simulations.

### 3.3 Tow Strength

In tension, tows fail by rupture. The rupture strength of a tow segment is believed to depend on its degree of irregularity as well as the presence of any fiber damage that may have occurred during processing. Because variations in irregularity cannot be predicted, the tow strength is regarded as a random variable.

In the simulations, tow failure is prescribed to occur when the strain in a tow element (which corresponds to the axial strain in the tow segment it represents) exceeds a critical value, e.g.

$$\varepsilon^{(i)} \geq \varepsilon_c^{(i)} \quad \text{for the } i^{\text{th}} \text{ tow element.} \quad (5)$$

The strengths of the entire set of  $N$  tow elements,  $\{ \varepsilon_c^{(i)}, i = 1, \dots, N \}$ , are random variables prescribed in various ways in the simulations. The distributions of  $\varepsilon_c^{(i)}$  in strength and in space will be varied. There are no restrictions on the distributions that can be fed into the Monte Carlo simulations. In the present simulations, only the stuffers and warp weavers are assigned finite strengths.

### 3.4 Debonding, Sliding, Friction, and Lockup

Whenever a stuffer fails, it is debonded near the site of its rupture from the surrounding composite by a circumferential matrix crack. (The debond crack does not in fact involve fiber matrix debonding, but is entirely contained in resin around the periphery of the stuffer [Cox et al., 1994].) The stuffer then slides along the debonded zone relative to the neighboring tows, against the resistance of friction. In the Binary Model, stuffer slip is enabled by allowing stuffer nodes and effective medium nodes, which were initially coincident, to separate and develop relative sliding displacements. Frictional resistance to the sliding is introduced by imposing balanced friction forces to the separated nodes (Fig. 6). The magnitudes of the friction forces are computed as follows.

For slip in the hardening phase, when intact warp weavers constrain the composite through the thickness, friction is greatly enhanced in the process called lockup. A micromechanical model of lockup has been derived for stuffers and fillers having the idealized irregularity of shape shown in Fig. 7. When the stuffer slides, the inclined facets on its surfaces force apart the neighboring fillers, whose facets are initially in registry with those of the stuffer, but then move out of registry. If the angle of inclination is  $\theta$  and the slip displacement in the direction  $x_1$  (the stuffer direction) is  $u_s$ , then a “normal sliding displacement”,  $w_s$ , at the sliding interface in the direction  $x_3$  must result, of magnitude

$$w_s = u_s \tan \theta \quad . \quad (6)$$

The normal sliding displacement causes dilation of the composite in the through-thickness direction, as seen experimentally late in the hardening phase. It will also create tension in any warp weaver that traverses the composite in the vicinity of the slip zone, which will be balanced by compression in the stuffers and fillers in the through-thickness direction. This additional compression will raise the coefficient of friction at the debond.

The facets of Fig. 7 have a period equal to the centre-to-centre spacing of fillers ( $\sim 2$  mm), which is consistent with irregularities observed in actual composites, although the observed irregularities are not exactly periodic. Sliding displacements cannot exceed  $\sim 1$  mm in the hardening phase, since this is the maximum total displacement in the gauge section. Therefore,  $u_s$  can fairly be assumed always less than the length of a facet in Fig. 7 and  $w_s$  a monotonically increasing function of  $u_s$  throughout the hardening phase, as in Eq. (6).

The normal sliding displacement can be introduced into the Binary Model as an eigenstrain (or strain in the stress-free state) within the effective medium elements adjoining the sliding stuffer. There are four such effective medium elements surrounding each stuffer element along the slip zone (Fig. 5), forming two pairs of elements stacked in the direction  $x_3$ . Only one pair of elements is shown around each stuffer element in Fig. 6.

Since each pair of elements has a total thickness of  $2a_3$  in the direction  $x_3$ , the eigenstrain,  $\varepsilon_s^{(i)}$ , which is treated as uniform over the pair, is defined as

$$\varepsilon_s^{(i)} = \frac{w_s^{(i)}}{2a_3} = \frac{\tan \theta}{2} \frac{u_s^{(i)}}{a_3} \quad (7)$$

with  $i$  identifying the stuffer element. The sliding displacement,  $u_s^{(i)}$ , is taken as the average at the two nodes bounding the  $i^{\text{th}}$  stuffer element. Since  $u_s^{(i)}$  can have the same order of magnitude as  $a_3$ ,  $\varepsilon_s^{(i)} \approx \tan \theta / 2$  is feasible: the local dilation strains can be considerably greater than the macroscopic axial strain in the composite in the hardening phase. For example, when  $\theta = 12^\circ$ ,  $\varepsilon_s^{(i)}$  will range up to approximately 0.1. The factor  $\tan \theta$  is the only measure of the lockup geometry that is carried into the Binary Model for computing  $\varepsilon_s^{(i)}$ . Clearly if  $\tan \theta$  is simply regarded as a modeling parameter, it could represent the effect of irregular tow geometry of much more general nature than the idealization of Fig. 6. The constitutive law for the elasticity of the four affected effective medium elements in the direction  $x_3$  is redefined as

$$\sigma_{ij}^{(m)} = C_{ijkl}^{(m)} (\varepsilon_{kl}^{(m)} - \varepsilon_s^{(i)} \delta_{k3} \delta_{l3}) \quad (8)$$

where  $\sigma_{ij}^{(m)}$ ,  $\varepsilon_{ij}^{(m)}$ , and  $C_{ijkl}^{(m)}$  are the stress, strain, and stiffness tensors for the effective medium element, the last defined consistently with the transversely isotropic engineering constants of Table 1.

With the eigenstrains  $\{\varepsilon_s^{(i)}, i \in S\}$ , where  $S$  represents the set of sliding stuffer elements, introduced into a simulation, the resulting effects on the stress distribution throughout the sample are at once computed by the model, including all details of the constraining effects of warp weavers. The compressive stresses acting upon a sliding stuffer element can be inferred from the stresses calculated at the neighboring Gaussian quadrature points

in the surrounding effective medium elements (Fig. 6). The contact stresses will be nonuniform, but the physics of lockup can be fairly represented by regarding them as uniform over each single tow element that slides. Let the relevant compressive stress component averaged over the eight quadrature points nearest the  $i^{\text{th}}$  stuffer element be denoted  $\sigma_3^{(i)}$ .

Given  $\sigma_3^{(i)}$ , the friction forces in Fig. 6 can be computed from the force equilibrium diagram of Fig. 7. The tractions acting on the facets that are in contact during the sliding motion (the stuffer slides to the left in the figure) can be resolved into a normal component,  $\sigma_n$ , and a tangential component,  $\tau_f$ . Let  $\sigma_1^{(s)}(x_1)$  denote the axial stress in the stuffer. Assume that the contacting facets are approximately half the upper and lower surfaces of the sliding tow segment (Fig. 7), so that each contacting facet has an area  $(a_1/2\cos\theta)a_2$ . Since the stuffer has a cross-sectional area  $a_2 t_s$ , where  $t_s = 2(a_3 - a'_3)$  is the thickness of the stuffer in the direction  $x_3$ , force equilibrium in the directions  $x_1$  and  $x_3$  requires

$$t_s [\sigma_1^{(s)}(x_i) - \sigma_1^{(s)}(x_i + a_1)] = a_1 [\tau_f - \sigma_n \tan \theta] \quad (\sigma_n < 0; \theta > 0; \tau_f > 0) \quad (9a)$$

and

$$2\sigma_3^{(i)} = \tau_f \tan \theta + \sigma_n \quad . \quad (9b)$$

If the shear traction  $\tau_f$  obeys Coulomb's law for some coefficient of friction,  $\mu$ :

$$\tau_f = \mu |\sigma_n| \quad (9c)$$

then the stress differential acting on the stuffer element is (from Eqs. (9a) and (9b))

$$\Delta\sigma_1^{(i)} \equiv \left[ \sigma_1^{(s)}(x_i) - \sigma_1^{(s)}(x_i + a_1) \right] = \frac{2a_1}{t_s} \mu_{\text{eff}} \left| \sigma_3^{(i)} \right| . \quad (10a)$$

where

$$\mu_{\text{eff}} \equiv \frac{\mu + \tan \theta}{1 - \mu \tan \theta} \quad (10b)$$

The factor  $\mu_{\text{eff}}$  can be regarded as an enhanced coefficient of friction, which represents the sum of friction effects due to small scale irregularity along the surface of the facets in Fig. 7 and the large scale irregularity of facets of slope  $\theta$ . If  $\theta \approx 0.1$  and  $\mu \approx 0.5$ , then  $\mu_{\text{eff}} \approx 1.2\mu$ , a modest increase. Lockup (as defined in this work) will arise mainly from the larger relative increase expected in  $\Delta\sigma_1^{(i)}$  due to the normal sliding displacement,  $w_s$ , and consequent increase in  $\left| \sigma_3^{(i)} \right|$ .

The lockup effect is quantified in simulations by the two parameters,  $\theta$  and  $\mu$ . Since tow irregularity is random in magnitude through the composite, in at least some simulations  $\theta$  will be prescribed as a random variable; and in that case the proportion of the dilation strain to the sliding displacement, and thence the magnitude of the lockup effect, will vary with location in the composite.

Other friction effects, e.g., due to compressive residual stresses in the composite, must also be accounted for. Friction will exist along the upper and lower surfaces of a sliding stuffer even before the constraint stress,  $\sigma_3^{(i)}$ , has significant magnitude. Friction will also be present along the lateral sides of a sliding stuffer (those normal to the direction  $x_2$ ). These other stress effects are considered independent of  $\sigma_3^{(i)}$  and are introduced by adding a constant,  $\Delta\sigma_1^{(\text{const})}$ , to the net stress differential acting along a sliding stuffer element, which is denoted  $\Delta\bar{\sigma}_1^{(i)}$ :

$$\Delta\bar{\sigma}_1^{(i)} = \Delta\sigma_1^{(i)} + \Delta\sigma_1^{(\text{const})} \quad (\text{hardening phase}). \quad (11)$$

In the pullout phase, there is no constraint, so

$$\Delta\bar{\sigma}_1^{(i)} = \Delta\sigma_1^{(\text{const})} \quad (\text{pullout phase}). \quad (12)$$

The constant friction contribution is assumed to act uniformly over the entire periphery of the stuffer. It is assigned a value consistent with the measured friction stress in the pullout phase,  $\tau_f^{(\text{const})}$ , to which according to shear lag analysis it must be related by

$$\Delta\sigma_1^{(\text{const})} = \frac{2a_1(a_2 + t_s)}{a_2 t_s} \tau_f^{(\text{const})} \quad . \quad (13)$$

All simulations are run with the assignment  $\tau_f^{(\text{const})} = 10 \text{ MPa}$  [Cox et al., 1996].

The net stress differential represented by  $\Delta\bar{\sigma}_1^{(i)}$  is introduced into a Binary Model simulation by imposing the forces

$$Q_s^{(i)} = t_s a_2 \Delta\bar{\sigma}_1^{(i)} \quad (14)$$

to the node at the left end of the  $i^{\text{h}}$  stuffer element (for sliding to the left) and a balancing force to the effective medium node to which it is coupled (Fig. 6). This procedure leads to an average stress gradient in the stuffer elements that is independent of the size of the stuffer elements [Cox et al., 1994].

By simple adjustment of the algorithms for computing the coupling forces, the site of a stuffer break may be located anywhere in a stuffer element (as specified by invoking a distribution function in a Monte Carlo simulation); and the slip zone can effectively be terminated at any location in some other stuffer element.

### 3.5 Numerical Implementation

The Binary Model is implemented as a finite element code in an updated Lagrangian formulation, which solves for increments in the displacements of nodes due to increments in the total nodal forces arising from applied displacements, friction forces, and tow element failures. Boundary conditions are imposed in terms of the displacements of end-planes normal to the stuffer direction. The applied displacement is incremented until failure is indicated in an effective medium or tow element. If failure is indicated for more than one element, only that for which the failure criterion is most exceeded following the applied displacement increment is allowed to fail.<sup>1</sup> Stress distributions are then recalculated and the failure criterion applied anew to all elements. This is repeated until no further element failures are indicated for the current displacement increment.

If a stuffer element fails, no other element failures are permitted until the slip lengths for the sliding zones on either side of the stuffer break have been evaluated. Similarly, when any element fails, the lengths of all existing slip zones are updated to be consistent with the new distribution of stresses. A slip zone is extended when the axial stress in the stuffer beyond the existing slip zone has risen sufficiently to cause extension of the zone by at least one element length.

If a slip zone reaches one end of the model, it is continued from the other end of the model in a periodic fashion. This avoids indeterminacy where slip zones intersect the model boundaries. However, this condition is relatively rare and will have no effect on questions of interest. This is the only circumstance in which periodicity is invoked – the model is in every other regard non-periodic.

Considerable computation is involved in calculating the stress distribution following every displacement increment and every element failure, since the determination of slip lengths and friction forces is nonlinear and must be done by iteration. However, the

---

<sup>1</sup> This and some other requirements placed on admissible developments have proven impossible to implement in commercial finite element codes.

efficiency of the computation can be improved by noting that the configuration of the model does not change rapidly unless there is substantial damage. Therefore, the stiffness matrix need be recalculated only after some damage accumulates or when errors reach certain tolerances.

#### **4. Simulations: The Link Between Mechanisms, Architecture, and Flaw Distribution**

Numerous Binary Model simulations were executed to investigate how the nature of the tensile fracture process depends on the way flaws are distributed in strength and space and the role of the lockup mechanism. The simulations were executed by Monte Carlo methods. In each simulation, particular values of strength or nodal offset or other property were assigned to each element or node according to probability distributions using a pseudo-random number generator. The simulation was then carried forward as a deterministic problem. Statistics of the fracture process were collected from a significant number of simulations and qualitative differences in the failure process were examined. All simulations reported here were for a layer-to-layer angle and orthogonal interlock weaves similar to those designated *h-L-1* and *h-O-1* in [Cox et al., 1996] (Fig. 1a; Appendix A). The volume of composite simulated was 10 stuffer wide in the direction  $x_2$ , 24 stuffer elements long in the direction  $x_1$ , and nine layers thick (counting both stuffer and filler layers) in the direction  $x_3$ , yielding specimen dimensions of approximately 50 x 10 x 5.6 mm. This is similar to the gauge sections of the specimens reported in [Cox et al., 1996].

The main focus of the simulations was on variations in the nature of the distributions in the strength and location of flaws in stuffer elements. Several distributions of strength and location were studied, based on combinations of different normal distributions.

#### 4.1 Flaws Correlated with Features in the Weave Architecture

Let  $S^{(u)}$  and  $S^{(c)}$  denote normal distributions with means  $\mu^{(u)}$  and  $\mu^{(c)}$  and variances  $\sigma^{(u)}$  and  $\sigma^{(c)}$ , respectively, and define  $g_\mu \equiv \mu^{(c)}/\mu^{(u)}$  and  $g_\sigma \equiv \sigma^{(c)}/\sigma^{(u)}$ . Here the superscript “*u*” indicates “uncrimped” and  $S^{(u)}$  represents the strengths expected in tow segments that have minimal distortion; while the superscript “*c*” indicates “crimped” and  $S^{(c)}$  represents the somewhat lower strengths of tow segments that are crimped, e.g., as depicted in Fig. 2. The magnitude of the knockdown of strength due to crimping is represented by the value assigned to  $g_\mu$ .

In the first set of simulations to be described, the spatial distribution of flaws was made to correspond to the locations of stuffer segments that abut turning points of warp weavers (Fig. 2). Approximately 6% of stuffer segments (20 stuffer segments in all) randomly chosen from those abutting warp weaver turning points were assigned strengths according to the distribution with lower mean,  $S^{(c)}$ . All other stuffer segments were assigned strengths according to the distribution  $S^{(u)}$ . This leads to a model in which relatively weak flaws are distributed fairly sparsely throughout the specimen and are correlated with certain locations in the composite (see the details of the layer-to-layer architecture in Appendix A), but are distributed fairly uniformly throughout the specimen. The mean of the distribution  $S^{(u)}$  was set to a spring constant  $k_s$  that corresponds to a critical strain of 1.35 %. The standard deviation for  $S^{(u)}$  was set to  $\sigma^{(u)}/\mu^{(u)} = 0.15$ . The distribution of relatively weak flaws was set by assigning  $g_\mu = 0.7$ . Warp weaver tow elements were assigned the deterministic failure strain 1.5%.

In the same set of simulations, a study was also conducted of the effect of varying the coefficient of friction,  $\mu$ , acting along sliding stuffers, with values assigned from the set {0.25, 0.5, 0.75, 1.0}. The angle parameter,  $\theta$ , was set everywhere to 6.75°, which generates quite a strong dilation strain. With  $\mu$  and  $\theta$  set, the lockup algorithm is determined via Eqs. (7) and (10).

The last effect included was that of random misalignment of the nodes of stuffer elements. The misalignment parameter,  $g_s$  (Eq. (3)), was assigned values from the set {0.05, 0.1, 0.15, 0.2}. In principle, correlation would be expected between the lockup angle parameter,  $\theta$ , and the offset of stuffer nodes, but since  $\theta$  was set to a constant, no such correlation existed in this set of simulations. Thus misalignment introduced through  $g_s$  has no direct role in lockup. Instead, its main effect is to introduce local fluctuations in the axial loads in stuffer elements and the shear stresses in adjoining effective medium elements. While it may seem unrealistic for  $\theta$  and the offset of stuffer nodes not to be correlated, separating them in simulations permits lockup and load fluctuation effects to be distinguished.

In this set of simulations, the critical strain for tensile failure in effective medium elements was set to 1.3% (Eq. (4)), beyond which the affected stiffness component was set to a negligible value, representing the effect of interfiller or interstuffer cracking. No plasticity was considered.

Typical stress-strain histories from this set of simulations are shown in Fig. 8. The four cases shown represent the extreme values of the misalignment and friction parameters. All the curves exhibit similar behavior in the hardening phase. An approximately linear initial response is interrupted at a strain just below 1% by the first stuffer failure. A sequence of small load drops and periods of load recovery ensues, with the stress not far from the ultimate strength, each load drop corresponding to another stuffer failure. In all cases the primary load drop occurs at a strain less than 1.5%, regardless of the strength of the lockup effect or the degree of misalignment of stuffers (the magnitude of nodal offsets).

Beyond the primary load drop, significant loads continue to be borne in the pullout phase. Here the magnitude of the lockup effect (the friction coefficient,  $\mu$ ) and the degree of misalignment ( $g_s$ ) have their greatest effect, both favoring higher pullout loads. Pullout is exhausted at the right end of each curve.

The simulations of Fig. 8 are appealingly realistic reproductions of tensile failure histories for many textile composites that would be expected to exhibit random tow failures and extensive pullout. However, the primary load drop is predicted at strains well below those at which it has been observed in the particular interlock weaves being modeled. *This set of simulations implies that, where the spatial distribution of flaws is fairly uniform, the hardening phase cannot endure far beyond the nominal failure strain of individual stuffer tows.*

#### 4.2 Spatial Distribution of Flaws and the Endurance of the Hardening Phase

The experimentally observed endurance of the hardening phase beyond the failure strain of individual tows (Fig. 3) is the source of the highest values measured for the work of fracture and therefore of considerable technological significance. The primary goal of the next set of simulations was to discover conditions under which this behavior can be reproduced.

In experiments on the subject composites, stuffers exposed on the halves of a fractured specimen were often observed to extend by approximately uniform lengths from the fracture surface (Fig. 4; [Cox et al., 1996]). They are therefore inferred to have failed approximately on a plane; and the two planes on which the two sets of protruding stuffers have failed are inferred to have been separated by  $\sim 10$  mm in the pristine specimen. Furthermore, the stuffers found on one fragment are not usually neighbors in the  $x_2$  direction. Neighbors tend to have fractured on opposite failure planes. Whatever the source of this unusual distribution of failure sites, it clearly can have an important role in the mechanics of failure.

The next set of simulations was designed to mimic this spatial distribution of failure sites. All stuffers were assigned one weak element from the distribution of somewhat reduced strengths,  $S^{(c)}$ . Half of the weak elements intersected one failure plane, the other half intersected a second failure plane removed from the first by a distance,  $\Delta$ . The weaker elements were chosen to avoid stuffers that are neighbors in the direction  $x_2$  both being

relatively weak in the same failure plane (Fig. 9). All other stuffer elements were assigned strengths from the distribution  $S^{(u)}$ . The ratio  $g_\mu$  was set high enough to ensure that only stuffer elements in the two planes would fail. The dilation parameter was assigned the moderate value  $\theta = 4.5^\circ$  and the friction coefficient set to  $\mu = 0.5$ . The offset parameter for stuffer nodes was set to  $g_s = 0.1$ . Warp weaver tow elements were assigned the deterministic failure strain  $\varepsilon_c = 1.5\%$ . The critical strain for effective medium elements was set to 1.3 % (Eq. (4)) and no plasticity was considered.

Figure 10 presents a typical stress-strain prediction for one simulation in which the separation of the two failure planes was set to  $\Delta = 16$  mm. Once again a nearly linear initial response is terminated by the first stuffer rupture at a strain near 1%. All other stuffers rupture in the interval 1 – 1.7 %. The ruptures tend to occur in bursts, alternating between one failure plane and the other, with no more than four elements failing in succession in either plane before a failure occurs in the other. However, in this simulation, even after the last stuffer has failed, the macroscopic axial stress remains near the ultimate strength (700 – 900 MPa) until the applied strain has reached 3%.

Figure 11 shows variations in Poisson's ratio,  $\nu_{13}$ , during the simulation. Prior to the first stuffer failure,  $\nu_{13}$  is positive and close to the value 0.45 expected in the elastic regime [Cox and Dadkhah, 1995]. As stuffers begin to break and slide, generating the normal sliding displacement,  $w_3$ , the composite swells in the through-thickness direction and  $\nu_{13}$  declines and becomes negative, until  $\nu_{13} \approx -0.5$  following the final stuffer rupture. This trend and ultimate value are consistent with observations reported in [Cox et al., 1996].

The simulations represented by Figs. 10 and 11 appear to capture all the quantitative trends in measured stress-strain curves such as those in Fig. 3. *They demonstrate that the hardening phase can indeed endure well beyond the failure strain of individual tows for feasible assignments of all material parameters, when flaws are distributed in space in a favourable way.*

### 4.3 Further Conditions for an Enduring Hardening Phase

Further simulations were run that were similar to the preceding set but with different values of the separation of the failure planes ( $\Delta = 24$  mm or 8 mm), varying lockup angle parameter ( $\theta = 2.25^\circ$  or  $9^\circ$ ), and different coefficients of friction ( $\mu = 0.25$  or 1.0). In these simulations, no offset was applied to stuffer nodal positions ( $g_s = 0$ ), but plasticity was included in the effective medium elements. The threshold for plasticity was set to be  $\tau_{ij} = 75$  MPa for any component of shear stress. The assigned constitutive law in plasticity was that for an elastic/perfectly plastic material.

The flaws on the two failure planes were assigned by sampling distributions in the same way as described in the simulations of the preceding section.

Typical stress-strain predictions are shown in Fig. 12. They lead to the following conclusions. The endurance of the hardening phase beyond the failure strain for individual stuffers is strongly correlated with the separation of the failure planes,  $\Delta$ , the lockup dilation angle,  $\theta$ , and the friction coefficient,  $\mu$ . Reviewing the entire set of simulations from which those in Figs. 10 and 12 were drawn leads to the conclusion that an enduring hardening phase with load at or near the ultimate strength requires  $\Delta \geq 12$  mm and a strong lockup effect, with  $\theta > 6^\circ$  and  $\mu \approx 1.0$ . Initial waviness in stuffers as a source of local stress fluctuations (represented by the parameter  $g_s$ ) favors prolongation of the hardening phase, but is a relatively minor factor. Plasticity in effective medium elements, while essential to certain details of the stress-strain curves, does not appear to have a significant role in determining the duration of the hardening phase.

### 4.4 Work of Fracture

In a large specimen, nonlinear processes during failure will be mainly confined to a damage band within which the final tensile fracture surface will develop. The displacement discontinuity across the band may be regarded as a crack opening displacement. The experiments in [Cox et al., 1996] showed that the damage band is

somewhat narrower than the gauge length in the specimens tested and thus confined within the volume considered here in model simulations. Furthermore, the bridged zone in the wake of damage propagation through a large panel will be many tens of mm long [Cox et al., 1996], so that the crack displacement should be approximately uniform over volumes similar to those modeled here. Therefore, the stress-strain predictions of the simulations can be used to estimate the work of fracture as though the model represented a slice of material lying across a propagating damage band in a large fracture specimen.

The work of fracture may be written

$$W_f = 2 \int_0^{\sigma_l} \sigma_l(u_l) du_l \quad (15)$$

where  $\sigma_l$  is the macroscopic stress in the loading direction and the total crack displacement,  $2u_l$ , is defined by

$$2u_l = \left( \varepsilon_l - \frac{\sigma_l}{E_l} \right) L \quad (16)$$

with  $\varepsilon_l$  the applied strain,  $E_l$  the macroscopic Young's modulus in the direction  $x_l$ , and  $L$  the simulated gauge length.

Figure 13 summarizes predictions of  $W_f$  from the complete set of simulations from which those of Fig. 12 were drawn. Clearly, the dominant factor is the assumed separation,  $\Delta$ , of the failure planes. The assumed strength of the lockup effect (the effective coefficient of friction,  $\tau_{\text{eff}}$ , of Eq. (10b)) plays a lesser role.

Experimental stress-strain curves reported in [Cox et al., 1996] for the layer-to-leyaer angle interlock composite designated *h-L-1* yielded  $W_f = 760 \text{ MJm}^{-2}$ . The average pullout length, which can be associated with  $\Delta$ , was measured to be 5-6 mm. Figure 13 shows a prediction of  $W_f \approx 600 \text{ MJm}^{-2}$  for  $\Delta = 6 \text{ mm}$ , in reasonable agreement.

## 5. Summary Remarks

The Binary Model has been demonstrated to be a viable computational tool for simulating the details of ultimate tensile failure in textile composites. Various nonlinear mechanisms, which are all important at some stage of the evolution to failure, have been successfully incorporated, including irregularity in the tow deployment, continuous plastic shear, matrix cracking (here in the form of cracking between tows), tow rupture, debonding and slip, enhanced friction (lockup) due to the constraint of 3D reinforcement, and pullout. The model does not assume periodicity in the structure or invoke the popular concept of a purportedly representative unit cell, which is an essential level of generality for simulating complex textile structures.

The entire stress-strain history through to ultimate failure, including an enduring hardening phase, the primary load drop, and the pullout phase, have been simulated realistically by Monte Carlo methods with reasonable values assumed for material parameters and probability distributions.

While falling short of a rigorous proof, the Binary Model simulations quantify the roles of various material and geometrical factors in determining the work of fracture of 3D interlock weaves. The highest values of work of fracture arise when the hardening phase of the failure sequence endures significantly beyond the failure strain of individual tows. This phenomenon has been shown to require an unusual spatial distribution of flaws in stuffers, as well as a strong lockup effect during the sliding of ruptured stuffers through the surrounding composite. The required spatial distribution of flaws is that planes of flaws should exist separated by 10 – 20 mm. The mechanism for the creation of such planes during the manufacture of a textile composite is unknown, but their existence is certainly feasible. For example, variations in tensioning or in the beating up of weft yarns during the weaving process can lead to bands of shear or buckling defects in the dry fiber preform. Post-mortem studies of the specimens tested in [Cox et al., 1996] certainly suggest that flaws populated planes or near-planes. For designing materials with the

highest possible work of fracture, a systematic method of introducing flaws of known strength at preferred locations would be very useful.

Regardless of the spatial distribution of flaws, the three-dimensional nature of the reinforcement in angle interlock weaves has a profound influence on the work of fracture through the lockup mechanism or enhanced friction. Even when the hardening phase terminates near the failure strain of individual tows, usefully large values of the work of fracture are obtained, which are attributable to high friction prior to the primary load drop and substantial pullout loads following it.

### **Acknowledgments**

BNC was supported by the U.S. Army Research Office, program monitor Dr. Will Simmons, Contract No. DAAH04-95-C-0050.

## Appendix A. Definition of the Weave Patterns Studied

The dimensions of tow elements and effective medium elements in models of interlock weaves are related to the centre-to-centre separations of stuffers and fillers. The dimensions  $a_1$ ,  $a_2$ ,  $a_3$ , and  $a'_3$  of Fig. 5 are given in terms of weave specifications and the measured total fibre volume fraction,  $V$ , by

$$a_1 = \frac{n_s + 1}{f_f V y_f \rho_f t} \quad (A.1)$$

$$a_2 = \frac{n_s}{f_s V y_s \rho_s t} \quad (A.2)$$

$$a_3 = \frac{t}{2} \frac{p y_s + e y_f}{(n_s + 1) p y_s + n_s e y_f} \quad (A.3)$$

$$a'_3 = \frac{t}{2} \frac{p y_s}{(n_s + 1) p y_s + n_s e y_f} \quad (A.4)$$

where  $n_s$  is the number of layers of stuffers (and  $n_s + 1$  the number of layers of fillers);  $f_s$  and  $f_f$  are the fractions of all fibers that lie in stuffers and fillers, respectively;  $y_s$  and  $y_f$  are the yields (length per unit mass) of the stuffer and filler tows, respectively;  $\rho_s$  and  $\rho_f$  are the densities of the fibers in stuffers and fillers, respectively;  $e$  is the number of stuffers per unit length in the direction  $x_2$  and  $p$  is the number of fillers per unit length in the direction  $x_1$ ; and  $t$  is the measured total thickness of the composite in the direction  $x_3$ . The thickness,  $t_f$ , of a layer of fillers in the direction  $x_3$  follows as  $t_f = 2a'_3$ ; and that of a layer of stuffers,  $t_s$ , via  $t_s + t_f = 2a_3$ .

## Appendix B. Constitutive Properties Used in Modeling.

The prescription of constitutive laws for tow and effective medium elements in the elastic regime for a 3D angle interlock weave is summarized here from the paper by Xu et al. [1995].

Each tow element in the grid represents the axial stiffness of a short straight tow segment in the composite. Each solid effective medium element represents the transverse stiffness, Poisson's effect, and shear stiffness of one or more short straight tow segments or straight parts of tows that are contained within the element's boundaries. Thus constitutive laws for both types of element represent the behavior of volumes of material that on the scale of a single element are close to unidirectional (UD) composites with fiber volume fraction the same as the overall fiber volume fraction in the whole composite.

The UD composite is transversely isotropic on scales much larger than the fiber diameter. The required UD elastic properties are Young's modulus in the fiber direction,  $E_x^{(UD)}$ , Poisson's ratio for loading along the fibers,  $\nu_{xy}^{(UD)}$ , the axial shear modulus,  $G_{xy}^{(UD)}$ , and the shear modulus,  $G_{yz}^{(UD)}$ , and Poisson's ratio,  $\nu_{yz}^{(UD)}$ , in planes of isotropy (normal to the fiber direction). These properties can be accurately estimated from those of the fibers and resin (Table B.1) by micromechanical models in the literature. For anisotropic fibers, the average of Hashin's bounds [Hashin, 1979] is recommended and leads for a typical fiber volume fraction to the UD composite properties shown in Table 2. For isotropic fibers, Christensen's model [Christensen, 1990] gives virtually identical results.<sup>2</sup>

**Table B.1 Fiber and resin properties for AS4 fibers and Shell 1895 resin**

Fiber properties (transversely isotropic)

Axial Young's modulus (GPa)	Axial Poisson's ratio	Axial shear modulus (GPa)	Transverse Young's modulus (GPa)	Transverse Poisson's ratio	Density (kg-m <sup>-3</sup> )
235	0.25	55	17	0.27	1850

Resin Properties (isotropic)

Young's modulus (GPa)	Poisson's ratio
3.7	0.3

**Table B.2 UD composite properties for a typical fiber volume fraction**

$E_x^{(UD)}$ (GPa)	$\nu_{xy}^{(UD)}$	$G_{xy}^{(UD)}$ (GPa)	$E_y^{(UD)}$ (GPa)	$\nu_{yz}^{(UD)}$
147	0.267	5.50 <sup>(a)</sup>	8.72	0.340

The stiffness components of effective medium elements in the global coordinate system of Fig. 5 are prescribed as follows:

$$E_3^{(m)} = E_y^{(UD)} \quad (B.1)$$

$$G_{12}^{(m)} = G_{xy}^{(UD)} \quad (B.2)$$

<sup>2</sup> Experimental data may be available for  $\{E_x^{(UD)}, \nu_{xy}^{(UD)}, G_{xy}^{(UD)}, G_{yz}^{(UD)}, \nu_{yz}^{(UD)}\}$  from tests on UD composites rather than data for the fibers and matrix separately. In this case, the micromechanical models for UD composites need not be used or perhaps used only to fill out UD properties that are not included in the data base.

$$G_{31}^{(m)} = G_{23}^{(m)} = G_{yz}^{(UD)} \quad (B.3)$$

$$\nu_{23}^{(m)} = \nu_{31}^{(m)} = \nu_{12}^{(m)} = \nu_{xy}^{(UD)} \quad (B.4)$$

$$E_1^{(m)} = E_2^{(m)} = 2(1 + \nu_{12}^{(m)})G_{12}^{(m)} \quad (B.5)$$

The spring constants for stuffer and filler tow elements are prescribed as follows.

$$k_s = \frac{a_2 f_s}{n_s} [E_x^{(UD)} - E_y^{(UD)}] \quad (B.6)$$

$$k_f = \frac{a_1 f_f}{n_s + 1} [E_x^{(UD)} - E_y^{(UD)}] \quad (B.7)$$

where  $n_s$  is the number of layers of stuffers,  $f_s$  and  $f_f$  are the fractions of all fibers contained in stuffers and fillers respectively,  $a_1$  and  $a_2$  are defined in Fig. 5, and  $t$  is the total thickness of the composite in the direction  $x_3$ . Warp weaver spring constants are prescribed by

$$k_w = \frac{E_x^{(UD)} - E_y^{(UD)}}{y_w V \rho_w} \quad (B.8)$$

for either body or surface warp weavers, where  $y_w$  is the yield of the tow (length per unit mass),  $V$  the overall volume fraction of fibers, and  $\rho_w$  the density of the fibers in the tow. The contact spring between a warp weaver and the filler around which it wraps is prescribed by

$$k_{wf} = a_1 \sqrt{\frac{1}{y_w V \rho_w} E_y^{(UD)}} \quad (B.9)$$

## References.

Ashby, M. F., *Cambridge Materials Selector*, Cambridge University Press, Cambridge, 1995.

R.M. Christensen, "A Critical Evaluation for a Class of Micromechanics Models," *J. Mech. Phys. Solids*, **38**, 379-404 (1990).

B. N. Cox, "Delamination and Buckling in 3D Composites," *J. Comp. Mater.*, **28** (1994) 1114-26.

B. N. Cox, M. S. Dadkhah, R. V. Inman, W. L. Morris, and J. Zupon, "Mechanisms of Compressive Failure in 3D Composites," *Acta Met. Mater.* **40**, 3285-3298 (1992).

B. N. Cox, M. S. Dadkhah, W. L. Morris, and J. G. Flintoff, "Failure Mechanisms of 3D Woven Composites in Tension, Compression, and Bending," *Acta Metallurgica et Materialia*, **42** (1994a) 3967-84.

B. N. Cox, W. C. Carter, and N. A. Fleck, "A Binary Model of Textile Composites: I Formulation," *Acta Metall. Mater.* **42**, 3463-79 (1994b).

B. N. Cox and M. S. Dadkhah, "The Macroscopic Elasticity of 3D Woven Composites," *J. Comp. Mater.* **29**[6], 785-819 (1995).

M. S. Dadkhah, W. L. Morris, and B. N. Cox, "Compression-Compression Fatigue in 3D Woven Composites," *Acta Metall. Mater.* **43**[12], 4235-45 (1995).

B. N. Cox, M. S. Dadkhah, and W. L. Morris, "On the Tensile Failure of 3D Woven Composites," *Composites* **27A**, 447-58 (1996).

Fleck, N. A. (1991), Brittle Fracture due to an Array of Microcracks, *Proc. Roy. Soc. London A* **432**, 55-76.

Z. Hashin, "Analysis of Properties of Fiber Composites with Anisotropic Constituents," *J. Appl. Mech.*, **46**, 543-550 (1979).

Mouritz, A., Tensile failure paper, 1999.

Xia, Z. C., and Hutchinson, J. W. (1994), Mode II Fracture toughness of a Brittle Adhesive Layer, *Int. J. Solids Structures*, **31**, 1133-1148.

J. Xu, B. N. Cox, M. A. McGlockton, and W. C. Carter, "A Binary Model of Textile Composites: II Elastic Regime," *Acta Metall. Mater.* **43**, 3511-24 (1995).

**Table 1. Element Dimensions, Spring Constants, Elastic Constants, with Typical Values for a Layer-to-Layer Angle Interlock Weave (specimen *h-L-1*).**

Symbol	Parameter	Typical Value
$a_1$	Centre-to-centre separation of fillers	2.06 mm
$a_2$	Centre-to-centre separation of stuffers	0.96 mm
$a_3$	Centre-to-centre separation of fillers and stuffers in direction $x_3$	0.65 mm
$a_3'$	Half-thickness of outer layer of fillers	0.21 mm
$t$	Composite thickness in direction $x_3$	5.62 mm
$n_s$	Number of layers of stuffers	4
$k_s$	Spring constant for stuffer element	218,000 N = 218 GPa-mm <sup>2</sup>
$k_f$	Spring constant for filler element	109,000 N = 109 GPa-mm <sup>2</sup>
$k_w$	Spring constant for warp weaver element <sup>(a)</sup>	51,000 N = 51 GPa-mm <sup>2</sup>
$k_{wf}$	Spring constant for warp weaver/filler coupling <sup>(a)</sup>	10,600 N = 10.6 GPa-mm <sup>2</sup>
$E_i^{(m)}$	Young's modulus of effective medium element in direction $x_i$	8.72 GPa
$G_{23}^{(m)}, G_{31}^{(m)}$	Out-of-plane shear moduli of effective medium element	3.253 GPa
$G_{12}^{(m)}$	In-plane shear modulus of effective medium element	5.497 GPa
$\nu_{23}^{(m)}, \nu_{31}^{(m)}$	Out-of-plane Poisson's ratios of effective medium element	0.3402
$\nu_{12}^{(m)}$	In-plane Poisson's ratio of effective medium element	0.2665

<sup>(a)</sup>The layer-to layer angle interlock architecture contains two distinct classes of warp weaver: body warp weavers, which are the greater in number and primarily responsible for through-thickness cohesion; and surface warp weavers, which are relatively few and light in denier and hold in place some fillers in the outermost layers only. The spring constants shown are those for the body warp weavers.

## Figure Captions.

1. Sections of interlock weaves, showing nominally straight stuffers, normal sections of fillers, and fragmentary traces of warp weaver yarns.
2. Schematic showing a stuffer distorted by the pressure imposed by a filler around which a warp weaver turns. This distortion occurs during weaving and consolidation. Once the composite is consolidated, the orientations of segments of tows are not observed to change significantly, even after the severe damage associated with ultimate tensile failure and pullout.
3. Stress-strain data for (a) layer-to-layer and (b) through-the-thickness angle interlock weaves (from [Cox et al., 1996]).
4. Half a specimen after failure, showing evidence of extensive tow pullout (from [Cox et al., 1996]).
5. Small part of a Binary Model element array for a simulation of a through-the-thickness angle weave. All tow elements are shown, but only one representative effective medium element.
6. Schematic of an  $(x_1, x_3)$  plane in a Binary Model simulation showing the separation of stuffer and effective medium nodes when a stuffer slides following rupture. The effective medium and stuffer elements are drawn separately but are superimposed in the model. The stuffer elements are sliding to the left away from the rupture. The sliding displacement and disappears at the left end of the slip zone. Friction forces,  $Q_s^{(i)}$ , couple the displaced stuffer and effective medium nodes.
7. Schematic of an idealized tow geometry used to derive a micromechanical model of lockup (enhanced friction) when a stuffer slips to the left after failing in tension. The material depicted corresponds to the composite around the  $i^{\text{th}}$  stuffer element of Fig. 6.
8. Stress-strain predictions for simulations in which weak stuffer elements are correlated with the turning points of warp weavers, but are fairly uniformly distributed in space. With relatively strong lockup dilation (parameter  $\theta = 6.75^\circ$ ) and the marked values of the random stuffer misalignment parameter,  $g_s$ , and the friction coefficient,  $\mu$ .
9. Schematic showing weak flaws in two failure planes.
10. Stress-strain prediction for a simulation in which weak flaws are restricted to two failure planes lying 16 mm apart. With moderate lockup dilation (parameter  $\theta = 4.5^\circ$ ), random stuffer misalignment parameter,  $g_s = 0.1$ , and the friction coefficient,  $\mu = 0.5$ .

---

11. Evolution of the through-thickness Poisson's ratio,  $\nu_{13}$ , in the simulation of Fig. 10.
12. Stress-strain predictions for simulations in which weak flaws are restricted to two failure planes lying 24 mm apart (a – d) or 8 mm apart (e – f). The lockup dilation angle  $\theta = 2.25^\circ$  or  $9^\circ$  and the friction coefficient  $\mu = 0.25$  or  $1.0$ , as marked. Plasticity is considered in effective medium elements, but not stuffer misalignment ( $g_s = 0$ ).
13. The work of fracture predicted in the simulations represented by Fig. 12.

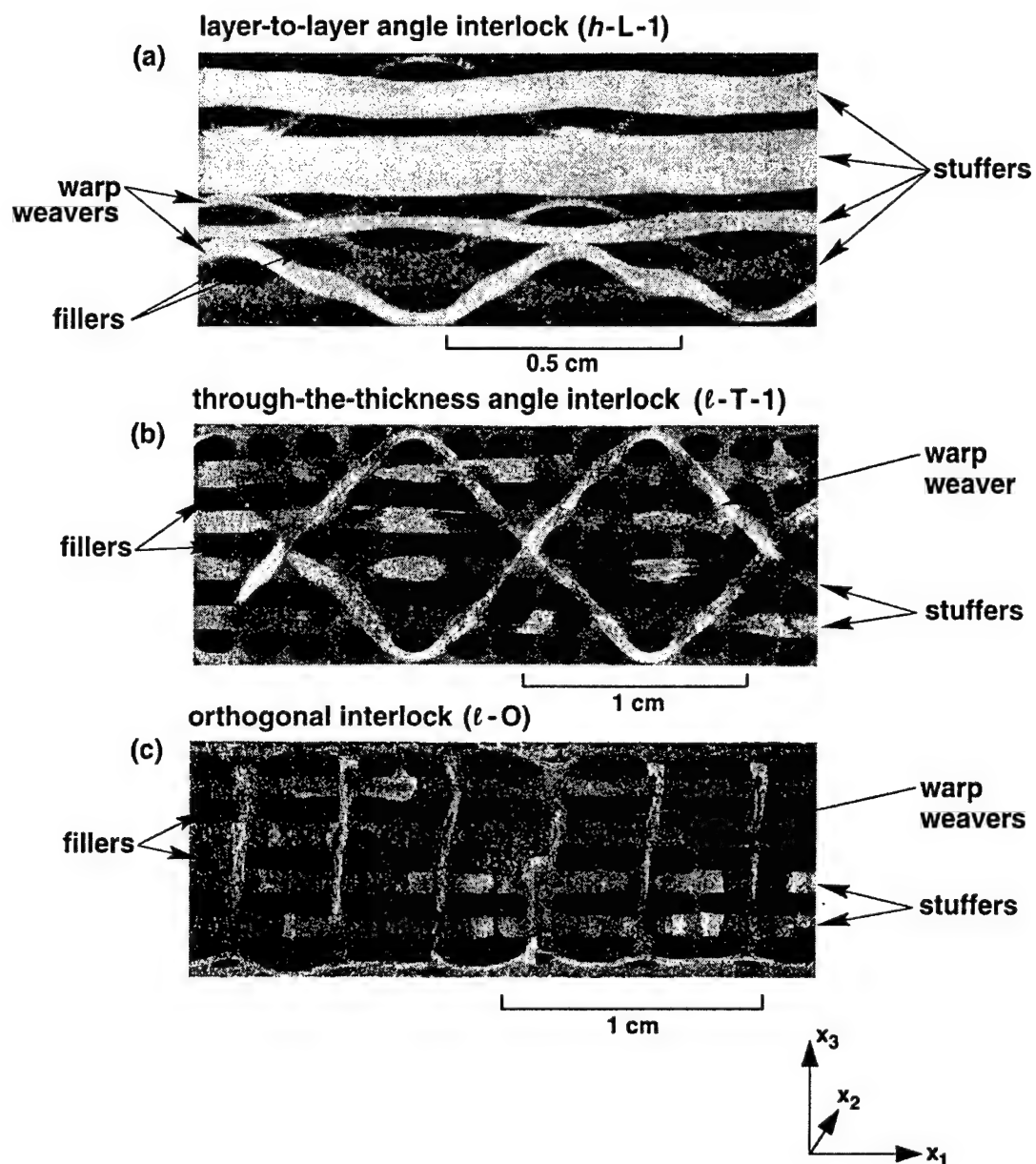
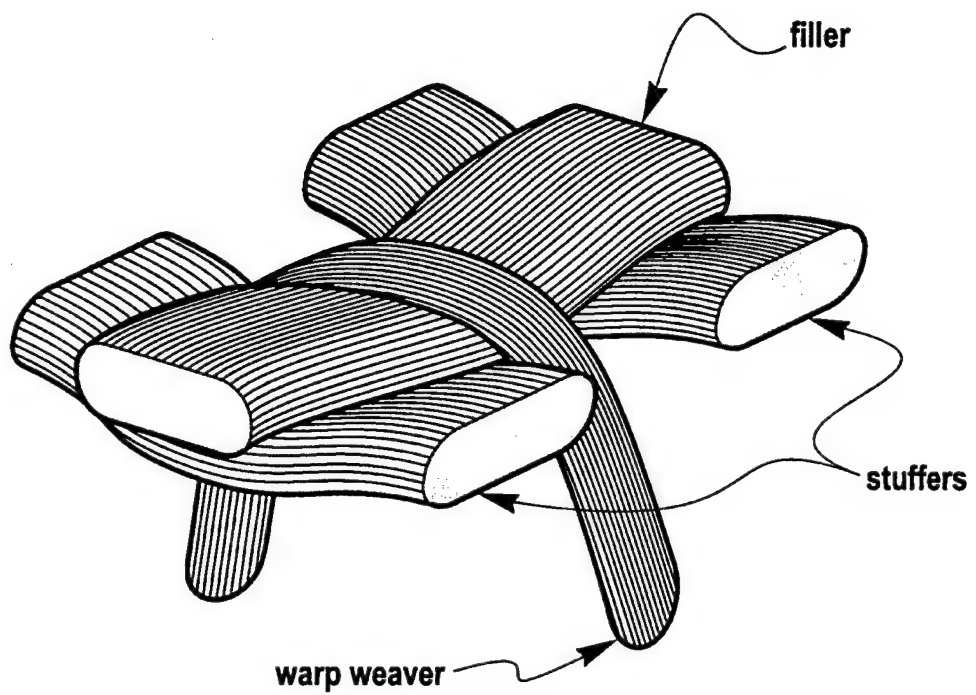


Figure 1



SC.0712C.040198

Figure 2

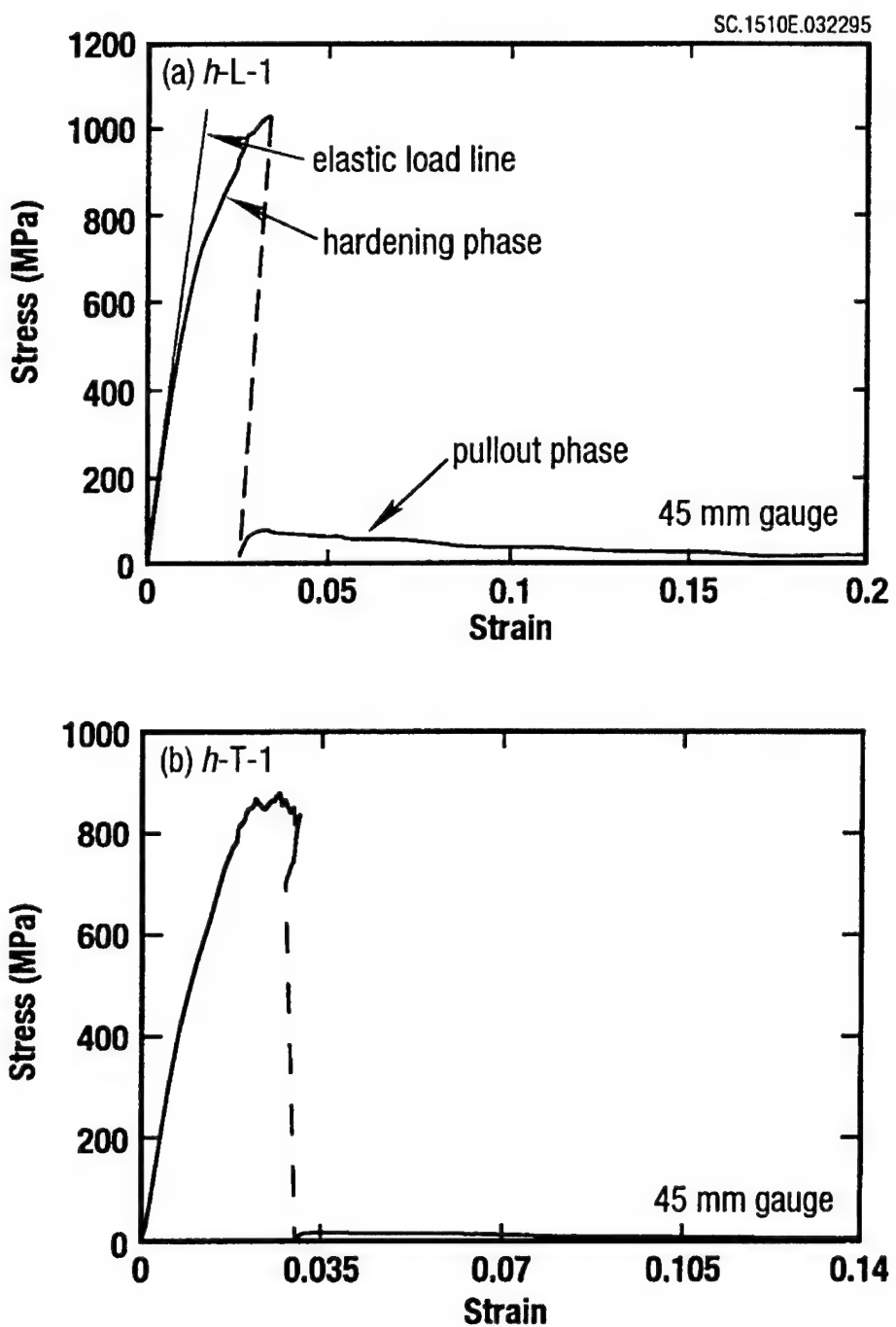


Figure 3

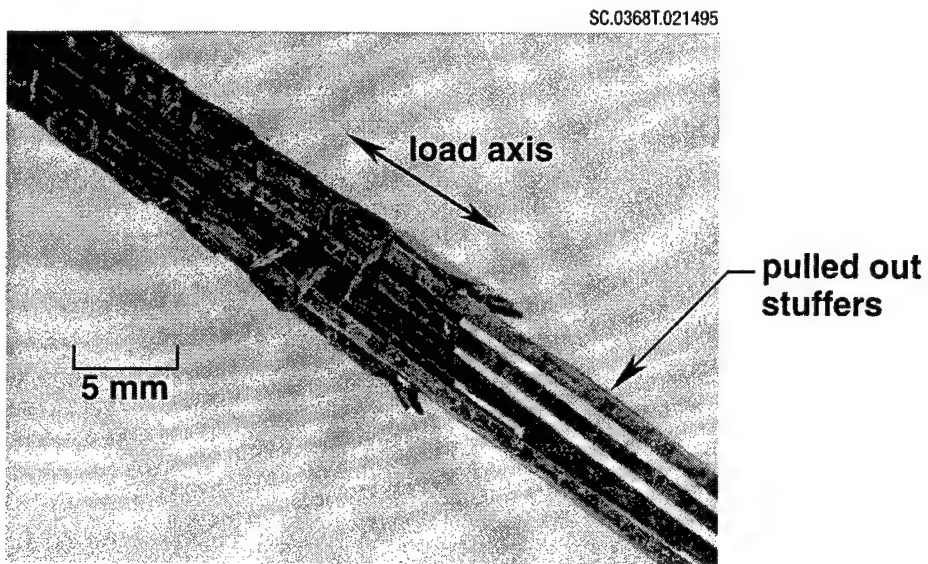


Figure 4

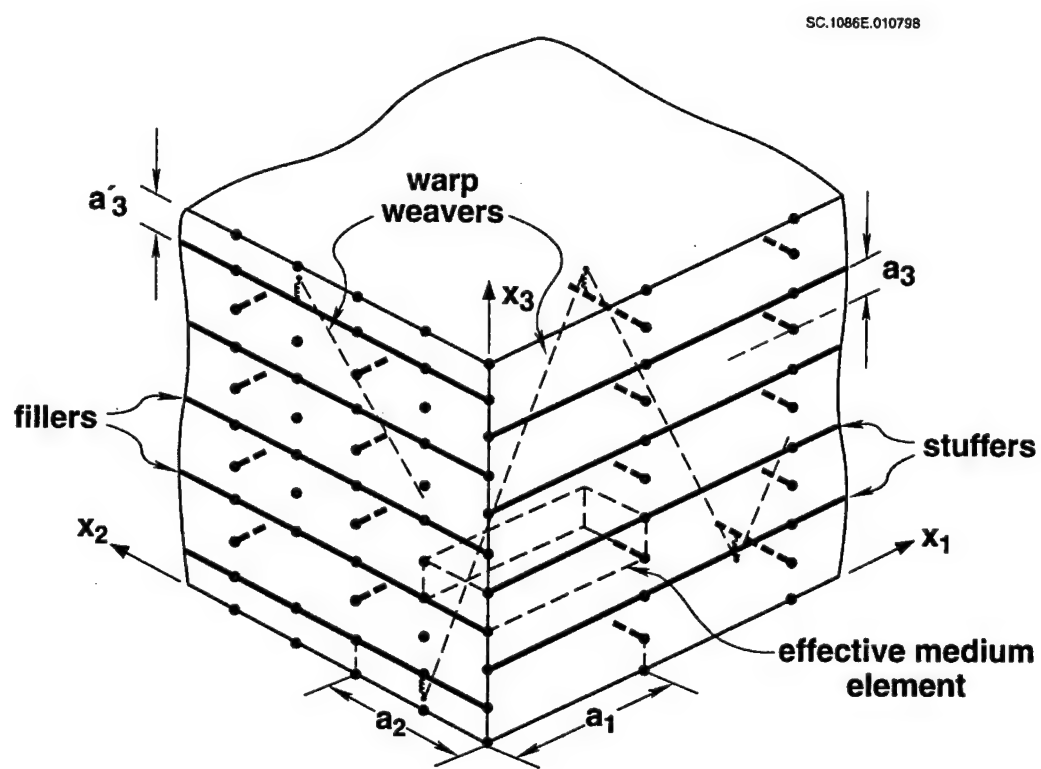


Figure 5

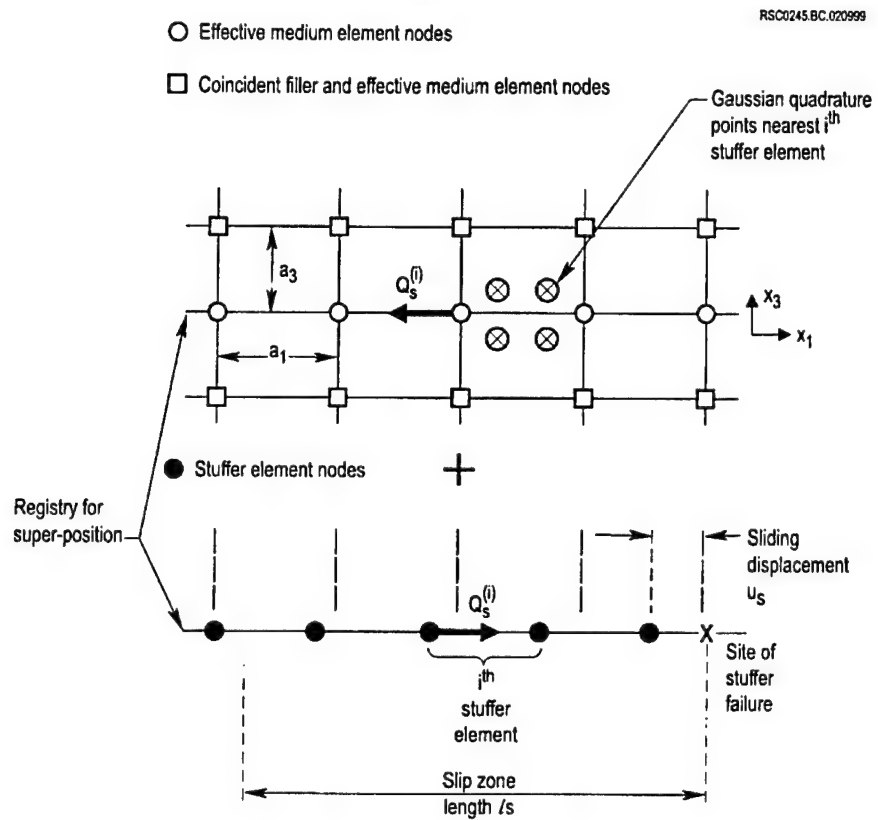


Figure 6

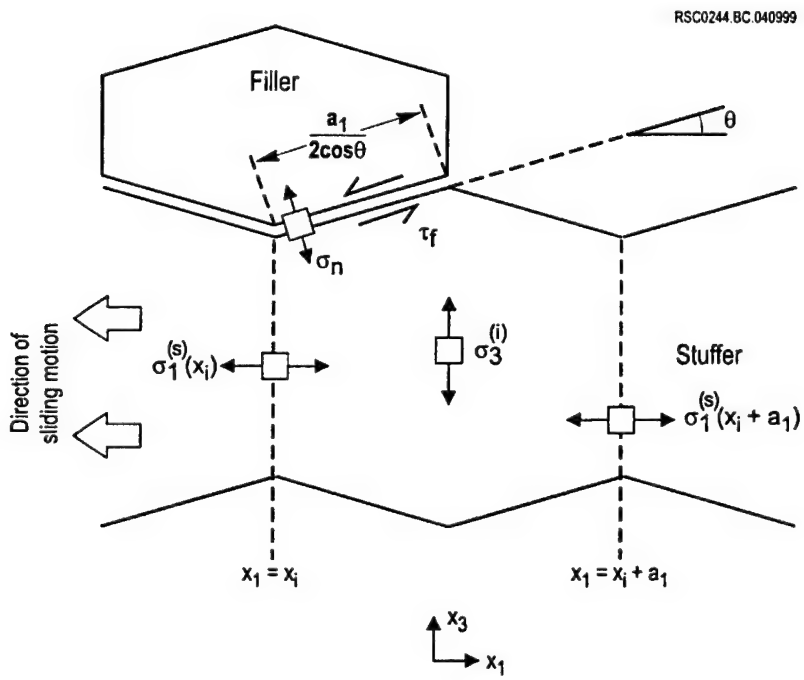


Figure 7

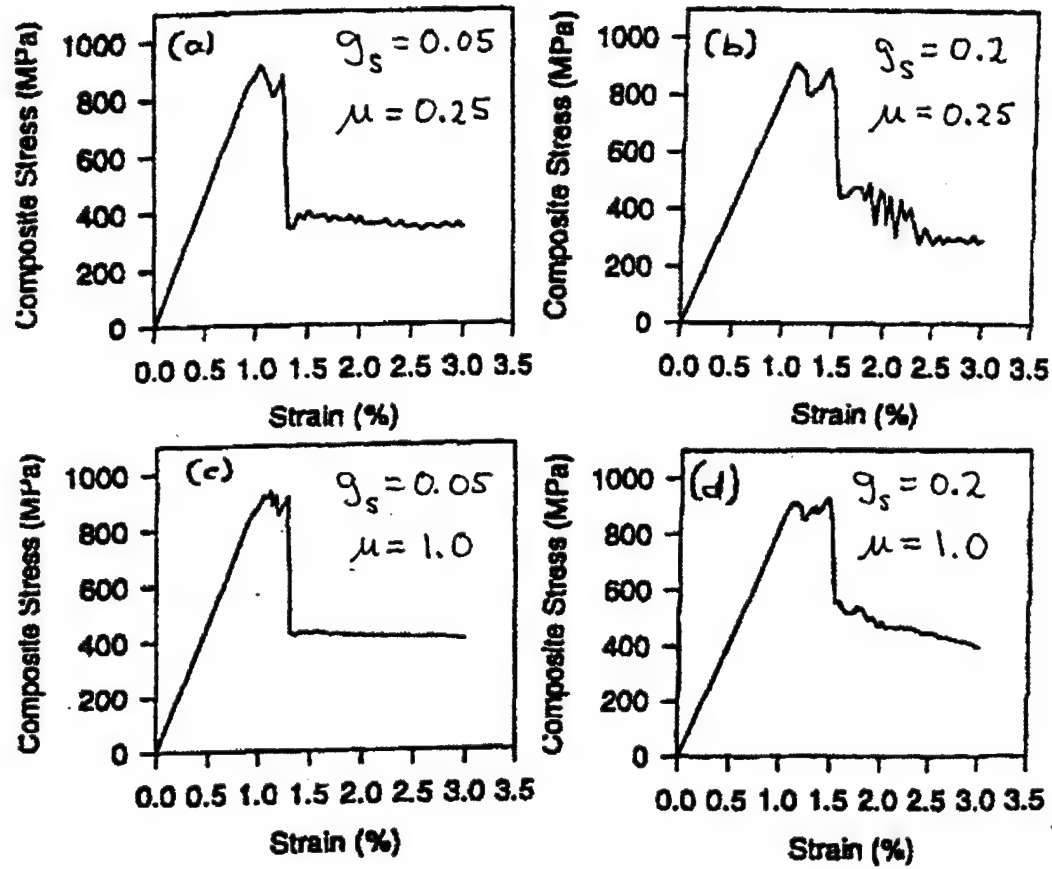


Figure 8

**Figure 9. (Unavailable at time of printing)**

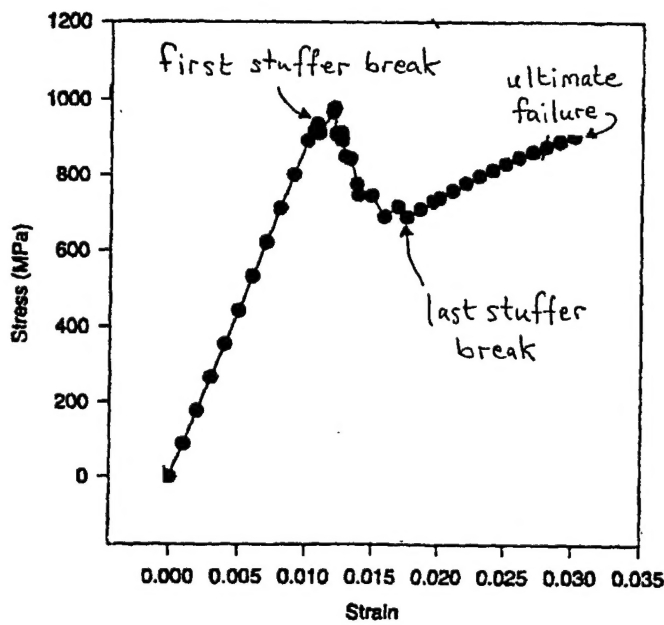


Figure 10

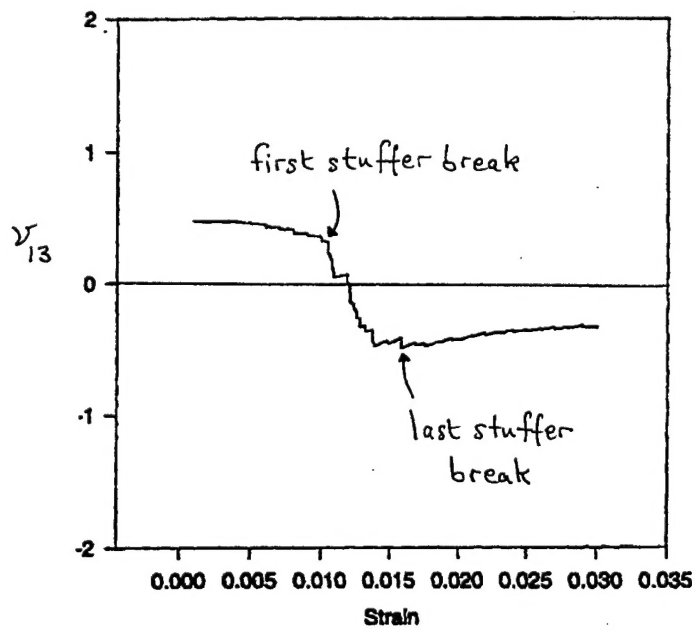


Figure 11

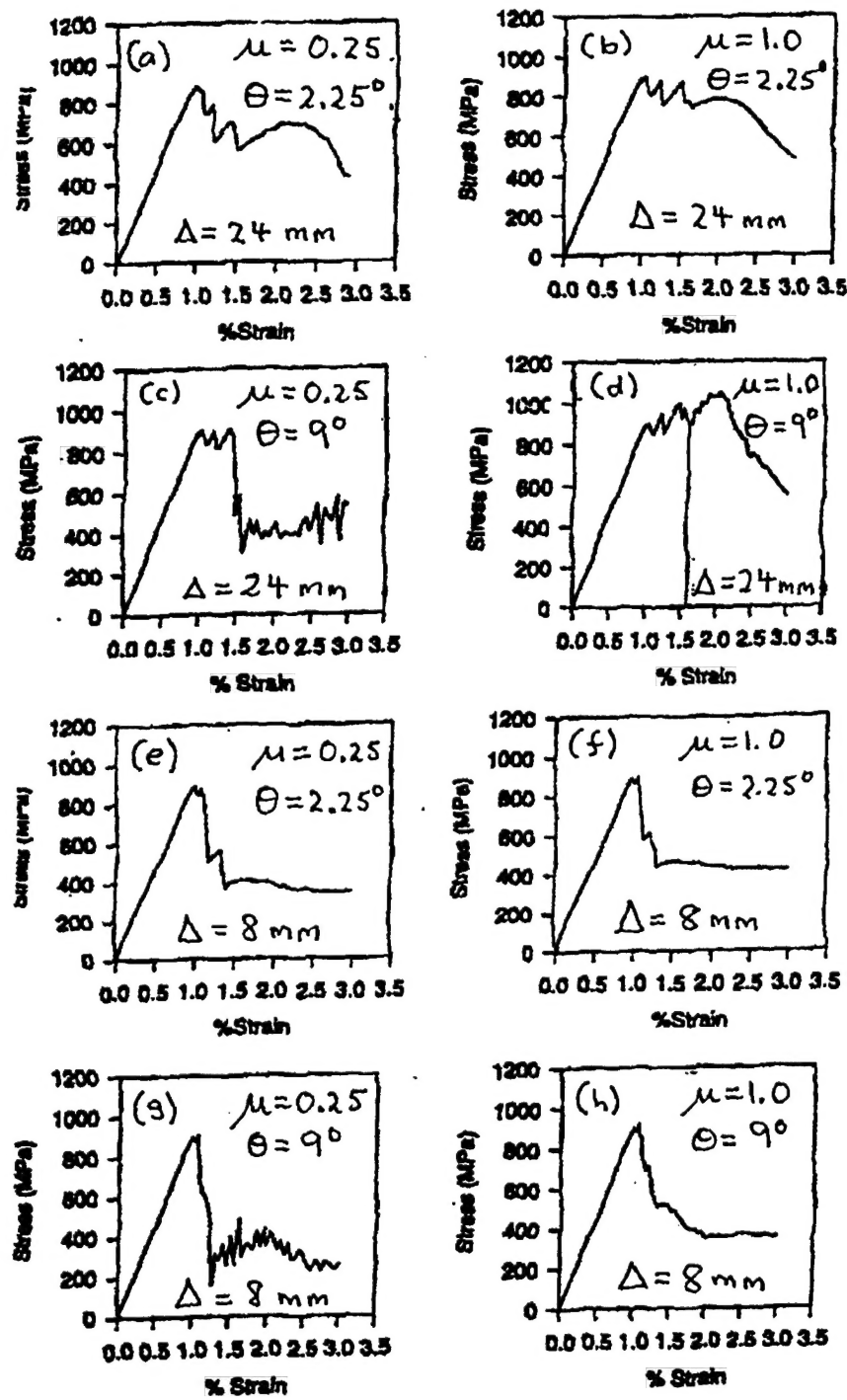


Figure 12

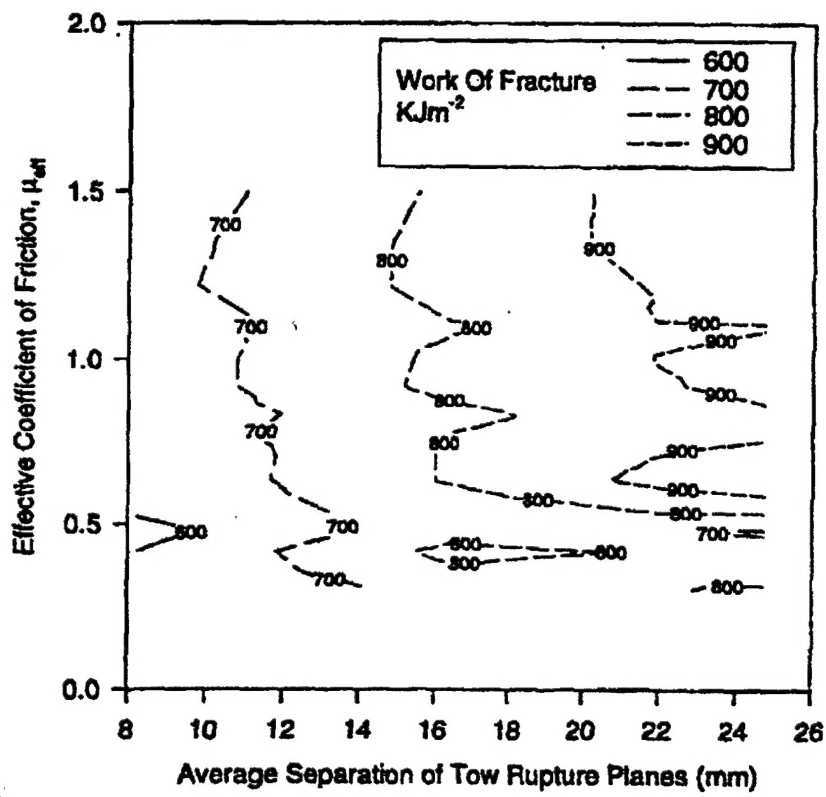


Figure 13